Scalable carbon nanotube growth and design of efficient catalysts for Fischer-Tropsch synthesis

by

Haider H. Almkhelfe

B.S., University of Technology, Baghdad, 2004
M.S., Florida Institute of Technology, 2013

AN ABSTRACT OF A DISSERTATION

submitted in partial fulfillment of the requirements for the degree

DOCTOR OF PHILOSOPHY

Department of Chemical Engineering
College of Engineering

KANSAS STATE UNIVERSITY
Manhattan, Kansas

2017

Abstract

The continued depletion of fossil fuels and concomitant increase in greenhouse gases have encouraged worldwide research on alternative processes to produce clean fuel. Fischer-Tropsch synthesis (FTS) is a heterogeneous catalytic reaction that converts syngas (CO and H_2) to liquid hydrocarbons. FTS is a well-established route for producing clean liquid fuels. However, the broad product distribution and limited catalytic activity are restricting the development of FTS. The strong interactions between the active metal catalyst (Fe or Co) and support (Al_2O_3, SiO_2 and TiO_2) during post-synthesis treatments of the catalyst (such as calcination at ~500°C and reduction ~550°C) lead to formation of inactive and unreducible inert material like Fe_2SiO_4, $CoAl_2O_4$, Co_2SiO_4. The activity of FTS catalyst is negatively impacted by the presence of these inactive compounds. In our study, we demonstrate the use of a modified photo-Fenton process for the preparation of carbon nanotube (CNT)-supported Co and Fe catalysts that are characterized by small and well-dispersed catalyst particles on CNTs that require no further treatments. The process is facile, highly scalable, and involves the use of green catalyst precursors and an oxidant. The reaction kinetic results show high CO conversion (85%), selectivity for liquid hydrocarbons and stability.

Further, a gaseous product mixture from FTS (C1-C4) was utilized as an efficient feedstock for the growth of high-quality, well-aligned single-wall carbon nanotube (SWCNT) carpets of millimeter-scale heights on Fe and (sub) millimeter-scale heights on Co catalysts via chemical vapor deposition (CVD). Although SWCNT carpets were grown over a wide temperature range (between 650 and 850°C), growth conducted at optimal temperatures for Co (850°C) and Fe (750°C) yielded predominantly SWCNTs that are straight, clean, and with sidewalls that are largely free of amorphous carbon. Also, low-temperature CVD growth of CNT carpets from Fe and Fe–Cu catalysts using a gaseous product mixture from FTS as a superior carbon feedstock is demonstrated. The efficiency of the growth process is evidenced by the highly dense, vertically aligned CNT structures from both Fe

and Fe–Cu catalysts even at temperatures as low as 400°C–a record low growth temperature for CNT carpets obtained via conventional thermal CVD. The use of FTS-GP facilitates low-temperature growth of CNT carpets on traditional (alumina film) and nontraditional substrates (aluminum foil) and has the potential of enhancing CNT quality, catalyst lifetime, and scalability.

We demonstrate growth of SWCNT carpets with diameter distributions that are smaller than SWCNTs in conventional carpets using a CVD process that utilizes the product gaseous mixture from Fischer-Tropsch synthesis (FTS-GP). The high-resolution transmission electron microscopic (HR-TEM) and Raman spectroscopic results reveal that the use of a high melting point metal as a catalyst promoter in combination with either Co (1.5 nm ± 0.7) at 850ºC or Fe (1.9 nm ± 0.8) at 750ºC yields smaller-diameter SWCNT arrays with narrow diameter distributions.

Scalable synthesis of carbon nanotubes (CNTs), carbon nanofibers (CNFs), and onion like carbon (OLC) in a batch reactor using supercritical fluids as a reaction media is demonstrated. The process utilizes toluene, ethanol, or butanol as a carbon precursor in combination with ferrocene that serves as a catalyst precursor and a secondary carbon source. The use of supercritical fluids for growth does not only provide a route for selective growth of a variety of carbon nanomaterials, but also provides a unique one-step approach that is free of aggressive acid treatment for synthesis of CNT-supported metallic nanoparticle composites for catalysis and energy storage applications.

Scalable carbon nanotube growth and design of efficient catalysts for Fischer-Tropsch synthesis

by

Haider H. Almkhelfe

B.S., University of Technology, Baghdad, 2004
M.S., Florida Institute of Technology, 2013

A DISSERTATION

submitted in partial fulfillment of the requirements for the degree

DOCTOR OF PHILOSOPHY

Department of Chemical Engineering
College of Engineering

KANSAS STATE UNIVERSITY
Manhattan, Kansas

2017

Approved by:

Major Professor
Placidus Amama

Copyright

Abstract

The continued depletion of fossil fuels and concomitant increase in greenhouse gases have encouraged aworldwide research on alternative processes to produce clean fuel. Fischer-Tropsch synthesis (FTS) is a heterogeneous catalytic reaction that converts syngas (CO and H_2) to liquid hydrocarbons. FTS is a well-established route for producing clean liquid fuels. However, the broad product distribution and limited catalytic activity are restricting the development of FTS. The strong interactions between the active metal catalyst (Fe or Co) and support (Al_2O_3, SiO_2 and TiO_2) during post-synthesis treatments of the catalyst (such as calcination at ~500°C and reduction ~550°C) lead to formation of inactive and unreducible inert material like Fe_2SiO_4, $CoAl_2O_4$, Co_2SiO_4. The activity of FTS catalyst is negatively impacted by the presence of these inactive compounds. In our study, we demonstrate the use of a modified photo-Fenton process for the preparation of carbon nanotube (CNT)-supported Co and Fe catalysts that are characterized by small and well-dispersed catalyst particles on CNTs that require no further treatments. The process is facile, highly scalable, and involves the use of green catalyst precursors and an oxidant. The reaction kinetic results show high CO conversion (85%), selectivity for liquid hydrocarbons and stability.

Further, a gaseous product mixture from FTS (C1-C4) was utilized as an efficient feedstock for the growth of high-quality, well-aligned single-wall carbon nanotube (SWCNT) carpets of millimeter-scale heights on Fe and (sub) millimeter-scale heights on Co catalysts via chemical vapor deposition (CVD). Although SWCNT carpets were grown over a wide temperature range (between 650 and 850°C), growth conducted at optimal temperatures for Co (850°C) and Fe (750°C) yielded predominantly SWCNTs that are straight, clean, and with sidewalls that are largely free of amorphous carbon. Also, low-temperature CVD growth of CNT carpets from Fe and Fe–Cu catalysts using a gaseous product mixture from FTS as a superior carbon feedstock is demonstrated. The efficiency of the growth process is evidenced by the highly dense, vertically aligned CNT structures from both Fe

and Fe–Cu catalysts even at temperatures as low as 400 °C–a record low growth temperature for CNT carpets obtained via conventional thermal CVD. The use of FTS-GP facilitates low-temperature growth of CNT carpets on traditional (alumina film) and nontraditional substrates (aluminum foil) and has the potential of enhancing CNT quality, catalyst lifetime, and scalability.

We demonstrate growth of SWCNT carpets with diameter distributions that are smaller than SWCNTs in conventional carpets using a CVD process that utilizes the product gaseous mixture from Fischer-Tropsch synthesis (FTS-GP). The high-resolution transmission electron microscopic (HR-TEM) and Raman spectroscopic results reveal that the use of a high melting point metal as a catalyst promoter in combination with either Co (1.5 nm ± 0.7) at 850ºC or Fe (1.9 nm ± 0.8) at 750ºC yields smaller-diameter SWCNT arrays with narrow diameter distributions.

Scalable synthesis of carbon nanotubes (CNTs), carbon nanofibers (CNFs), and onion like carbon (OLC) in a batch reactor using supercritical fluids as a reaction media is demonstrated. The process utilizes toluene, ethanol, or butanol as a carbon precursor in combination with ferrocene that serves as a catalyst precursor and a secondary carbon source. The use of supercritical fluids for growth does not only provide a route for selective growth of a variety of carbon nanomaterials, but also provides a unique one-step approach that is free of aggressive acid treatment for synthesis of CNT-supported metallic nanoparticle composites for catalysis and energy storage applications.

Table of Contents

List of Figures xi
List of Tables xvi
Acknowledgements xvii
Dedication xviii
Chapter 1 Introduction 1
1.1 Overview of Fischer Tropsch Synthesis (FTS) 1
1.2 Objectives of This Study 3
References 6
Chapter 2 Carbon Nanotube-Supported Catalysts Prepared by a Modified Photo-Fenton Process for Fischer-Tropsch Synthesis 7
2.1 Introduction 8
2.2 Experimental 11
2.2.1 Catalyst Preparation 11
2.2.2 Catalyst Characterization 12
2.2.3 Catalytic Testing 14
2.3 Results and Discussion 15
2.3.1 Functionalization of CNTs and Catalyst Deposition 15
2.3.2 Characterization of Catalysts 19
2.3.3 Catalytic Testing 25
2.4 Conclusions 34
References 35
Chapter 3 Gaseous Product Mixture from Fischer-Tropsch Synthesis as an Efficient Carbon Feedstock for Low Temperature CVD Growth of Carbon Nanotube Carpets 41
3.1 Introduction 42
3.2 Results and Discussion 45
3.3 Experimental Details 62
References 64
Chapter 4 Catalytic CVD Growth of Millimeter-Tall Single-Wall Carbon Nanotube Carpets Using Industrial Gaseous Waste as a Feedstock 69

4.1 Introduction 70
4.2 Experimental 72
4.3 Results 73
4.4 Discussion 85
4.5 Conclusions 88
References 89
Chapter 5 In-Situ Generation of Water during FTS-GP CVD 95
5.1 Introduction 95
5.2 Experimental 95
5.3 Results and Discussion 96
5.4 Conclusions 99
References 100
Chapter 6 Chiral and Diameter Control of SWCNTs Using High Melting Point Metals as Promoters 101
6.1 Introduction 102
6.2 Experimental 105
6.3 Result and Discussion 107
6.4 Conclusions 112
References 113
Chapter 7 Batch Reactor for the Scale-up Production of Carbon Nanomaterials 116
7.1 Introduction: 117
7.2 Experimental: 119
7.3 Characterization: 119
7.4 Results and Discussion: 121
7.5 Conclusions 131
References 132
Chapter 8 Conclusions and Future Work 137
8.1 Conclusions 137
8.2 Future work 140
Appendix A - Supplemental Information for Chapter 2 141
Appendix B - Supplemental Information for Chapter 3 149

Appendix C - Supplemental Information for Chapter 4 156
Appendix D - Supplemental Information for Chapter 6 162
Appendix E - Supplemental Information for Chapter 7..... 165
Appendix F - Copyright permissions..... 172

List of Figures

Figure 1-1 Schematic of closed-Loop Material Model –FTS and CNT Synthesis..... 5
Figure 2-1 Schematic illustration of the modified photo-Fenton process for CNT oxidation and catalyst deposition..... 11
Figure 2-2 Deconvolution of XPS C 1s spectra of (a) as-received CNTs, (b) H_2O_2-treated CNTs, (c) UV/H_2O_2-treated CNTs, and (d) HNO_3-treated CNTs..... 18
Figure 2-3 Loading amount of Fe or Co on CNTs as a function of time during photo-Fenton process..... 19
Figure 2-4 XRD patterns of fresh Fe and Co catalysts on different supports (CNTs and SiO_2) synthesized by photo-Fenton and IWI methods..... 20
Figure 2-5 Low- and high-magnification TEM images and corresponding histograms of PSDs with Gaussian analysis fittings of fresh catalysts: Co/CNT-Fenton (a,b), Fe/CNT-Fenton (c,d), Co/CNT-IWI (e,f), and Fe/CNT-IWI (g,h)..... 22
Figure 2-6 H_2-TPR profiles of prepared catalysts: (a) Fe/CNT-Fenton and Co/CNT-Fenton, (b) Fe/CNT-IWI and Co/CNT-IWI, and (c) Fe/SiO_2-IWI and Co/SiO_2-IWI..... 24
Figure 2-7 CO conversion and selectivity of liquid hydrocarbon (C5+) as functions of FTS reaction temperature for catalysts synthesized by photo-Fenton and IWI: (a, b) CNT and SiO_2-supported Co, and (c, d) CNT and SiO_2-supported Fe..... 27
Figure 2-8 High-resolution TEM images of (a) Co/CNT-IWI and (b) Co/CNT-Fenton with their selected-area electron diffraction patterns as inserts showing a phase consistent FCC for sample (a) and HCP for sample (b)..... 29
Figure 2-9 Variation of FTS activity and stability with time. (a) CO conversion of CNT- and SiO_2-supported Co catalysts (b) and CNT- and SiO_2-supported Fe catalysts as a function of time. 31
Figure 2-10 Low- and high-magnification TEM images and corresponding histograms of PSDs with Gaussian analysis fittings of used catalysts: Co/CNT-Fenton (a,b), Fe/CNT-Fenton (c,d), Co/CNT-IWI (e,f), and Fe/CNT-IWI (g,h)..... 32
Figure 2-11 Amount of catalyst particles detached from CNTs during mild sonication of Co/CNT-IWI, Fe/CNT-IWI, Co/CNT-Fenton, and Fe/CNT-Fenton..... 33

Figure 3-1 CNT carpets grown at low temperatures using FTS-GP for 1h. SEM images of carpets grown on Al_xO_y/Fe at 400°C (A), Al_xO_y/Fe-Cu at 400°C (B), Al_xO_y/Fe at 450°C (C), Al_xO_y/Fe-Cu at 450°C (D), Al_xO_y/Fe at 500°C (E), Al_xO_y/Fe-Cu at 500°C (F), Al_xO_y/Fe at 550°C (G), and Al_xO_y/Fe-Cu at 550°C (H). 46

Figure 3-2 Raman spectra of CNT carpets grown on Al_xO_y/Fe (black) and Al_xO_y/Fe-Cu (red) at different temperatures under excitation of 532 nm laser. 47

Figure 3-3 CNT carpet properties after 30 min of CVD process over Fe and Fe-Cu catalysts. Quality of CNT carpets (I_G/I_D) as a function of growth temperature (A). Product mass obtained on catalysts as a function of growth temperature (B). CNT carpet height as a function of growth temperature (C). CNT carpet quality (I_G/I_D) and yield or density (I_G/I_{Si}) as a function of the Cu thickness in Al_xO_y/Fe-Cu catalyst (D). 49

Figure 3-4 TEM micrographs of CNTs grown at 400°C over Al_xO_y/Fe (A and B) and Al_xO_y/Fe-Cu (C and D) catalysts after 1 h. 51

Figure 3-5 High-resolution TEM micrographs of CNTs grown at 400°C over Al_xO_y/Fe (A and B) and Al_xO_y/Fe-Cu (C and D) catalysts after 1 h. Panels B and D illustrate the hollow interior, parallel graphitic planes along the tube walls; the insets show the distinct inter-wall spacing of ~0.34 nm. 52

Figure 3-6 TEM micrographs of CNTs grown at 500°C over Al_xO_y/Fe (A and B) and Al_xO_y/Fe-Cu (C and D); their corresponding high-resolution micrographs are shown in panels B and D. (E) CNT diameter distribution obtained from Fe and Fe-Cu catalysts and their Gaussian fits with means of 4.4 nm and 5.6 nm, respectively [sigma (Fe) = 0.77, sigma (Fe-Cu) = 1.69]. 54

Figure 3-7 Average CNT carpet height as a function of time for growth conducted at 400, 450, 500, and 550°C over Al_xO_y/Fe (A) and Al_xO_y/Fe-Cu (B) catalysts. Arrhenius plots for CNT carpet growth on Al_xO_y/Fe-Cu and Al_xO_y/Fe catalysts with estimated apparent activation energy, E_a of 0.72 and 0.54 eV, respectively (C). 56

Figure 3-8 FESEM images of CNT carpets grown at 450°C on aluminum foil with Fe catalyst directly deposited on aluminum (A), and Fe catalyst deposited on aluminum with a 10 nm-thick Al_xO_y barrier layer (B). 59

Figure 3-9 Proposed mechanism to explain the role of FTS-GP in low-temperature growth of CNT carpets. The Gibbs free energies for the decomposition reactions of CH_4, C_2H_6, C_3H_8, C_2H_4, and C_3H_6 are 20, -35, -80, -300, and -410 kJ/mol, respectively (Ref. 58). 61
Figure 4-1 Raman spectra of SWCNT carpets grown by FTS-GP CVD at different temperatures (650, 750 and 850°C) on a Fe catalyst (a) and a Co catalyst (b), using a laser excitation energy source of 1.96 eV. 74
Figure 4-2 TEM characterization of SWCNT carpets grown by FTS-GP CVD at optimum temperatures. (a, b) Low- and high-magnification images of SWCNTs grown on an Fe catalyst at 750°C. (c and d) Low- and high-magnification images of SWCNTs grown on a Co catalyst at 850°C. Histograms of SWCNT diameter distributions and their Gaussian fits of SWCNT carpets grown on Fe catalysts (e) and Co catalysts (f); SWCNT diameters were measured from 90 nanotubes by HRTEM; mean diameters for SWCNTs from Fe and Co catalysts were 3.1 and 2.2 nm, respectively. 76
Figure 4-3 TGA/DTA profiles of SWCNT carpets grown on an Fe catalyst (a) and a Co catalyst (b) obtained using a ramp rate of 5°C/min under air flow. 77
Figure 4-4 Characterization of SWCNT carpets by SEM. SEM images of SWCNT carpets grown from (a) an Fe catalyst at 750°C and (b) a Co catalyst at 850°C after 90 min. Plots of SWCNT carpet height measured from their respective SEM images as a function of growth time for Fe (c) and Co (d) catalysts. Growth temperature for each catalyst corresponds to the temperature that showed the highest SWCNT selectivity. 79
Figure 4-5 SEM images of SWCNT carpets grown on an Fe catalyst at 750°C (a) and a Co catalyst at 850°C (b) for 90 min after ethanol-induced densification to estimate areal density of the carpets. Panels (c) and (d) are respective false-color versions of (a) and (b), showing the compacted area of the densified carpets. Areal coverage of SWCNTs grown on Fe and Co are 21.4% and 30.5%, respectively. 81
Figure 4-6 SWCNT carpet height and mass density as functions of FTS-GP fraction in growth gas with Ar as the diluent for (a) Fe catalyst at 750°C and (b) Co catalyst at 850°C (growth time = 90 min). 84
Figure 4-7 SWCNT carpet height as a function of growth time for FTS-GP CVD, compared to previous studies involving various feedstocks (hydrocarbon, alcohol, and hydrocarbon in combination with water or supergrowth). 85

Figure 4-8 Schematic illustration of the role of FTS-GP in enhancing catalyst lifetime of Fe catalyst during FTS-GP CVD. 87
Figure 5-1 (a) A plot of amount of water generated during thermal decomposition of FTS-GP in a batch reactor as a function of temperature. (b) Plots of amount of water generated for various FTS-GP fraction as a function of temperature determined from theoretical calculations using Equation 5. 97
Figure 5-2 (a) Growth rate of FTS-GP (10 vol. %) on Fe catalyst at different growth temperature, (b) Raman spectra of SWCNT carpets grown by FTS-GP CVD at different temperatures (650, 700, 750 and 800°C) on an Fe catalyst using a laser excitation energy source of 1.96 eV. 99
Figure 6-1 AFM images of catalysts nanoparticles formed on the substrate after annealing for 5 min in H_2 at 850ºC for (a) Co catalyst and (b) Co/Ru catalyst. 107
Figure 6-2 HR-TEM images of SWCNT grown by FTS-GP CVD at 850˚C. (a,b) High-and low-magnification images of SWCNTs grown on a Co/Ru catalyst. (d,e) High-and low-magnification images of SWCNTs grown on a Co catalyst. Histogram of SWCNT diameter distributions and their Gaussian fits of SWCNT grown on Co/Ru catalysts (c) and Co catalysts (f); mean diameters for SWCNTs from Co/Ru and Co catalysts were 1.5 and 2.5 nm, respectively. 108
Figure 6-3 Multi-excitation Raman spectra of SWCNT synthesized at 750˚C on (a) Fe catalyst and (b) Fe/Ru catalyst. 109
Figure 6-4 Multi-excitation Raman spectra of SWCNT synthesized as 850˚C on (a) Co catalyst and (b) Co/Ru catalyst. 110
Figure 7-1 SEM images and Raman spectra of carbon nanomaterials synthesized in supercritical toluene in the absence of water using ferrocene as catalyst at 400ºC (a,b), 500ºC (c,d), and 600ºC (e,f). 122
Figure 7-2 SEM image and EDS analysis of carbon nanofilament with encapsulated Fe nanowire obtained by heating 0.035 mole/liter of ferrocene in toluene solution at 500ºC. 123
Figure 7-3 TEM images of CNTs and filaments prepared using 0.2 g of ferrocene and 30 ml of toluene, (a) filament with bigger catalyst particle at the end of the tube, (b) CNT with defined hallow interior, and (c) particles embedded at the tip of nanotube. 124

Figure 7-4 (a) Plots of product yield and pressure of batch reactor as functions of ferrocene concentration using 30 ml of toluene at 600ºC; (b) picture of bulk quantity ~12.5 g filament and CNTs powder obtained at 0.036 mole/liter ferrocene in toluene solution; (c) Inset low-magnification SEM image of filament and CNTs. 125
Figure 7-5 Raman spectra of CNTs with different amount of water: 0.075 ml (a), 0.050 ml (b), 0.025 ml (c), and no water (d), under excitation of 633 nm laser. SEM images and corresponding histograms of diameter size distributions with Gaussian analysis fittings of CNTs: 0.05 ml of water (e) and no water (f). 126
Figure 7-6 SEM (a,b) and TEM (c,d) images of carbon-like onion (OLC) structure synthesized by using 0.035 mole/liter ferrocene in toluene solutions with 0.1 ml of water at 600ºC. Inset TEM image of OLC (e) exhibit concentrically stacked graphite sheets. 127
Figure 7-7 Illustration of the synthesis pathways for CNTs and OLC using aromatic and alcohols precursors in a batch reactor. 129
Figure 7-8 SEM images of OLCs grown at 600ºC and 0.035 mole/liter of ferrocene with: ethanol (a,b), propanol (c,d), and butanol (e,f). 130

List of Tables

Table 2-1 Summary of properties of catalyst supports (as-received) and supported catalysts prepared by photo-Fenton and IWI. 16
Table 2-2 Summary of hydrogen consumption, degree of reduction, and dispersion ratio for the different catalysts measured by TPR. 25
Table 2-3 Summary of catalytic activity and C5+ selectivity of Fe and Co catalysts synthesized by photo-Fenton and IWI deposition techniques. 28
Table 3-1 Summary of studies on low temperature growth of CNTs. 58
Table 4-1 Comparison of area densities of CNT carpets obtained from different catalyst configurations and feedstocks, including SWCNT carpets obtained from FTS-GP CVD. .. 82

Acknowledgements

I owe my deepest gratitude to my advisor, Dr. Placidus Amama, for his professional guidance, caring, patience and thoughts about both scientific research and life in general. He has taught me more than I could ever give him credit for here. He has shown me, by his example, what a good scientist (and person) should be. I would like to thank the members of my committee for their extreme patience in the face of numerous obstacles. I would especially like to thank Dr. James H. Edgar, the chairman of my committee, for all the opportunities and support that he had provided during my study. Also I would like to thank Dr. Keith Hohn for his valuable insights to this work and for providing the GC/fume hood to carry out my reaction experiments. I deeply thank all my wonderful labmates and colleagues who have been my constant source of support.

I gratefully acknowledge the TEM facility at the Air Force Research Laboratory (AFRL), Dr. Ahmad Islam for assisting with thickness measurements of the various films using AFM, Dr. Sammy Saber, and Dr. Pasha Nikolaev for assistance with initial TEM and Raman spectroscopic characterization.

Nobody has been more important to me in the pursuit of this project than the members of my family. I would like to thank my father and siblings, whose love and guidance are with me in whatever I pursue. Most importantly, I wish to thank my loving and supportive wife, Nadeen, and my two wonderful children, Qaswara and Dareen, who provide unending inspiration.

Dedication

I dedicate this dissertation to the memory of my mother,
a great woman whom I still miss every day.

Chapter 1

Introduction

1.1 Overview of Fischer Tropsch Synthesis (FTS)

World War I gave scientists the first motivation to come up with another source of fuel instead of depending on natural crude oil. Unlike the Allies that had adequate crude oil reserves for the war, Germany did not, and that alone negatively impacted them during the war. Therefore the concept of converting coal to synthesis gas and then to transportation fuels was initiated in Germany.[1] The first major work on the hydrogenation of carbon monoxide was carried out by Sabatier and co-workers in 1902. In 1923, Franz Fischer and Hans Tropsch showed that liquid fuel can be produced from synthesis gas ($CO + H_2$) obtained from gasification of coal.[2] With support from the German government, Kaiser-Wilhelm-Institute (KWI) led by Fischer conducted extensive investigations to understand and improve FTS, as well as commercialize the process.[3] Initial investigations revealed important features of FTS such as exothermicity of the reaction, the need maintain a uniform temperature in the reactor, and the advantages of using catalyst in liquid media (slurry reactor) for the reaction. After World War II, the discovery of new oil fields in the Middle East affected the economic viability of FTS process. However, fears of oil reserves depletion and rapid increase in energy demand caused a wide interest in FTS process again.[4]

Fischer-Tropsch synthesis (FTS) is a heterogeneous catalytic reaction that converts syngas (CO and H_2) to a liquid hydrocarbons. FTS is a well-established route for production of clean liquid fuels. However, the broad product distribution and limited catalytic activity are restricting the development of FTS. One of the important factors that should be considered during the design of an effective heterogeneous catalyst for FTS is the catalyst support since the mechanical strength, porosity and the interaction between the active metal and support determine the catalyst performance. The metal

dispersion, reducibility and diffusion coefficient of the reactants and products highly depend on the support's surface structure and pore size; the most common supports used in FTS reaction are SiO_2, Al_2O_3, TiO_2, ZrO_2, AC and most recently carbon nanotubes (CNTs), a novel support.[5] To examine how the supports type can influence the activity of FTS reaction, Ordomsky et al. test three different catalyst supports: SiO_2, activated carbon and CNTs supported Fe,[6] under the same operation conditions. The results showed the conversion of CO using Fe/CNTs (~85%) was much higher than the CO conversion using Fe/SiO_2. The strong interactions between the active metal catalyst (Fe or Co) and oxide support (Al_2O_3, SiO_2 and TiO_2) during post-synthesis treatments of the catalyst (such as calcination at ~500°C and reduction ~550°C) lead to formation of inactive and unreducible inert material like Fe_2SiO_4, $CoAl_2O_4$, Co_2SiO_4. The activity of FTS catalyst is negatively impacted by the presence of these inactive compounds.

Thus there is growing interest in using non-oxidic supports such as CNTs due to the high strength, better metal dispersion control and minimal formation of inactive/ unreducible components (like silicate and aluminate).[7-9] However, the use of CNTs as catalyst supports require several aggressive treatments before nanoparticles deposition due to the high hydrophobicity of CNTs (inert surfaces). Researchers have functionalized CNTs by acid treatment to create functional groups (hydroxyl, carbonyl and carboxyl) that serve as anchoring sites for active metal nanoparticles and, more importantly, increase the dispersion of active metal, which helps to increase the FTS reaction rate.[9-10]

Achieving a 100% selectivity towards liquid hydrocarbons in FTS is banned based on the kinetic rate law. So, in addition to the CO conversion and product selectivity, the undesirable gas products (C1-C4) should be wisely used to make the FTS process more feasible and efficient. It is a very common now days to see a gas flames roaring from FTS and oil refinery through a process called

flaring. However, they are a huge problem for environment, since it contributes to greenhouse gases, and waste of a valuable energy resource.

1.2 Objectives of This Study

The main objective of this study is to enhance the performance of Fischer-Tropsch synthesis (FTS) using Co and Fe as an active metals supported on CNT. It is important to find different approaches to oxidize (functionalize) the CNT without destroying its structure. Also, synthesizing the FTS catalyst in such a way that doesn't require a high calcination temperature to maximize the density of the metal active sites. Also, avoid the presence of foreign components (nitrate, chloride and acetate) which can possibly effect the catalyst activity.

We have investigated the possibility of combining the oxidation and active metal deposition in one step via the modify photo-Fenton reaction. The catalytic activity of CNT supported Co or Fe by the (photo Fenton method) was compared with conventional oxidation (strong acid treatments) and deposition method (incipient wetness impregnation).

We demonstrate improved control of Single Walled Carbon Nanotubes (SWCNTs) diameters and hence their chiralities via CVD using gaseous mixture from Fischer-Tropsch synthesis (FTS-GP) as a carbon precursor over Fe or Co catalyst with a high-melting point metal (Ru) as a catalyst promoter. The growth results show improved stabilization of catalyst in the presence of Ru as well as a shift in the diameter distributions of SWCNTs from 2.5 nm to 1.5 nm and 3.1 to 1.9 nm for Co and Fe catalyst, respectively.

Also, the role of supercritical fluid (SCF) was explored for the selective growth of carbon nanomaterials using a single-step batch reactor and super critical fluid approach with a variety of precursors: aromatics (toluene, xylene) and alcohols (ethanol, propanol and butanol) along in combination with ferrocene as a catalyst source. The effect of water in the growth process using

different precursors has been examined along with the growth temperature and loading ratio of ferrocene.

Further, this approach used the side products (C1-C4) of the FTS process to create a close loop of making materials (CNTs) via chemical vapor deposition (CVD) that can highly impact the feasibility of the FTS in a friendly environment. The schematic below, summarize the goals of this study.

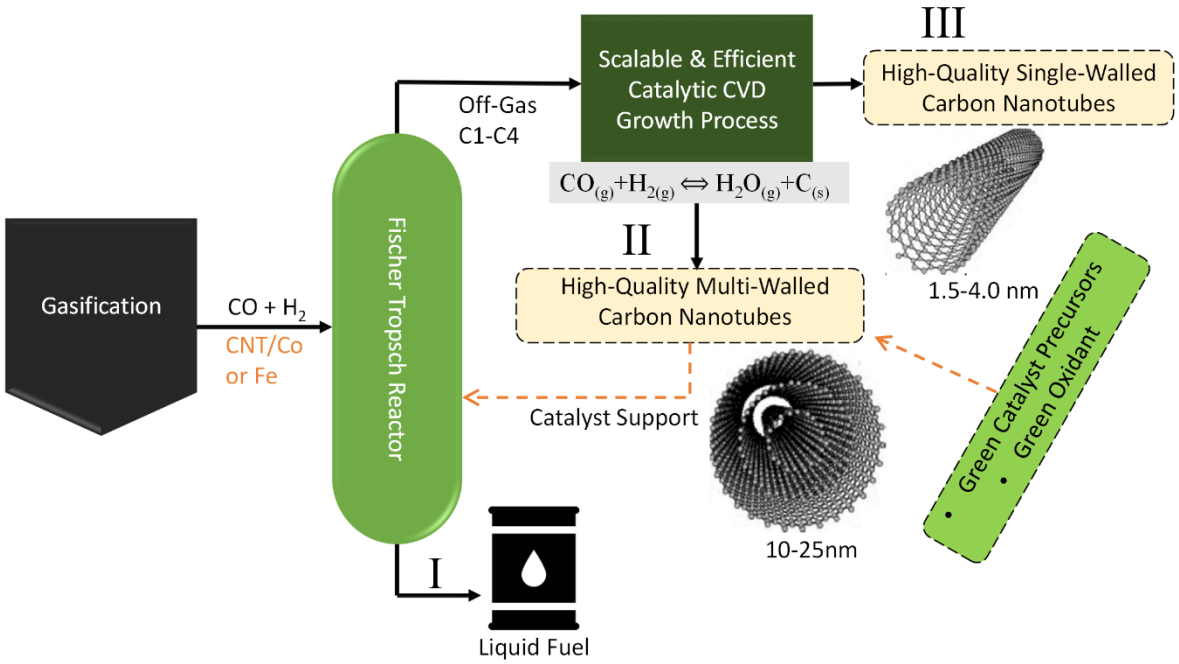

Figure 1-1 Schematic of closed-Loop Material Model –FTS and CNT Synthesis

I) Liquid hydrocarbons are produced by using carbon nanotube (CNT)-supported Co and Fe catalysts that were prepared by using a modified photo-Fenton process.

II) Low temperature growth of Multi-Walled Carbon Nanotubes (MWCNTs) carpet on traditional (Si as substrate/Al_2O_3/ Fe or Fe- promoted Cu) and nontraditional substrates (Al foil/ Al_2O_3/Fe or Al foil/Fe) at low temperatures (550-400˚C). Using a gaseous product mixture from Fischer-Tropsch synthesis (FTS-GP) as a carbon feedstock.

III) Single Walled Carbon Nanotubes (SWCNTs) carpets on Fe and on Co catalysts using a FTS-GP as a carbon feedstock.

References

1. Davis, B. H., Overview of reactors for liquid phase Fischer–Tropsch synthesis. *Catalysis Today* **2002,** *71* (3–4), 249-300.

2. Janardanarao, M., Direct catalytic conversion of synthesis gas to lower olefins. *Industrial & engineering chemistry research* **1990,** *29* (9), 1735-1753.

3. Stranges, A. N., A History of the Fischer-Tropsch Synthesis in Germany 1926–45. In *Studies in Surface Science and Catalysis*, Davis, B. H.; Occelli, M. L., Eds. Elsevier: 2007; Vol. Volume 163, pp 1-27.

4. Veziroğlu, T. N.; Şahi¨n, S., 21st Century's energy: Hydrogen energy system. *Energy Conversion and Management* **2008,** *49* (7), 1820-1831.

5. Díaz, J. A.; Akhavan, H.; Romero, A.; Garcia-Minguillan, A. M.; Romero, R.; Giroir-Fendler, A.; Valverde, J. L., Cobalt and iron supported on carbon nanofibers as catalysts for Fischer–Tropsch synthesis. *Fuel Processing Technology* **2014,** *128*, 417-424.

6. Cheng, K.; Ordomsky, V. V.; Virginie, M.; Legras, B.; Chernavskii, P. A.; Kazak, V. O.; Cordier, C.; Paul, S.; Wang, Y.; Khodakov, A. Y., Support effects in high temperature Fischer-Tropsch synthesis on iron catalysts. *Applied Catalysis A: General* **2014,** *488*, 66-77.

7. Trépanier, M.; Dalai, A. K.; Abatzoglou, N., Synthesis of CNT-supported cobalt nanoparticle catalysts using a microemulsion technique: Role of nanoparticle size on reducibility, activity and selectivity in Fischer–Tropsch reactions. *Applied Catalysis A: General* **2010,** *374* (1–2), 79-86.

8. Tavasoli, A.; Abbaslou, R. M. M.; Trepanier, M.; Dalai, A. K., Fischer–Tropsch synthesis over cobalt catalyst supported on carbon nanotubes in a slurry reactor. *Applied Catalysis A: General* **2008,** *345* (2), 134-142.

9. Trépanier, M.; Tavasoli, A.; Dalai, A. K.; Abatzoglou, N., Fischer–Tropsch synthesis over carbon nanotubes supported cobalt catalysts in a fixed bed reactor: Influence of acid treatment. *Fuel Processing Technology* **2009,** *90* (3), 367-374.

10. Li, C.-H.; Yao, K.-F.; Liang, J., Influence of acid treatments on the activity of carbon nanotube-supported catalysts. *Carbon* **2003,** *41* (4), 858-860.

Chapter 2

Carbon Nanotube-Supported Catalysts Prepared by a Modified Photo-Fenton Process for Fischer-Tropsch Synthesis

Abstract

We demonstrate use of a green catalyst precursor and oxidant in a modified photo-Fenton process for synthesis of efficient Fischer-Tropsch catalysts. The facile, scalable process yields small and well-dispersed catalyst nanoparticles (Fe or Co) on carbon nanotubes (CNTs) that do not require calcination due to the absence of foreign components (nitrate, chloride, or acetate) that has to be removed during post-synthesis treatment. The synthesized catalysts were characterized by X-ray diffraction (XRD), N_2 physisorption, H_2 temperature-programmed reduction (H_2-TPR), Raman spectroscopy, transmission electron microscopy (TEM), and inductively coupled plasma (ICP) spectroscopy. The results show high catalyst dispersion and smaller catalyst particles with narrow particle size distributions in comparison to catalysts synthesized by incipient wetness impregnation (IWI). The performance of CNT-supported catalysts (CO conversion, C5+ selectivity, and catalyst lifetime) prepared by photo-Fenton process was evaluated during Fischer-Tropsch synthesis (FTS) and compared to CNT- and SiO_2-supported catalysts synthesized via conventional method (IWI). In general, CNT-based Fe or Co catalyst prepared by photo-Fenton process shows a higher performance at a lower FTS reaction temperature (200°C for Co and 250°C for Fe) in comparison to conventional catalysts. In particular, Co catalyst obtained from photo-Fenton process shows high CO conversion (~80%) and outstanding selectivity for liquid hydrocarbons (C5+) ~ 70%. The process demonstrates a new synthesis route for exploiting the outstanding material properties of CNTs in catalysis.

2.1 Introduction

Fischer-Tropsch Synthesis (FTS) is a valuable catalytic process for the transformation of syngas derived from low-value biomass, natural gas, and coal to high-value clean fuel over transition metal catalysts. An important factor in the design of efficient catalysts for FTS is the support because catalyst-support interactions and resulting catalyst performance are determined by physico-chemical properties of the support.[1] The dispersion and reducibility of metal catalysts and the diffusion coefficient of the reactants and products highly depend on the surface structure and pore size of the support.[2-3] Typically, FTS catalysts undergo high-temperature post-treatment steps like calcination (~500°C) that is required to remove precursor salts (nitrate, sulfide, or chloride) and H_2 reduction (~600°C) that forms the metallic states of the active metal. Unfortunately, these post-treatment steps promote strong interactions between the active metal and oxide support (Al_2O_3, SiO_2 and TiO_2),[4] resulting in the formation of inactive and unreducible inert materials like $CoAl_2O_4$, $CoTiO_4$, and $CoSiO_4$ that are known to limit catalyst activity.[2, 5-6]

Besides the type of catalyst support, the calcination step during catalyst preparation was also found to have a significant impact on the morphology of Co particles, causing agglomeration and low dispersion of Co particles on the support.[7] In fact, Kababji *et al.*[8] have shown that the calcination step has a stronger effect on catalyst performance than support properties like surface area and pore diameter; in particular, by reducing the calcination temperature, higher CO conversion and lower CH_4 selectivity were obtained. High-temperature exposure of catalysts during calcination has been found to affect the crystallographic structure and particle size.[9] At high temperature, formation of Co particles with face-centered cubic (FCC) structure is favored, which has low catalytic activity; whereas at low temperature, the formation of Coparticles with hexagonal close-packed (HCP) structure that are characterized by high catalytic activity are favored.[10] In addition, the catalyst particle size has a strong effect on the catalyst activity. It has been shown that Co catalyst activity increases with decreasing

particle size, which is attributed to the increase in the surface area of Co catalyst.[11] The aforementioned studies illustrate the negative impacts of post thermal treatment of catalysts on FTS activity. Further, the heat produced during the exothermic FTS reaction is not well dissipated in the presence of catalysts supported on relatively poor thermally conductive SiO_2 or Al_2O_3, resulting in a temperature gradient in the packed bed reactor, which could make the catalyst susceptible to sintering and deactivation.

To prevent catalyst deactivation induced by the catalyst support and post-synthesis treatment steps, new catalyst supports that are efficient in dispersing and stabilizing catalyst nanoparticles, as well as not requiring aggressive post thermal treatments after catalyst deposition. More recently, there is growing interest in using non-oxidic catalyst supports such as carbon nanotubes (CNTs) due to their high mechanical strength, improved metal dispersion control, and ability to minimize or eliminate the formation of inactive/unreducible components like silicates and aluminates.[11-14] However, current use of CNTs as catalyst supports require aggressive acid treatment for catalyst nanoparticles to be deposited. Acid treatment of CNTs creates a number of functional groups (hydroxyl, carbonyl, and carboxyl) on the surface that serve as anchoring sites for metal nanoparticles, and more importantly, increase the dispersion of active metal, which helps to increase FTS reaction rate.[14-15] Other approaches that have been used to oxidize CNTs include hydrogen peroxide treatment,[16] dry oxidation method involving UV-ozone treatment,[17-18] and treatment with a combination of hydrogen peroxide and UV light.[19] Unlike strong acids such as HNO_3 and H_2SO_4, hydrogen peroxide does not cause structural damage to CNTs or incorporate foreign elements into the CNT surface.[16, 20]

Several efforts have been made to synthesize catalyst nanoparticles on either mesoporous carbon materials or CNTs for different applications. A widely used approach is liquid injection chemical vapor deposition (LICVD) or plasma enhanced CVD (PECVD) with ferrocene ($C_{10}H_{10}Fe$) as a feedstock that serves as a single source of carbon and Fe.[21] This technique offers a high yield of Fe nanoparticles decorated on CNTs, however, a large fraction of the nanoparticles agglomerate due to the high growth temperature.[22-23] Another technique that has been reported is physical vapor infiltration (PVI) with hard

templating replication to deposit Fe on mesoporous carbon,[24] whereby mesoporous silica, serving as a template, is mixed with ferrocene in a sealed vessel at 110°C for 48 h. The resulting powder required calcination at 450°C and treatment with NaOH solution at 80°C to remove the silica template. As the foregoing studies demonstrate, available methods for depositing catalyst nanoparticles on CNTs for catalytic applications are plagued with significant drawbacks.

In this study, a modified photo-Fenton approach for depositing active metal nanoparticles (Fe or Co) on CNTs is demonstrated. Photo-Fenton process is typically used to treat wastewater by oxidizing organic pollutants via UV illumination of a mixture of hydrogen peroxide and ferrous ion (Fe^{2+}).[25] The reaction process, as illustrated in Figure 2-1, involves generation of OH* radicals, oxidation of CNTs by OH*, and deposition of catalyst particles. There are two main steps OH* generation:[26] First, the ferrous ions (Fe^{2+}) are oxidized by hydrogen peroxide to ferric ions (Fe^{3+}), producing hydroxyl radicals (OH*) as active intermediates, which are the second strongest oxidizing agent after fluorine (Equation 1). Second, UV illumination accelerates the reduction of ferric ions (Fe^{3+}) to ferrous ions (Fe^{2+}) as shown in Equation 2.

$$Fe^{2+} + H_2O_2 \rightarrow Fe^{3+} + OH^- + OH^{\bullet} \quad (1)$$

$$Fe^{3+} + H_2O_2 + h\nu \rightarrow Fe^{2+} + HO_2^{\bullet} + H^+ \quad (2)$$

$$H_2O_2 + h\nu \rightarrow 2HO^{\bullet} \quad (3)$$

The use of UV illumination prevents the second step from being slower than the first step, which can cause an early termination of the reaction.[27] In addition, OH* are produced via direct UV illumination of H_2O_2 (Equation 3). Hydroxyl radicals generated via Equations 1 – 3 oxidize the CNT surface in the presence of Fe or Co ions that subsequently precipitate on the CNT surface and form nanoparticles as depicted in Figure 2-1. Note that modified photo-Fenton reaction utilizes green materials (catalyst precursors and an oxidant). The process is facile and scalable and provides a new pathway for controlled deposition of transition metal nanoparticles like Fe or Co on CNTs. We emphasize that the

process yields catalysts that are free of possible catalyst inhibitors that are typically present in conventional catalysts synthesized from metal precursors like sulfite, chloride, and nitrate. For this reason, modified photo-Fenton process does not require further treatment like calcination that induces changes in the morphology of metal nanoparticles and thus offers new opportunities for controlled synthesis of well-dispersed CNT-supported catalysts.

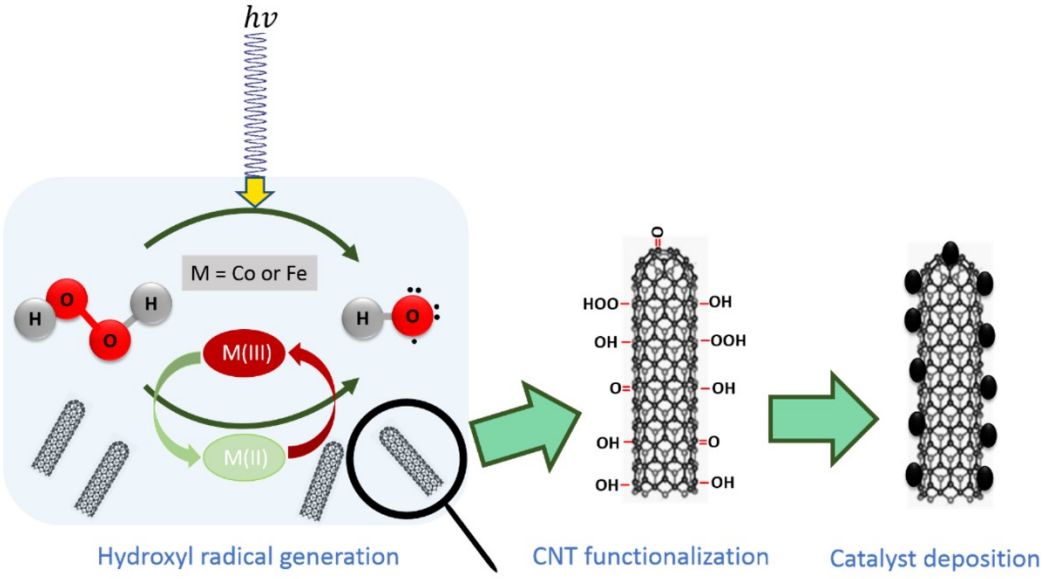

Figure 2-1 Schematic illustration of the modified photo-Fenton process for CNT oxidation and catalyst deposition.

2.2 Experimental

2.2.1 Catalyst Preparation

Two types of CNT-supported Co and Fe catalysts were prepared. CNTs (purchased from Chengdu Organic Chemicals Co., Ltd) with outer diameters of 50 – 70 nm and lengths of 10 – 20 μm were used. The first group of catalysts was prepared by a modified photo-Fenton process, which involves CNT functionalization and anchoring of Co or Fe species on the functionalized CNT surface in a single step. A distinguishing feature of the process is the use of cobalt (II) hydroxide (Aldrich,

95%) and iron (II) hydroxide (Aldrich, 95%) as "green" catalyst precursors. In brief, the process was carried out by stirring 150 ml mixture of hydrogen peroxide (30%) and 1g of CNTs in a 300 ml single-neck flat-bottom flask at 60°C. The total amount of catalyst precursor was divided into four batches that were added each day to the reaction mixture over a period of four days with a targeted metal loading of 10 – 15 wt%. After adding the first batch, the flask containing the mixture was exposed to UV illumination with a wavelength of 300 nm. 20 ml of hydrogen peroxide mixed with one batch of catalyst precursor was added each day over a four-day period to replenish the catalyst and sustain the process, as well as maintain the acidity of the solution near the desired pH of 4. Note that the addition of the total amount of catalyst precursors at once would cause a dramatic increase in acidity level, and subsequently induce termination of the reaction.[28] At the completion of the process, the catalyst obtained was filtered through a 0.2μm filter paper, and then vacuum-dried overnight at 150°C to remove adsorbed hydrogen peroxide. The resulting samples are referred to as fresh catalysts and labeled as Fe/CNT-Fenton and Co/CNT-Fenton.

For comparison, the second group of CNT- and SiO_2-supported Co and Fe catalysts were prepared by conventional incipient wetness impregnation (IWI). The IWI process followed the standard procedure reported by Eschemann *et al.*[28] and Abbaslou *et al.*[29] Unlike photo-Fenton process that utilizes a "green" precursor and an oxidant, the catalyst precursors used in IWI were cobalt (II) nitrate hexahydrate and iron (III) nitrate nonahydrate. In addition, an aggressive oxidation treatment (HNO_3, 90°C, 24 h) was employed for functionalization of CNTs prior to anchoring the metal ions. The resulting CNT-supported catalysts after calcination at 350°C are described as fresh catalysts and denoted as Fe/CNT-IWI and Co/CNT-IWI, while SiO_2-supported catalysts are Fe/SiO_2-IWI and Co/SiO_2-IWI.

2.2.2 Catalyst Characterization

X-ray powder diffraction (XRD) measurement was carried using Rigaku Miniflex II desktop X-ray diffractometer with monochromatic Cu Kα radiation (λ = 0.154 nm) with a step size of 0.1º and a

scan speed of 2.0º per minute. The values of 2θ were in the range 10 – 80º. The phases were identified by comparing patterns obtained with JCDPS database. The average crystallite sizes (Dp) for the synthesized catalyst particles have been estimated from full-width at half maximum of the most intense peaks (2θ =36º for Co_3O_4 and 2θ = 32º for Fe_2O_3) using the Debye–Scherrer equation.

Hydrogen temperature-programmed reduction (H_2-TPR) was conducted with AMI-200 Catalyst Characterization Instrument.[29] The consumption amount of H_2 obtained from TPR was used to calculate the number of moles of active sites for each catalyst, which was then used to determine the catalyst dispersion (D) on the different supports.[30] The amount of catalyst deposited on the support was determined by inductively coupled plasma spectroscopy (ICP-Varian 720-ES). The percentage reduction was included in the dispersion calculation by assuming H: metal stoichiometric ratio of 1:1 as reported by Jacobs *et al.*[2] The calibration curve for H_2 consumption was generated using 0.03 g of CuO. Catalyst dispersion (*D*) and diameter of the particles (*d*) were calculated based on the assumption that the shape of catalyst particles is spherical.

$$\% D = \frac{Number\ of\ surface\ Co^{\circ}\ atoms \times 100}{number\ of\ total\ Co\ atoms} \quad (4)$$

$$d = \frac{(6000)}{(density)(maximum\ area)(dispersion)} \quad (5)$$

Nitrogen adsorption-desorption measurements were conducted at -196°C using a Quantachrome Autosorb-1 instrument, and the BET specific surface area (SA_{BET}) and total pore volume were determined from the isotherms. Prior to adsorption measurements, the samples were degassed at 250º C for 12 h to obtain the base weight of the samples. SA_{BET} was determined from the adsorption branch in the linear range of relative pressure from 0.02 to 0.35. The total pore volume was evaluated by a single-point pore volume at a relative pressure of 0.95.

Transmission electron microscopic (TEM) images and lattice structures were obtained using FEI Tecnai F20 XT operating at 200 kV and equipped with energy-dispersive X-ray spectroscopy (EDS). The samples were dispersed in ethanol by sonication for 5 min, dropped on copper microgrid coated

with lacy carbon film. The Tecnai Imaging & Analysis tool (TIA) was used to measure the lattice spacing and angle between the lattice spaces. The lattice information and the diffraction patterns obtained were used to confirm the crystalline structure of the elements. The quality of CNTs was evaluated by Raman spectroscopy (λ = 532 nm). X-ray photoelectron spectroscopy (XPS) was used to characterize the degree of functionalization of CNTs after photo-Fenton process were and the chemical properties of the as-synthesized catalysts. XPS measurements were performed on a Kratos Ultra XPS system (Kratos, Kanagawa, Japan) with a monochromatic Al Kα source (*hv* =1486.6 eV). A charge neutralizer was used to prevent energy shifts during spectral acquisition; for all samples, the C1s peak was centered at a binding energy of 284.5 eV. The analysis of the XPS spectra was performed using CasaXPS software; the least square fitting of the spectra was performed using mixed Gaussian-Lorentzian peak components in the quantification process.

2.2.3 Catalytic Testing

FTS was conducted in a fixed bed reactor. A catalyst sample of ~ 2 g (MWCNT or SiO_2 = 85%, active metal = 15%) was loaded into a 1/2 inch 316 stainless steel tube. Fe-based catalysts were activated in H_2 (100 sccm) at atmospheric pressure by increasing the temperature from 30°C to 400°C, whereas for Co-based catalysts, from 30°C to 350°C at a rate of 15°C/min. The catalysts were activated at their respective activation temperature for 4h. After activation, the reactor temperature was decreased to 200°C for Co and 250°C for Fe. FTS reaction was initiated by switching to H_2/CO (100/50 v/v and 100 sccm of N_2 as internal standard, GHSV 1066 h^{-1}) and the reaction was carried out under 10 bar and H_2/CO = 2. The reaction products (unreacted CO, CO_2, and C1 – C20 hydrocarbons) from the reactor were analyzed using an on-line gas chromatograph (SRI 8610C) equipped with a thermal conductivity detector (TCD) and flame ionization detector (FID) and quantified by injecting calibration standards. The tube lines after each mass flow controller (MFC) is equipped with a check valve to

ensure that there is no back flow. A backpressure regulator valve is used to maintain the pressure inside the reactor during the reaction. The catalytic activity was determined by CO conversion and the selectivity of different hydrocarbons after reaching steady-state condition for each run.[31] The %CO conversion, selectivity (Si) of each hydrocarbon (xi), and FTS rate (R_{FTS}) are calculated from Equations 6, 7, and 8, respectively.

$$\text{CO (\%)} = \left[\frac{\text{CO in} - \text{CO out} \times \text{gas contraction}}{\text{CO in}}\right] \times 100 \quad (6)$$

$$\text{Si} = \left[\frac{\text{mass of component xi}}{\sum \text{xi}}\right] \times 100\% \quad (7)$$

$$R_{FTS} = \left[\frac{\text{weight of H.C produced (g)}}{\text{weight of catalyst (g)} \times \textit{reaction time (h)}}\right] \quad (8)$$

The final products were classified as CH_4, $C_2 - C_4$, and C5+ (liquid hydrocarbons) with carbon numbers 5–20, including olefins and paraffinic components.

2.3 Results and Discussion

2.3.1 Functionalization of CNTs and Catalyst Deposition

A summary of properties of as-received catalyst supports and supported catalysts prepared by photo-Fenton and IWI are presented in Table 2-1. The SA_{BET} and pore volume of CNTs do not change after UV-H_2O_2 treatment while those of CNTs treated with HNO_3 increases. CNT oxidation using strong acids is known to impart substantial defects on CNTs and result in CNTs with open caps, leading to increased specific surface area.[32] The SA_{BET} of CNTs oxidized following UV-H_2O_2 treatment remained unchanged after oxidation. However, an increase in the surface area is observed only after catalyst deposition, indicating that UV-H_2O_2 oxidation treatment is less aggressive than the conventional method. This observation is supported by TEM data (Figure S1) showing that their CNT caps remain intact after UV-H_2O_2 oxidation. The Raman spectra of pristine and oxidized CNTs exhibit the G-band ~1575 cm^{-1} that is omnipresent in sp^2 carbon systems and the disorder-induced D-band ~1330 cm^{-1}. The decrease in the ratio of integrated intensity of the G-band and the D-band (I_G/I_D) from

their Raman spectra (Figure S2) for the oxidized CNTs may be evidence of functionalization. The practical Co and Fe loadings as determined by ICP were in the range of 15.7 – 18.5wt% and the analysis did not reveal the presence of impurities in all the synthesized catalysts.

Table 2-1 Summary of properties of catalyst supports (as-received) and supported catalysts prepared by photo-Fenton and IWI.

Sample	SA_{BET} (m^2/g)	Total Pore Volume (cm^3/g)	Particle Size (nm), XRD	Metal Content (wt%), ICP	I_G/I_D Raman Spectroscopy
As-received CNTs	162.8	0.65	-	-	1.6
CNT-HNO_3	192.6	0.78	-	-	0.7
CNT-UV/H_2O_2	164.3	0.67	-	-	1.0
As-received SiO_2	480.0	0.75	-	-	-
Fe/CNT-Fenton	186.9	0.65	4.5	16.35	1.0
Co/CNT-Fenton	184.5	0.68	3.7	15.70	1.0
Fe/CNT-IWI	150.1	0.58	12.2	18.47	0.7
Co/CNT-IWI	148.7	0.61	9.5	17.65	0.7
Fe/SiO_2-IWI	325.0	0.60	12.4	18.41	-
Co/SiO_2-IWI	310.0	0.64	11.8	17.43	-

The microstructure of CNTs after acid and UV-H_2O_2 treatments was investigated by TEM. Figure S3 shows high- and low-magnification images of as-received CNTs, HNO_3-treated, and UV-H_2O_2-treated CNTs. The as-received CNTs are long with even wall structure. It is apparent from the results that acid treatment tends to cut the CNTs, destroy the concentric layers of the graphitic planes, and degrade the CNT structure. The arrows in Figure S3 show areas on the CNT surface that have been destroyed by HNO_3 treatment. Conversely, UV-H_2O_2 treatment appears to preserve the CNT length, concentric layers, and quality.

Further investigations were carried out by XPS to determine the degree of functionalization of HNO_3-treated, H_2O_2-treated, and UV/H_2O_2-treated CNT samples. The deconvolution of the high-resolution C 1s spectra (Figure 2-2) reveals the presence of several types of carbon species in the oxidized samples: C=C (284.5 eV), C–C (285.1 eV), C–O (286.4 eV), C=O (287.6 eV), C–OOH (288.8 eV), and carbonates (291.0 eV).[20, 33] The curve fitting results are summarized in Table S1. The ratio between the functionalized carbon species (C_f) and sp2 graphitic carbon (C_f/sp2) is indicative of the degree of functionalization; the C_f/sp2 values for as-received CNTs, H_2O_2-treated CNTs, UV-H_2O_2-treated CNTs, and HNO_3-treated CNTs are 0.23, 0.27, 0.63, and 0.76, respectively. From the degree of functionalization, it is apparent that UV-assisted oxidation using H_2O_2 achieves roughly the same level of oxidation as CNTs oxidized via the conventional method (refluxing in HNO_3 at 90°C) while preserving the structural integrity (Figure S3).

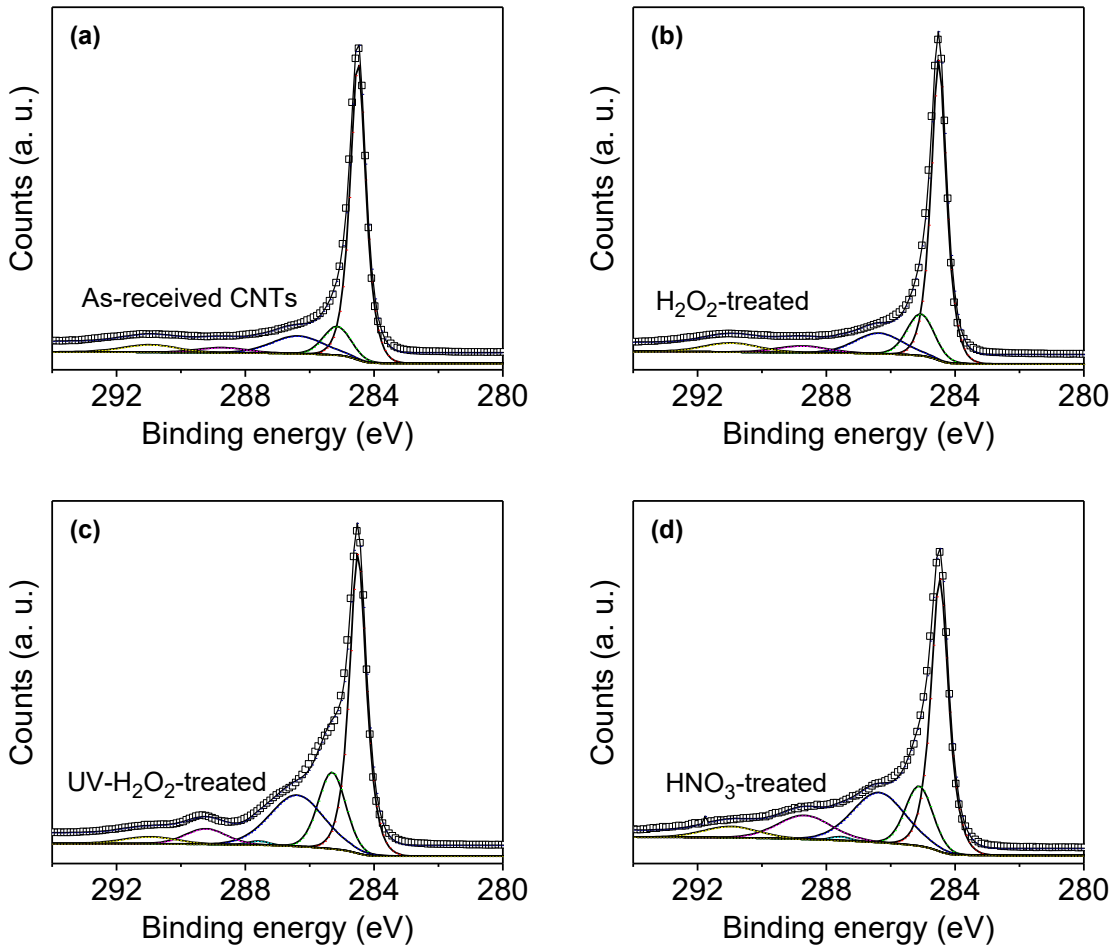

Figure 2-2 Deconvolution of XPS C 1s spectra of (a) as-received CNTs, (b) H_2O_2-treated CNTs, (c) UV/H_2O_2-treated CNTs, and (d) HNO_3-treated CNTs.

The deposition rate of catalyst particles on CNTs via photo-Fenton process was evaluated at different times using ICP spectroscopy (Figure 3). The amount of active metal (Co or Fe) loaded on CNTs increases with time. After four days of photo-Fenton reaction, the loading amount reaches a maximum ~90 wt% of the initial amount of metals, indicating the optimum CNT oxidation and metal deposition time for photo-Fenton process.

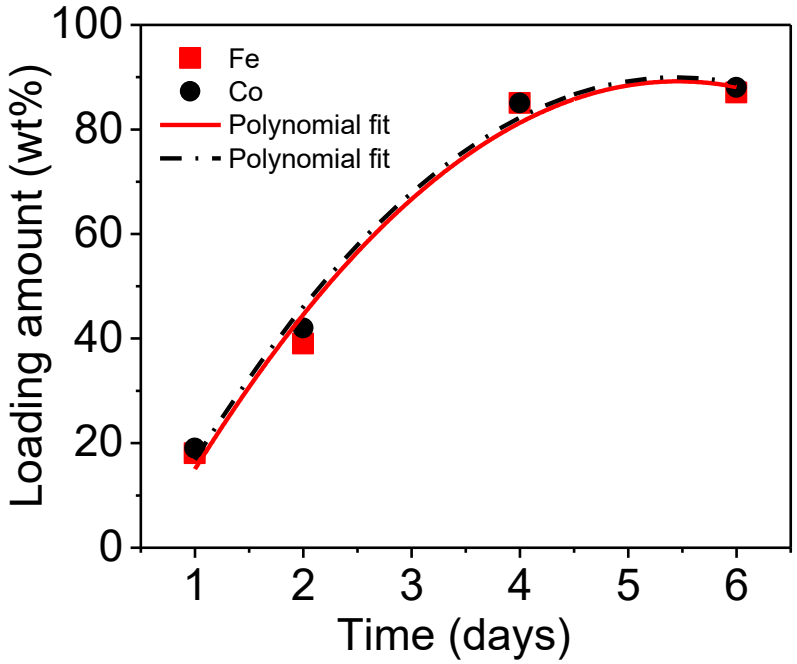

Figure 2-3 Loading amount of Fe or Co on CNTs as a function of time during photo-Fenton process.

2.3.2 Characterization of Catalysts

The XRD profiles in Figure 2-4 provide insights into the crystallographic structure and composition of the catalysts. The diffraction peaks at 2θ values of 26 and 44° are reflections of hexagonal graphite and correspond to CNTs[34] while the peak at 22.3° correspond to SiO_2 support. For comparison, XRD patterns of pure SiO_2 and CNTs are presented in Figure S4. For Fe catalysts, peaks at 2θ values of 33, 36, 41, 50, 54, 62, and 64° marked with circles were indexed as hematite,[35] consistent with the JCPDS number (α-Fe_2O_3, JCPDS 00-0011053). For Co catalyst, the diffraction peak at 2θ value of 19, 31, 37, and 65° marked with squares are attributed to Co_3O_4.[36] These peak assignments for Co are in agreement with data in their respective JCPDS card numbers (Co_2O_3, JCPDS 00-002-0770).[37] There are no diffraction peaks that are associated with metallic Co or Fe; this conclusion is corroborated by XPS spectra of samples synthesized by photo-Fenton in Figure S5 and previous studies on catalysts synthesized by IWI. The full-width at half-maximum (FWHM) of the

most intense peaks, positioned at 34° for Fe catalysts and 36.4° for Co catalysts, have been used with the Scherrer equation for estimating their particle sizes (Table 2-1). The average particle sizes of Co_3O_4 and Fe_2O_3 prepared by photo-Fenton are smaller than those prepared by IWI.

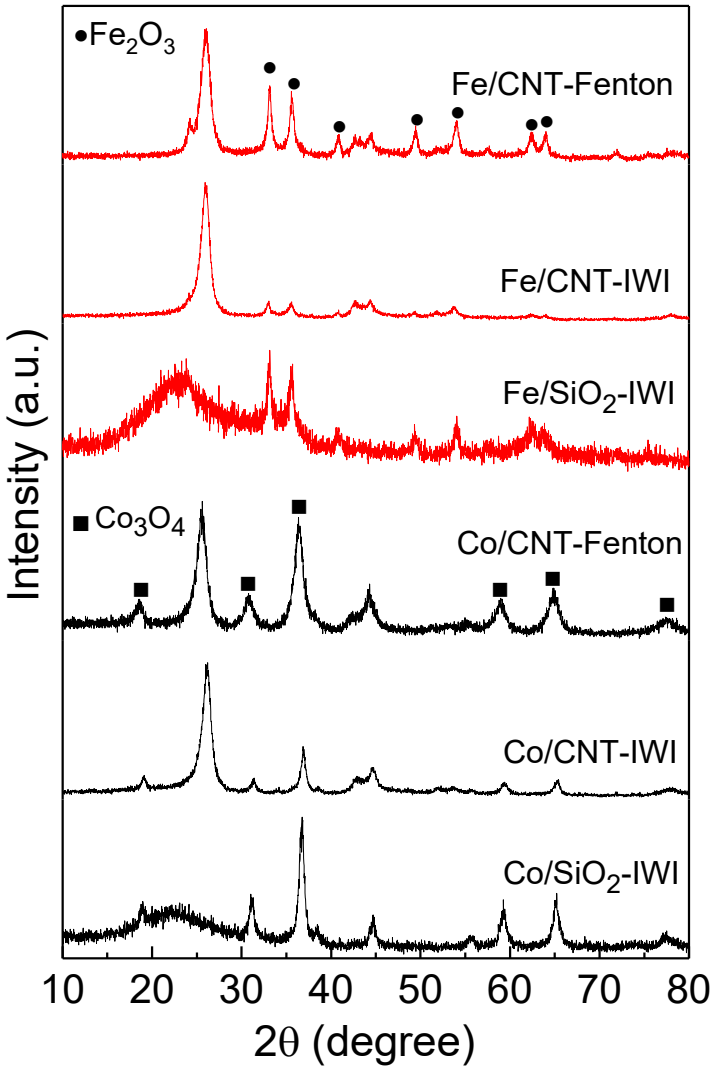

Figure 2-4 XRD patterns of fresh Fe and Co catalysts on different supports (CNTs and SiO_2) synthesized by photo-Fenton and IWI methods.

Figure 2-5 shows representative TEM images and corresponding histograms of particle size distributions (PSDs) with Gaussian analysis fittings of CNT-supported catalysts prepared by photo-Fenton and IWI. For comparison, similar data for catalyst supported on SiO_2 are presented in Figure S6. The average particle size for the fresh catalysts are as follows: Co/CNT-Fenton (3.1±0.5 nm),

Fe/CNT-Fenton (2.3±0.5 nm), Co/CNT-IWI (16.9±3.9 nm), Fe/CNT-IWI (16.5±4.3 nm), Co/SiO_2-IWI (5.0±0.8 nm), and Fe/SiO_2-IWI (28.7±10.4 nm). Catalyst particles deposited on CNTs by photo-Fenton are relatively small (< 10 nm), highly uniform, and well dispersed on the CNT surface. In contrast, catalyst particles deposited on CNTs and SiO_2 by IWI are poorly dispersed and tend to form large agglomerates (> 10 nm) that are not anchored on the CNT surface. The TEM data are in agreement with the crystallite sizes of catalysts obtained from XRD measurement (Table 2-1), although TEM analysis reveals that the large aggregates in Co/SiO_2-IWI consist of small particles < 10nm. In general, particles synthesized by IWI appear isolated from CNTs, experience severe agglomeration, and are prone to sintering. In particular, Figure 2-5 reveal that unlike Co/CNT-IWI and Fe/CNT-IWI, Co/CNT-Fenton and Fe/CNT-Fenton have particles that are well anchored on CNTs that retain their structural integrity during photo-Fenton process.

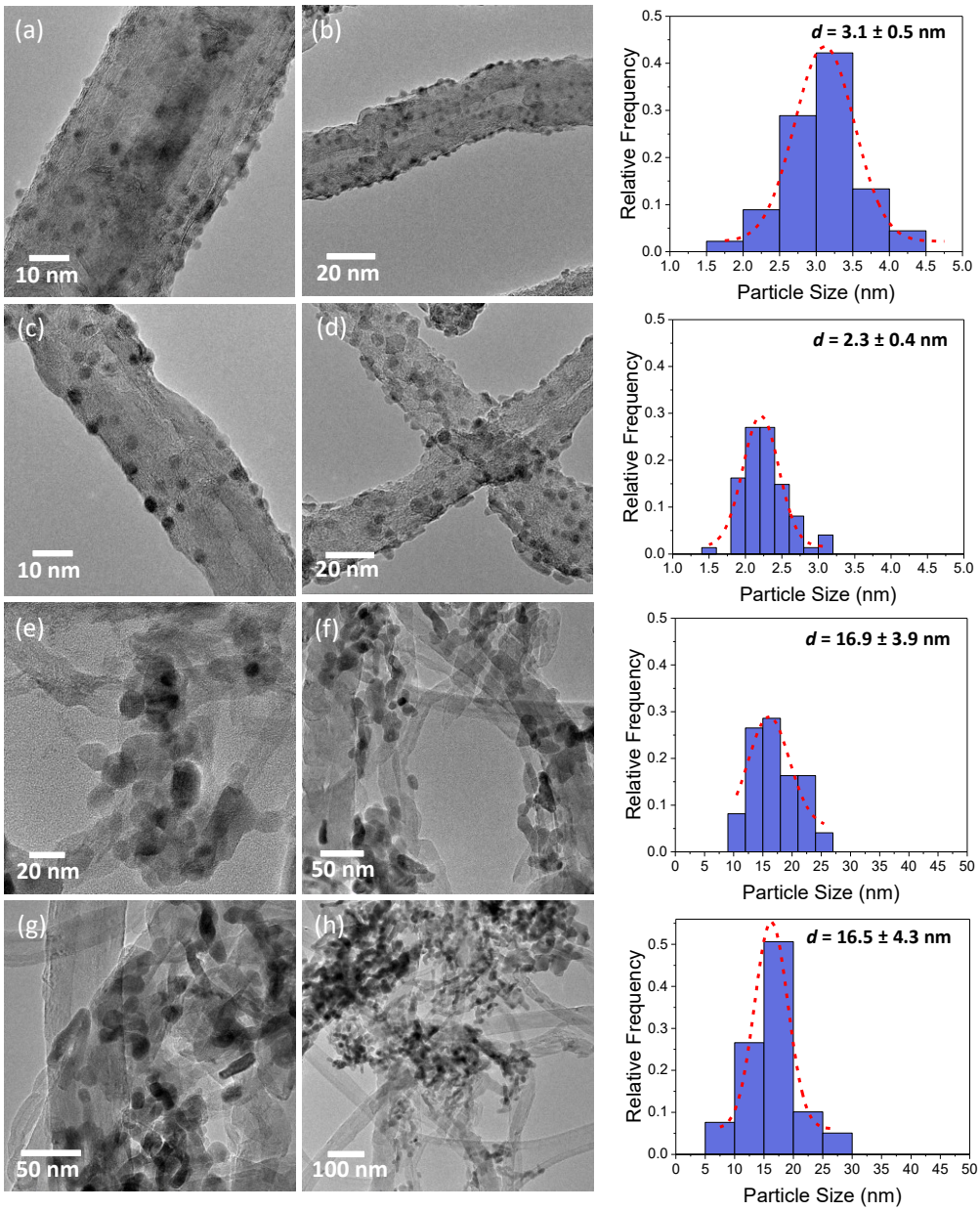

Figure 2-5 Low- and high-magnification TEM images and corresponding histograms of PSDs with Gaussian analysis fittings of fresh catalysts: Co/CNT-Fenton (a,b), Fe/CNT-Fenton (c,d), Co/CNT-IWI (e,f), and Fe/CNT-IWI (g,h).

The TPR profiles of SiO_2- and CNT-supported Fe and Co catalysts prepared by IWI and photo-Fenton process are shown in Figure 2-6. The results show that reduction of catalysts prepared by photo-Fenton is relatively easier than conventional catalysts synthesized by IWI; this may be due to the absence of impurities that are typically associated with conventional Co and Fe precursors such as

nitrate, chloride, and acetate. Post-synthesis treatments like drying and calcination hardly ensure complete removal of catalyst salts, unless severe thermal treatment is applied, which often lead to sintering and strong interactions with the catalyst support.[2] For Co/CNT-Fenton, the profile of the first peak at 343°C is assigned to the reduction of Co_2O_3 to Co_3O_4,[38] where the XRD results confirmed the presence of Co_2O_3 with a hexagonal structure (Figure 2-4). While peak at 380°C is assigned to the reduction of Co_3O_4 to CoO and 420°C to the reduction step from CoO to Co^0. The TPR profile of Co/CNT-IWI is much broader, due to the higher agglomeration rate of neighboring particles.[39] The peak at 305˚C for Fe/CNT-Fenton is assigned to the reduction of Fe_2O_3 to Fe_3O_4 while peak at 350°C is assigned to Fe_3O_4 to FeO (wustite) and 386°C to reduction of FeO to Fe^0.[40] The shift to higher reduction temperatures for catalysts synthesized via IWI method is attributed to the use of iron nitrate[31, 41] as opposed to the green precursors used in the photo-Fenton process. H_2-TPR results for Fe or Co supported on silica show a high temperature reduction peak ~640˚C, which corresponds to the formation of metal silicate.[42]

Table 2-2 shows a summary of the degree of reduction, amount of hydrogen consumed, and catalyst dispersion obtained from H_2-TPR measurements. It is clear from the results that, irrespective of synthesis method, H_2 consumption is higher for CNT-supported catalysts than SiO_2-supported catalysts, which is consistent with previous studies.[13, 43] However, CNT-supported catalysts synthesized via photo-Fenton process show H_2 consumptions that are higher by almost a factor of two than those synthesized by IWI. In addition, catalysts synthesized by photo-Fenton exhibit the lowest TPR peaks maximum temperature (T_{max}) ~ 420 and 386°C. On the basis of TPR data, there is a remarkable improvement in the percentage of catalyst dispersion achieved by photo-Fenton process, which is in agreement with TEM results (Figure 2-5) that show well-dispersed, small catalyst particles on CNTs – features that are expected to increase the number of active sites available for FTS reaction. The TPR and TEM data are in agreement with studies[44-45] that have shown dependence of catalyst dispersion and reducibility on catalyst support and preparation method.

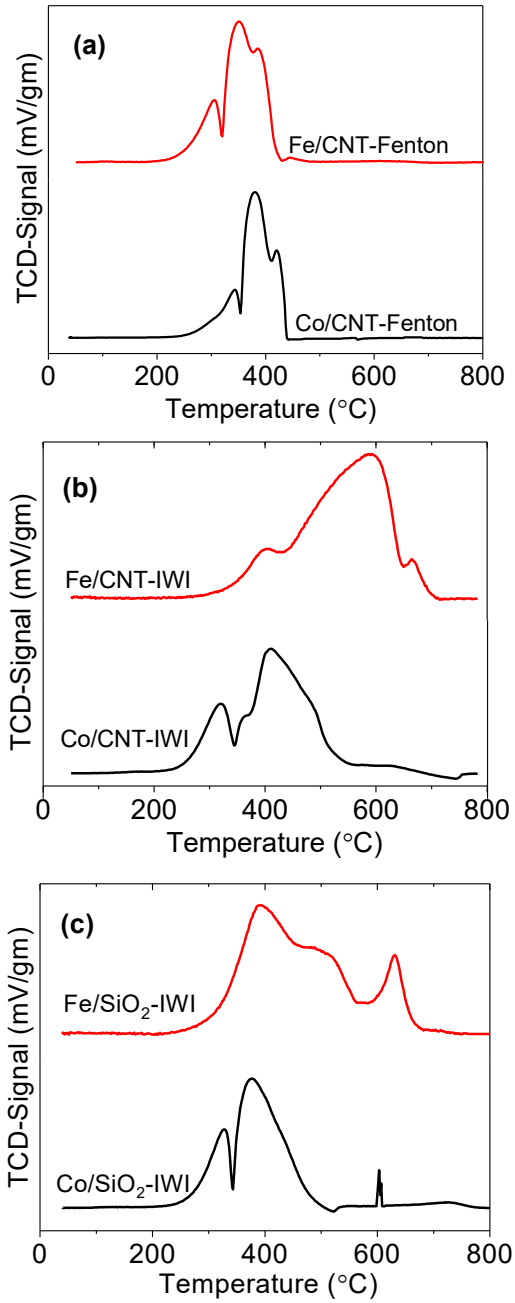

Figure 2-6 H_2-TPR profiles of prepared catalysts: (a) Fe/CNT-Fenton and Co/CNT-Fenton, (b) Fe/CNT-IWI and Co/CNT-IWI, and (c) Fe/SiO_2-IWI and Co/SiO_2-IWI.

Table 2-2 Summary of hydrogen consumption, degree of reduction, and dispersion ratio for the different catalysts measured by TPR.

Catalyst	Calcination Temperature (°C)	T_{max} (°C)	H_2-Consumption (µmol/g-cat)	Diameter (nm)	Dispersion (%)
Fe/CNT-Fenton	Not required	386	285	4.4	21.5
Co/CNT-Fenton	Not required	420	301	4.1	23.3
Fe/CNT-IWI	350	645	145	8.6	11.2
Co/CNT-IWI	350	615	167	7.5	12.90
Fe/SiO_2-IWI	350	640	115	11.0	8.71
Co/SiO_2-IWI	350	610	135	9.2	10.40

2.3.3 Catalytic Testing

The catalytic activity of Co and Fe catalysts on different supports (CNTs and SiO_2) prepared by photo-Fenton and IWI reveal marked differences in catalytic performance (CO conversion, C5+ selectivity, and catalyst stability). Figure 2-7 shows the effect of temperature on CO conversion in a temperature range of 170 – 240°C for Co/CNT and 190 – 270°C for Fe/CNT; the results are summarized in Table 2-3. Typically, Co-based catalysts produce long chain hydrocarbons ~230°C while slightly higher temperatures ~250°C are favorable for Fe-based catalysts that yield short chain hydrocarbons.[46] Our results in Figure 2-7 reveal that CNT-supported Co catalysts tend to have higher CO conversion at lower reaction temperature (180 –200°C) in comparison to SiO_2-supported Co catalysts. As temperature increases in the range of 190 – 240°C, the CO conversion of Co/SiO_2 increases faster than Co/CNT-IWI and Co/CNT-Fenton. The Co/CNT-IWI and Co/CNT-Fenton catalysts exhibit higher CO conversion and C5+ selectivity at lower temperatures, as low as 180°C, which is unprecedented for Co/SiO_2 catalysts. The optimum reaction temperature for Co/CNT-IWI

was found to be 200°C; however, Co/CNT-Fenton showed a higher CO conversion (~80%) and C5+ selectivity (~70%) at the same temperature. The Co/SiO_2-IWI shows a CO conversion of ~90% at a reaction temperature of 240°C, albeit with a selectivity of C5+ that drops to ~25%.

Operating FTS reaction at higher temperatures (>270°C) lead to higher selectivity of CH_4 and formation of large amount of coke that is associated with deactivation of FTS catalysts.[47-50] Given the exothermicity of FTS reaction, we hypothesize that the difference in thermal conductivity between CNT and SiO_2 may be playing a dominant role in the observed difference in activity of catalysts at different temperatures.[51-52] Given that the high exothermicity of FTS reaction makes it thermodynamically favorable at low temperatures, it is highly desirable to design FTS catalysts that can function at low reaction temperatures while maintaining excellent catalytic performance.[53] Note that for maximum catalytic activity to be achieved at lower temperature (< 200°C) as shown in this study, there has to be limited or no heat transfer resistance in the catalyst bed.[54] We hypothesize that the use of CNT networks as catalyst supports minimize the temperature gradient (radial and axial temperature gradients) across the reactor bed. Conversely, using SiO_2 as a catalyst support, an inert diluent material with high thermal conductivity such as SiC (k = 4W/cm.K) is required to enhance isothermicity of the reaction bed.[55] However, achieving uniform mixing in the bed is often challenging due to the difference in the bulk density of SiC and SiO_2.

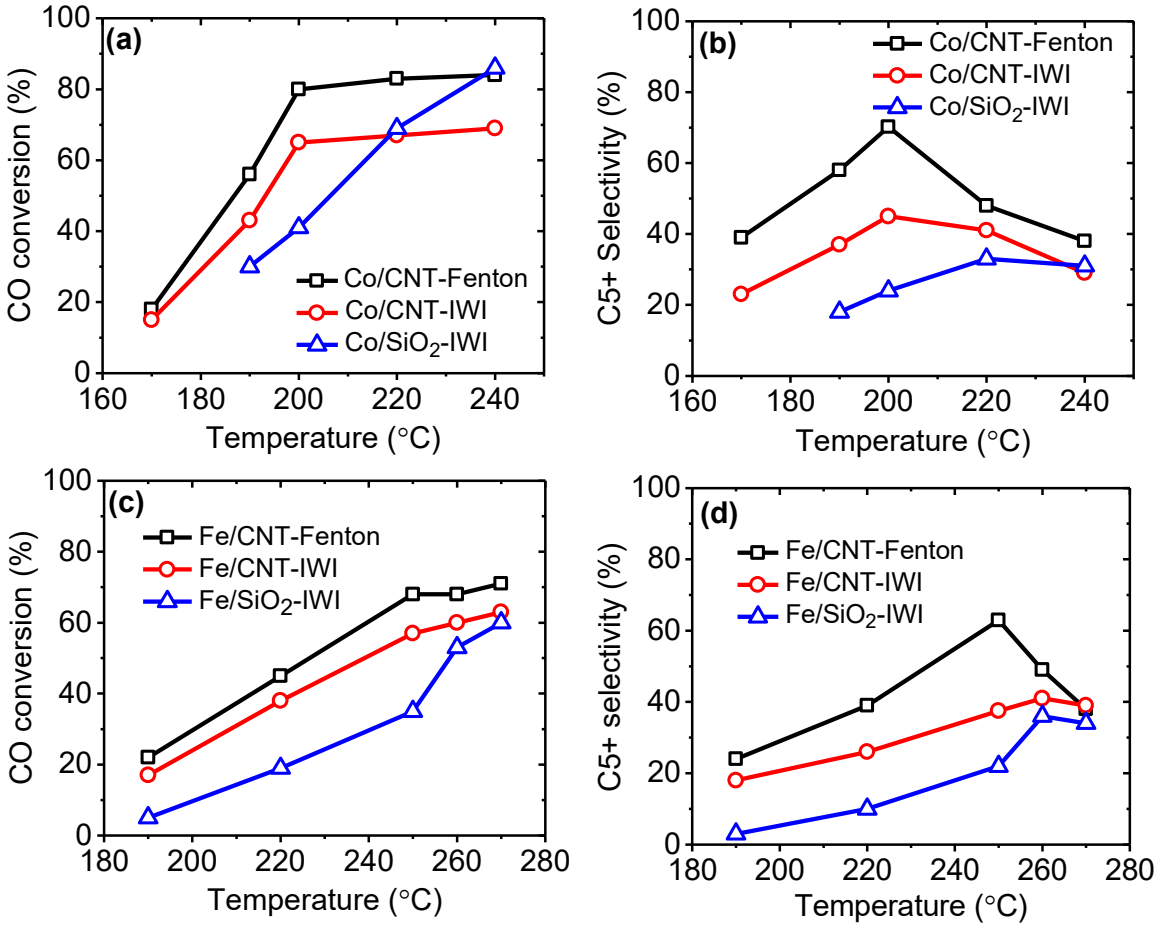

Figure 2-7 CO conversion and selectivity of liquid hydrocarbon (C5+) as functions of FTS reaction temperature for catalysts synthesized by photo-Fenton and IWI: (a, b) CNT and SiO_2-supported Co, and (c, d) CNT and SiO_2-supported Fe.

The activity of Fe-based catalysts decrease in the following order: Fe/CNT-Fenton > Fe/CNT-IWI > Fe/SiO_2-IWI (Figure 2-7 and Table 2-3); this observation is in agreement with a study by Cheng *et al.*[56] whereby Fe/CNT was reported to show a higher CO conversion than Fe/SiO_2. The CO conversion of Fe/CNT-Fenton and Fe/CNT-IWI show almost the same trend. The comparatively lower catalytic activity of Fe/SiO_2-IWI is unsurprising as the TPR data (Figure 2-6) confirm the existence of strong interactions between Fe and SiO_2 that result in the formation of inactive and unreducible species (iron silicates).[56-58] The reaction rate, CO conversion, and product selectivity after 30 h on stream and after the system had reached steady state at the optimum reaction temperature for the respective

catalysts are summarized in Table 2-3. The activity of Co-based catalysts decrease in the same order observed for Fe. Surprisingly, Co/CNT-Fenton shows outstanding C5+ selectivity at 200°C in comparison to Co/CNT-IWI and Co/SiO_2-IWI. The FTS reaction data are in a good agreement with those of H_2-TPR since Co/CNT-Fenton shows a higher catalyst dispersion (23.3%). The high C5+ selectivity and catalytic activity of Co/CNT-Fenton may be attributed to the green and less aggressive environment of the photo-Fenton process, which do not only preserve the structural integrity of CNTs, but also eliminate the calcination step. It has been demonstrated that a high calcination temperature (> 500°C) can change the crystallographic structure of Co catalyst from HCP to FCC phase,[59] and Co catalysts with HCP phase have been reported to have a higher catalytic activity than those with FCC.[60-61] Electron diffraction pattern of Co/CNT-IWI in Figure 2-8a reveal lattice constants of a = 0.36 nm, b = 0.36 nm, and c= 0.36 nm that correspond to the (111) plane of FCC phase. Conversely, Co/CNT-Fenton in Figure 2-8b exhibit a phase that is consistent with (100) plane of HCP with lattice constants of a = 0.242 nm, b = 0.242 nm, and c = 0.383 nm. The electron diffraction data confirm that photo-Fenton process yields HCP Co phase that is catalytically superior in FTS.

Table 2-3 Summary of catalytic activity and C5+ selectivity of Fe and Co catalysts synthesized by photo-Fenton and IWI deposition techniques.

Catalyst	Fe/CNTIWI *T*=250°C	Fe/CNT Fenton *T*=250°C	Fe/SiO_2 IWI *T*=250°C	Co/CNT IWI *T*=200°C	Co/CNT Fenton *T*=200°C	Co/SiO_2 IWI *T*=200°C
CO conversion (%)	57	68	35	65	80	41
CH_4 selectivity (%)	42.0	12.5	45.0	30.5	9.4	38.4
C2-C4 selectivity (%)	10.0	21.6	31.4	22.0	18.4	35.0
C5+ selectivity (%)	37.5	62.9	22.0	45.0	70.2	24.0
FTS rate $g_{H.C}/g_{Cat.}/h$	0.21	0.26	0.21	0.34	0.39	0.22

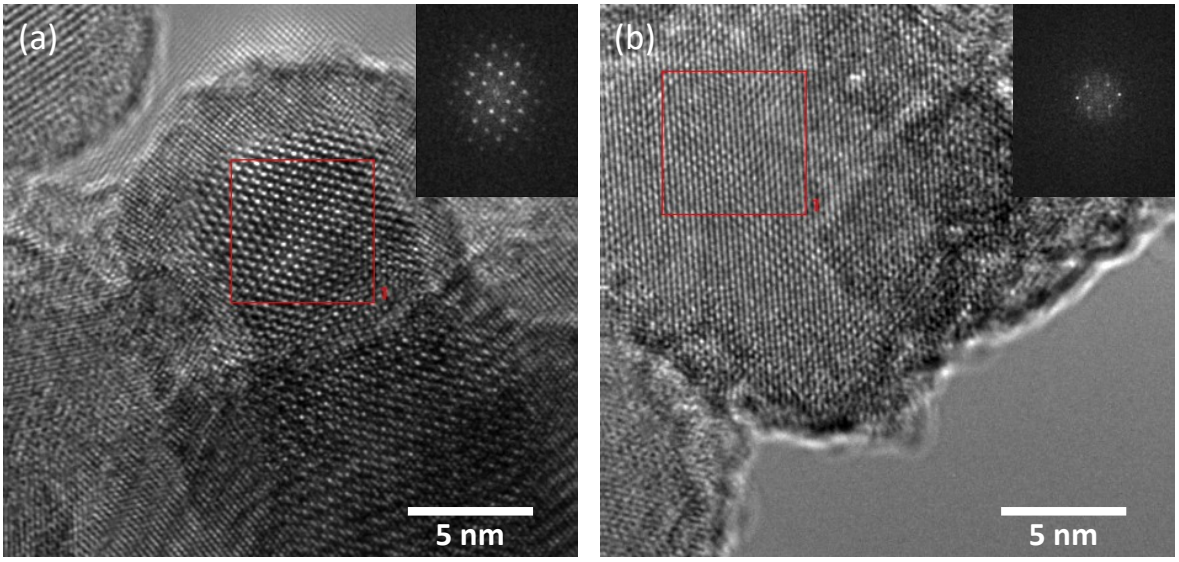

Figure 2-8 High-resolution TEM images of (a) Co/CNT-IWI and (b) Co/CNT-Fenton with their selected-area electron diffraction patterns as inserts showing a phase consistent FCC for sample (a) and HCP for sample (b).

Unlike Fe/CNT-Fenton, high selectivity of C1 – C4 products (76 %) is observed with Fe/SiO_2-IWI. CNT-supported catalysts prepared by photo-Fenton process show a higher CO conversion and C5+ selectivity in comparison to similar catalyst prepared by IWI (Table 2-3). It is apparent that the catalytic activity and product selectivity are not only affected by the nature of the support, but also by the catalyst deposition method, in agreement with Bukur et al.[62] The reducibility of Fe catalyst plays a crucial role in product selectivity, as the partially reduced Fe catalyst behave as a redox catalyst that is selective for low cut hydrocarbons.[63] Our results show that CNT-supported catalysts synthesized by photo-Fenton are not only characterized by high number of anchoring sites for high catalyst dispersion but also have high reducibility that ensures long catalyst lifetime. Table S2 and S3 summarize the Fe and Co catalytic activity for Fenton and IWI approaches. IWI process involves multiple steps including strong acid treatment to oxidize the CNTs, deposition of catalyst particles on the functionalized CNT surface using metal salt (such as nitrate) as a precursor, and calcination to remove the precursor salt. Post synthesis treatments lead to the degradation of CNT structure and an increase in the amount of

amorphous carbon (see I_G/I_D ratio in Table 2-1), which has been found to cause internal mass transfer limitation,[64] and could inhibit the catalytic activity.

A low CH_4 selectivity is observed for catalysts prepared by photo-Fenton process (Co/CNT and Fe/CNT) while catalysts prepared by IWI for both CNT and SiO_2 show high CH_4 selectivity. This may be attributed to the catalyst particle size, as photo-Fenton process yields catalyst particles with average sizes in the range of 2 – 5 nm (Figure 2-5 and Tables 1 and 2). Although the influence of catalyst particle size on FTS reaction is still controversial, our data support the theory by Quek *et al.*[65] that there is a minimum particle size required to maintain step-edge sites needed for facile CO dissociation. In the absence of step-edge sites, CO dissociation may favor H_2-assisted route.[66-67] DFT calculations by Liu *et al*.[9] suggest that higher step-edge sites of Co catalyst (HCP) prefer the direct dissociation pathway while lower step-edge sites of Co catalyst (FCC) prefer the H_2-assisted pathway. Based on quantum-chemical calculations for Ru, Shetty *et al*.[68] hypothesized that the step-edge sites is preferable for direct CO dissociation over H_2-assisted dissociation.

The reaction stability of the catalysts after reaching steady state was studied for 30 h (Figure 2-9). Unlike Co/CNT-Fenton and Fe/CNT-Fenton, Co/CNT-IWI and Fe/CNT-IWI start showing a decrease in CO conversion rate after 5 h, which may be attributed to loss of active sites. Calculation of the particle size from XRD and H_2-TPR results (Table 2-2) suggest that IWI method yields catalyst particles that are significantly larger than particles obtained via photo-Fenton method; this may explain the gradual deactivation of Co/CNT-IWI and Fe/CNT-IWI with time.

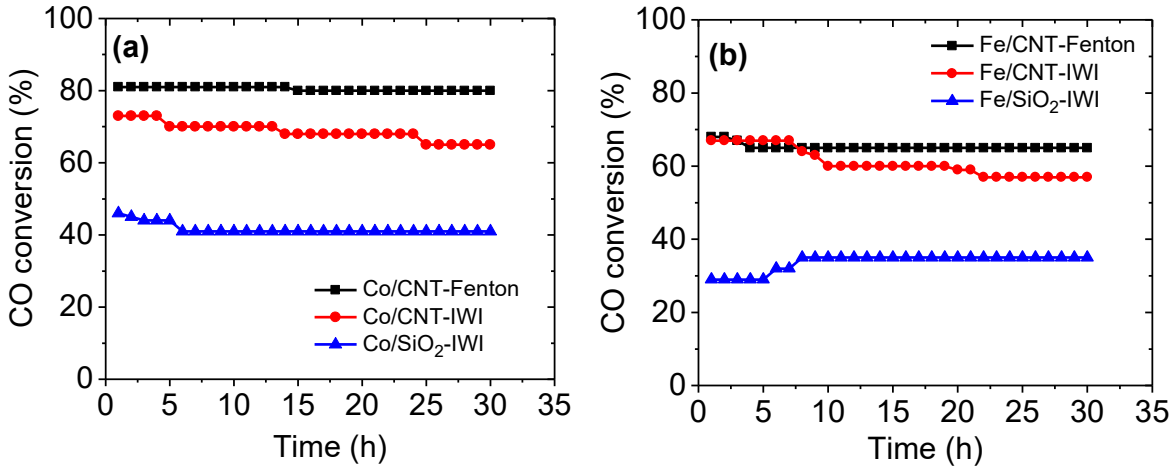

Figure 2-9 Variation of FTS activity and stability with time. (a) CO conversion of CNT- and SiO_2-supported Co catalysts (b) and CNT- and SiO_2-supported Fe catalysts as a function of time.

To obtain further insights into the structural evolution of the catalyst during the reaction, characterization of the used catalysts (after 30h on stream) by TEM and XRD was carried out. TEM images and corresponding histograms of PSDs with Gaussian fittings of CNT-supported catalysts and SiO_2-supported catalysts are presented in Figure 2-10 and Figure S6, respectively. Co/CNT-Fenton and Fe/CNT-Fenton catalysts are characterized by high stability, evident by the reduced sintering, which we attribute to the high catalyst dispersion, absence of a calcination step, and strong anchoring of catalyst on CNTs. We therefore hypothesize that the above features of photo-Fenton catalysts effectively impede sintering and extends catalyst lifetime. The XRD patterns (Figure S7) for the used catalyst reveal the disappearance of the CNT peak at 2θ value of 26° probably due to detachment of particles from CNTs and severe sintering that diminish the signal from CNTs. Also, there is the emergence of peaks associated with carbides for Fe/CNT-Fenton at 47.6º that is attributed to Fe_5C_2 and a small peak of Co_2C at 42.95º for Co/CNT-Fenton and an intense peak of CO_2C for Co/CNT-IWI.

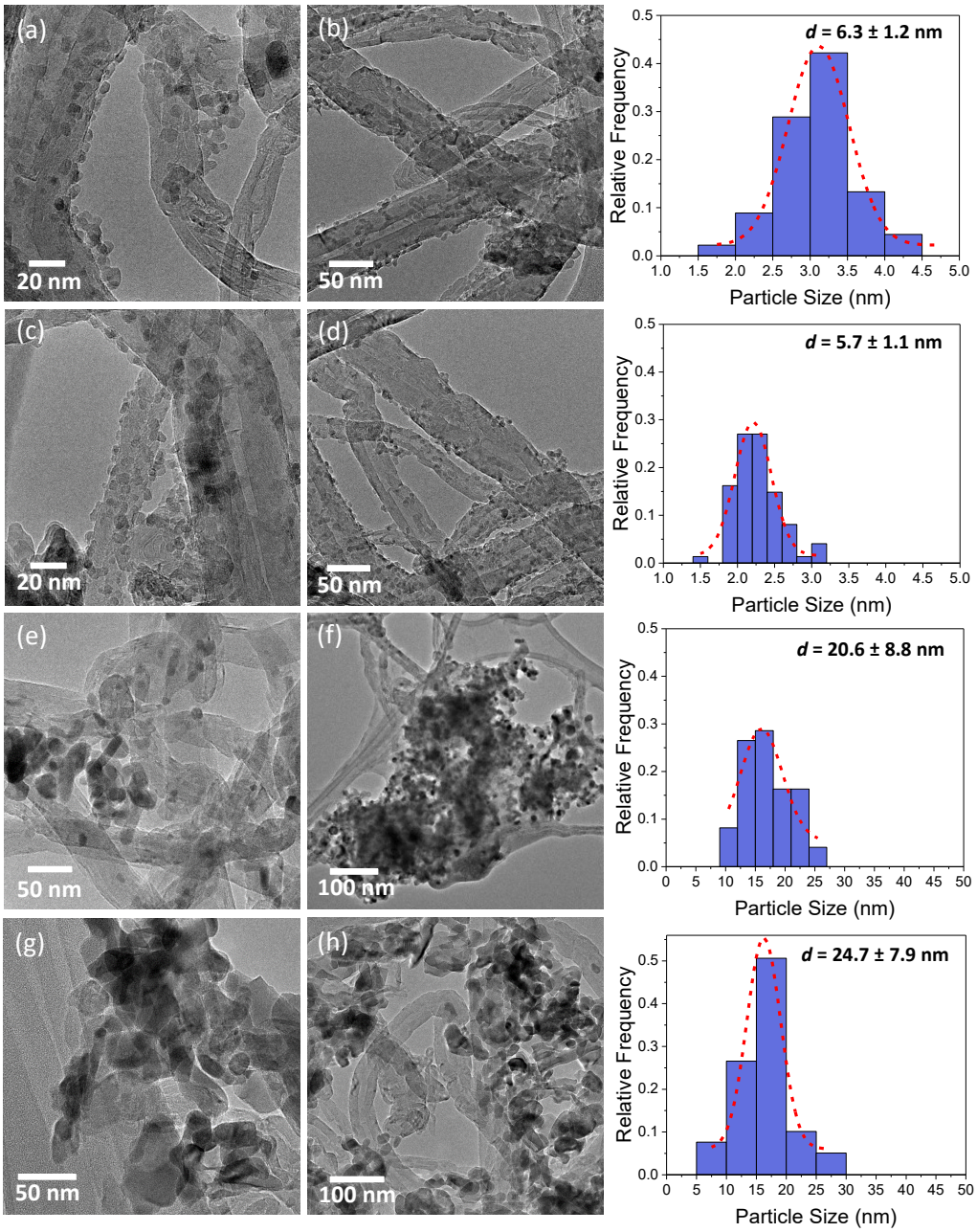

Figure 2-10 Low- and high-magnification TEM images and corresponding histograms of PSDs with Gaussian analysis fittings of used catalysts: Co/CNT-Fenton (a,b), Fe/CNT-Fenton (c,d), Co/CNT-IWI (e,f), and Fe/CNT-IWI (g,h).

To test the proposed hypothesis of deactivation, a 0.5 g of each catalyst was dispersed in ethanol under sonication at different times (1, 5, 8, and 10 h). After evaporating ethanol, the remaining particles (detached from the CNTs surface) were dissolved in Aqua regia solution and measured by ICP

spectroscopy and the results are shown in Figure 2-11. The detachment of particles increases with time, for catalyst prepared by IWI, indicating a total loss of 11.5 and 16.0 wt% after 10 h in a continuous sonication environment for Co and Fe, respectively. On the other hand, photo-Fenton catalysts (Fe, Co) show high adhesion to CNTs in the sonication environment, evidenced by a total loss of only 3.5 wt% of catalyst after 10 h. The photo-Fenton process is therefore well adapted for depositing well-anchored particles of narrow diameter distributions on CNTs, which minimizes loss of particles during sonication or FTS reaction. The high loss of catalyst particles supported on CNTs by IWI (Figure 2-11) is consistent with TEM data (Figure 2-10); we attribute this phenomenon to the high temperatures used during post-synthesis treatments and the presence of amorphous carbon deposits on the CNT surface after aggressive acid treatment. Kundu *et al.*[69] have shown that surface atomic concentration of functional groups on CNTs decreases with increasing treatment temperature.

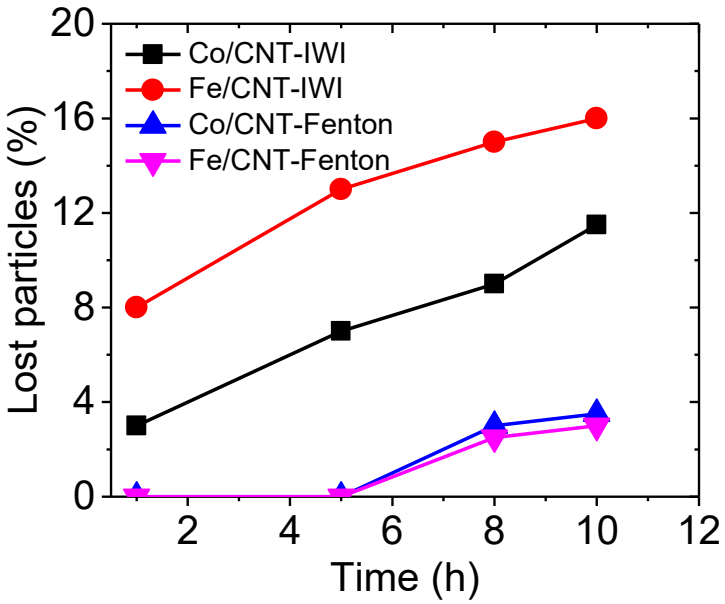

Figure 2-11 Amount of catalyst particles detached from CNTs during mild sonication of Co/CNT-IWI, Fe/CNT-IWI, Co/CNT-Fenton, and Fe/CNT-Fenton.

2.4 Conclusions

Modified photo-Fenton process offers an efficient and a green environment to oxidize CNTs and decorate the surface of CNTs with metal nanoparticles in a single step. The photo-Fenton process is facile, highly scalable, and involves the use of "green" materials: metal hydroxides as catalyst precursors and H_2O_2 as an oxidant. The process yields CNT-supported Fe or Co nanoparticles that are well dispersed and highly uniform in the size range of 2 – 5 nm. Following photo-Fenton process, the CNT structure is preserved, and there is no calcination step required due to the absence of foreign components that are usually introduced by conventional catalyst precursors. The H_2-TPR results reveal that photo-Fenton process yields small and highly uniform catalyst nanoparticles with high dispersion, which positively impacts the number of sites available for FTS reaction. In addition to the high catalyst stability during FTS, photo-Fenton catalysts show high CO conversion (~80% for Co/CNT-Fenton and 65% for Fe/CNT-Fenton) under the same operation conditions. In particular, unlike conventional catalysts, photo-Fenton catalysts show high selectivity to liquid hydrocarbons (~70% for Co/CNT and ~63% for Fe/CNT) at low reaction temperatures. The photo-Fenton catalysts show a higher stability with time with no evidence of deactivation after 30h while CNT- and SiO_2-based catalysts prepared by IWI show early deactivation (after 5 h). The deactivation rate of CNT-based catalysts shows direct correlation with adhesion of catalyst particles on CNT surface. The photo-Fenton process enhances the anchoring strength of catalysts and provides a promising synthesis route for exploiting the outstanding

References

1. Storsæter, S.; Tøtdal, B.; Walmsley, J. C.; Tanem, B. S.; Holmen, A., Characterization of alumina-, silica-, and titania-supported cobalt Fischer–Tropsch catalysts. *Journal of Catalysis* **2005,** *236* (1), 139-152.

2. Jacobs, G.; Das, T. K.; Zhang, Y.; Li, J.; Racoillet, G.; Davis, B. H., Fischer–Tropsch synthesis: support, loading, and promoter effects on the reducibility of cobalt catalysts. *Applied Catalysis A: General* **2002,** *233* (1–2), 263-281.

3. Vengsarkar, P. S.; Xu, R.; Roberts, C. B., Deposition of Iron Oxide Nanoparticles onto an Oxidic Support Using a Novel Gas-Expanded Liquid Process to Produce Functional Fischer–Tropsch Synthesis Catalysts. *Industrial & Engineering Chemistry Research* **2015,** *54* (47), 11814-11824.

4. Malek Abbaslou, R. M.; Tavasoli, A.; Dalai, A. K., Effect of pre-treatment on physico-chemical properties and stability of carbon nanotubes supported iron Fischer–Tropsch catalysts. *Applied Catalysis A: General* **2009,** *355* (1–2), 33-41.

5. Fu, T.; Huang, C.; Lv, J.; Li, Z., Fuel production through Fischer–Tropsch synthesis on carbon nanotubes supported Co catalyst prepared by plasma. *Fuel* **2014,** *121*, 225-231.

6. van Berge, P. J.; van de Loosdrecht, J.; Barradas, S.; van der Kraan, A. M., Oxidation of cobalt based Fischer–Tropsch catalysts as a deactivation mechanism. *Catalysis Today* **2000,** *58* (4), 321-334.

7. Iglesia, E., Design, synthesis, and use of cobalt-based Fischer-Tropsch synthesis catalysts. *Applied Catalysis A: General* **1997,** *161* (1), 59-78.

8. Kababji, A. H.; Joseph, B.; Wolan, J. T., Silica-Supported Cobalt Catalysts for Fischer–Tropsch Synthesis: Effects of Calcination Temperature and Support Surface Area on Cobalt Silicate Formation. *Catalysis Letters* **2009,** *130* (1), 72-78.

9. Liu, J.-X.; Su, H.-Y.; Sun, D.-P.; Zhang, B.-Y.; Li, W.-X., Crystallographic Dependence of CO Activation on Cobalt Catalysts: HCP versus FCC. *Journal of the American Chemical Society* **2013,** *135* (44), 16284-16287.

10. Gnanamani, M. K.; Jacobs, G.; Shafer, W. D.; Davis, B. H., Fischer–Tropsch synthesis: Activity of metallic phases of cobalt supported on silica. *Catalysis Today* **2013,** *215*, 13-17.

11. Jahangiri, H.; Bennett, J.; Mahjoubi, P.; Wilson, K.; Gu, S., A review of advanced catalyst development for Fischer-Tropsch synthesis of hydrocarbons from biomass derived syn-gas. *Catalysis Science and Technology* **2014,** *4* (8), 2210-2229.

12. Trépanier, M.; Dalai, A. K.; Abatzoglou, N., Synthesis of CNT-supported cobalt nanoparticle catalysts using a microemulsion technique: Role of nanoparticle size on reducibility, activity and selectivity in Fischer–Tropsch reactions. *Applied Catalysis A: General* **2010,** *374* (1–2), 79-86.

13. Tavasoli, A.; Abbaslou, R. M. M.; Trepanier, M.; Dalai, A. K., Fischer–Tropsch synthesis over cobalt catalyst supported on carbon nanotubes in a slurry reactor. *Applied Catalysis A: General* **2008,** *345* (2), 134-142.

14. Trépanier, M.; Tavasoli, A.; Dalai, A. K.; Abatzoglou, N., Fischer–Tropsch synthesis over carbon nanotubes supported cobalt catalysts in a fixed bed reactor: Influence of acid treatment. *Fuel Processing Technology* **2009,** *90* (3), 367-374.

15. Li, C.-H.; Yao, K.-F.; Liang, J., Influence of acid treatments on the activity of carbon nanotube-supported catalysts. *Carbon* **2003,** *41* (4), 858-860.

16. Peng, Y.; Liu, H., Effects of Oxidation by Hydrogen Peroxide on the Structures of Multiwalled Carbon Nanotubes. *Industrial & Engineering Chemistry Research* **2006,** *45* (19), 6483-6488.

17. Grujicic, M.; Cao, G.; Rao, A. M.; Tritt, T. M.; Nayak, S., UV-light enhanced oxidation of carbon nanotubes. *Applied Surface Science* **2003,** *214* (1–4), 289-303.

18. Najafi, E.; Kim, J.-Y.; Han, S.-H.; Shin, K., UV-ozone treatment of multi-walled carbon nanotubes for enhanced organic solvent dispersion. *Colloids and Surfaces A: Physicochemical and Engineering Aspects* **2006,** *284–285* (0), 373-378.

19. Czech, B.; Oleszczuk, P.; Wiącek, A., Advanced oxidation (H2O2 and/or UV) of functionalized carbon nanotubes (CNT-OH and CNT-COOH) and its influence on the stabilization of CNTs in water and tannic acid solution. *Environmental Pollution* **2015,** *200*, 161-167.

20. Datsyuk, V.; Kalyva, M.; Papagelis, K.; Parthenios, J.; Tasis, D.; Siokou, A.; Kallitsis, I.; Galiotis, C., Chemical oxidation of multiwalled carbon nanotubes. *Carbon* **2008,** *46* (6), 833-840.

21. Aguiló-Aguayo, N.; Castaño-Bernal, J. L.; García-Céspedes, J.; Bertran, E., Magnetic response of CVD and PECVD iron filled multi-walled carbon nanotubes. *Diamond and Related Materials* **2009,** *18* (5–8), 953-956.

22. Qian, W.; Wei, F.; Liu, T.; Wang, Z. W., The formation mechanism of the coaxial carbon–metal nanowires in a chemical vapor deposition process. *Solid State Communications* **2003,** *126* (7), 365-367.

23. Singh, C.; Shaffer, M. S. P.; Windle, A. H., Production of controlled architectures of aligned carbon nanotubes by an injection chemical vapour deposition method. *Carbon* **2003,** *41* (2), 359-368.

24. Wang, M.; Zhang, L.; Fan, X.; Zhou, Y.; Chen, L.; Kong, Q.; Shi, J., A unique route to fabricate mesoporous carbon with abundant ferric species as a heterogeneous Fenton catalyst under neutral conditions. *RSC Advances* **2015,** *5* (122), 101241-101246.

25. Ruppert, G.; Bauer, R.; Heisler, G., The photo-Fenton reaction — an effective photochemical wastewater treatment process. *Journal of Photochemistry and Photobiology A: Chemistry* **1993,** *73* (1), 75-78.

26. Bokare, A. D.; Choi, W., Review of iron-free Fenton-like systems for activating H2O2 in advanced oxidation processes. *Journal of Hazardous Materials* **2014,** *275*, 121-135.

27. Chen, R.; Pignatello, J. J., Role of Quinone Intermediates as Electron Shuttles in Fenton and Photoassisted Fenton Oxidations of Aromatic Compounds. *Environmental Science & Technology* **1997,** *31* (8), 2399-2406.

28. Feng, J.; Hu, X.; Yue, P. L., Effect of initial solution pH on the degradation of Orange II using clay-based Fe nanocomposites as heterogeneous photo-Fenton catalyst. *Water Research* **2006,** *40* (4), 641-646.

29. Nakhaei Pour, A.; Housaindokht, M., Fischer–Tropsch Synthesis Over CNT Supported Cobalt Catalysts: Role of Metal Nanoparticle Size on Catalyst Activity and Products Selectivity. *Catalysis Letters* **2013,** *143* (12), 1328-1338.

30. Webb, P. A., Introduction to chemical adsorption analytical techniques and their applications to catalysis. *Micromeritics Instrument Corp. Technical Publications* **2003**.

31. Duvenhage, D. J.; Coville, N. J., Fe:CoTiO2 bimetallic catalysts for the Fischer-Tropsch reaction I. Characterization and reactor studies. *Applied Catalysis A: General* **1997,** *153* (1–2), 43-67.

32. Ovejero, G.; Sotelo, J. L.; Romero, M. D.; Rodríguez, A.; Ocaña, M. A.; Rodríguez, G.; García, J., Multiwalled Carbon Nanotubes for Liquid-Phase Oxidation. Functionalization, Characterization, and Catalytic Activity. *Industrial & Engineering Chemistry Research* **2006,** *45* (7), 2206-2212.

33. Mazov, I.; Kuznetsov, V. L.; Simonova, I. A.; Stadnichenko, A. I.; Ishchenko, A. V.; Romanenko, A. I.; Tkachev, E. N.; Anikeeva, O. B., Oxidation behavior of multiwall carbon nanotubes with different diameters and morphology. *Applied Surface Science* **2012,** *258* (17), 6272-6280.

34. Subrahmanyam, K. S.; Vivekchand, S. R. C.; Govindaraj, A.; Rao, C. N. R., A study of graphenes prepared by different methods: characterization, properties and solubilization. *Journal of Materials Chemistry* **2008,** *18* (13), 1517-1523.

35. Cheng, W.; Tang, K.; Qi, Y.; Sheng, J.; Liu, Z., One-step synthesis of superparamagnetic monodisperse porous Fe3O4 hollow and core-shell spheres. *Journal of Materials Chemistry* **2010,** *20* (9), 1799-1805.

36. Griboval-Constant, A.; Butel, A.; Ordomsky, V. V.; Chernavskii, P. A.; Khodakov, A. Y., Cobalt and iron species in alumina supported bimetallic catalysts for Fischer–Tropsch reaction. *Applied Catalysis A: General* **2014,** *481*, 116-126.

37. Karimi, S.; Tavasoli, A.; Mortazavi, Y.; Karimi, A., Cobalt supported on Graphene – A promising novel Fischer–Tropsch synthesis catalyst. *Applied Catalysis A: General* **2015,** *499*, 188-196.

38. Lin, H.-K.; Wang, C.-B.; Chiu, H.-C.; Chien, S.-H., In situ FTIR Study of Cobalt Oxides for the Oxidation of Carbon Monoxide. *Catalysis Letters* **2003,** *86* (1), 63-68.

39. Sánchez, M. D.; Chen, P.; Reinecke, T.; Muhler, M.; Xia, W., The Role of Oxygen- and Nitrogen-containing Surface Groups on the Sintering of Iron Nanoparticles on Carbon Nanotubes in Different Atmospheres. *ChemCatChem* **2012,** *4* (12), 1997-2004.

40. Subramanian, V.; Ordomsky, V. V.; Legras, B.; Cheng, K.; Cordier, C.; Chernavskii, P. A.; Khodakov, A. Y., Design of iron catalysts supported on carbon-silica composites with enhanced catalytic performance in high-temperature Fischer-Tropsch synthesis. *Catalysis Science & Technology* **2016,** *6* (13), 4953-4961.

41. Díaz, J. A.; Akhavan, H.; Romero, A.; Garcia-Minguillan, A. M.; Romero, R.; Giroir-Fendler, A.; Valverde, J. L., Cobalt and iron supported on carbon nanofibers as catalysts for Fischer–Tropsch synthesis. *Fuel Processing Technology* **2014,** *128*, 417-424.

42. Moradi, G. R.; Basir, M. M.; Taeb, A.; Kiennemann, A., Promotion of Co/SiO2 Fischer–Tropsch catalysts with zirconium. *Catalysis Communications* **2003,** *4* (1), 27-32.

43. Trépanier, M.; Tavasoli, A.; Dalai, A. K.; Abatzoglou, N., Co, Ru and K loadings effects on the activity and selectivity of carbon nanotubes supported cobalt catalyst in Fischer–Tropsch synthesis. *Applied Catalysis A: General* **2009,** *353* (2), 193-202.

44. Tavasoli, A.; Sadagiani, K.; Khorashe, F.; Seifkordi, A. A.; Rohani, A. A.; Nakhaeipour, A., Cobalt supported on carbon nanotubes — A promising novel Fischer–Tropsch synthesis catalyst. *Fuel Processing Technology* **2008,** *89* (5), 491-498.

45. Reuel, R. C.; Bartholomew, C. H., The stoichiometries of H2 and CO adsorptions on cobalt: Effects of support and preparation. *Journal of Catalysis* **1984,** *85* (1), 63-77.

46. Chew, L. M.; Xia, W.; Düdder, H.; Weide, P.; Ruland, H.; Muhler, M., On the role of the stability of functional groups in multi-walled carbon nanotubes applied as support in iron-based high-temperature Fischer–Tropsch synthesis. *Catalysis Today* **2016,** *270*, 85-92.

47. Arsalanfar, M.; Mirzaei, A. A.; Bozorgzadeh, H. R.; Atashi, H., Effect of process conditions on the surface reaction rates and catalytic performance of MgO supported Fe–Co–Mn catalyst for CO hydrogenation. *Journal of Industrial and Engineering Chemistry* **2012,** *18* (6), 2092-2102.

48. Liu, Y.; Teng, B.-T.; Guo, X.-H.; Li, Y.; Chang, J.; Tian, L.; Hao, X.; Wang, Y.; Xiang, H.-W.; Xu, Y.-Y.; Li, Y.-W., Effect of reaction conditions on the catalytic performance of Fe-Mn catalyst for Fischer-Tropsch synthesis. *Journal of Molecular Catalysis A: Chemical* **2007,** *272* (1–2), 182-190.

49. Donnelly, T. J.; Satterfield, C. N., Product distributions of the Fischer-Tropsch synthesis on precipitated iron catalysts. *Applied Catalysis* **1989,** *52* (1), 93-114.

50. Bukur, D. B.; Patel, S. A.; Lang, X., Fixed bed and slurry reactor studies of Fischer-Tropsch synthesis on precipitated iron catalyst. *Applied Catalysis* **1990,** *61* (1), 329-349.

51. Yang, D. J.; Zhang, Q.; Chen, G.; Yoon, S. F.; Ahn, J.; Wang, S. G.; Zhou, Q.; Wang, Q.; Li, J. Q., Thermal conductivity of multiwalled carbon nanotubes. *Physical Review B* **2002,** *66* (16), 165440.

52. Andersson, S.; Dzhavadov, L., Thermal conductivity and heat capacity of amorphous SiO 2 : pressure and volume dependence. *Journal of Physics: Condensed Matter* **1992,** *4* (29), 6209.

53. Pendyala, V. R. R.; Shafer, W. D.; Jacobs, G.; Davis, B. H., Fischer–Tropsch Synthesis: Effect of Reaction Temperature for Aqueous-Phase Synthesis Over a Platinum Promoted Co/Alumina Catalyst. *Catalysis Letters* **2014,** *144* (6), 1088-1095.

54. Guettel, R.; Turek, T., Comparison of different reactor types for low temperature Fischer–Tropsch synthesis: A simulation study. *Chemical Engineering Science* **2009,** *64* (5), 955-964.

55. Berger, R. J.; Pérez-Ramírez, J.; Kapteijn, F.; Moulijn, J. A., Catalyst performance testing: Radial and axial dispersion related to dilution in fixed-bed laboratory reactors. *Applied Catalysis A: General* **2002,** *227* (1–2), 321-333.

56. Cheng, K.; Virginie, M.; Ordomsky, V. V.; Cordier, C.; Chernavskii, P. A.; Ivantsov, M. I.; Paul, S.; Wang, Y.; Khodakov, A. Y., Pore size effects in high-temperature Fischer–Tropsch synthesis over supported iron catalysts. *Journal of Catalysis* **2015,** *328*, 139-150.

57. Wielers, A. F. H.; Kock, A. J. H. M.; Hop, C. E. C. A.; Geus, J. W.; van Der Kraan, A. M., The reduction behavior of silica-supported and alumina-supported iron catalysts: A Mössbauer and infrared spectroscopic study. *Journal of Catalysis* **1989,** *117* (1), 1-18.

58. Mogorosi, R. P.; Fischer, N.; Claeys, M.; van Steen, E., Strong-metal–support interaction by molecular design: Fe–silicate interactions in Fischer–Tropsch catalysts. *Journal of Catalysis* **2012,** *289*, 140-150.

59. Enache, D. I.; Rebours, B.; Roy-Auberger, M.; Revel, R., In Situ XRD Study of the Influence of Thermal Treatment on the Characteristics and the Catalytic Properties of Cobalt-Based Fischer–Tropsch Catalysts. *Journal of Catalysis* **2002,** *205* (2), 346-353.

60. Fischer, N.; van Steen, E.; Claeys, M., Preparation of supported nano-sized cobalt oxide and fcc cobalt crystallites. *Catalysis Today* **2011,** *171* (1), 174-179.

61. Kitakami, O.; Sato, H.; Shimada, Y.; Sato, F.; Tanaka, M., Size effect on the crystal phase of cobalt fine particles. *Physical Review B* **1997,** *56* (21), 13849-13854.

62. Bukur, D. B.; Lang, X.; Mukesh, D.; Zimmerman, W. H.; Rosynek, M. P.; Li, C., Binder/support effects on the activity and selectivity of iron catalysts in the Fischer-Tropsch synthesis. *Industrial & Engineering Chemistry Research* **1990,** *29* (8), 1588-1599.

63. Gao, Y.; Neal, L. M.; Li, F., Li-Promoted LaxSr2–xFeO4−δ Core–Shell Redox Catalysts for Oxidative Dehydrogenation of Ethane under a Cyclic Redox Scheme. *ACS Catalysis* **2016,** *6* (11), 7293-7302.

64. Liu, F.; Sun, J.; Zhu, L.; Meng, X.; Qi, C.; Xiao, F.-S., Sulfated graphene as an efficient solid catalyst for acid-catalyzed liquid reactions. *Journal of Materials Chemistry* **2012,** *22* (12), 5495-5502.

65. Quek, X.-Y.; Pestman, R.; van Santen, R. A.; Hensen, E. J. M., Structure sensitivity in the ruthenium nanoparticle catalyzed aqueous-phase Fischer-Tropsch reaction. *Catalysis Science & Technology* **2014,** *4* (10), 3510-3523.

66. Ciobica, I. M.; van Santen, R. A., Carbon Monoxide Dissociation on Planar and Stepped Ru(0001) Surfaces. *The Journal of Physical Chemistry B* **2003,** *107* (16), 3808-3812.

67. Ojeda, M.; Nabar, R.; Nilekar, A. U.; Ishikawa, A.; Mavrikakis, M.; Iglesia, E., CO activation pathways and the mechanism of Fischer–Tropsch synthesis. *Journal of Catalysis* **2010,** *272* (2), 287-297.

68. Shetty, S.; Jansen, A. P. J.; van Santen, R. A., Direct versus Hydrogen-Assisted CO Dissociation. *Journal of the American Chemical Society* **2009,** *131* (36), 12874-12875.

69. Kundu, S.; Wang, Y.; Xia, W.; Muhler, M., Thermal Stability and Reducibility of Oxygen-Containing Functional Groups on Multiwalled Carbon Nanotube Surfaces: A Quantitative High-Resolution XPS and TPD/TPR Study. *The Journal of Physical Chemistry C* **2008,** *112* (43), 16869-16878.

Chapter 3

Gaseous Product Mixture from Fischer-Tropsch Synthesis as an Efficient Carbon Feedstock for Low Temperature CVD Growth of Carbon Nanotube Carpets

Reproduced by permission of The Royal Society of Chemistry

http://dx.doi.org/10.1039/C6NR03679A

Abstract

Low-temperature chemical vapor deposition (CVD) growth of carbon nanotube (CNT) carpets from Fe and Fe-Cu catalysts using a gaseous product mixture from Fischer-Tropsch synthesis (FTS-GP) as a superior carbon feedstock is demonstrated. This growth approach addresses a persistent issue of obtaining thick CNT carpets on temperature-sensitive substrates at low temperatures using a non-plasma CVD approach without catalyst pretreatment and/or preheating of the carbon feedstock. The efficiency of the process is evidenced by the highly dense, vertically aligned CNT structures from both Fe and Fe-Cu catalysts even at temperatures as low as 400°C – a record low growth temperature for CNT carpets obtained via conventional thermal CVD. The grown CNTs exhibit a straight morphology with hollow interior and parallel graphitic planes along the tube walls. The apparent activation energies for CNT carpet growth on Fe and Fe-Cu catalysts are 0.71 and 0.54 eV, respectively. The synergistic effect of Fe and Cu show a strong dependence on the growth temperature, with Cu being more influential at temperatures higher than 450°C. The low activation energies and long catalyst lifetimes observed are rationalized based on the unique composition of FTS-GP and Gibbs free energies of the component gases. The use of FTS-GP facilitates low-temperature growth of CNT carpets on traditional (alumina film) and nontraditional substrates (aluminum foil) and has the potential of enhancing CNT quality, catalyst lifetime, and scalability.

3.1 Introduction

To harness the outstanding properties of carbon nanotubes (CNTs) in applications that require vertically aligned CNT structures (or "CNT carpets") to be grown directly on temperature-sensitive substrates, the compatibility between the growth process and the targeted technology is critical. The widely preferred catalytic chemical vapor deposition (CCVD) process[1-3] used for CNT growth requires undesirably high temperatures. Therefore, research efforts continue to focus on the modification of the CCVD process to allow for efficient and controlled CNT carpet growth at low temperatures. CNT carpets directly grown on specific substrates with low temperature tolerance are highly desired in important applications. As examples, aluminum and glass substrates have a temperature tolerance of ~550°C and a strain point at 550°C, respectively. CNT carpets supported on aluminum can be used as hybrid electrodes in electric double layer capacitors (EDLCs)[4] while CNT carpets supported on glass are promising field emitters.[5] In addition, the integration of CNTs with complementary metal-oxide semiconductor (CMOS) technology will require lowering the growth temperature to or below 400°C to prevent mechanical deterioration of the low dielectric constant of inter-metal materials in the device structures.[6] Although there have been numerous reports on CCVD growth of CNTs at low temperatures,[7,8] the growth of CNT carpets of good quality below 450°C via conventional thermal CCVD process remains a challenge.

Based on the generally adopted carbon filament growth model (derived from the vapor-liquid-solid theory developed by Wagner and Ellis)[9] used for describing CNT growth via CCVD, there are three critical and relatively independent steps involved in the growth process.[10] The first step is the dissociation of the carbon precursor on the catalyst surface to form carbon atoms, followed by the diffusion of the carbon atoms through the particle to the end of the initially formed cap where the attachment to the particle is strong. The third step involves the incorporation of carbon atoms into the ends of the cap to form a well-organized CNT structure. These steps are heavily dependent on

temperature. For low-temperature growth via CCVD, the dissociation of the carbon precursor has been identified as the rate-limiting step.[10,11] Consequently, a number of strategies aimed at overcoming this reaction barrier have been explored such as the use of bimetallic catalysts,[8] relatively unstable carbon precursors,[12] plasma atmospheres from a variety of sources,[13-15] metal-support interactions,[16,17] and preheating of the precursor gas mixture.[11] As delineated below, reports on low-temperature growth of CNTs usually involve the implementation of one or a combination of these strategies.

CNT carpets have been widely synthesized by plasma-enhanced CVD (PECVD) at temperatures below 450°C.[14,18] Also, low-temperature growth of CNT carpets in the range of 350–440°C has been achieved by a photo-thermal CVD process using high power optical sources to provide energy for the decomposition of the precursor on the growth surface.[19] Using engineered Ni catalyst (annealed at 400°C), Noda and coworkers[20] demonstrated the growth of CNT carpets at 400°C by CVD using acetylene as the carbon feedstock. Although these growth processes yield CNT carpets at low temperatures, the additional steps and equipment involved may present scalability issues; in the case of PECVD, the impingement of high-energy radicals generated by the plasma on the substrate creates substantial structural defects on the CNTs.[3,15,21 22]

In the case of conventional thermal CVD, binary-layered catalysts such as NiCo, CoMo,[23] FeMo,[24] FeNi,[25,26] FeAl,[27] CoTi,[27-29] and FeCu[8,22,30] have shown higher catalytic activity at relatively low temperatures in comparison to their pristine counterparts (Co, Fe, and Ni). Quantum mechanical studies of the CNT growth process have rationalized the special catalytic properties of bimetallic catalysts to be due to the role the different metal components play in the nucleation and growth processes.[31] Low-temperature growth of CNT carpets has also been achieved using a combination of a mono-, bi- or trimetallic catalyst and relatively unstable carbon precursors such as acetylene and cyclopentene oxide;[12,31] these carbon precursors are characterized by low thermal stability due to the weak π bonds between the carbon atoms. Nessim et al.[11] demonstrated that by appropriately preheating

the gas mixture and ensuring good catalyst-substrate interactions, high-quality CNT carpets can be grown on conductive substrates at 500°C. The thermal excitation of molecules during preheating of the carbon precursor has been shown to effectively enhance CNT growth at low temperatures from binary catalysts (Fe/Al and Co/Ti) supported on glass.[27] We note that for conventional thermal CCVD, growth temperatures higher than 400°C are usually required for CNT carpet growth.

Here, we propose a new thermal CCVD approach for the efficient growth of CNT carpets on traditional and nontraditional substrates at low temperatures. The approach involves the use of a gaseous product mixture from Fischer-Tropsch synthesis (FTS) process (hereinafter referred to as FTS-GP) as a carbon feedstock. FTS is an environmentally friendly approach used in industry for the conversion of syngas (CO and H_2), usually obtained from low-value natural gas, biomass, and coal, to high-value hydrocarbon liquid fuels over Fe or Co catalysts. The typical CO conversion to C5+ (desirable products) during FTS is 70 – 80% and the rest of the undesired products, which constitute FTS-GP, are light hydrocarbons (C1 to C3 saturated and unsaturated hydrocarbons) and unconverted CO and H_2. Some of the FTS-GP mixture is used as a fuel gas while the rest is sent to the flare unit and treated as waste gases. Additionally, the hydrocracking unit in oil refineries also produce FTS-GP[32] as a side product, which is similarly treated as waste gases. Therefore, there are several potential benefits of using FTS-GP as a standard carbon source for CNT growth. First, this approach is expected to enhance sustainability of the growth process and lower the cost of producing scalable amounts of CNTs. Second, the unsaturated hydrocarbons with low energy covalent bonds present in FTS-GP can initiate the thermal decomposition of the more stable saturated hydrocarbons that make up more than 50% of FTS-GP, thus enabling efficient CNT carpet growth at record low temperatures from a monometallic catalyst supported on traditional and nontraditional substrates. Third, the low CO partial pressure in FTS-GP favors a reaction with hydrogen, which could produce water that oxidizes excess

carbon and amorphous carbon from the catalyst surface, thus extending the catalyst lifetime in accordance with the mechanism proposed for "supergrowth."[33,34]

3.2 Results and Discussion

The use of FTS-GP as a carbon feedstock for CNT carpet growth in the presence of Fe and Fe-Cu catalysts has enabled significant reduction in the growth temperatures of CNT carpets by CCVD. The composition of FTS-GP used in this study is as follows: CH_4 (30%), C_2H_6 (8%), C_2H_4 (6%), C_3H_8 (5%), C_3H_6 (2%), H_2 (40%), CO (5%), and N_2 (4%). It should be noted that the reaction conditions used during FTS process determines the composition of FTS-GP. The above composition broadly represents a typical product mixture from FTS[35-37] and is consistent with the product distribution reported by Emerson Inc.[38] Figure 3-1 panels A – H show representative scanning electron microscopy (SEM) images of CNT carpet morphologies grown at different temperatures (400, 450, 500, and 550°C) on alumina-supported Fe and Fe-Cu catalysts. The efficiency of the low temperature growth process using FTS-GP is illustrated by the highly dense vertically aligned CNT structures produced on both catalysts even at a record low temperature of 400°C. Even though CNT length and density decrease with decreasing growth temperature,[12,14,39] as evidenced by the difficulty in achieving growth of CNT carpets at temperatures below 450°C,[8,12,28] the use of FTS-GP resulted in CNT carpets of relatively high density and uniform coverage on the substrate with heights up to a few micrometers at 400°C after 60 min.

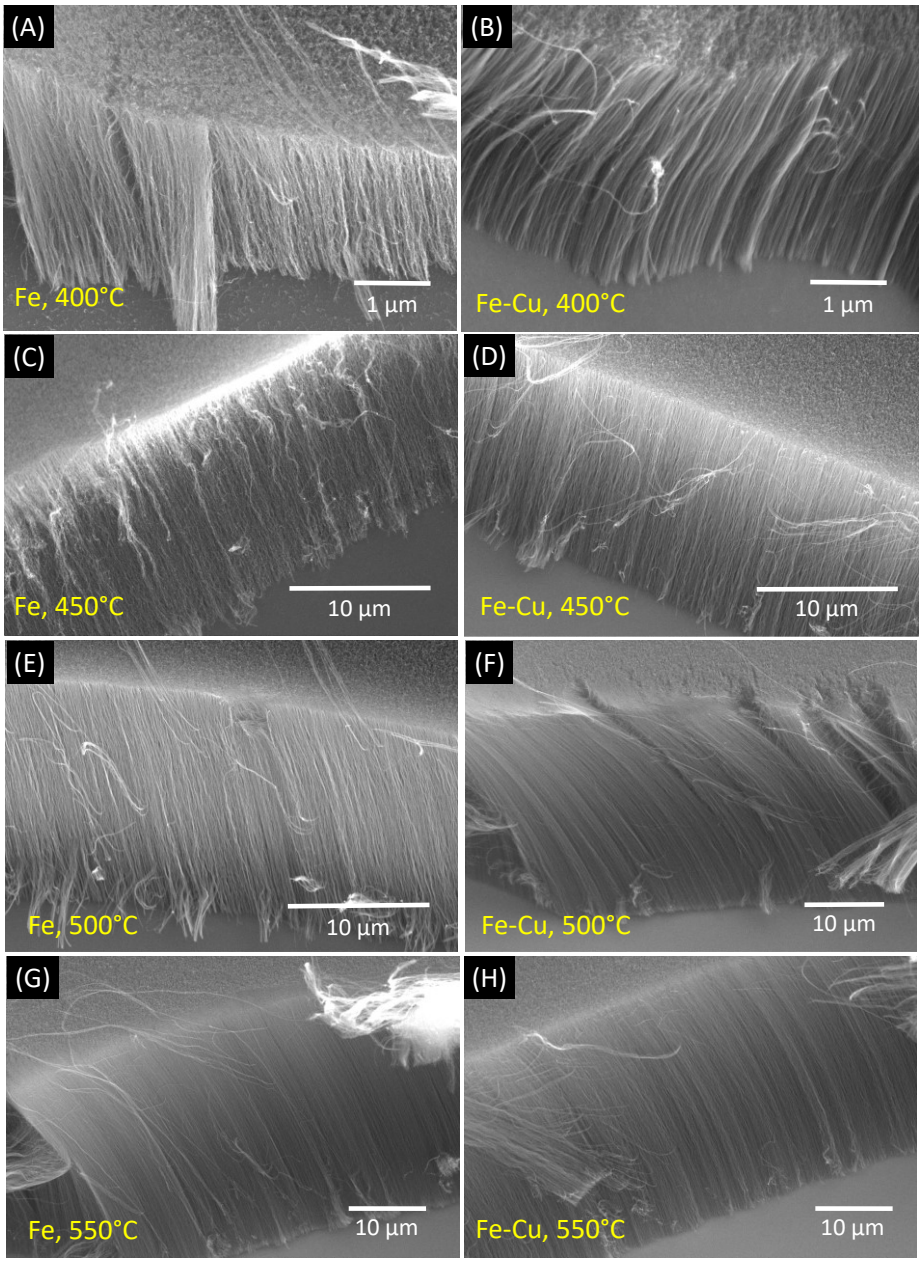

Figure 3-1 CNT carpets grown at low temperatures using FTS-GP for 1h. SEM images of carpets grown on Al_xO_y/Fe at 400°C (A), Al_xO_y/Fe-Cu at 400°C (B), Al_xO_y/Fe at 450°C (C), Al_xO_y/Fe-Cu at 450°C (D), Al_xO_y/Fe at 500°C (E), Al_xO_y/Fe-Cu at 500°C (F), Al_xO_y/Fe at 550°C (G), and Al_xO_y/Fe-Cu at 550°C (H).

The Raman spectra of as-grown CNT carpets from Fe and Fe-Cu catalysts at 400, 450, 500, and 550°C are presented in Figure 3-2. The spectra exhibit unambiguously the characteristic modes of CNTs: the disorder-induced mode (D-band) at ~1345 cm^{-1} that is attributed to defects, and a tangential stretch mode (G-band) at ~1593 cm^{-1} that is due to the highly oriented hexagonal lattice of graphite whose intensity and width are related to the crystallinity of CNTs. The shoulder peak at ~1600 cm^{-1} (D′ line)[40,41] on the G-band that is usually induced by disorders in the CNTs is generally absent in the spectra, indicating the decent quality of the CNTs produced from FTS-GP at low temperatures.

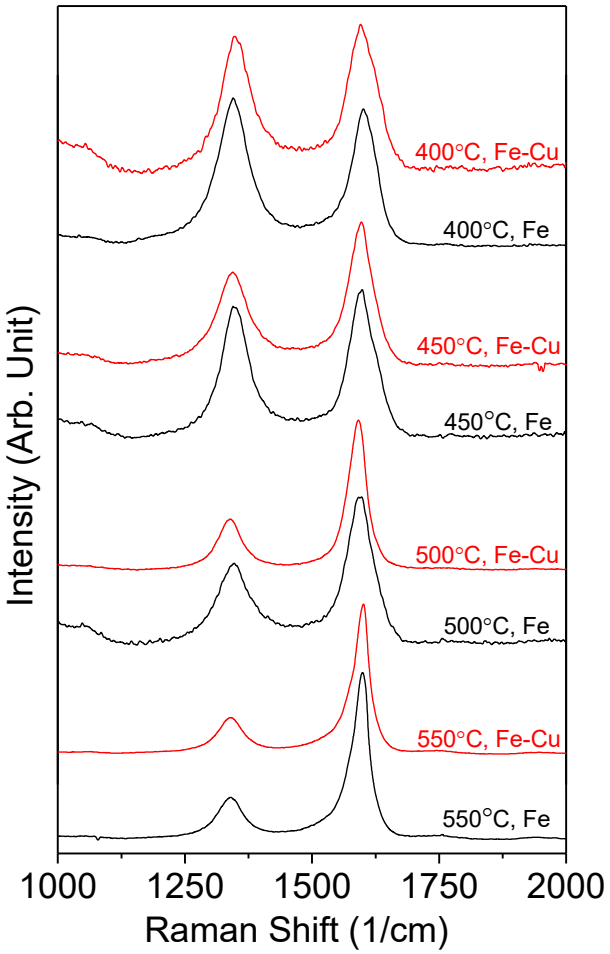

Figure 3-2 Raman spectra of CNT carpets grown on Al_xO_y/Fe (black) and Al_xO_y/Fe-Cu (red) at different temperatures under excitation of 532 nm laser.

The integrated G- and D-band intensity ratio (I_G/I_D) is used as an index to evaluate the quality of CNTs produced. Figure 3-3A shows the dependence of I_G/I_D on the growth temperature. As expected, there is increased graphitization of the CNTs with growth temperature as shown by the increasing I_G/I_D. Figures 3B and C show the dependence of the product yield and the maximum CNT carpet height after 30 min on growth temperature; in general, these CNT carpet properties increase with the growth temperature and the superior catalytic behavior of Fe-Cu is evident. Figures 3A, B, and C reveal that the dependence of the CNT carpet properties on the growth temperature appears to have two distinct regimes. The first regime occurs below 450°C where the effect of Cu promoter on CNT carpet growth is low, evidenced by the slight increase in I_G/I_D, product mass, and CNT carpet height, while the second occurs above 450°C where the presence of Cu promoter leads to marked enhancement in the carbon yield and CNT quality. The existence of similar growth regimes at low temperatures has been reported for alcohol CVD growth of CNTs with bimetallic and trimetallic catalysts whereby a sudden increase in the product mass occurred above 400°C.[7] There is a moderate linear correlation between carpet height or product mass and growth temperature (Figures 3B and C). The CNT carpet height obtained after 30 min is higher for Fe-Cu than Fe catalysts at all temperatures (400, 450, 500, and 550°C); it increases from 2.4 μm at 400°C to 21.2 μm at 550°C for Fe catalyst and from 3.6 μm at 400°C to 26.6 μm at 550°C for Fe-Cu. The enhanced catalytic activity of Fe-Cu catalysts has been attributed to the special role played by Cu as a promoter, by enhancing the stability and reducing the reduction temperature of Fe.[8,42,43] The striking difference in the activity of Fe-Cu and Fe catalysts in our work, especially at temperatures higher than 450°C, suggests that the synergistic effect between Fe and Cu is temperature dependent as it appears to be highly favorable beyond 450°C. We therefore conclude that the CNT carpet growth efficiency observed at 400 and 450°C, temperatures where the role of Cu appear to be weak, is largely due to the unique properties of FTS-GP. Note that the use of acetylene,

the conventional precursor for low-temperature growth, seldom yields CNT carpets at 400°C using a standard monometallic catalyst.[7,8,17,20,28,44] These results provide strong evidence of the high suitability of FTS-GP as a carbon feedstock for efficient low-temperature growth of CNT carpets.

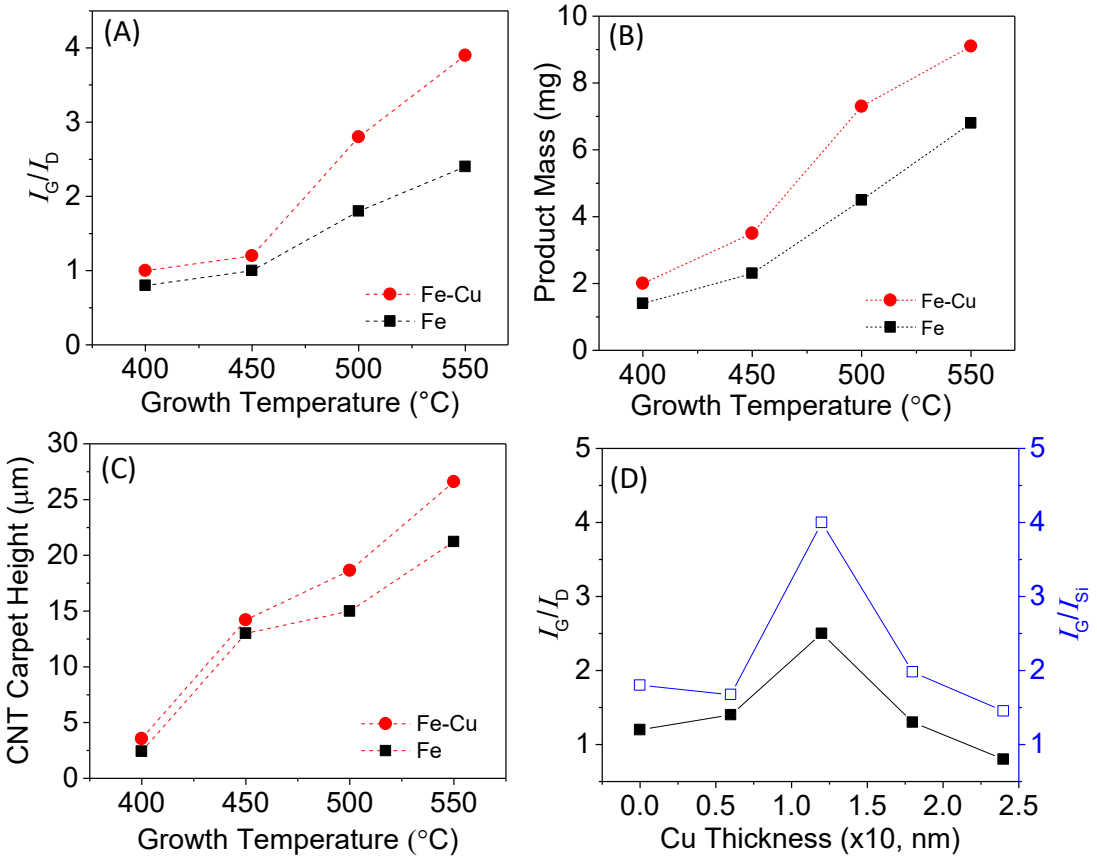

Figure 3-3 CNT carpet properties after 30 min of CVD process over Fe and Fe-Cu catalysts. Quality of CNT carpets (I_G/I_D) as a function of growth temperature (A). Product mass obtained on catalysts as a function of growth temperature (B). CNT carpet height as a function of growth temperature (C). CNT carpet quality (I_G/I_D) and yield or density (I_G/I_{Si}) as a function of the Cu thickness in Al_xO_y/Fe-Cu catalyst (D).

To determine the optimum Cu thickness in Fe-Cu catalyst, we conducted low-temperature growth on the catalysts with different nominal thicknesses of Cu in Cu/Fe layers corresponding to 0.1/1.0, 0.2/1.0, 0.3/1.0, and 0.35/1.0 (nm/nm). Prior to optimizing the Cu layer thickness, we reversed the sequence of Cu and Fe depositions to investigate how the stacking order of the metallic layers on Al_xO_y affects the growth of CNT carpets. As shown in Figure S1, the catalyst configuration with the Cu layer

sandwiched between Fe and Al_xO_y resulted in a higher activity, and consequently, this catalyst configuration was used throughout this study. The optimization of the Cu layer thickness was based on the CNT carpet coverage on the substrate and the CNT carpet density, determined from their Raman spectra by comparing the ratio of the phonon peak intensity of Si at 520 cm^{-1} and the G-peak intensity at ~1593 cm^{-1}. As shown in Figure 3D, the density and quality of CNTs produced depend on the Cu fraction in Fe-Cu catalysts, with highest CNT quality and density (corresponding to the highest I_G/I_D and I_G/I_{Si}) at Cu thickness of 0.12 nm. Using Cu layers with higher thickness (> 0.12 nm) results in a progressive decrease in I_G/I_D and I_G/I_{Si}, possibly due to the changes in the carbon solubility and diffusion in the catalysts. The XPS survey scans of Fe and Fe-Cu catalysts with the optimal Cu thickness after exposure to CNT carpet growth conditions are presented in Figure S2; the composition for Fe-Cu is determined to be ~10 at% Cu and ~90 at% Fe, which is somewhat consistent with the optimum Cu ratio (10–20 wt%) reported by Wielers et al.[42] for FTS reaction. The result is also in agreement with the work of He et al.[22] whereby the growth of high-quality SWCNTs was achieved only for catalysts with the optimum Fe and Cu concentrations. The observed decrease in the activity of Fe-Cu with increasing Cu thickness (> 0.12 nm) is attributed to the disappearance of the active species on the surface of the bimetallic catalyst; this is consistent with the disappearance of islets of the active Fe phase on the catalyst surface with increasing ratio of Cu beyond the optimum amount, as demonstrated by Wielers et al.[42]

The microstructure of the as-grown CNT carpets was characterized by transmission electron microscopy (TEM). Panels A and B of Figure 3-4 show representative images of CNTs grown from Fe catalysts at 400°C while images of CNTs grown from Fe-Cu catalysts are shown in panels C and D; the images reveal the high purity of the CNT arrays. As further demonstrated by the high-resolution TEM images in Figure 3-5, the CNTs exhibit a tubular morphology and well-aligned graphitic sheets

that are parallel to the tube axis, with a distinct inter-wall spacing of ~0.34 nm, in agreement with the standard spacing.

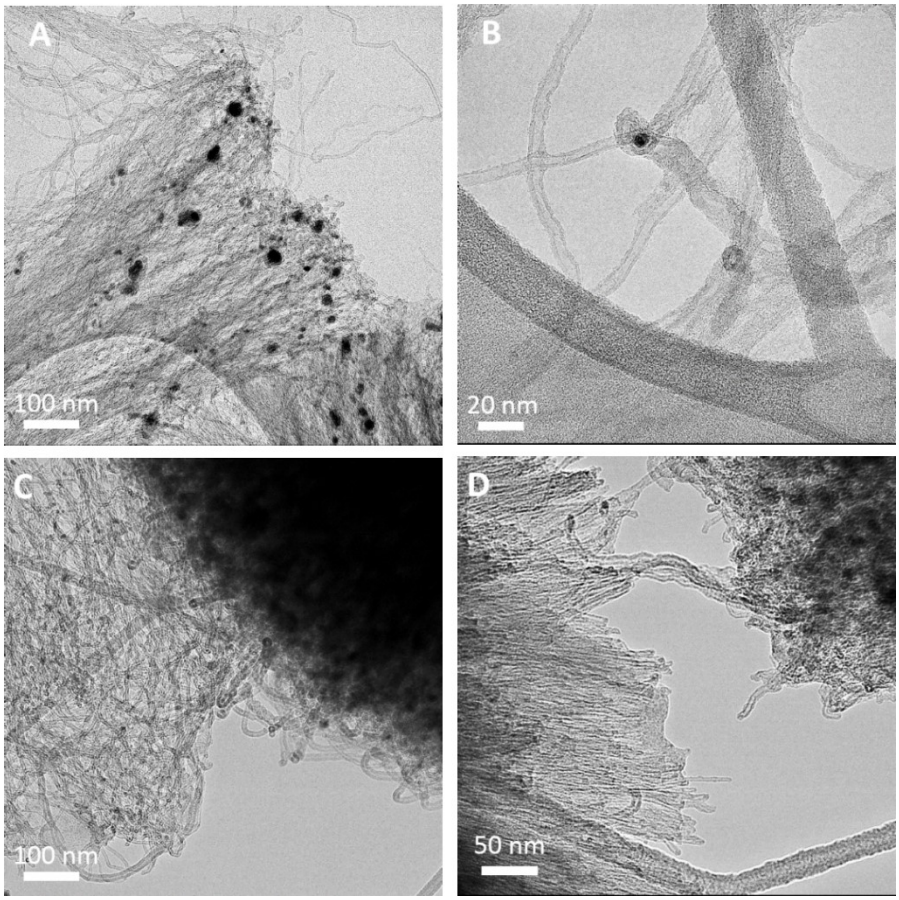

Figure 3-4 TEM micrographs of CNTs grown at 400°C over Al_xO_y/Fe (A and B) and Al_xO_y/Fe-Cu (C and D) catalysts after 1 h.

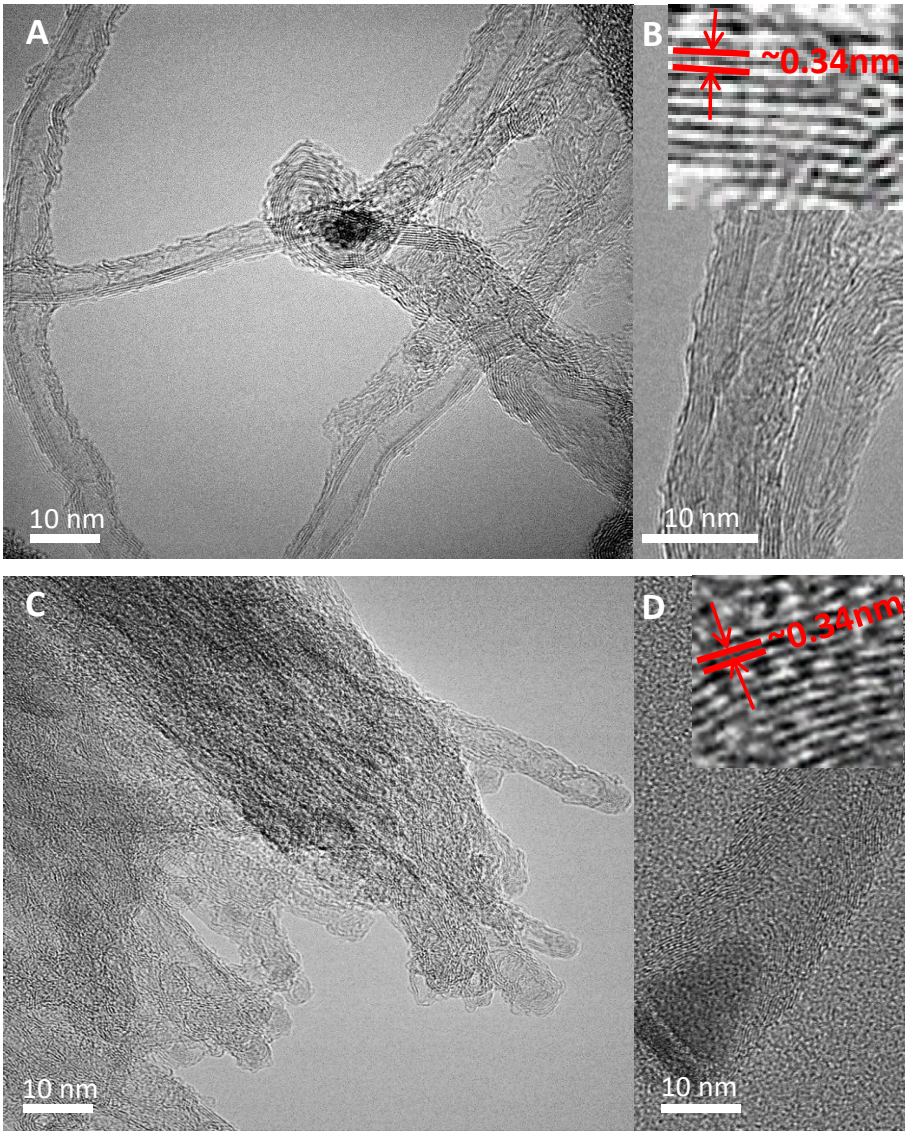

Figure 3-5 High-resolution TEM micrographs of CNTs grown at 400°C over Al_xO_y/Fe (A and B) and Al_xO_y/Fe-Cu (C and D) catalysts after 1 h. Panels B and D illustrate the hollow interior, parallel graphitic planes along the tube walls; the insets show the distinct inter-wall spacing of ~0.34 nm.

The outer average CNT diameter [mean ± standard deviation (sigma)] from TEM analysis for CNTs grown on Fe and Fe-Cu catalysts at 400°C are 7.8 ± 3.4 and 15.6 ± 3.0 nm, respectively; the corresponding inner diameter of CNTs from Fe is 3.3 ± 0.5 nm while for CNTs from Fe-Cu is 5.12 ± 1.2 nm. We note that the high-resolution images of CNT carpets grown at 400°C reveal some defect features on the walls that completely disappear at 500°C due to improved crystallinity, as evidenced

by the TEM images in Figure 3-6. The inset histogram shows the CNT outer diameter distributions for CNTs grown on Fe and Fe-Cu catalysts with their Gaussian fits and respective means and standard deviations of 4.4 ± 0.77 and 5.6 ± 1.69nm. The average CNT diameters follow the trend observed at 400°C with CNTs grown on Fe-Cu having a larger diameter than CNTs from Fe. However, the overall structure of CNTs obtained at 400°C is still comparable to CNT structures obtained at higher temperatures (≥ 450°C).[7,17,28] The Raman and TEM data confirm the decent quality of CNTs produced at 400°C from FTS-GP on Fe and Fe-Cu catalysts.

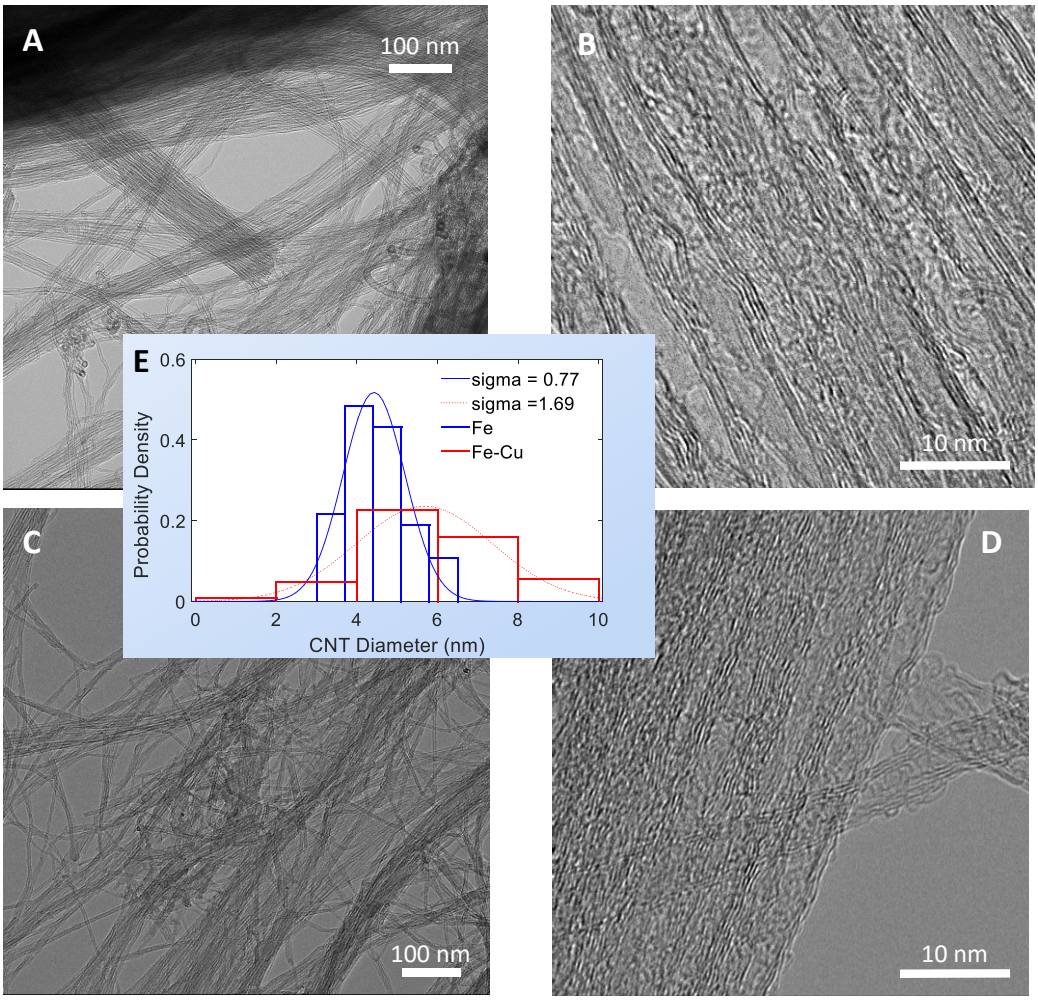

Figure 3-6 TEM micrographs of CNTs grown at 500°C over Al_xO_y/Fe (A and B) and Al_xO_y/Fe-Cu (C and D); their corresponding high-resolution micrographs are shown in panels B and D. (E) CNT diameter distribution obtained from Fe and Fe-Cu catalysts and their Gaussian fits with means of 4.4 nm and 5.6 nm, respectively [sigma (Fe) = 0.77, sigma (Fe-Cu) = 1.69].

Next, our focus shifts to the kinetics of the growth process with FTS-GP. Figure 3-7 shows profiles of the average carpet height as a function of growth time at 400, 450, 500, and 550°C for Fe catalyst (panel A) and Fe-Cu catalyst (panel B) as measured by SEM. The carpet height increases somewhat linearly with time up to the lifetime of the catalyst. The lifetime is defined as the duration until growth termination occurs. For both catalysts, there is a slight increase in the slope of the curve as the temperature increases, and the tallest carpets after 75 min were 27.3 μm for Fe-Cu and 21.2 μm for Fe at the highest growth temperature (550°C). The profiles also reveal that the lifetime of the

catalysts at the different temperatures is ~60 min except for Fe-Cu catalyst at 500 and 550°C that continue to show slight activity up to 75 min. The apparent long lifetime and higher activity observed for Fe-Cu catalyst at these temperatures are consistent with the improved synergistic effect of Cu at higher temperatures (Figure 3, panels B and C). The reported CNT growth rates for temperatures in the range of 450 – 550°C using conventional carbon sources are between 0.1 and 0.15 μm/min;[45] although the growth rates observed in this study are quite comparable, growth with Fe-Cu catalysts at 550°C shows a higher growth rate of 0.77 μm/min. This result further confirms the synergistic effect of Fe and Cu.

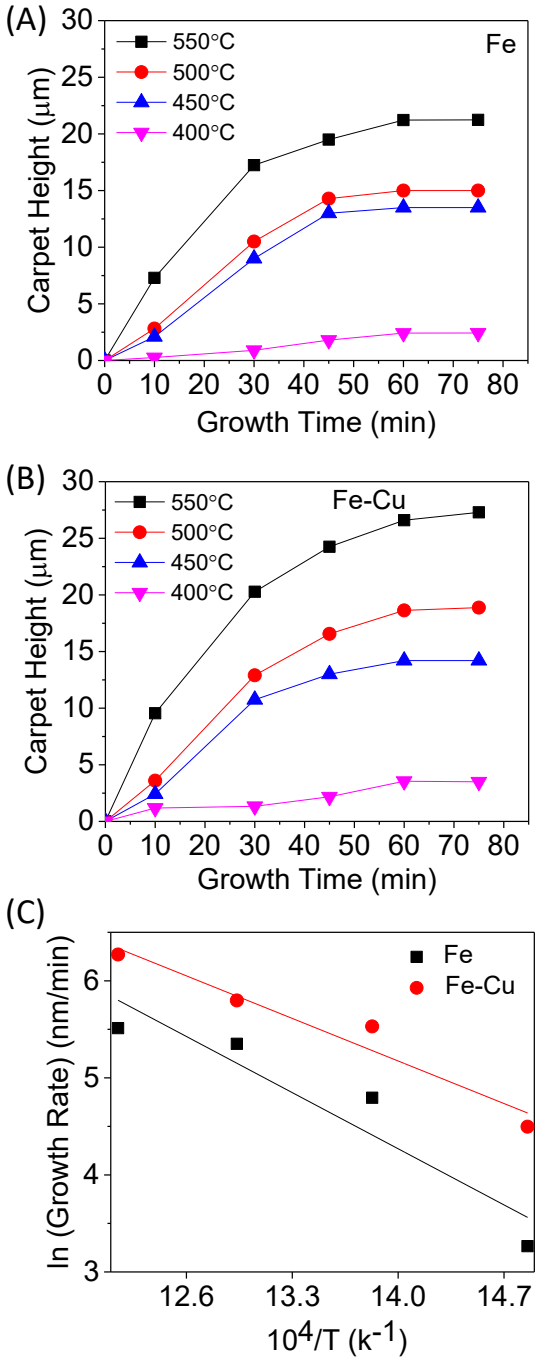

Figure 3-7 Average CNT carpet height as a function of time for growth conducted at 400, 450, 500, and 550°C over Al_xO_y/Fe (A) and Al_xO_y/Fe-Cu (B) catalysts. Arrhenius plots for CNT carpet growth on Al_xO_y/Fe-Cu and Al_xO_y/Fe catalysts with estimated apparent activation energy, E_a of 0.72 and 0.54 eV, respectively (C).

The apparent activation energy (E_a) has been computed using the Arrhenius equation, $k = Aexp\left(-\frac{E_a}{RT}\right)$, whereby k is the reaction rate constant, A is the frequency factor, T is the temperature, and R is the gas constant. Since the composition of the reactant gas mixture and the flow rates were kept constant, we have assumed that the growth rate of the carpets is directly proportional to the rate constant (k). The growth rate is defined as the slope from the fitting curve of carpet height as a function of time. The Arrhenius plots of the natural logarithms of CNT growth rate as a function of the reciprocal of temperature are shown in Figure 7, panel C. From the slopes of the linear fits to the data, E_a for CNT carpet growth on Fe and Fe-Cu catalysts are estimated to be 0.71 and 0.54 eV, respectively. The E_a reported for thermal CVD is in the range of 1.2 – 1.5 eV while E_a for PECVD is in the range of 0.2 – 0.8 eV.[46] The E_a values obtained in this study are lower than those typically reported for thermal CVD growth with monometallic catalysts,[46] and in fact, are comparable to E_a values reported for thermal CVD with bimetallic catalysts[39] or PECVD.[18] We attribute the low E_a values in our study to the unique properties of FTS-GP.

We compare our low-temperature growth results to several related published papers[19,29,47-52] in Table 3-1. The table summarizes the type of CVD, carbon feedstock, the lowest CNT growth temperature achieved, and the corresponding CNT morphology for the respective studies. It is clear that the growth of aligned CNT structures (or CNT carpets) below 400ºC has so far been achieved mainly by PECVD and photo-thermal CVD[19] processes. Conversely, for conventional thermal CCVD, the growth for the most part yields unaligned CNT structures. However, our results demonstrate that the use of FTS-GP as a carbon precursor in thermal CVD enables the growth of CNT carpets below the standard low-temperature range of 450 – 550 ºC.

Table 3-1 Summary of studies on low temperature growth of CNTs.

CVD Method	Carbon Feedstock	Catalyst	Growth Temperature (°C)	CNT Morphology	References
Thermal CVD	C_2H_2 or CH_3OH	Co-Fe or Ni-Co-Fe	400	Unaligned	Ref. 7
Thermal CVD	C_2H_2	Fe-Cu	450	Unaligned	Ref. 8
Thermal CVD	C_2H_2 & CO_2	Fe-Co	400	Unaligned	Ref. 12
Thermal CVD	C_2H_4	Cu	500	Unaligned	Ref. 16
Thermal CVD	C_2H_2	Ni	550	Unaligned	Ref. 47
Thermal CVD	C_2H_2	Cu-Al	500	Unaligned	Ref. 48
Thermal CVD	C2H2	Ni–P–Pd	400	Unaligned	Ref. 52
Thermal CVD	C_2H_4 (preheated)	Fe	400	Aligned	Ref. 11
Thermal CVD	C_2H_2	Co-Ti	550	Aligned	Ref. 27
Thermal CVD	C_2H_2	Co-Ti	450	Aligned	Ref. 28
Thermal CVD	C_2H_2 (preheated)	Co-Ti	450	Aligned	Ref. 29
Thermal CVD	C_2H_2	Co-Al-Mo	450	Aligned	Ref. 17
Thermal CVD	C_2H_2	Ni (annealed)	400	Aligned	Ref. 21
Thermal CVD	**FTS-GP**	**Fe or Fe-Cu**	**400**	**Aligned**	**This Work**
Photo-thermal CVD	**C_2H_2**	**Fe-Al-Tin**	**350**	**Aligned**	**Ref. 19**
Plasma CVD	**CH_4**	**Fe**	**400**	**Unaligned**	**Ref. 13**
Plasma CVD	**CH_4**	**Ni**	**520**	**Unaligned**	**Ref. 49**
Plasma CVD	**C_2H_2**	**Co-Mo**	**450**	**Aligned**	**Ref. 44**
Plasma CVD	**CH_4**	**Co**	**400**	**Aligned**	**Ref. 46**
Plasma CVD	**CH_4**	**Ni**	**400**	**Aligned**	**Ref. 50**
Plasma CVD	**CH_4& CO_2**	**Fe**	**330**	**Aligned**	**Ref. 51**

FTS-GP is a highly suitable and versatile carbon feedstock for CNT carpet growth, as further evidenced by our ability to conduct CNT carpet growth at low temperatures on nontraditional and temperature-sensitive substrates. In particular, CNT carpet growth was achieved from a 2 nm-thick Fe catalyst deposited directly on aluminum foil (Figure 3-8A) and on aluminum foil with a 30 nm-thick amorphous Al_xO_y barrier layer (Figure 8B) at 450°C, which is well below the melting point of aluminum. Based on the SEM images (Figure 8) and Raman spectra (Figure S3), it can be concluded that the properties of the CNT carpets obtained at 450°C from catalyst deposited directly on aluminum are comparable to carpets obtained from the standard CNT carpet catalyst (Al_xO_y/Fe).[53,54] In general, CNT carpet growth on metals using conventional carbon precursors typically requires the use of a barrier layer to prevent interdiffusion and catalyst poisoning.[55] The presence of an insulating barrier

layer in the supported catalyst structure is expected to increase the substrate/CNT contact resistance, thus limiting the applications of the CNT carpets. Note that although the direct growth of CNTs on aluminum has been achieved by direct electrochemical deposition of Ni catalyst on aluminum (without the use of barrier layers), the resulting CNT growth, however, was unaligned.[56] Our results reveal that the use of FTS-GP as a carbon feedstock can broaden the substrates used for CNT carpet growth.

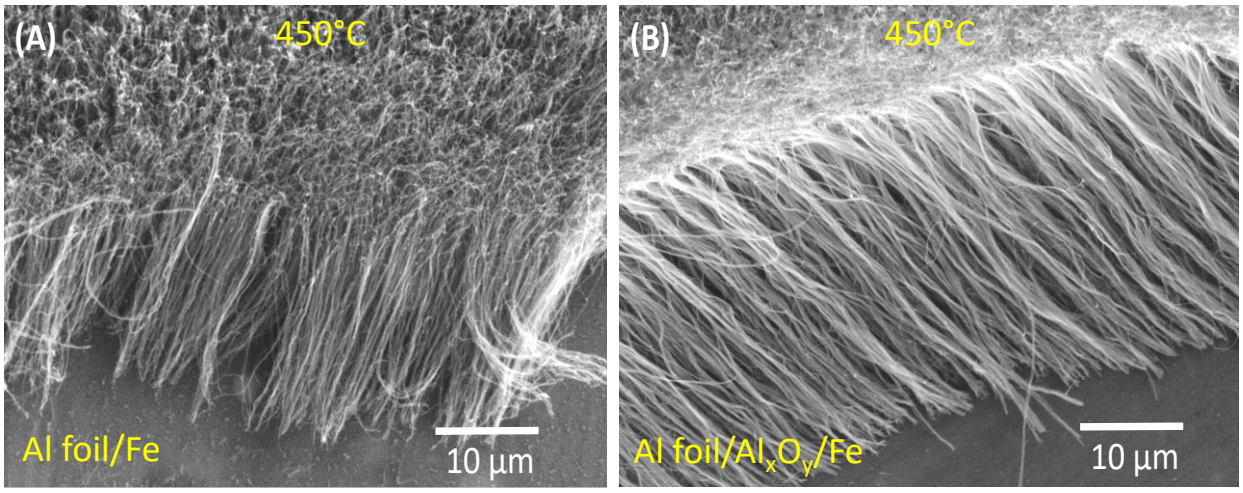

Figure 3-8 FESEM images of CNT carpets grown at 450°C on aluminum foil with Fe catalyst directly deposited on aluminum (A), and Fe catalyst deposited on aluminum with a 10 nm-thick Al_xO_y barrier layer (B).

To understand the role of FTS in achieving low-temperature growth, it is necessary to consider the contributions of the individual components in the mixture. From the composition of FTS-GP stated earlier, a high fraction (> 50 vol%) of the carbon-containing species is composed of CH_4, which is highly stable. Unlike CH_4, the decomposition of the unsaturated hydrocarbon components (C_2H_4 and C_3H_6) requires much less energy. The unsaturated hydrocarbons have more negative free energy in comparison to saturated hydrocarbons due to the presence of easily disrupted π-bonds in their structure.[57] The thermal stabilities of the various components of FTS-GP are evaluated based on the reported Gibbs free energies as a function of temperature.[58] Under our growth conditions at low temperatures, we hypothesize that the unsaturated hydrocarbons are easily decomposed to form

unstable free radicals that attack the saturated hydrocarbons and promote their decomposition at temperatures that would otherwise have been unfavorable. The decomposition reactions create a higher carbon-feeding rate, which can lead to faster deactivation of the catalyst nanoparticles. However, the Fe and Fe-Cu catalysts used in our study are generally characterized by reasonably long lifetime; we attribute this observation to the oxidative removal of excess carbon and amorphous carbon by water produced from CO dissociation in accordance with the mechanisms proposed for "supergrowth."[33,34,54,59] It has been shown that the dissociation of CO has two distinct pathways depending on the partial pressure of CO. At higher partial pressure of CO, the dissociation is favored at less negative free energy (-70 kJ/mole) and high reaction temperature is required (> 600°C) to achieve the self-disproportionation reaction (also known as the Boudouard reaction)[57,60] as shown in Equation 1.

$$CO_{(g)}+CO_{(g)} \Leftrightarrow C_{(s)}+CO_{2(g)} \quad (1)$$

Conversely, at low partial pressure of CO, which is similar to our reaction condition (5 vol%), the reaction is favored at a more negative free energy value of -90 kJ/mole, and the required dissociation temperature is above 400°C in the presence of hydrogen as shown in Equation 2.[57,61]

$$CO_{(g)}+H_{2(g)} \Leftrightarrow H_2O_{(g)}+C_{(s)} \quad (2)$$

We therefore propose the following mechanism to explain the role of FTS-GP in low-temperature growth as depicted in the schematic in Figure 3-9. First, the unsaturated hydrocarbons dissociate forming unstable radicals (CH_3*, C_2H_3* and C_2H_5*) that attack the more stable saturated hydrocarbon in the mixture (CH_4, C_2H_6, and C_3H_8) promoting a high carbon feeding rate to the catalyst. Second, the low concentration of CO (5 vol%) in FTS-GP favors the reaction with hydrogen to release energy (-90 kJ/mole) and form water that oxidizes excess carbon or amorphous carbon impurities generated by hydrocarbon dissociation and the carbon supplied by the reaction between CO and H_2 (Equation 2).

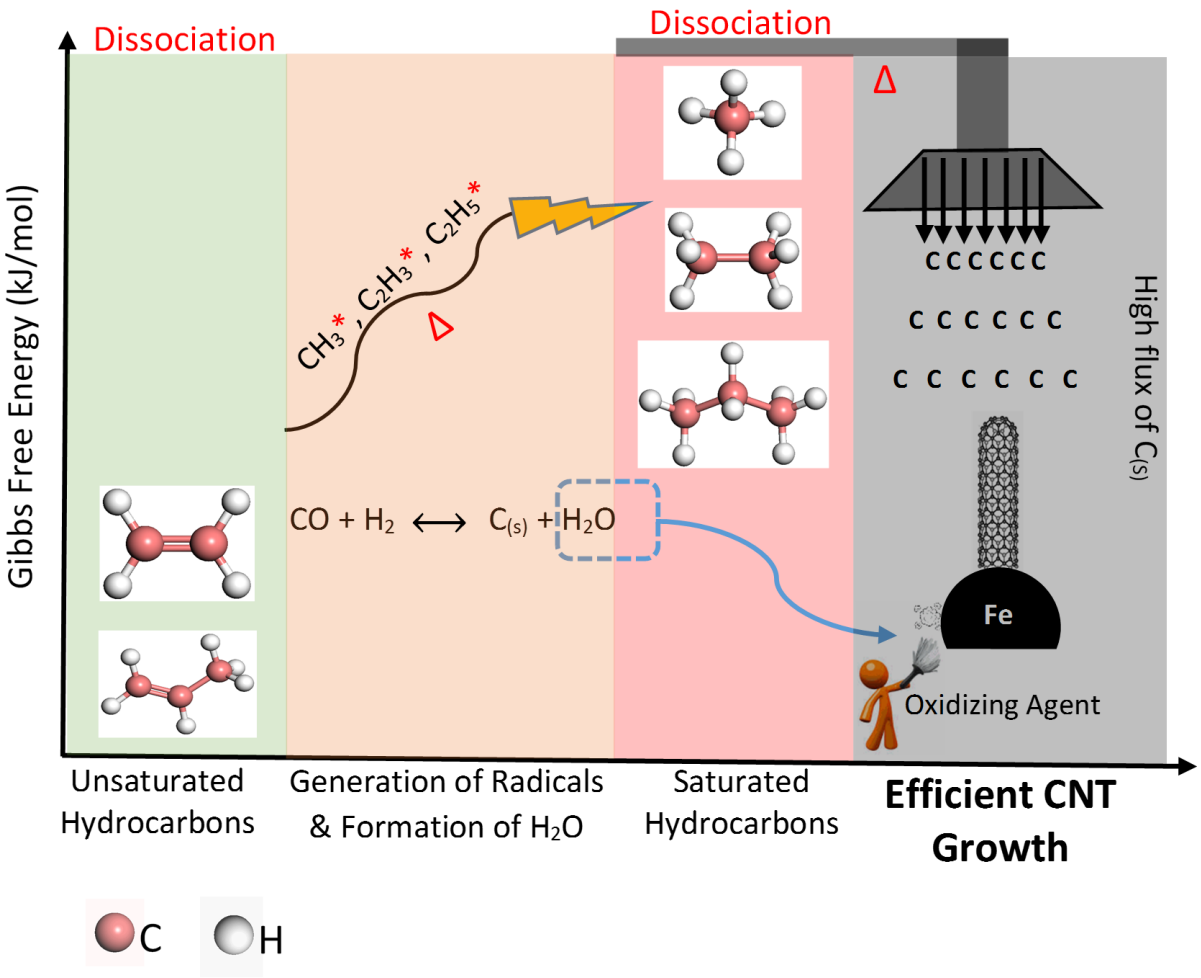

Figure 3-9 Proposed mechanism to explain the role of FTS-GP in low-temperature growth of CNT carpets. The Gibbs free energies for the decomposition reactions of CH_4, C_2H_6, C_3H_8, C_2H_4, and C_3H_6 are 20, -35, -80, -300, and -410 kJ/mol, respectively (Ref. 58).

In summary, we present a new CCVD approach for efficient low-temperature growth of CNT carpets of good quality on traditional and nontraditional substrates using an industrial waste gas mixture (FTS-GP) as a carbon feedstock. The efficiency of the process is evidenced by the growth of highly dense, vertically aligned CNT structures from both Fe and Fe-Cu catalysts at 400, 450, 500, and 550°C. The CNTs produced even at a record low temperature of 400°C consist of well-aligned graphitic sheets and exhibit a straight morphology with hollow interior and parallel graphitic planes along the tube walls. The synergistic effect of Fe and Cu show a strong temperature dependence, with Cu being more influential at temperatures greater than 450°C. The apparent activation energies for

CNT carpets grown on Fe and Fe-Cu catalysts are 0.71 and 0.54 eV, respectively. The low activation energies, long catalyst lifetimes, and the growth of CNT carpets at 400°C, where the influence of Cu is low, are attributed to the unique composition of FTS-GP. Our growth results also reveal that FTS-GP is not only an efficient carbon feedstock but also a versatile feedstock that support CNT carpet growth on aluminum foil. This new CCVD approach is expected to broaden CNT growth substrates, enhance sustainability of the process and CNT scalability.

3.3 Experimental Details

The catalysts used were Fe supported on amorphous alumina (Al_xO_y/Fe) and a binary-layered catalyst (Fe-Cu) supported on alumina (Al_xO_y/Fe-Cu). The nominal thickness of the Fe, Al_xO_y, and Cu films were 1.3, 30, and 0.12 nm, respectively; all the films were deposited by an ion beam sputter deposition and etching system (IBS/e, South Bay Technology). The metal targets were etched using a voltage of 5 kV and a current of 3 mA for 2 min to remove the native oxide layer prior to deposition. Two configurations of Al_xO_y/Cu/Fe catalysts were investigated based on the sequence of Fe and Cu depositions. In the first case, the thin layer of Cu was deposited prior to the Fe layer and in the second case, the sequence was reversed. All the films were deposited on Si (100) substrates with a native oxide layer (P type and B-doped) at 10^{-4} Torr chamber pressure without exposing the films to air between depositions. The thicknesses of the films deposited were measured by a quartz crystal thickness monitor and corroborated by height profile measurements using atomic force microscopy (AFM). The FTS-GP mixture used as carbon source was supplied by Matheson Inc with the following composition: CH_4 (30%), C_2H_6 (8%), C_2H_4 (6%), C_3H_8 (5%), C_3H_6 (2%), H_2 (40%), CO (5%), and N_2 (4%).

CNT growth was carried out at atmospheric pressure using the EasyTube 101 CVD system (CVD Equipment Corporation); it is equipped with several important features including a LabView-based process control software, a static mixer for optimum gas mixing, and a control system for precise

temperature control. A typical growth run involved heating the catalyst sample to the desired temperature (400, 450, 500, or 550°C) at a rate of 45 °C/min in flowing Ar atmosphere. At the growth temperature, the catalyst was exposed to a copious amount of H_2 in combination with Ar for 10 min to reduce the catalyst; the respective flow rates were 250 standard cubic centimeters per minute (sccm) H_2 and 250 sccm Ar. Thereafter, CNT growth was initiated by introducing the growth gas mixture (100 sccm FTS-GP and 1000 sccm Ar) for various times. At the end of the growth run, the samples were rapidly cooled in H_2 followed by slow cooling to room temperature in 700 sccm Ar. The product mass was determined by weighing the substrate before and after CNT growth. Representative temperature profiles of the CVD furnace obtained from the process control software (CVD*WinPrC*™) are presented in Figures S4 and S5.

The morphologies and microstructures of the grown CNTs were studied using field emission scanning electron microscopy (FESEM) and transmission electron microscopy (TEM). For TEM imaging, a small amount of CNT carpet sample was mechanically exfoliated from the substrate and dispersed in isopropanol via ultrasonication. A drop of the homogeneous suspension was deposited on a holey carbon TEM grid and examined by TEM using an FEI Talos TEM at 120 and 200 KV. The growth products were further characterized by Raman spectroscopy using a laser excitation wavelength of 532 nm. X-ray photoelectron spectroscopy (XPS) was used to determine the chemical composition of the catalysts. The XPS spectra were recorded on a KRATOS spectrometer using Al Kα (hv =1486.69 eV) X-ray source. Survey scans were acquired at a pass energy of 160 eV. Each region was background corrected using a Shirley background.[62]

References

(1) Nessim, G. D. Properties, synthesis, and growth mechanisms of carbon nanotubes with special focus on thermal chemical vapor deposition. *Nanoscale* **2010**, *2*, 1306-1323.

(2) Dupuis, A.-C. The catalyst in the CCVD of carbon nanotubes—a review. *Prog. Mater. Sci.* **2005**, *50*, 929-961.

(3) Maschmann, M. R.; Amama, P. B.; Goyal, A.; Iqbal, Z.; Gat, R.; Fisher, T. S. Parametric study of synthesis conditions in plasma-enhanced CVD of high-quality single-walled carbon nanotubes. *Carbon* **2006**, *44*, 10-18.

(4) Simon, P.; Gogotsi, Y. Materials for electrochemical capacitors. *Nat Mater* **2008**, *7*, 845-854.

(5) Lee, C. J.; Park, J.; Han, S.; Ihm, J. Growth and field emission of carbon nanotubes on sodalime glass at 550°C using thermal chemical vapor deposition. *Chem. Phys. Lett.* **2001**, *337*, 398-402.

(6) Kondo, H.; Fukuoka, N.; Maruyama, T. Low Temperature Growth of Single-Walled Carbon Nanotubes from Pt Catalysts under Low Ethanol Pressure by Alcohol Gas Source Method. *Journal of Nanotechnology* **2012**, *2012*, 5.

(7) Halonen, N.; Sápi, A.; Nagy, L.; Puskás, R.; Leino, A.-R.; Mäklin, J.; Kukkola, J.; Tóth, G.; Wu, M.-C.; Liao, H.-C.; Su, W.-F.; Shchukarev, A.; Mikkola, J.-P.; Kukovecz, Á.; Kónya, Z.; Kordás, K. Low-temperature growth of multi-walled carbon nanotubes by thermal CVD. *Phys. Status Solidi B* **2011**, *248*, 2500-2503.

(8) Cartwright, R.; Esconjauregui, S.; Hardeman, D.; Bhardwaj, S.; Weatherup, R.; Guo, Y.; D'Arsié, L.; Bayer, B.; Kidambi, P.; Hofmann, S.; Wright, E.; Clarke, J.; Oakes, D.; Cepek, C.; Robertson, J. Low temperature growth of carbon nanotubes on tetrahedral amorphous carbon using Fe–Cu catalyst. *Carbon* **2015**, *81*, 639-649.

(9) Wagner, R. S.; Ellis, W. C. The vapor-liquid-solid mechanism of crystal growth and its applications to silicon. *T. Metall. Soc. AIME* **1965**, *233*, 1053-1064.

(10) Mora, E.; Pigos, J. M.; Ding, F.; Yakobson, B. I.; Harutyunyan, A. R. Low-Temperature Single-Wall Carbon Nanotubes Synthesis: Feedstock Decomposition Limited Growth. *J. Am. Chem. Soc.* **2008**, *130*, 11840-11841.

(11) Nessim, G. D.; Seita, M.; O'Brien, K. P.; Hart, A. J.; Bonaparte, R. K.; Mitchell, R. R.; Thompson, C. V. Low Temperature Synthesis of Vertically Aligned Carbon Nanotubes with Electrical Contact to Metallic Substrates Enabled by Thermal Decomposition of the Carbon Feedstock. *Nano Lett.* **2009**, *9*, 3398-3405.

(12) Magrez, A.; Seo, J. W.; Smajda, R.; Korbely, B.; Andresen, J. C.; Mionić, M.; Casimirius, S.; Forró, L. Low-Temperature, Highly Efficient Growth of Carbon Nanotubes on Functional Materials by an Oxidative Dehydrogenation Reaction. *ACS Nano* **2010**, *4*, 3702-3708.

(13) Amama, P. B.; Ogebule, O.; Maschmann, M. R.; Sands, T. D.; Fisher, T. S. Dendrimer-assisted low-temperature growth of carbon nanotubes by plasma-enhanced chemical vapor deposition. *Chem. Commun.* **2006**, 2899-2901.

(14) Hofmann, S.; Ducati, C.; Robertson, J.; Kleinsorge, B. Low-temperature growth of carbon nanotubes by plasma-enhanced chemical vapor deposition. *Appl. Phys. Lett.* **2003**, *83*, 135-137.

(15) Lim, S.; Luo, Z.; Shen, Z.; Lin, J. Plasma-Assisted Synthesis of Carbon Nanotubes. *Nanoscale Res. Lett.* **2010**, *5*, 1377-1386.

(16) Lin, J.-H.; Zeng, Z.-Y.; Lai, Y.-T.; Chen, C.-S. Low-temperature growth of bamboo-like multi-walled carbon nanotubes over an atomic layer epitaxy-Cu/SiO2 catalyst via metal-support interaction. *RSC Adv.* **2013**, *3*, 1808-1817.

(17) Sugime, H.; Esconjauregui, S.; D'Arsié, L.; Yang, J.; Robertson, A. W.; Oliver, R. A.; Bhardwaj, S.; Cepek, C.; Robertson, J. Low-Temperature Growth of Carbon Nanotube Forests Consisting of Tubes with Narrow Inner Spacing Using Co/Al/Mo Catalyst on Conductive Supports. *ACS Appl. Mater. Interfaces* **2015**, *7*, 16819-16827.

(18) Meyyappan, M.; Lance, D.; Alan, C.; David, H. Carbon nanotube growth by PECVD: a review. *Plasma Sources Sci. Technol.* **2003**, *12*, 205.

(19) Ahmad, M.; Anguita, J. V.; Stolojan, V.; Corless, T.; Chen, J.-S.; Carey, J. D.; Silva, S. R. P. High Quality Carbon Nanotubes on Conductive Substrates Grown at Low Temperatures. *Adv. Funct. Mater.* **2015**, *25*, 4419-4429.

(20) Na, N.; Kim, D. Y.; So, Y.-G.; Ikuhara, Y.; Noda, S. Simple and engineered process yielding carbon nanotube arrays with 1.2 × 1013 cm−2 wall density on conductive underlayer at 400 °C. *Carbon* **2015**, *81*, 773-781.

(21) Amama, P. B.; Lan, C.; Cola, B. A.; Xu, X.; Reifenberger, R. G.; Fisher, T. S. Electrical and Thermal Interface Conductance of Carbon Nanotubes Grown under Direct Current Bias Voltage. *J. Phys. Chem. C* **2008**, *112*, 19727-19733.

(22) He, M.; Chernov, A. I.; Obraztsova, E. D.; Jiang, H.; Kauppinen, E. I.; Lehtonen, J. Synergistic effects in FeCu bimetallic catalyst for low temperature growth of single-walled carbon nanotubes. *Carbon* **2013**, *52*, 590-594.

(23) Lim, S.; Shimizu, A.; Yoon, S.-H.; Korai, Y.; Mochida, I. High yield preparation of tubular carbon nanofibers over supported Co–Mo catalysts. *Carbon* **2004**, *42*, 1279-1283.

(24) Bae, E. J.; Min, Y.-S.; Kang, D.; Ko, J.-H.; Park, W. Low-Temperature Growth of Single-Walled Carbon Nanotubes by Plasma Enhanced Chemical Vapor Deposition. *Chem. Mater.* **2005**, *17*, 5141-5145.

(25) Yang, Y.; Hu, Z.; Tian, Y. J.; Y, N. L.; Wang, X. Z.; Chen, Y. High-yield production of quasi-aligned carbon nanotubes by catalytic decomposition of benzene. *Nanotechnology* **2003**, *14*, 733.

(26) Shyu, Y.-M.; Chau-Nan Hong, F. The effects of pre-treatment and catalyst composition on growth of carbon nanofibers at low temperature. *Diam. Relat. Mater.* **2001**, *10*, 1241-1245.

(27) Yoshikazu, N.; Lujun, P.; Goichi, T. Low-Temperature Growth of Vertically Aligned Carbon Nanotubes Using Binary Catalysts. *Jpn. J. Appl. Phys.* **2006**, *45*, 369.

(28) Tsai, T.-Y.; Tai, N.-H.; Chen, K. C.; Lee, S. H.; Chan, L. H.; Chang, Y. Y. Growth of vertically aligned carbon nanotubes on glass substrate at 450 °C through the thermal chemical vapor deposition method. *Diam. Relat. Mater.* **2009**, *18*, 307-311.

(29) Goichi, T.; Lujun, P.; Seiji, A.; Yoshikazu, N. Vertically Aligned Carbon Nanotubes Grown at Low Temperatures for Use in Displays. *Jpn. J. Appl. Phys.* **2005**, *44*, 5642.

(30) He, M.; Liu, B.; Chernov, A. I.; Obraztsova, E. D.; Kauppi, I.; Jiang, H.; Anoshkin, I.; Cavalca, F.; Hansen, T. W.; Wagner, J. B.; Nasibulin, A. G.; Kauppinen, E. I.; Linnekoski, J.; Niemelä, M.; Lehtonen, J. Growth Mechanism of Single-Walled Carbon Nanotubes on Iron–Copper Catalyst and Chirality Studies by Electron Diffraction. *Chem. Mater.* **2012**, *24*, 1796-1801.

(31) Deng, W.-Q.; Xu, X.; Goddard, W. A. A Two-Stage Mechanism of Bimetallic Catalyzed Growth of Single-Walled Carbon Nanotubes. *Nano Lett.* **2004**, *4*, 2331-2335.

(32) Management, E. P.: Measuring Hydrogen Sulfide in Refinery Fuel Gas with a Simple TCD-based Gas Chromatograph. Analytical, R., Ed.; Refining, 2012.

(33) Yamada, T.; Maigne, A.; Yudasaka, M.; Mizuno, K.; Futaba, D. N.; Yumura, M.; Iijima, S.; Hata, K. Revealing the Secret of Water-Assisted Carbon Nanotube Synthesis by Microscopic Observation of the Interaction of Water on the Catalysts. *Nano Lett.* **2008**, *8*, 4288-4292.

(34) Hata, K.; Futaba, D. N.; Mizuno, K.; Namai, T.; Yumura, M.; Iijima, S. Water-Assisted Highly Efficient Synthesis of Impurity-Free Single-Walled Carbon Nanotubes. *Science* **2004**, *306*, 1362-1364.

(35) Hall, W. K.; Kokes, R. J.; Emmett, P. H. Mechanism Studies of the Fischer-Tropsch Synthesis. The Addition of Radioactive Methanol, Carbon Dioxide and Gaseous Formaldehyde. *J. Am. Chem. Soc.* **1957**, *79*, 2983-2989.

(36) Kibby, C.; Jothimurugesan, K.; Das, T.; Lacheen, H. S.; Rea, T.; Saxton, R. J. Chevron's gas conversion catalysis-hybrid catalysts for wax-free Fischer–Tropsch synthesis. *Catalysis Today* **2013**, *215*, 131-141.

(37) Tavasoli, A.; Sadagiani, K.; Khorashe, F.; Seifkordi, A. A.; Rohani, A. A.; Nakhaeipour, A. Cobalt supported on carbon nanotubes — A promising novel Fischer–Tropsch synthesis catalyst. *Fuel Process. Technol.* **2008**, *89*, 491-498.

(38) Measuring Hydrogen Sulfide in Refinery Fuel Gas with a Simple TCD-based Gas Chromatograph. www.RosemountAnalytical.com (accessed 12/10/2015.

(39) Chiang, W.-H.; Sankaran, R. M. Synergistic Effects in Bimetallic Nanoparticles for Low Temperature Carbon Nanotube Growth. *Adv. Mater.* **2008**, *20*, 4857-4861.

(40) Nemanich, R. J.; Solin, S. A. First- and second-order Raman scattering from finite-size crystals of graphite. *Phys. Rev. B* **1979**, *20*, 392-401.

(41) Li, W.; Zhang, H.; Wang, C.; Zhang, Y.; Xu, L.; Zhu, K.; Xie, S. Raman characterization of aligned carbon nanotubes produced by thermal decomposition of hydrocarbon vapor. *Appl. Phys. Lett.* **1997**, *70*, 2684-2686.

(42) Wielers, A. F. H.; Koebrugge, G. W.; Geus, J. W. On the properties of silica-supported bimetallic Fe-Cu catalysts Part II. Reactivity in the Fischer-Tropsch synthesis. *J. Catal.* **1990**, *121*, 375-385.

(43) E. Wachs, I.; J. Dwyer, D.; Iglesia, E. Characterization of Fe, Fe-Cu, And Fe-Ag fischer-tropsch catalysts. *Appl. Catal.* **1984**, *12*, 201-217.

(44) Sugime, H.; Esconjauregui, S.; Yang, J.; apos; Arsié, L.; Oliver, R. A.; Bhardwaj, S.; Cepek, C.; Robertson, J. Low temperature growth of ultra-high mass density carbon nanotube forests on conductive supports. *Appl. Phys. Lett.* **2013**, *103*, 073116.

(45) Chen, G.; Davis, R. C.; Kimura, H.; Sakurai, S.; Yumura, M.; Futaba, D. N.; Hata, K. The relationship between the growth rate and the lifetime in carbon nanotube synthesis. *Nanoscale* **2015**, *7*, 8873-8878.

(46) Masayuki, K.; Naoshi, S.; Yuichi, Y.; Mariko, S.; Shintaro, S.; Mizuhisa, N.; Tadashi, S.; Yuji, A. Low-Temperature Growth of Multiwalled Carbon Nanotubes by Surface-Wave Plasma-Enhanced Chemical Vapor Deposition Using Catalyst Nanoparticles. *Jpn. J. Appl. Phys.* **2009**, *48*, 090205.

(47) Ducati, C.; Alexandrou, I.; Chhowalla, M.; Amaratunga, G. A. J.; Robertson, J. Temperature selective growth of carbon nanotubes by chemical vapor deposition. *J. Appl. Phys.* **2002**, *92*, 3299-3303.

(48) Yang, X.; Shi, C.; Liu, E.; He, C.; Du, X.; Li, J.; Zhao, N. Low-temperature synthesis of multi-walled carbon nanotubes over Cu catalyst. *Mater. Lett.* **2012**, *72*, 164-167.

(49) Choi, Y. C.; Bae, D. J.; Lee, Y. H.; Lee, B. S.; Park, G.-S.; Choi, W. B.; Lee, N. S.; Kim, J. M. Growth of carbon nanotubes by microwave plasma-enhanced chemical vapor deposition at low temperature. *J. Vac. Sci. Technol. A* **2000**, *18*, 1864-1868.

(50) Baro, M.; Gogoi, D.; Pal, A. R.; Adhikary, N. C.; Bailung, H.; Chutia, J. Pulsed PECVD for Low-temperature Growth of Vertically Aligned Carbon Nanotubes. *Chem. Vapor Depos.* **2014**, *20*, 161-169.

(51) Chen, M.; Chen, C.-M.; Chen, C.-F. Preparation of high yield multi-walled carbon nanotubes by microwave plasma chemical vapor deposition at low temperature. *J. Mater. Sci.* **2002**, *37*, 3561-3567.

(52) Liu, Y.-M.; Sung, Y.; Chen, T.-T.; Wang, H.-T.; Ger, M.-D. Low temperature growth of carbon nanotubes by thermal chemical vapor deposition using non-isothermal deposited Ni–P–Pd as co-catalyst. *Mater. Chem. Phys.* **2007**, *106*, 399-405.

(53) Amama, P. B.; Pint, C. L.; Kim, S. M.; McJilton, L.; Eyink, K. G.; Stach, E. A.; Hauge, R. H.; Maruyama, B. Influence of Alumina Type on the Evolution and Activity of Alumina-Supported Fe Catalysts in Single-Walled Carbon Nanotube Carpet Growth. *ACS Nano* **2010**, *4*, 895-904.

(54) Amama, P. B.; Pint, C. L.; McJilton, L.; Kim, S. M.; Stach, E. A.; Murray, P. T.; Hauge, R. H.; Maruyama, B. Role of Water in Super Growth of Single-Walled Carbon Nanotube Carpets. *Nano Lett.* **2008**, *9*, 44-49.

(55) Radu Reita, J. N., W. Jud Ready. Growth time performance dependence of vertically aligned carbon nanotube supercapacitors grown on aluminum substrates. *Electrochimica Acta* **2013**, *91*, 5.

(56) Reza Kavian, A. V., Massimiliano Bestetti. Growth of carbon nanotubes on aluminium foil for supercapacitors electrodes. *J Mater Sci* **2011**, *46*, 7.

(57) Anna, M.; Albert, G. N.; Esko, I. K. The role of metal nanoparticles in the catalytic production of single-walled carbon nanotubes - a review. *J. Phys.: Condens. Matter* **2003**, *15*, S3011.

(58) Du, X.; Yao, B.; Gonzalez-Cortes, S.; Kuznetsov, V. L.; AlMegren, H.; Xiao, T.; Edwards, P. P. Catalytic dehydrogenation of propane by carbon dioxide: a medium-temperature thermochemical process for carbon dioxide utilisation. *Faraday Discuss.* **2015**, *183*, 161-176.

(59) Kim, S. M.; Pint, C. L.; Amama, P. B.; Zakharov, D. N.; Hauge, R. H.; Maruyama, B.; Stach, E. A. Evolution in catalyst morphology leads to carbon nanotube growth termination. *J. Phys. Chem. Lett.* **2010**, *1*, 918-922.

(60) Nasibulin, A. G.; Moisala, A.; Brown, D. P.; Kauppinen, E. I. Carbon nanotubes and onions from carbon monoxide using Ni(acac)2 and Cu(acac)2 as catalyst precursors. *Carbon* **2003**, *41*, 2711-2724.

(61) Zheng, B.; Lu, C.; Gu, G.; Makarovski, A.; Finkelstein, G.; Liu, J. Efficient CVD Growth of Single-Walled Carbon Nanotubes on Surfaces Using Carbon Monoxide Precursor. *Nano Lett.* **2002**, *2*, 895-898.

(62) Shirley, D. A. High-Resolution X-Ray Photoemission Spectrum of the Valence Bands of Gold. *Phys. Rev. B* **1972**, *5*, 4709-4714.

Chapter 4

Catalytic CVD Growth of Millimeter-Tall Single-Wall Carbon Nanotube Carpets Using Industrial Gaseous Waste as a Feedstock

Reproduced by permission of Elsevier

https://doi.org/10.1016/j.carbon.2017.01.096

Abstract

A gaseous product mixture from Fischer-Tropsch synthesis (FTS-GP) was utilized as an efficient feedstock for growth of high-quality, well-aligned single-wall carbon nanotube (SWCNT) carpets of millimeter-scale heights on Fe and (sub) millimeter-scale heights on Co catalysts via chemical vapor deposition (CVD). Although the SWCNT carpets were grown over a wide temperature range (between 650 and 850°C), growth conducted at optimal temperatures for Co (850°C) and Fe (750°C) yielded predominantly SWCNTs that were straight and clean, with sidewalls largely free of amorphous carbon. Growth on Fe is characterized by a relatively high growth rate (~50 μm/min) and long catalyst lifetime (> 90 min), with the catalyst showing no decay of activity, while growth on a Co catalyst shows a lifetime of ~60 min, with a slower growth rate of ~7μm/min. The resulting area densities of SWCNT carpets grown on Fe and Co, determined by the weight-gain method, were 1.0×10^{12} and 6.0×10^{12} cm^{-2}, respectively — among the highest achieved for SWCNT carpets on standard catalysts. Unlike SWCNT carpet growth involving conventional feedstocks, growth rate and density of SWCNTs on Fe are less sensitive to the FTS-GP fraction and thus allow for relatively easy optimization and scale-up.

4.1 Introduction

The emergence of single-wall carbon nanotube (SWCNT) carpets, consisting of self-aligned SWCNTs grown via chemical vapor deposition (CVD) from closely packed catalyst nanoparticles on a substrate has created new application opportunities in important areas such as nanofiltration membranes, energy storage devices, "gecko" adhesives, thermal management, and composites.[1-3] Unlike multi-walled carbon nanotube (MWCNT) carpets, conditions for efficient growth of SWCNT carpets via catalytic CVD are quite stringent and typically require specific catalyst configuration (type and thickness of supporting and active layers) and feedstocks.[4-7] The initial report on SWCNT carpet growth by Murakami *et al* [8] and the subsequent groundbreaking discovery of water-assisted CVD (or 'supergrowth')[9] were significant steps toward growth of SWCNT carpets. Both reports employed an oxidant (hydroxyl group in alcohol[8] or water vapor as an additive to the hydrocarbon[9]) to achieve vertically aligned SWCNT growth. However, poor control of SWCNT carpet density, diameter, and chirality, as well as limited catalyst lifetime during growth are major obstacles still impeding applications. To maximize SWCNT growth rates and catalyst lifetimes, research activities have focused primarily on rational catalyst design, and control of nucleation and growth processes at the catalyst site [10-15] while less attention has been paid to innovating the carbon feedstock.

Standard carbon feedstocks used in catalytic CVD for SWCNT carpet growth are C_2H_5OH [5, 8, 16], C_2H_4,[9, 17] and C_2H_2.[4, 7, 18-19] CVD processes involving these feedstocks can be classified into three types: alcohol CVD, supergrowth, and conventional CVD utilizing a pure hydrocarbon in the absence of an oxidant. Although these feedstocks are known to produce high-quality SWCNT carpets, their implementation requires tight process control and extensive optimization. First, SWCNT carpets obtained by alcohol CVD are either limited in height [8, 20] or only obtained with a specific catalyst type (usually Co or its alloys). Additional steps, such as preheating the feedstock at higher temperatures, are usually required to obtain millimeter-tall SWCNT carpets.[5,16] Moreover, Xiang *et al.,*[21]

demonstrated that SWCNT carpet growth by alcohol CVD requires the addition of C_2H_2 to the growth mixture to maintain the optimum ratio between oxygenated byproducts and the amount of carbon required to initiate CNT growth. Second, in the case of supergrowth, whereby a miniscule amount of water is added to the growth gas to dramatically enhance catalyst activity and result in ultralong SWCNT,[9, 22-24] a precise process control is required as the water concentration needs to be maintained within a narrow range (20 – 500 ppm). Third, conventional CVD with a pure hydrocarbon feedstock (C_2H_2 or C_2H_4) is characterized by low growth rate and short catalyst lifetime, making the growth process highly inefficient.[9, 25]

In this study, we demonstrate the growth of highly dense, well-aligned SWCNT carpets of millimeter-scale heights on Fe and (sub)millimeter-scale heights on Co catalysts using a gaseous product (GP) mixture from Fischer-Tropsch synthesis (FTS) as a feedstock (hereinafter referred to as FTS-GP). FTS-GP is a waste gas mixture that results from an environmentally friendly process (FTS) used in industry for the conversion of syngas (CO and H_2), usually obtained from low-value biomass, natural gas, and coal, to high-value hydrocarbon liquid fuels over transition metal catalysts. As demonstrated recently, FTS-GP is highly suitable for low-temperature growth of CNT carpets on traditional and nontraditional substrates.[26] There are several benefits of adopting FTS-GP as a standard carbon source for SWCNT carpet growth. FTS-GP CVD is efficient for SWCNT carpet growth on an Fe catalyst with a growth rate of ~50 μm/min and long catalyst lifetime (> 90 min), and does not require tight process control. In addition, FTS-GP CVD has the potential of providing a viable pathway for scalable growth of SWCNTs at low cost. Further, FTS-GP CVD promotes a closed-loop material model in Fischer-Tropsch and CNT syntheses, — whereby a waste gas mixture from FTS is used as a feedstock for scalable growth of CNTs. The resulting CNTs obtained from a scalable CVD process could serve as catalyst supports in FTS or other heterogeneous catalytic reactions.

4.2 Experimental

4.2.1 Catalyst Fabrication. The catalyst film (Fe or Co) and supporting layer (Al_xO_y) were deposited on Si (100) wafers with a native oxide layer by ion beam sputtering (IBS/e, South Bay Technology). The nominal thickness of Fe and Co films in Al_xO_y/Fe and Al_xO_y/Co was 0.5 nm, while Al_xO_y thickness was 30 nm. The metal targets were etched to remove the native oxide layer prior to deposition. All films were deposited at 10^{-4} Torr chamber pressure using a voltage of 8 kV and a current of 6 mA under Ar flow, without exposing the films to air between depositions. Thicknesses of films deposited were measured by a quartz crystal thickness monitor and corroborated by height profile measurements using atomic force microscopy (AFM).

4.2.2 SWCNT Carpet Growth. The carbon feedstock (FTS-GP), supplied by Matheson Inc., had the following composition: H_2 (40%), CH_4 (30%), C_2H_6 (8%), C_2H_4 (6%), CO (5%), C_3H_8 (5%), N_2 (4%), and C_3H_6 (2%) — a typical product mixture obtained from FTS process [27-28]. SWCNT growth was carried out at atmospheric pressure using the EasyTube 101 CVD system (CVD Equipment Corporation), equipped with several important features including LabView-based process control software, static mixer for optimum gas mixing, and control system for precise temperature control. In addition, the CVD system is equipped with a shower head gas inlet for providing uniform gas flow to the substrate. A typical growth run involved heating the catalyst sample to the desired temperature (650, 750, or 850°C) at a rate of 45 °C/min in flowing Ar. At the growth temperature, the catalyst was exposed to a copious amount of H_2 in combination with Ar for 2 min to reduce the catalyst; the respective flow rates were 250 standard cubic centimeters per minute (sccm) H_2 and 250 sccm Ar. Thereafter, SWCNT growth under optimum conditions on an Fe catalyst was initiated by introducing a growth gas mixture of 25 sccm FTS-GP and 250 sccm Ar while growth on a Co catalyst was initiated by introducing 10 sccm FTS-GP and 100 sccm Ar at various times. At the end of the growth run, the samples were rapidly cooled in H_2, followed by slow cooling to room temperature in 700 sccm Ar.

Growth at various temperatures was carried out using the optimum FTS-GP fraction (10%), while growth at different FTS-GP fractions was carried out at the optimum temperature for Fe (750°C) and Co (850°C).

4.2.3 Characterization of SWCNT Carpets. The morphologies and microstructures of the grown SWCNT carpets were characterized by field emission scanning electron microscopy (SEM) and transmission electron microscopy (TEM). For TEM imaging, a small amount of CNT carpet sample was mechanically exfoliated from the substrate and dispersed in ethanol via ultrasonication. A drop of the homogeneous suspension was deposited on a holey carbon TEM grid and examined by TEM. The structure and quality of SWCNTs were characterized by Raman spectroscopy using laser excitation energies of 1.54, 1.96, 2.41, and 2.54 eV. Raman spectra were collected at multiple spots from the samples using a Renishaw inVia Raman microscope. Thermal gravimetric analysis (TGA) and differential thermal analysis (DTA) data were obtained using a thermogravimetric analyzer-differential scanning calorimeter (TA SDT Q600); samples were heated in flowing air (100 sccm) from room temperature to 800°C at 5°C/min.

4.3 Results

A CVD process utilizing FTS-GP as a new feedstock for SWCNT carpet growth on conventional catalysts is demonstrated. A unique feature of FTS-GP is that it simultaneously provides a high flux of carbon atoms to the catalysts and protects the catalysts from early deactivation. The composition of FTS-GP [H_2 (40%), CH_4 (30%), C_2H_6 (8%), C_2H_4 (6%), CO (5%), C_3H_8 (5%), N_2 (4%), and C_3H_6 (2%)] used in this study broadly represents a typical product mixture from the FTS process [27-29] and is consistent with the product distribution reported by Emerson Inc. FTS-GP CVD supports growth of SWCNT carpets on Fe and Co catalysts over a wide temperature range as verified by Raman spectroscopy and electron microscopy. Figure 4-1 shows the Raman spectra collected with 633 nm

(1.96 eV) excitation from SWCNT carpets grown on 0.5-nm-thick Fe and Co catalyst films at 650, 750, and 850°C. The spectra exhibit unambiguously the characteristic signature of SWCNTs, i.e., low-frequency radial breathing modes (RBMs). The spectra are generally characterized by intense G-bands and RBMs for SWCNT carpets, with intensity ratio of the G-band to D-band (I_G/I_D) of ~7.5 for carpets grown at 750 and 850°C, and I_G/I_D of ~6 for carpets grown at 650°C. The Raman features (including those from other excitation energies in Figures S1 and S2) suggest the nanotubes are composed predominantly of SWCNTs. Since the disorder-induced D-band is magnified for SWCNTs containing symmetry-breaking defects and impurities,[30] the high I_G/I_D associated with the SWCNT carpets is evidence of their high quality. The Raman data indicate that FTS-GP CVD has a wide window for SWCNT carpet growth.

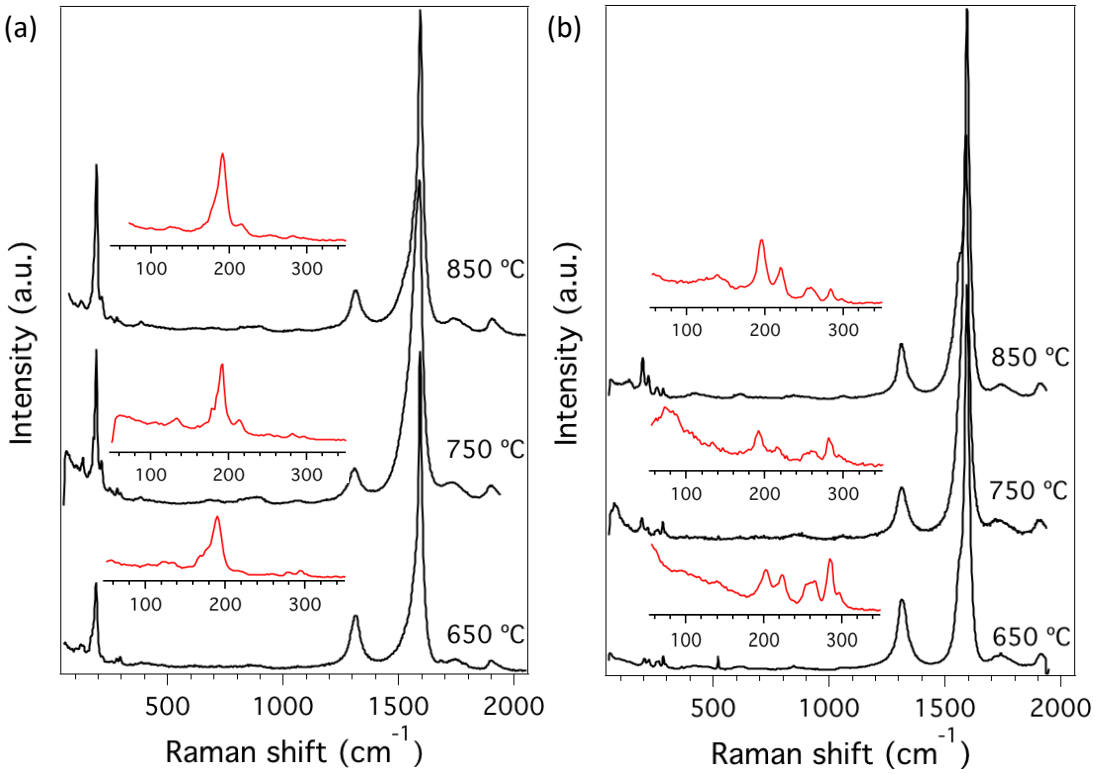

Figure 4-1 Raman spectra of SWCNT carpets grown by FTS-GP CVD at different temperatures (650, 750 and 850°C) on a Fe catalyst (a) and a Co catalyst (b), using a laser excitation energy source of 1.96 eV.

To determine optimum growth temperature for each catalyst, further structural characterization was conducted on SWCNT carpet samples grown at 750 and 850°C, because these samples showed the highest I_G/I_D. TEM images of SWCNTs (Figure 4-2) grown on Fe and Co at 750 and 850°C, respectively, indicate the presence of predominantly SWCNTs and a few double-walled CNTs. As shown in Figure S3, SWCNT carpet growth conducted at 850°C for Fe and 750°C for Co catalysts yielded mixtures of MWCNTs and SWCNTs, and nanotubes with comparatively higher defects. Based on this assessment, optimum growth temperatures for Fe and Co were assumed to be 750 and 850°C, respectively. The TEM images reveal that SWCNT carpets obtained at these optimum growth temperatures for the respective catalysts consist of SWCNTs that are straight and clean, with sidewalls largely free of amorphous carbon. Histograms of the diameter distributions of SWCNTs grown on Fe (Figure 4-2e) and Co (Figure 4-2f) were obtained from analysis of more than 90 individual SWCNTs from the TEM images. Gaussian fits to the histograms show SWCNT diameters centered at 3.1 and 2.2 nm for SWCNTs grown on Fe and Co, respectively. In agreement with the mean diameters obtained from the TEM images, the multi-excitation Raman spectra presented in Figures S1 and S2 indicate that for all laser excitations, RBMs at higher frequencies (which correspond to smaller diameter SWCNTs) are more intense for SWCNT carpets from Co than Fe.

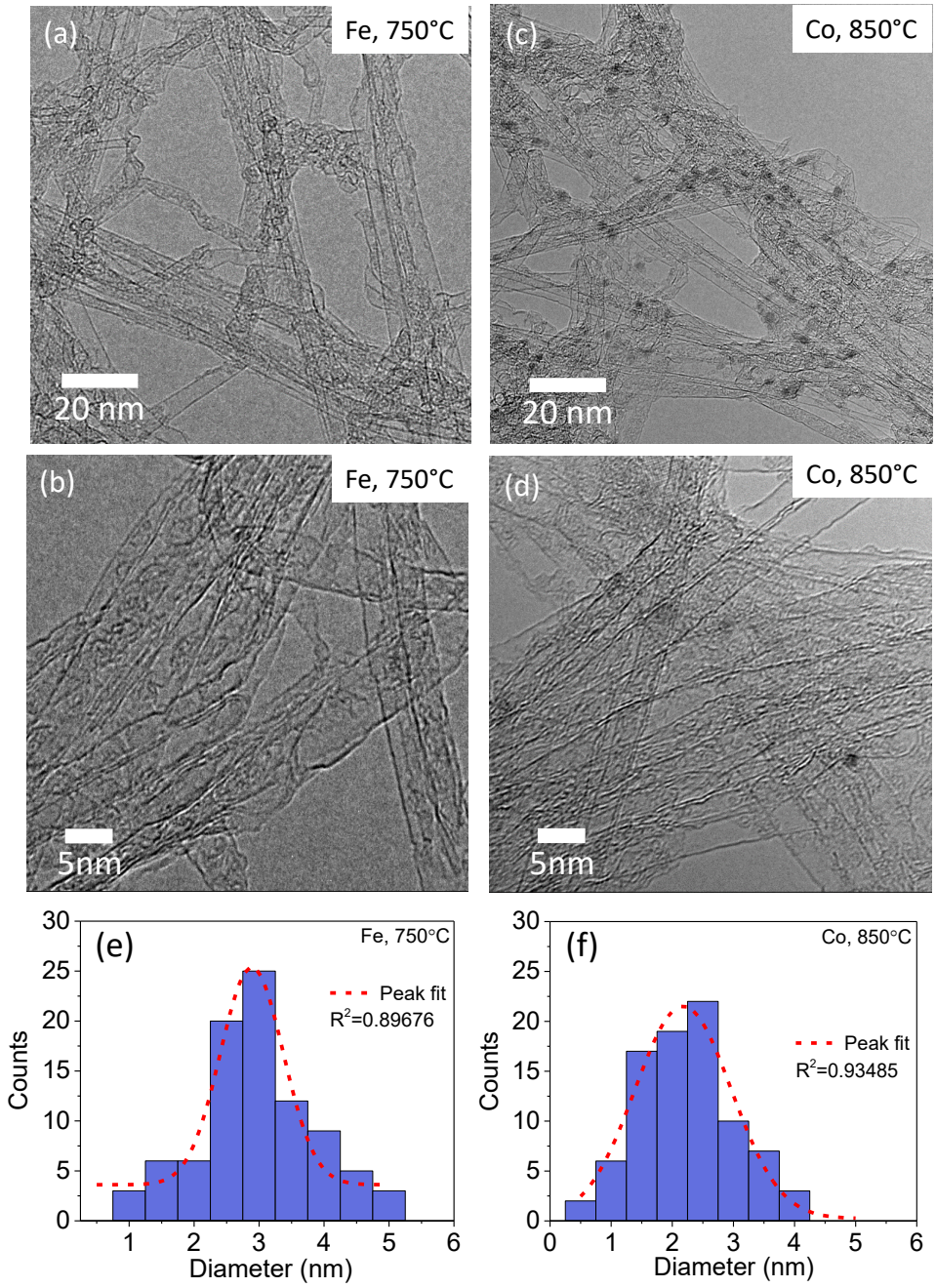

Figure 4-2 TEM characterization of SWCNT carpets grown by FTS-GP CVD at optimum temperatures. (a, b) Low- and high-magnification images of SWCNTs grown on an Fe catalyst at 750°C. (c and d) Low- and high-magnification images of SWCNTs grown on a Co catalyst at 850°C. Histograms of SWCNT diameter distributions and their Gaussian fits of SWCNT carpets grown on Fe catalysts (e) and Co catalysts (f); SWCNT diameters were measured from 90 nanotubes by HRTEM; mean diameters for SWCNTs from Fe and Co catalysts were 3.1 and 2.2 nm, respectively.

The purity of SWCNTs grown on Fe and Co catalysts was further investigated by TGA/DTA in air; profiles of SWCNT carpets grown on Fe and Co are presented in Figure 4-3. We note that for unpurified nanotubes, oxidation temperatures of various carbon species have been reported to vary significantly due to the influence of catalyst residues in the samples. However, it is generally assumed that for unpurified SWCNTs, weight loss below 400°C with a DTA peak maximum ~350°C

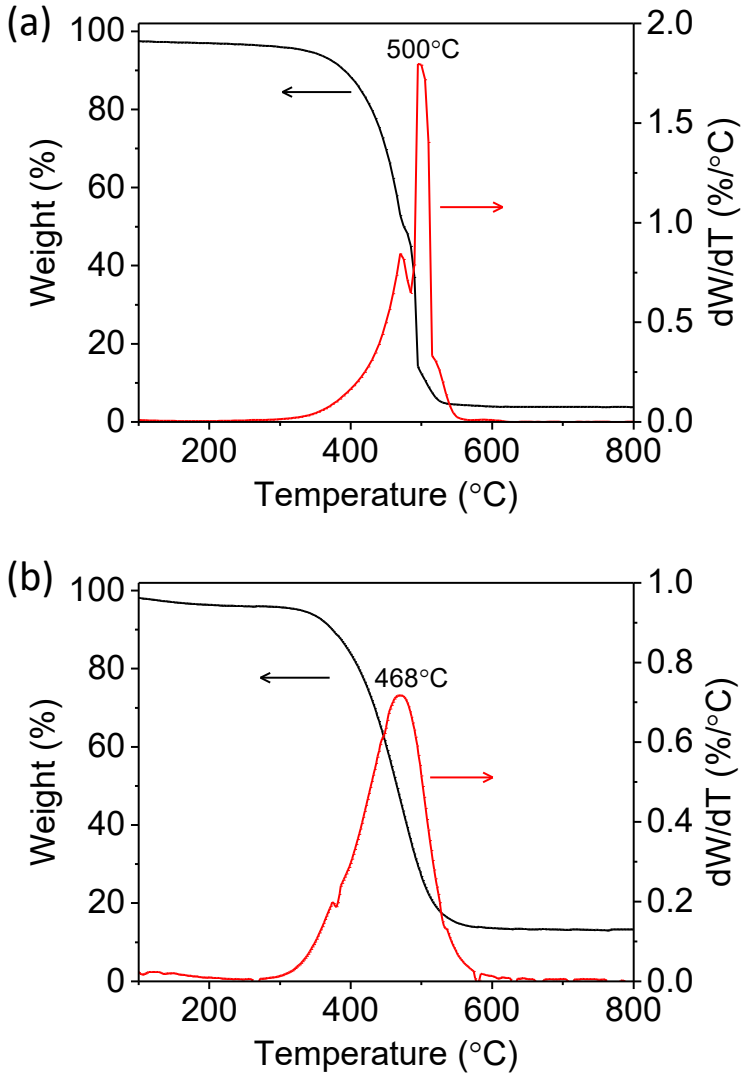

Figure 4-3 TGA/DTA profiles of SWCNT carpets grown on an Fe catalyst (a) and a Co catalyst (b) obtained using a ramp rate of 5°C/min under air flow.

corresponds to amorphous carbon content;[31-32] also, weight loss (or DTA peak) ~500°C is ascribed to SWCNTs, while weight loss above 600°C is associated with oxidation of MWCNTs, nanofibers, and

graphitic carbon.[33] Weight loss below 400°C for SWCNTs grown on Fe and Co are 8.9% and 14.6% of the total sample weight, respectively. The absence of an oxidation peak above 600°C is additional evidence of the absence or low amounts of MWCNTs in the SWCNT carpet samples. The TGA/DTA data further confirm the high quality of SWCNT carpets grown on the catalysts, with Fe producing SWCNTs of slightly higher quality.

Our focus now shifts to comparing growth behavior of Fe and Co catalysts at their respective optimum growth temperatures. Three noteworthy observations can be gleaned from the SEM data of SWCNT carpets grown on Fe and Co in Figure 4-4.

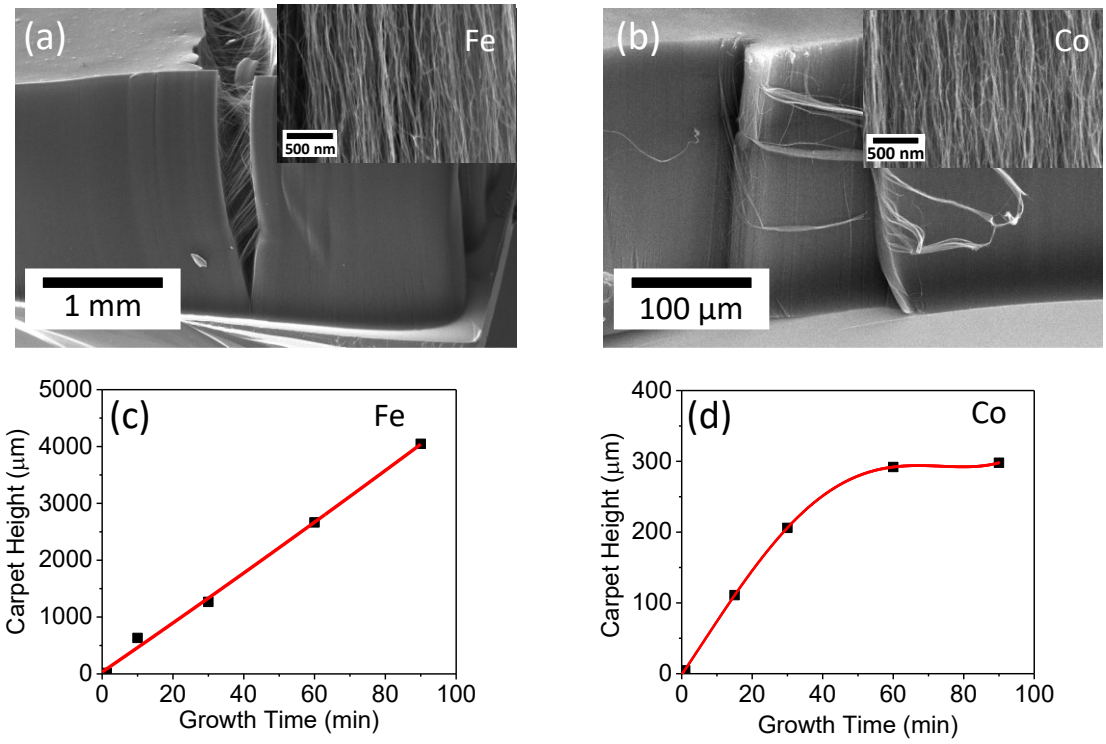

Figure 4-4 Characterization of SWCNT carpets by SEM. SEM images of SWCNT carpets grown from (a) an Fe catalyst at 750°C and (b) a Co catalyst at 850°C after 90 min. Plots of SWCNT carpet height measured from their respective SEM images as a function of growth time for Fe (c) and Co (d) catalysts. Growth temperature for each catalyst corresponds to the temperature that showed the highest SWCNT selectivity.

First, the SEM images (Figures 4a and b and their respective insets) reveal that the SWCNTs are well aligned and comparable to other SWCNT carpets grown by thermal CVD.[5, 8, 14, 19, 34] Second, SWCNT carpet growth on an Fe catalyst is characterized by relatively high growth rate (~50 µm/min) and long catalyst lifetime, as shown in Figure 4-4c. Figure 4-4a and the insert shows a tall SWCNT carpet up to 4 mm in height after 90 min of growth, with the Fe catalyst showing no decay of activity. We also note the high catalytic activity of Fe can be exploited for growth of different SWCNT morphologies; Figure S4 shows different SWCNT morphologies grown on patterned Fe catalyst films. Third, SWCNT carpet growth on a Co catalyst experiences growth termination after ~60 min (Figure 4-4d) and shows

significantly lower growth rate (~7 μm/min) that resulted in a maximum height of ~300 μm. Growth enhancement observed with the Fe catalyst is consistent with previous growth studies.[9, 35-38]

To determine the area density of the as-grown SWCNT carpets, two independent methods were used. The first method was solvent-induced densification, which provides a rough comparison of area densities of SWCNT carpets. This method involves soaking the carpets in ethanol, followed by drying in air, inducing densification of the nanotubes via capillary forces.[18, 39] SEM images of the top view of SWCNTs grown on Fe and Co after densification are compared in Figures 4-5a and b, with their respective false color versions showing their densified regions in Figures 4-5c and d. Areal coverages of SWCNTs grown on Fe and Co, estimated using ImageJ, [40] are 21.4% and 30.5%, respectively. The second method used in evaluating the density was measurement of the weight gain,[19, 41] generally considered as the most quantitative method for determining area density of tall nanotube carpets. The mass density of SWCNT carpet grown on Fe was 0.26 g/cm^3, while SWCNT carpet grown on Co was 0.32 g/cm^3. Using known values of mass density and average SWCNT diameters, the area density was extrapolated from the density chart presented in Ref. [41] Detailed steps for determination of SWCNT area density are summarized in Figure S5. The resulting area densities of SWCNT carpets grown on Fe and Co from the weight-gain method are 1.0×10^{12} and 6×10^{12} cm^{-2}, respectively.

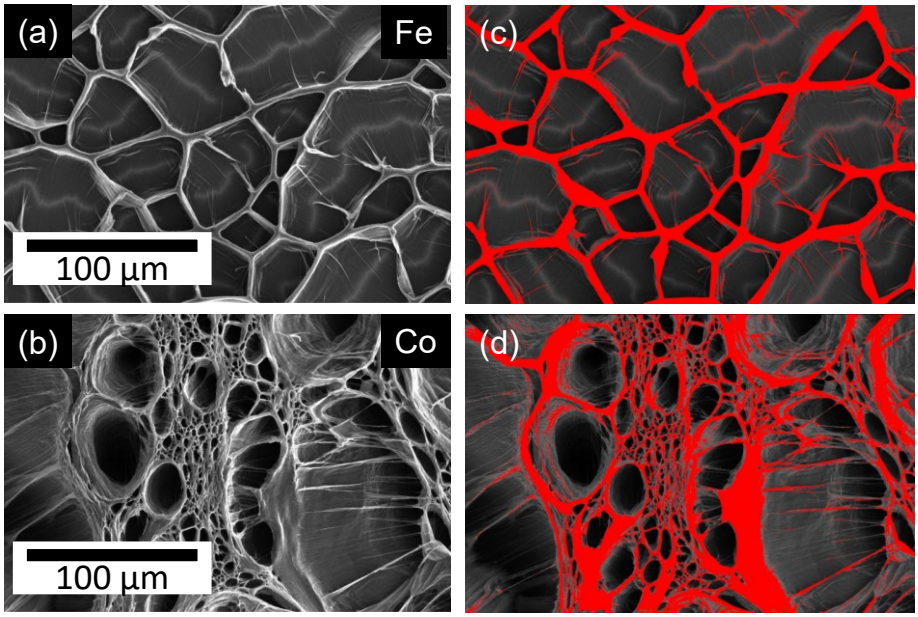

Figure 4-5 SEM images of SWCNT carpets grown on an Fe catalyst at 750°C (a) and a Co catalyst at 850°C (b) for 90 min after ethanol-induced densification to estimate areal density of the carpets. Panels (c) and (d) are respective false-color versions of (a) and (b), showing the compacted area of the densified carpets. Areal coverage of SWCNTs grown on Fe and Co are 21.4% and 30.5%, respectively.

The two methods used here for characterizing area density give consistent results, suggesting that Co produces denser SWCNT carpets than Fe. Table 4-1 shows a comparison of nanotube densities obtained from CVD processes (involving different feedstocks and catalysts) in the literature [42-46] and SWCNT carpets obtained using FTS-GP CVD. Note that the highest area densities of SWCNT carpets in the literature were obtained using a special catalyst design. Zhong *et al.* [19] achieved a SWCNT area density of 1.48×10^{13} cm^{-2} using a multilayered catalyst structure consisting of Al_2O_3, Fe, and Al_2O_3 layers, with the bottom Al_2O_3 pretreated to increase it diffusion barrier properties. Esconjauregui *et al.* [18] reported growth of ultrahigh SWCNT area density of at least ~10^{13} cm^{-2} by conducting cycles of ultrathin catalyst film deposition, annealing, and immobilization. SWCNT area density reported for carpets grown from standard Al_2O_3-supported catalysts (the type used in this study) are generally in the range of 10^{11} to 10^{12} cm^{-1};[47-49] this indicates that the area density of SWCNT carpets obtained in this study are comparable to SWCNT carpets grown on standard catalysts. In addition to the high

SWCNT densities, the Fe catalyst has the additional advantage of being characterized by a long catalyst lifetime.

Table 4-1 Comparison of area densities of CNT carpets obtained from different catalyst configurations and feedstocks, including SWCNT carpets obtained from FTS-GP CVD.

Catalyst	Precursor	Diameter (nm)	Area Density (cm^{-2})	Reference
Fe/quartz	CH_4	1.5	1×10^{10}	Ref.42
Fe / Al_2O_3	CH_4	2.1	2×10^{12}	Ref.48
Fe / Al_2O_3	C_2H_2	3.7	2×10^{12}	Ref.43
Fe / Al_2O_3	C_2H_4	3.0	6×10^{11}	Ref.9
Fe/ Al_2O_3 Cyclic deposition	C_2H_2	2.3	1×10^{13}	Ref.18
Al_2O_3/Fe/ Al_2O_3	C_2H_2	1.2	2×10^{13}	Ref.19
Co/TiN/TaN	CH_4	7.0	2×10^{12}	Ref.44
Co/TiN/TaN	CH_4	7.0	3×10^{11}	Ref.45
Fe / Al_2O_3	C_2H_4	3.0	5.2×10^{11}	Ref.46
Co/Al_2O_3	FTS-GP	2.2	6×10^{12}	This work
Fe/Al_2O_3	FTS-GP	3.1	1×10^{12}	This work

To test the sensitivity of SWCNT carpet growth efficiency to changes in the carbon feed rate, the flow rate of FTS-GP was increased from 2 to 30% for Fe and 2 to 20% for Co, with Ar as the diluent. Conventional feedstocks such as C_2H_2,[19] C_2H_5OH,[50] CO,[51] and C_2H_4 [52] show high sensitivity to partial pressure of the feedstock, thus requiring strict optimization of the gas composition ratio. Figure 4-6a shows height and density of SWCNT carpets grown on Fe stay somewhat constant for the FTS-GP fraction in a broad range from 5 to 30%, except for the modest increase in carpet height at 5 and 10% FTS-GP. Co catalyst shows a narrower range of FTS-GP fractions — between 2 and 15% FTS-GP — that can sustain efficient SWCNT carpet growth. The mass density of SWCNT carpet grown on Co under optimum FTS-GP fractions (2 – 10%) is ~0.3 g/cm^3. From the plots of I_G/I_D as a function of FTS-GP fractions in Figure S6, we conclude that the high SWCNT quality is maintained over a wide

FTS-GP fraction (5 – 30% FTS-GP) for growth on Fe, and over a narrower FTS-GP fraction (5 – 15% FTS-GP) for growth on Co. The results show stark differences in the catalytic behavior of Fe and Co. In general, highly dense carpets have been associated with low growth rate. This observation is consistent with growth on a 0.4-nm-thick Fe catalyst whereby highly dense SWCNT carpets were characterized by a lower growth rate.[19] Fe catalysts appear to have higher tolerance for fluctuations in FTS-GP composition than Co. The growth rate and area density of SWCNTs are less sensitive to changes in the FTS-GP fraction, and thus allow for relatively easy optimization and scale-up. FTS-GP CVD with an Fe or Co catalyst yield highly dense, high-quality SWCNT carpet, albeit with different catalyst lifetimes and growth rates.

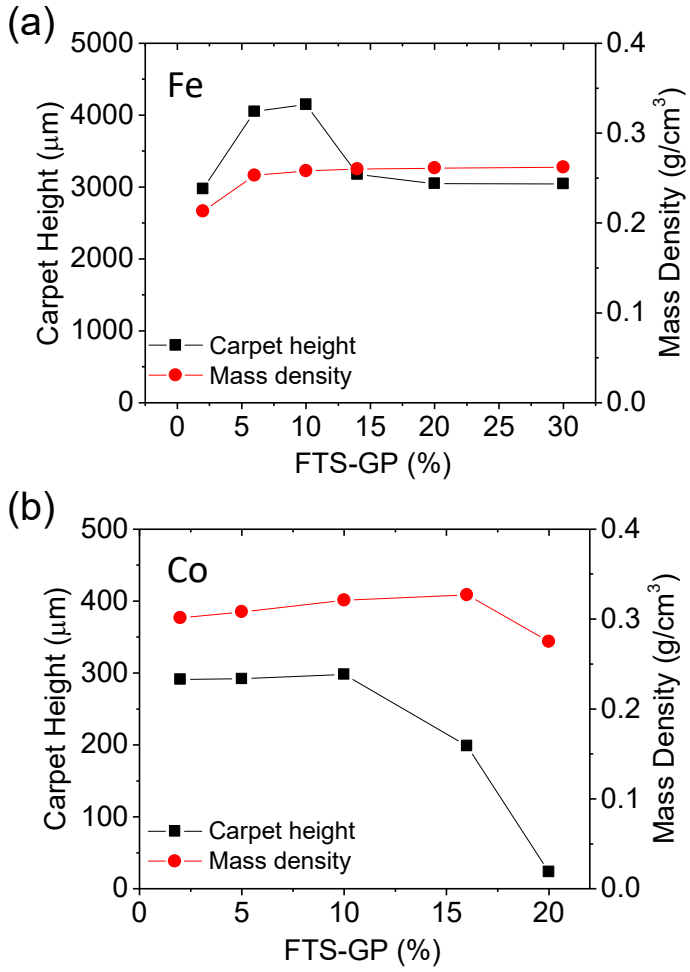

Figure 4-6 SWCNT carpet height and mass density as functions of FTS-GP fraction in growth gas with Ar as the diluent for (a) Fe catalyst at 750°C and (b) Co catalyst at 850°C (growth time = 90 min).

As demonstrated by Chen *et al.,*[53]a universal inverse relationship exists between the growth rate of SWCNT carpets and the catalyst lifetime, which makes it difficult to simultaneously achieve high growth rate and long catalyst lifetime during growth. While high carbon flux to the catalyst enhances the growth rate, the resulting formation of carbon impurities can deactivate the catalyst. In Figure 4-7, we compare the growth curve of FTS-GP CVD with an Fe catalyst to relevant growth curves from the literature.[54-56] We emphasize that the growth curve for FTS-GP CVD with an Fe catalyst shows a

relatively high and constant growth rate with no loss in activity after 90 min. On the other hand, growth profiles for SWCNT carpets obtained from other CVD studies utilizing CH_4, C_2H_4, or C_2H_2 as feedstocks, are characterized by comparatively lower growth rates that gradually decay at higher growth times (> 30 min), or experience early growth termination. Although alcohol CVD shows a similar initial growth rate as FTS-GP CVD, it is characterized by a shorter catalyst lifetime. Supergrowth is characterized by a higher growth rate than FTS-GP CVD (by a factor of 2); however, the catalyst lifetime is extremely short, experiencing deactivation within ~10 min.[53]

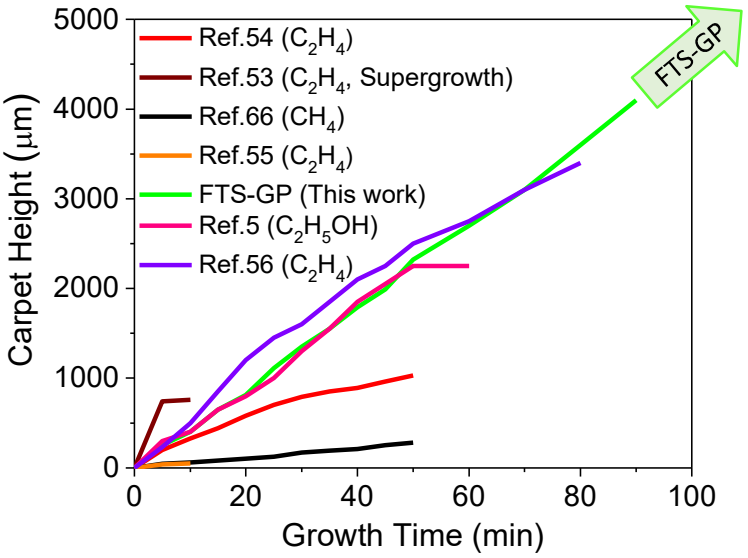

Figure 4-7 SWCNT carpet height as a function of growth time for FTS-GP CVD, compared to previous studies involving various feedstocks (hydrocarbon, alcohol, and hydrocarbon in combination with water or supergrowth).

4.4 Discussion

A unique feature of FTS-GP CVD is that it supports reasonably fast growth rates without experiencing early deactivation. To clarify the role of FTS-GP in SWCNT carpet growth, we take a closer look at the composition of FTS-GP. We hypothesize that the decomposition reaction of the highly rich hydrocarbon mixture creates a high carbon flux to the catalyst, which enhances growth and can lead to

rapid deactivation of the catalyst. In our case, growth is enhanced without the typical early deactivation of catalysts shown in Figure 4-8, because of the ability of FTS-GP to protect or keep the catalyst clean via oxidative removal of excess carbon and amorphous carbon from the catalyst surface. Note the dissociation of CO has two distinct pathways depending on the partial pressure of CO.[57-58] At high partial pressure of CO under CVD growth conditions, the Boudouard reaction (or CO disproportionation reaction) is favored. However, when the partial pressure of CO is low under CVD conditions, a reaction between H_2 and CO is favored, according to the reaction in Equation 1. We emphasize that FTS-GP has a low CO volume fraction of 5 vol%.

$$CO_{(g)}+H_{2(g)} \Leftrightarrow H_2O_{(g)}+C_{(s)} \quad (1)$$

The low CO partial pressure in FTS-GP favors the latter reaction pathway, which produces water vapor that serves as an oxidant, thus extending the catalyst lifetime in accordance with the mechanisms proposed for supergrowth.[9, 25, 47] In addition, it has been shown that higher reducibility of Fischer-Tropsch catalysts is achieved with CO than H_2 [59]; it is, therefore, possible that the CO in FTS-GP helps to keep the catalysts in their metallic states during SWCNT growth, thereby extending their catalyst lifetimes.

The sensitivity of Fe and Co to the FTS-GP fraction can be explained based on their respective phase diagrams with carbon [60]. The solubility of carbon in Fe is relatively high, which means that a higher carbon flux is required to oversaturate Fe nanoparticles and initiate SWCNT growth. Typically, the increase in carbon flux will lead to the formation of metastable carbide (Fe_3C), which has been speculated to induce growth termination.[61-62] We hypothesize that the *in situ* generation of water by FTS-GP via Equation 1 may promote the oxidation of Fe_3C, resulting in reactivation of the catalyst and extension of its lifetime.[63] The oxidation of Fe_3C by steam, as confirmed by Hisa *et al.*,[64] follows the reaction:

$$Fe_3C + 4H_2O \rightarrow Fe_3O_4 + 4H_2 + C \quad (2)$$

A schematic showing deactivation and reactivation pathways is illustrated in Figure 4-8. The formation of metastable species such as Fe_3C, followed by its reactivation to Fe_3O_4 and FeO by the oxidizer, is unique to Fe, and may explain, in part, why most of the millimeters-tall SWCNT carpet growth reported so far has been grown on Fe (or binary catalysts involving Fe).[9, 19, 24, 65-67] In comparison to Fe, carbon solubility in Co is lower, so a controllable amount of carbon flux to Co catalyst is required for efficient and sustained growth. Also, unlike Fe, formation of a metastable component is yet to be associated with a Co catalyst during SWCNT growth.[61] This behavior may account for the relatively shorter SWCNT carpets that are grown on Co. Note that even supergrowth that yields SWCNT carpets of millimeter-scale heights on Fe, growth on Co yields SWCNT carpets with heights that are lower by several hundreds of microns.[68] We hypothesize that the observed decay in catalyst activity and decreased SWCNT area density observed on Co for growth with FTS-GP fractions >10% may be due to oversupply of carbon to the catalyst that induces deactivation.

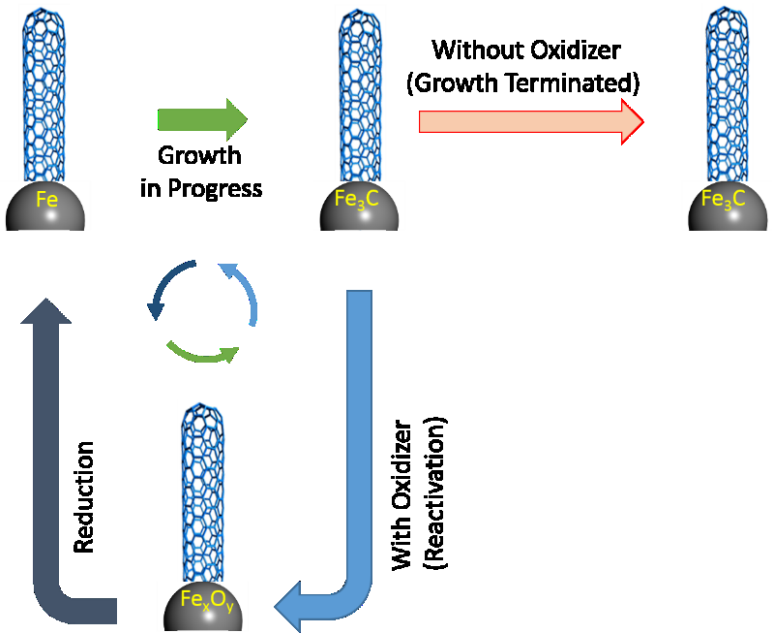

Figure 4-8 Schematic illustration of the role of FTS-GP in enhancing catalyst lifetime of Fe catalyst during FTS-GP CVD.

4.5 Conclusions

SWCNT carpets of high quality were grown over a wide temperature range (650, 750, and 850°C) using a novel feedstock (FTS-GP). High SWCNT selectivity for Fe and Co catalysts were observed at 750 and 850°C, respectively. Growth on Fe is characterized by a relatively high growth rate (~50 μm/min) and long catalyst lifetime (> 90 min), with the catalyst showing no loss of activity, while growth rate on the Co catalyst is slower (~7μm/min) with a limited lifetime of ~60 min. The area densities of SWCNT carpets grown on Fe and Co from the weight-gain method are 1.0×10^{12} and 6×10^{12} cm^{-2}, respectively — among the highest achieved for SWCNT carpet growth on standard catalysts without special treatments or use of a multiple-layered catalyst structure. Unlike conventional feedstocks that require strict process control, growth rate, area density of SWCNT carpets, and SWCNT quality (I_G/I_D) are generally less sensitive to the FTS-GP fraction in growth gas and thus allow for easy optimization and scale-up. In addition to the growth efficiency, the window for SWCNT carpet growth is wider for an Fe catalyst than a Co catalyst. A comparison of the growth curve of FTS-GP CVD, using an Fe catalyst with other conventional CVD methods for SWCNT carpet growth, reveals a growth behavior superior to existing approaches.

References

1. Qu, L.; Dai, L., Gecko-Foot-Mimetic Aligned Single-Walled Carbon Nanotube Dry Adhesives with Unique Electrical and Thermal Properties. *Adv. Mater.* **2007,** *19* (22), 3844-3849.

2. De Volder, M. F. L.; Tawfick, S. H.; Baughman, R. H.; Hart, A. J., Carbon Nanotubes: Present and Future Commercial Applications. *Science* **2013,** *339* (6119), 535-539.

3. Behabtu, N.; Young, C. C.; Tsentalovich, D. E.; Kleinerman, O.; Wang, X.; Ma, A. W. K.; Bengio, E. A.; ter Waarbeek, R. F.; de Jong, J. J.; Hoogerwerf, R. E.; Fairchild, S. B.; Ferguson, J. B.; Maruyama, B.; Kono, J.; Talmon, Y.; Cohen, Y.; Otto, M. J.; Pasquali, M., Strong, Light, Multifunctional Fibers of Carbon Nanotubes with Ultrahigh Conductivity. *Science* **2013,** *339* (6116), 182-186.

4. Hasegawa, K.; Noda, S., Moderating carbon supply and suppressing Ostwald ripening of catalyst particles to produce 4.5-mm-tall single-walled carbon nanotube forests. *Carbon* **2011,** *49* (13), 4497-4504.

5. Sugime, H.; Noda, S., Millimeter-tall single-walled carbon nanotube forests grown from ethanol. *Carbon* **2010,** *48* (8), 2203-2211.

6. Matsumoto, N.; Oshima, A.; Sakurai, S.; Yamada, T.; Yumura, M.; Hata, K.; Futaba, D., The Application of Gas Dwell Time Control for Rapid Single Wall Carbon Nanotube Forest Synthesis to Acetylene Feedstock. *Nanomaterials* **2015,** *5* (3), 1200.

7. Zhong, G.; Hofmann, S.; Yan, F.; Telg, H.; Warner, J. H.; Eder, D.; Thomsen, C.; Milne, W. I.; Robertson, J., Acetylene: A Key Growth Precursor for Single-Walled Carbon Nanotube Forests. *J. Phys. Chem. C* **2009,** *113* (40), 17321-17325.

8. Murakami, Y.; Chiashi, S.; Miyauchi, Y.; Hu, M. H.; Ogura, M.; Okubo, T.; Maruyama, S., Growth of vertically aligned single-walled carbon nanotube films on quartz substrates and their optical anisotropy. *Chem. Phys. Lett.* **2004,** *385* (3-4), 298-303.

9. Hata, K.; Futaba, D. N.; Mizuno, K.; Namai, T.; Yumura, M.; Iijima, S., Water-Assisted Highly Efficient Synthesis of Impurity-Free Single-Walled Carbon Nanotubes. *Science* **2004,** *306* (5700), 1362-1364.

10. Amama, P. B.; Pint, C. L.; Kim, S. M.; McJilton, L.; Eyink, K. G.; Stach, E. A.; Hauge, R. H.; Maruyama, B., Influence of Alumina Type on the Evolution and Activity of Alumina-Supported Fe Catalysts in Single-Walled Carbon Nanotube Carpet Growth. *ACS Nano* **2010,** *4* (2), 895-904.

11. Amama, P. B.; Pint, C. L.; Mirri, F.; Pasquali, M.; Hauge, R. H.; Maruyama, B., Catalyst–support interactions and their influence in water-assisted carbon nanotube carpet growth. *Carbon* **2012,** *50* (7), 2396-2406.

12. Amama, P. B.; Putnam, S. A.; Barron, A. R.; Maruyama, B., Wetting behavior and activity of catalyst supports in carbon nanotube carpet growth. *Nanoscale* **2013,** *5* (7), 2642-2646.

13. Islam, A. E.; Nikolaev, P.; Amama, P. B.; Saber, S.; Zakharov, D.; Huffman, D.; Erford, M.; Sargent, G.; Semiatin, S. L.; Stach, E. A.; Maruyama, B., Engineering the Activity and Lifetime of Heterogeneous

Catalysts for Carbon Nanotube Growth via Substrate Ion Beam Bombardment. *Nano Lett.* **2014,** *14* (9), 4997-5003.

14. Magrez, A.; Smajda, R.; Seo, J. W.; Horváth, E.; Ribič, P. R.; Andresen, J. C.; Acquaviva, D.; Olariu, A.; Laurenczy, G.; Forró, L., Striking Influence of the Catalyst Support and Its Acid–Base Properties: New Insight into the Growth Mechanism of Carbon Nanotubes. *ACS Nano* **2011,** *5* (5), 3428-3437.

15. Mattevi, C.; Wirth, C. T.; Hofmann, S.; Blume, R.; Cantoro, M.; Ducati, C.; Cepek, C.; Knop-Gericke, A.; Milne, S.; Castellarin-Cudia, C.; Dolafi, S.; Goldoni, A.; Schloegl, R.; Robertson, J., In-situ X-ray Photoelectron Spectroscopy Study of Catalyst−Support Interactions and Growth of Carbon Nanotube Forests. *J. Phys. Chem. C* **2008,** *112* (32), 12207-12213.

16. Sugime, H.; Noda, S., Cold-gas chemical vapor deposition to identify the key precursor for rapidly growing vertically-aligned single-wall and few-wall carbon nanotubes from pyrolyzed ethanol. *Carbon* **2012,** *50* (8), 2953-2960.

17. Chen, G.; Davis, R. C.; Futaba, D. N.; Sakurai, S.; Kobashi, K.; Yumura, M.; Hata, K., A sweet spot for highly efficient growth of vertically aligned single-walled carbon nanotube forests enabling their unique structures and properties. *Nanoscale* **2016,** *8* (1), 162-171.

18. Esconjauregui, S.; Fouquet, M.; Bayer, B. C.; Ducati, C.; Smajda, R.; Hofmann, S.; Robertson, J., Growth of Ultrahigh Density Vertically Aligned Carbon Nanotube Forests for Interconnects. *ACS Nano* **2010,** *4* (12), 7431-7436.

19. Zhong, G.; Warner, J. H.; Fouquet, M.; Robertson, A. W.; Chen, B.; Robertson, J., Growth of Ultrahigh Density Single-Walled Carbon Nanotube Forests by Improved Catalyst Design. *ACS Nano* **2012,** *6* (4), 2893-2903.

20. Maruyama, S.; Kojima, R.; Miyauchi, Y.; Chiashi, S.; Kohno, M., Low-temperature synthesis of high-purity single-walled carbon nanotubes from alcohol. *Chem. Phys. Lett.* **2002,** *360* (3-4), 229-234.

21. Xiang, R.; Einarsson, E.; Okawa, J.; Miyauchi, Y.; Maruyama, S., Acetylene-Accelerated Alcohol Catalytic Chemical Vapor Deposition Growth of Vertically Aligned Single-Walled Carbon Nanotubes. *The Journal of Physical Chemistry C* **2009,** *113* (18), 7511-7515.

22. Nessim, G. D.; Al-Obeidi, A.; Grisaru, H.; Polsen, E. S.; Ryan Oliver, C.; Zimrin, T.; John Hart, A.; Aurbach, D.; Thompson, C. V., Synthesis of tall carpets of vertically aligned carbon nanotubes by in situ generation of water vapor through preheating of added oxygen. *Carbon* **2012,** *50* (11), 4002-4009.

23. In, J. B.; Grigoropoulos, C. P.; Chernov, A. A.; Noy, A., Growth Kinetics of Vertically Aligned Carbon Nanotube Arrays in Clean Oxygen-free Conditions. *ACS Nano* **2011,** *5* (12), 9602-9610.

24. Chakrabarti, S.; Kume, H.; Pan, L.; Nagasaka, T.; Nakayama, Y., Number of Walls Controlled Synthesis of Millimeter-Long Vertically Aligned Brushlike Carbon Nanotubes. *The Journal of Physical Chemistry C* **2007,** *111* (5), 1929-1934.

25. Amama, P. B.; Pint, C. L.; McJilton, L.; Kim, S. M.; Stach, E. A.; Murray, P. T.; Hauge, R. H.; Maruyama, B., Role of Water in Super Growth of Single-Walled Carbon Nanotube Carpets. *Nano Lett.* **2008,** *9* (1), 44-49.

26. Almkhelfe, H.; Carpena-Nunez, J.; Back, T. C.; Amama, P. B., Gaseous product mixture from Fischer-Tropsch synthesis as an efficient carbon feedstock for low temperature CVD growth of carbon nanotube carpets. *Nanoscale* **2016,** *8* (27), 13476-13487.

27. Hall, W. K.; Kokes, R. J.; Emmett, P. H., Mechanism Studies of the Fischer-Tropsch Synthesis. The Addition of Radioactive Methanol, Carbon Dioxide and Gaseous Formaldehyde. *J. Am. Chem. Soc.* **1957,** *79* (12), 2983-2989.

28. Kibby, C.; Jothimurugesan, K.; Das, T.; Lacheen, H. S.; Rea, T.; Saxton, R. J., Chevron's gas conversion catalysis-hybrid catalysts for wax-free Fischer–Tropsch synthesis. *Catal. Today* **2013,** *215*, 131-141.

29. Tavasoli, A.; Sadagiani, K.; Khorashe, F.; Seifkordi, A. A.; Rohani, A. A.; Nakhaeipour, A., Cobalt supported on carbon nanotubes — A promising novel Fischer–Tropsch synthesis catalyst. *Fuel Process. Technol.* **2008,** *89* (5), 491-498.

30. Dresselhaus, M. S.; Dresselhaus, G.; Jorio, A.; Souza Filho, A. G.; Saito, R., Raman spectroscopy on isolated single wall carbon nanotubes. *Carbon* **2002,** *40* (12), 2043-2061.

31. Wang, X.; Li, N.; Liu, C.; Pfefferle, L. D.; Haller, G. L., One-step synthesis of a Pt-Co-SWCNT hybrid material from a Pt-Co-MCM-41 catalyst. *J. Mater. Chem.* **2012,** *22* (48), 25083-25092.

32. Maeda, Y.; Takano, Y.; Sagara, A.; Hashimoto, M.; Kanda, M.; Kimura, S.-i.; Lian, Y.; Nakahodo, T.; Tsuchiya, T.; Wakahara, T.; Akasaka, T.; Hasegawa, T.; Kazaoui, S.; Minami, N.; Lu, J.; Nagase, S., Simple purification and selective enrichment of metallic SWCNTs produced using the arc-discharge method. *Carbon* **2008,** *46* (12), 1563-1569.

33. Alvarez, W. E.; Pompeo, F.; Herrera, J. E.; Balzano, L.; Resasco, D. E., Characterization of Single-Walled Carbon Nanotubes (SWNTs) Produced by CO Disproportionation on Co−Mo Catalysts. *Chem. Mater.* **2002,** *14* (4), 1853-1858.

34. Pint, C. L.; Pheasant, S. T.; Pasquali, M.; Coulter, K. E.; Schmidt, H. K.; Hauge, R. H., Synthesis of High Aspect-Ratio Carbon Nanotube “Flying Carpets” from Nanostructured Flake Substrates. *Nano Lett.* **2008,** *8* (7), 1879-1883.

35. Huang, Z. P.; Wang, D. Z.; Wen, J. G.; Sennett, M.; Gibson, H.; Ren, Z. F., Effect of nickel, iron and cobalt on growth of aligned carbon nanotubes. *Applied Physics A* **2002,** *74* (3), 387-391.

36. Kim, N. S.; Lee, Y. T.; Park, J.; Han, J. B.; Choi, Y. S.; Choi, S. Y.; Choo, J.; Lee, G. H., Vertically Aligned Carbon Nanotubes Grown by Pyrolysis of Iron, Cobalt, and Nickel Phthalocyanines. *The Journal of Physical Chemistry B* **2003,** *107* (35), 9249-9255.

37. Suriani, A. B.; Asli, N. A.; Salina, M.; Mamat, M. H.; Aziz, A. A.; Falina, A. N.; Maryam, M.; Shamsudin, M. S.; Roslan Md, N.; Abdullah, S.; Rusop, M., Effect of Iron and Cobalt Catalysts on The Growth of Carbon Nanotubes from Palm Oil Precursor. *IOP Conference Series: Materials Science and Engineering* **2013,** *46* (1), 012014.

38. Kaneko, A.; Yamada, K.; Kumahara, R.; Kato, H.; Homma, Y., Comparative Study of Catalytic Activity of Iron and Cobalt for Growing Carbon Nanotubes on Alumina and Silicon Oxide. *The Journal of Physical Chemistry C* **2012,** *116* (49), 26060-26065.

39. Rao, R.; Pierce, N.; Harutyunyan, A. R., Enhancement of Vertically Aligned Carbon Nanotube Growth Kinetics and Doubling of the Height by Graphene Interface. *J. Phys. Chem. C* **2014,** *118* (38), 22243-22248.

40. Schneider, C. A.; Rasband, W. S.; Eliceiri, K. W., NIH Image to ImageJ: 25 years of image analysis. *Nat Meth* **2012,** *9* (7), 671-675.

41. Esconjauregui, S.; Xie, R.; Fouquet, M.; Cartwright, R.; Hardeman, D.; Yang, J.; Robertson, J., Measurement of area density of vertically aligned carbon nanotube forests by the weight-gain method. *J. Appl. Phys.* **2013,** *113* (14), 144309.

42. Kang, S. J.; Kocabas, C.; Ozel, T.; Shim, M.; Pimparkar, N.; Alam, M. A.; Rotkin, S. V.; Rogers, J. A., High-performance electronics using dense, perfectly aligned arrays of single-walled carbon nanotubes. *Nat Nano* **2007,** *2* (4), 230-236.

43. Dijon, J.; Fournier, A.; Szkutnik, P. D.; Okuno, H.; Jayet, C.; Fayolle, M., Carbon nanotubes for interconnects in future integrated circuits: The challenge of the density. *Diamond and Related Materials* **2010,** *19* (5–6), 382-388.

44. Yuichi, Y.; Masayuki, K.; Naoshi, S.; Mariko, S.; Shintaro, S.; Mizuhisa, N.; Makoto, W.; Noriaki, M.; Tadashi, S.; Yuji, A., Synthesis of a Closely Packed Carbon Nanotube Forest by a Multi-Step Growth Method Using Plasma-Based Chemical Vapor Deposition. *Applied Physics Express* **2010,** *3* (5), 055002.

45. Yokoyama, D.; Iwasaki, T.; Yoshida, T.; Kawarada, H.; Sato, S.; Hyakushima, T.; Nihei, M.; Awano, Y., Low temperature grown carbon nanotube interconnects using inner shells by chemical mechanical polishing. *Applied Physics Letters* **2007,** *91* (26), 263101.

46. Futaba, D. N.; Hata, K.; Yamada, T.; Hiraoka, T.; Hayamizu, Y.; Kakudate, Y.; Tanaike, O.; Hatori, H.; Yumura, M.; Iijima, S., Shape-engineerable and highly densely packed single-walled carbon nanotubes and their application as super-capacitor electrodes. *Nat Mater* **2006,** *5* (12), 987-994.

47. Yamada, T.; Maigne, A.; Yudasaka, M.; Mizuno, K.; Futaba, D. N.; Yumura, M.; Iijima, S.; Hata, K., Revealing the Secret of Water-Assisted Carbon Nanotube Synthesis by Microscopic Observation of the Interaction of Water on the Catalysts. *Nano Lett.* **2008,** *8* (12), 4288-4292.

48. Zhong, G. F.; Iwasaki, T.; Kawarada, H., Semi-quantitative study on the fabrication of densely packed and vertically aligned single-walled carbon nanotubes. *Carbon* **2006,** *44* (10), 2009-2014.

49. Esconjauregui, S.; Bayer, B. C.; Fouquet, M.; Wirth, C. T.; Ducati, C.; Hofmann, S.; Robertson, J., Growth of high-density vertically aligned arrays of carbon nanotubes by plasma-assisted catalyst pretreatment. *Appl. Phys. Lett.* **2009,** *95* (17), 173115.

50. Maruyama, S.; Einarsson, E.; Murakami, Y.; Edamura, T., Growth process of vertically aligned single-walled carbon nanotubes. *Chemical Physics Letters* **2005,** *403* (4–6), 320-323.

51. Zheng, B.; Lu, C.; Gu, G.; Makarovski, A.; Finkelstein, G.; Liu, J., Efficient CVD Growth of Single-Walled Carbon Nanotubes on Surfaces Using Carbon Monoxide Precursor. *Nano Letters* **2002,** *2* (8), 895-898.

52. Yasuda, S.; Futaba, D. N.; Yamada, T.; Yumura, M.; Hata, K., Gas Dwell Time Control for Rapid and Long Lifetime Growth of Single-Walled Carbon Nanotube Forests. *Nano Letters* **2011,** *11* (9), 3617-3623.

53. Chen, G.; Davis, R. C.; Kimura, H.; Sakurai, S.; Yumura, M.; Futaba, D. N.; Hata, K., The relationship between the growth rate and the lifetime in carbon nanotube synthesis. *Nanoscale* **2015,** *7* (19), 8873-8878.

54. Chen, G.; Sakurai, S.; Yumura, M.; Hata, K.; Futaba, D. N., Highly pure, millimeter-tall, sub-2-nanometer diameter single-walled carbon nanotube forests. *Carbon* **2016,** *107*, 433-439.

55. Chen, G.; Seki, Y.; Kimura, H.; Sakurai, S.; Yumura, M.; Hata, K.; Futaba, D. N., Diameter control of single-walled carbon nanotube forests from 1.3–3.0 nm by arc plasma deposition. *Sci. Rep.* **2014,** *4*, 3804.

56. Yasuda, S.; Futaba, D. N.; Yamada, T.; Satou, J.; Shibuya, A.; Takai, H.; Arakawa, K.; Yumura, M.; Hata, K., Improved and Large Area Single-Walled Carbon Nanotube Forest Growth by Controlling the Gas Flow Direction. *ACS Nano* **2009,** *3* (12), 4164-4170.

57. Anna, M.; Albert, G. N.; Esko, I. K., The role of metal nanoparticles in the catalytic production of single-walled carbon nanotubes - a review. *J. Phys.: Condens. Matter* **2003,** *15* (42), S3011.

58. Zheng, B.; Lu, C.; Gu, G.; Makarovski, A.; Finkelstein, G.; Liu, J., Efficient CVD Growth of Single-Walled Carbon Nanotubes on Surfaces Using Carbon Monoxide Precursor. *Nano Lett.* **2002,** *2* (8), 895-898.

59. Jalama, K.; Kabuba, J.; Xiong, H.; Jewell, L. L., Co/TiO2 Fischer–Tropsch catalyst activation by synthesis gas. *Catal. Commun.* **2012,** *17*, 154-159.

60. Watson, A.; Cornish, L., Carbon – Cobalt – Iron. In *Refractory metal systems: Selected Systems from B-Mo-Ni to C-Ta-Ti*, Effenberg, G.; Ilyenko, S., Eds. Springer Berlin Heidelberg: Berlin, Heidelberg, 2010; pp 230-248.

61. Fu, Q.; Reed, L.; Liu, J.; Lu, J., Characterization of single-walled carbon nanotubes synthesized using iron and cobalt nanoparticles derived from self-assembled diblock copolymer micelles. *Applied Organometallic Chemistry* **2010,** *24* (8), 569-572.

62. Levchenko, E. V.; Evteev, A. V.; Belova, I. V.; Murch, G. E., Molecular dynamics simulation and theoretical analysis of carbon diffusion in cementite. *Acta Materialia* **2009,** *57* (3), 846-853.

63. Hisa, M.; Tsutsumi, A.; Akiyama, T., Reduction of iron oxides by nano-sized graphite particles observed in pre-oxidized iron carbide at temperatures around 873 K. *Mater Trans* **2004,** *45* (6), 1907-1910.

64. Hisa, M.; Tsutsumi, A.; Akiyama, T., Materialographic investigation on the mechanism of hydrogen production through the reaction between iron carbide and steam at a temperature of 673 K. *Mater. Trans.* **2004,** *45* (6), 1911-1914.

65. Pint, C. L.; Xu, Y.-Q.; Pasquali, M.; Hauge, R. H., Formation of Highly Dense Aligned Ribbons and Transparent Films of Single-Walled Carbon Nanotubes Directly from Carpets. *ACS Nano* **2008,** *2* (9), 1871-1878.

66. Zhong, G.; Iwasaki, T.; Robertson, J.; Kawarada, H., Growth Kinetics of 0.5 cm Vertically Aligned Single-Walled Carbon Nanotubes. *J. Phys. Chem. B* **2007,** *111* (8), 1907-1910.

67. Yang, Y.; Xiang, H.-W.; Tian, L.; Wang, H.; Zhang, C.-H.; Tao, Z.-C.; Xu, Y.-Y.; Zhong, B.; Li, Y.-W., Structure and Fischer–Tropsch performance of iron–manganese catalyst incorporated with SiO2. *Appl. Catal.s A: Gen.* **2005,** *284* (1–2), 105-122.

68. Vinten, P.; Marshall, P.; Lefebvre, J.; Finnie, P., Distinct termination morphologies for vertically aligned carbon nanotube forests. *Nanotechnology* **2010,** *21* (3), 035603.

Chapter 5

In-Situ Generation of Water during FTS-GP CVD

5.1 Introduction

As discussed in section 4.4, the high activity and long lifetime of catalyst observed during FTS-GP CVD[1-2] is attributed to the role of water as a growth enhancer – analogous to the so-called "supergrowth."[3] According to models proposed to explain supergrowth, water enhances growth by oxidizing carbon contaminants deposited on the catalyst surface and inhibiting mass loss (Ostwald ripening and subsurface diffusion), thus extending catalyst lifetime.[4-5] The proposed model for FTS-GP CVD assumes that water is formed by the thermodynamically favored reaction between H_2 and the low volume fraction of CO. To verify the in situ generation of water, we performed thermal decomposition of FTS-GP in a batch reactor at different reaction temperatures (650, 700, 750, and 800°C).

5.2 Experimental

The products formed during FTS-GP CVD in a batch reactor were analyzed by a Hewlett-Packard 6890 series gas chromatograph (GC) with a thermal conductivity detector (TCD). The injector port was held constant at 170 ºC, operated in slip mode with a 150:1 split ratio, and a split linear with deactivated wool (Agilent 5183-4711) was used. Samples were separated using a non-polar column [HP-5 (Agilent 19091J-413)] connected in series with a polar column [DB-Wax (Agilent 122-7032)]. Columns were connected using a press fit connector (Agilent 5190-6979). Columns were operated in constant flow (1.2 mL/minute) with helium as a carrier gas. The GC temperature was initially at 50 ºC and held at this temperature for 1 minute, followed by a ramp of 20 °C per minute to

a final temperature of 200°C; total run time was 8.5 minutes. The detector was maintained at 150°C with helium as the reference gas.

5.3 Results and Discussion

In the following, ΔG^0 of the Boudouard reaction is calculated to find out whether the reaction is capable of generating water, and estimate the amount of water produced. This theoretical thermodynamic perspective allows for direct comparison of the experimental and theoretical data. Using data for free energy of formation with respect to temperature presented on FactWeb[6], ΔG_0 (T) for CO, H_2, H_2O and C at standard conditions (1 atm partial pressures of CO, H_2 and H_2O) are obtained. First, ΔG^0reaction is calculated using Equation 1:

$$\Delta G^0_{rxn} = \sum n\Delta G^0_f \text{ (products)} - \sum n\Delta G^0_f \text{ (reactants)} \quad (1)$$

The free energy formation ΔG^0 as a function of temperature for CO, H_2, H_2O, and C is given as:

$$\Delta G^0{}_{\text{reaction}} = \Delta G^0 (H_2O) - \Delta G^0 (C) - \Delta G^0 (H_2) - \Delta G^0 (CO) \quad (2)$$

To calculate the ΔG under non-standard conditions, ΔG is expressed as:

$$\Delta G = \Delta G^0 + RT\, lnQ \quad (3)$$

Where Q is the reaction quotient:

$$Q = \frac{P_{H2O}}{P_{H2}\, P_{CO}} \quad (4)$$

Since the partial pressure of water is unknown, we can only pursue our calculations under at equilibrium.

At equilibrium, $\Delta G = 0$, to calculate the partial pressure of water:

$$P(H2O) = \mathrm{P(CO)} * \mathrm{P(H2)} \exp\left(-\frac{\Delta G^0}{RT}\right) \quad (5)$$

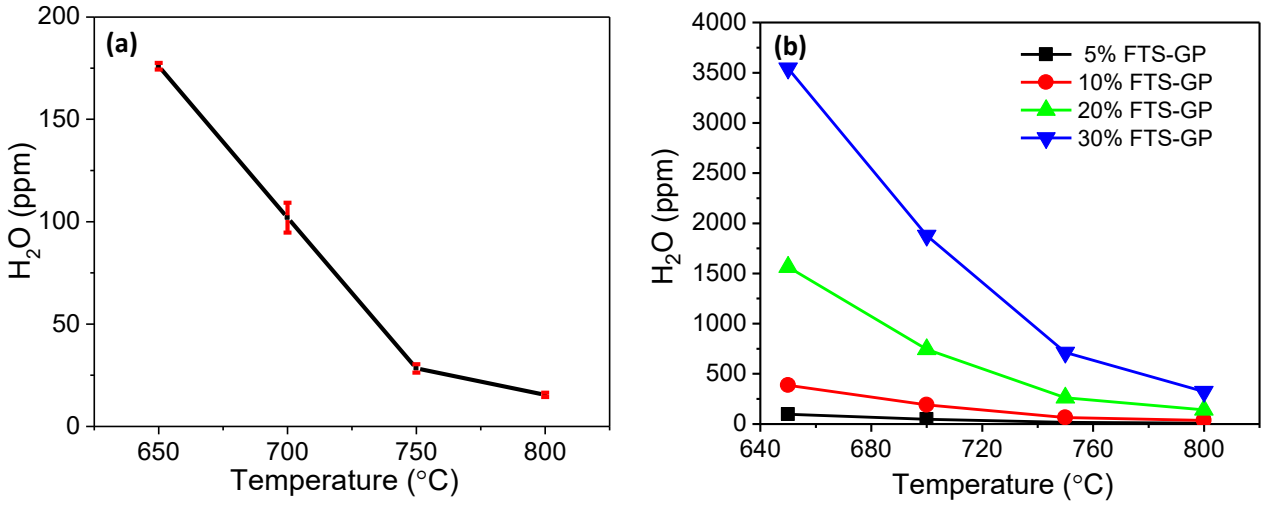

Figure 5-1 (a) A plot of amount of water generated during thermal decomposition of FTS-GP in a batch reactor as a function of temperature. (b) Plots of amount of water generated for various FTS-GP fraction as a function of temperature determined from theoretical calculations using Equation 5.

Figure 5-1a shows the amount of water generated in the batch reactor at different temperatures. The amount of water formed during FTS-GP decreases with increasing temperature. For the theoretical calculations, different fractions (dilutions) of FTS-GP (5, 10, 20, and 30 vol. %) were considered, and plots of water amount formed as a function of temperature are shown in Figure 5-1b. Therefore, the partial pressure of H_2 and CO were calculated using the composition of FTS-GP and diluent. The results show a good agreement with the experimental results. Also, for the theoretical calculations we assumed that the reaction proceeds on a small enough scale that it does not alter the partial pressures of H_2 and CO significantly.

The growth rate of SWCNTs using Fe catalyst at 650, 700, 750 and 800ºC after catalyst reduction always occurs at the growth temperature, were determined after 30 min whereby the slope of the linear fit plots of the average carpet height as function of growth temperature represent the growth rate. Temperature is a key factor that can influence the catalyst lifetime, the duration SWCNT growth is sustained before termination occurs (Figure 5-2a). The results suggest that 750°C is the optimum growth temperature for Fe catalyst with a growth rate of ~44 μm/min and no evidence of

deactivation. The growth of SWCNT was carried out at the optimum condition of the FTS-GP described in section (4-2.2). The profile also exhibit a long catalyst lifetime (>90 min) at 750°C. The growth rate for 650 and 700°C are 7.4 and 16.7μm/min, respectively, which is significantly lower than the growth rate at 750°C. By increasing the temperature to 800°C, the growth rate was 28.1μm/min with an early deactivation of the catalysts (after 30 min).

Our hypothesis suggest that the high growth rate and long catalyst lifetime at 750°C is related to the in situ generation of water that keeps the catalyst active. The results from Figure 5-2 suggest that ~32ppm (from experimental) is the optimum amount of water generated in situ to keep the Fe catalyst active and support growth of high quality SWCNTs, evidenced by the I_G/I_D ratio of different temperatures (Figure 5-2 (b)). Raman spectroscopy is a typical tool to evaluate the quality and diameter of SWCNTs.[7] Every spectra shows RBM, indicating the presence of SWCNTs.[8] The relative intensities of the G-band and D-band for 750°C were higher (I_G/I_D =9.1) compared with other growth temperatures, suggesting a better quality of SWCNTs inside the forest.

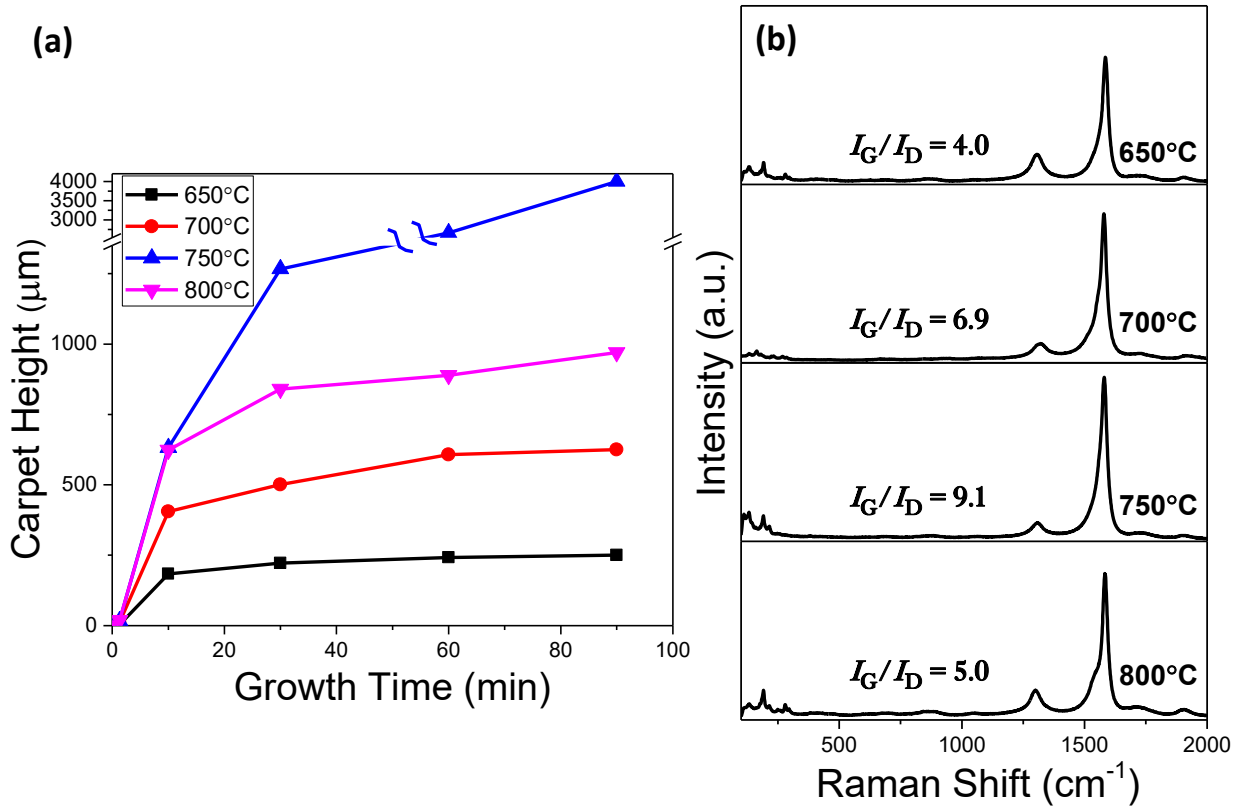

Figure 5-2 (a) Growth rate of FTS-GP (10 vol. %) on Fe catalyst at different growth temperature, (b) Raman spectra of SWCNT carpets grown by FTS-GP CVD at different temperatures (650, 700, 750 and 800°C) on an Fe catalyst using a laser excitation energy source of 1.96 eV.

5.4 Conclusions

The in-situ generation of water from FTS-GP has been demonstrated through theoretical and experimental approaches. The high growth rate (44 μm/min) and long catalyst lifetime (>90 min) on Fe catalyst at 750°C is related to the optimum amount of water (32 ppm) that keeps the catalyst active. The growth rate is not only influenced by growth temperature but also effected by the amount of water generated. The presence of water reactivated and extended the lifetime of Fe catalyst deactivated with amorphous carbon.

References

1. Almkhelfe, H.; Carpena-Nunez, J.; Back, T. C.; Amama, P. B., Gaseous product mixture from Fischer-Tropsch synthesis as an efficient carbon feedstock for low temperature CVD growth of carbon nanotube carpets. *Nanoscale* **2016,** *8* (27), 13476-13487.

2. Almkhelfe, H.; Li, X.; Rao, R.; Amama, P. B., Catalytic CVD growth of millimeter-tall single-wall carbon nanotube carpets using industrial gaseous waste as a feedstock. *Carbon* **2017,** *116* (Supplement C), 181-190.

3. Hata, K.; Futaba, D. N.; Mizuno, K.; Namai, T.; Yumura, M.; Iijima, S., Water-Assisted Highly Efficient Synthesis of Impurity-Free Single-Walled Carbon Nanotubes. *Science* **2004,** *306* (5700), 1362-1364.

4. Yamada, T.; Maigne, A.; Yudasaka, M.; Mizuno, K.; Futaba, D. N.; Yumura, M.; Iijima, S.; Hata, K., Revealing the Secret of Water-Assisted Carbon Nanotube Synthesis by Microscopic Observation of the Interaction of Water on the Catalysts. *Nano Letters* **2008,** *8* (12), 4288-4292.

5. Amama, P. B.; Pint, C. L.; McJilton, L.; Kim, S. M.; Stach, E. A.; Murray, P. T.; Hauge, R. H.; Maruyama, B., Role of Water in Super Growth of Single-Walled Carbon Nanotube Carpets. *Nano Letters* **2009,** *9* (1), 44-49.

6. C. W. Bale, E. B., P. Chartrand, S. A. Decterov, G. Eriksson, K. Hack, I. H. Jung, Y. B. Kang, J. Melançon, A. D. Pelton, C. Robelin and S. Petersen, FactSage Thermochemical Software and Databases - Recent Developments. 2009; Vol. 33, pp 295-311.

7. Kalbáč, M.; Kavan, L.; Dunsch, L., In Situ Raman Spectroelectrochemistry as a Tool for the Differentiation of Inner Tubes of Double-Wall Carbon Nanotubes and Thin Single-Wall Carbon Nanotubes. *Analytical Chemistry* **2007,** *79* (23), 9074-9081.

8. Rao, A. M.; Richter, E.; Bandow, S.; Chase, B.; Eklund, P. C.; Williams, K. A.; Fang, S.; Subbaswamy, K. R.; Menon, M.; Thess, A.; Smalley, R. E.; Dresselhaus, G.; Dresselhaus, M. S., Diameter-Selective Raman Scattering from Vibrational Modes in Carbon Nanotubes. *Science* **1997,** *275* (5297), 187-191.

Chapter 6

Chiral and Diameter Control of SWCNTs

Using High Melting Point Metals as Promoters

Abstract

Proper control of the geometry of single walled carbon nanotubes (SWCNTs) using chemical vapor deposition (CVD) will enable many their widespread applications. Here we demonstrate growth of SWCNT carpets with diameter distributions that are smaller than SWCNTs in conventional carpets using a CVD process that utilizes the product gaseous mixture from Fischer-Tropsch synthesis (FTS-GP). The high-resolution transmission electron microscopic (HR-TEM) and Raman spectroscopic results reveal that the use of a high melting point metal as a catalyst promoter in combination with either Co (1.5 nm ± 0.7) at 850ºC or Fe (1.9 nm ± 0.8) at 750ºC yields smaller-diameter SWCNT arrays with narrow diameter distributions. A time-dependent study of the evolution of catalyst particles during growth via FTS-GP CVD using atomic force microscopy (AFM) suggest that the presence of Ru (a high melting point metal) as a catalyst promoter inhibits sintering of catalyst particles.

6.1 Introduction

Controlling the diameter of single walled carbon nanotubes (SWCNTs) is considered one of the challenges that researchers face in the area of synthesizing SWCNTs. Electronic and optical properties of SWCNTs are highly influenced by their geometric orientations, like chirality index (n,m).[1] Generally, a SWNT is classified as either metallic (m-SWNT) or semiconductor (s-SWNT) depending on the tube diameter. The tube diameter is inversely proportional to the band gap[2], and therefore allows for the electronic property of SWNTs to be tuned. Large band gap tubes (s-SWNTs) are preferable in the field of electronics since those large band gaps will serve as channels in field-effective transistors (FETs)[3]. Extensive theoretical and experimental studies have concluded that catalyst particles size one of the key factors that determine the SWCNT diameter size.[4-6]

Typical SWNT carpets contain both metallic and semiconductor nanotubes (wide range of SWNT diameters) which limits their application. In order to increase the participation of SWCNTs in the electronics, tube diameter must be controlled more effectively. Recently, efforts have been focused on either directly controlling the diameters of SWCNTs during CVD growth or conducting post-synthesis separation of m-SWCNT and s-SWCNT mixtures via dielectrophoresis, density gradient centrifugation, adsorption of bromine and diazotization.[7-10] Note that post-synthesis approaches have significant drawbacks: (1) They frequently lead to short and defective tubes or cause significant contamination, which may affect the performance of the SWCNTs in a device.[3] (2) The techniques are non-scalable and do not always offer high chiral selectivity.[11] CVD method is a sufficient tool for control of the diameter of SWCNTs, if the catalyst size and stability are properly controlled. A number of studies have established direct correlations between catalyst size (prior to nucleation) and nanotube diameter, suggesting that catalyst particle size is in fact the main factor in nanotube diameter control.[12,13] Other factors such as growth temperature and precursor concentration have been used to control nanotube diameter. As examples, different nanotube diameters were obtained by manipulating

the growth temperatures; Tian et al.[14] was able to control SWCNTs diameters from 1.2-1.9 nm by changing the concentration of carbon dioxide. An extensive study using density functional theory (DFT) concluded that catalyst particle size is one of the main parameters responsible for nucleating SWCNTs with specific diameters.[15]

Catalyst sintering at CVD growth temperatures is a common phenomenon and it typically broadens the size distribution of catalyst particles and consequently yield nanotubes with wider diameter distributions. One way to overcome this problem is by leaving sufficient space between catalyst particles, which prevents them from aggregating and preserves the particle size distribution formed after annealing catalyst film or depositing particles.[13,15-18] However, the resulting SWCNT density from substrates with well-spaced catalyst particles is usually low and may not the requirements for many applications that require dense SWCNT arrays.[19] Mattevi et al.[20] suggested that the supported layer AlOy plays an important role in enhancing SWCNT nucleation density by reducing the mobility of the Fe catalyst and preventing Ostwald ripening effects due to the strong interaction with the support at high growth temperatures. Kim et al.[21] proposed that the growth termination step starts when Fe particles begin diffusing through the alumina support. Experiments and theoretical models have concluded that Ostwald ripening and subsurface diffusion are the two critical factors affecting the size of catalyst particles, and subsequently the diameter in SWCNTs.[22] Pretreatment of the catalyst support by ion beam bombardment and thermal annealing has been found to be an effective approach to minimize the effect of Ostwald ripening and obtain ultra-narrow tube diameter distributions in SWCNTs.[23] The introduction of controlled amount of water was shown to inhibit the diffusion rates of catalyst atoms during annealing.[24]

In this work, we demonstrate improved control of SWCNTs diameters and hence SWCNT chiralities via CVD using FTS-GP as a carbon precursor over Fe or Co catalyst with a high-melting point metal (Ru) as a catalyst promoter. The growth results show improved stabilization of catalyst in

the presence of Ru as well as a shift in the diameter distributions of SWCNTs from 2.5 nm to 1.5 nm and 3.1 to 1.9 nm for Co and Fe catalyst respectively.

6.2 Experimental

The morphologies and microstructures of the grown SWCNTs were studied by field emission scanning electron microscopy (FESEM) using FEI Versa 3D dual beam with multiple detectors and transmission electron microscopy (TEM). For TEM imaging, a small amount of SWCNT carpet sample was mechanically exfoliated from the substrate and dispersed in ethanol via sonication. A drop of the homogeneous suspension was deposited on a lacey carbon TEM grid and examined by TEM using FEI Tecnai F20 XT operating at 200 kv. The structure and quality of SWCNTs were characterized by Raman spectroscopy using multi laser wavelengths of 488, 514, 633, and 785nm. Raman spectra were collected at multiple spots from the samples using a Renishaw inVia Raman microscope. Atomic force microscopy (AFM) was used for studying the surface topography of catalysts before and after SWCNT growth.

The catalyst film with nominal thickness of 0.5 nm Co or Fe, 0.1 nm Ru (as catalyst promotor), and 30 nm supporting layer (Al_xO_y) were deposited on Si (100) wafers with a native oxide layer by ion beam sputtering (IBS/e, South Bay Technology). The metal targets were etched to remove the native oxide layer prior to deposition. All films were deposited at 10^{-4} Torr chamber pressure using a voltage of 8 kV and a current of 6 mA under Ar flow, without exposing the films to air between depositions. The carbon feedstock (FTS-GP), supplied by Matheson Inc., has the following composition: H_2 (40%), CH_4 (30%), C_2H_6 (8%), C_2H_4 (6%), CO (5%), C_3H_8 (5%), N_2 (4%), and C_3H_6 (2%); it represents a typical product mixture obtained from FTS process.[25,26] SWCNT growth was carried out at atmospheric pressure using the EasyTube 101 CVD system (CVD Equipment Corporation), equipped with several important features including LabView-based process control software, static mixer for optimum gas mixing, and control system for precise temperature control. A typical growth run involved heating the catalyst sample to the desired temperature (850°C) at a rate of 45 °C/min in flowing Ar. At the growth temperature, the catalyst was exposed to a copious amount of H_2 in combination with Ar

for 2 min to reduce the catalyst; the respective flow rates were 250 standard cubic centimeters per minute (sccm) H_2 and 250 sccm Ar. Thereafter, SWCNT growth under optimum conditions on a Co/Ru or Fe/Ru catalyst was initiated by introducing 10 sccm FTS-GP and 100 sccm Ar at various times. At the end of the growth run, the samples were rapidly cooled in H_2, followed by slow cooling to room temperature in 700 sccm Ar.

6.3 Result and Discussion

Thermal dewetting of the deposited metal films into finely/homogeneously nanoparticles is highly dependent on the melting point of that metal and porosity of the underlayer.[27] AFM images in Figure 6-1 show the effect of Ru on the stability of catalyst during annealing in CVD. In the absence of Ru, Co catalyst experiences severe Ostwald ripening and coalescence after annealing in hydrogen environment at 850˚C for 5 min as particles larger than 5 nm are formed. However, Co catalyst particles appear to be more stable in the presence of Ru as particles remain small and highly monodispersed (Figure 6-1b). The addition of a small amount of Ru as a promoter impedes sintering during the annealing conditions and ensures high uniformity of catalyst particles before and during growth.[28]

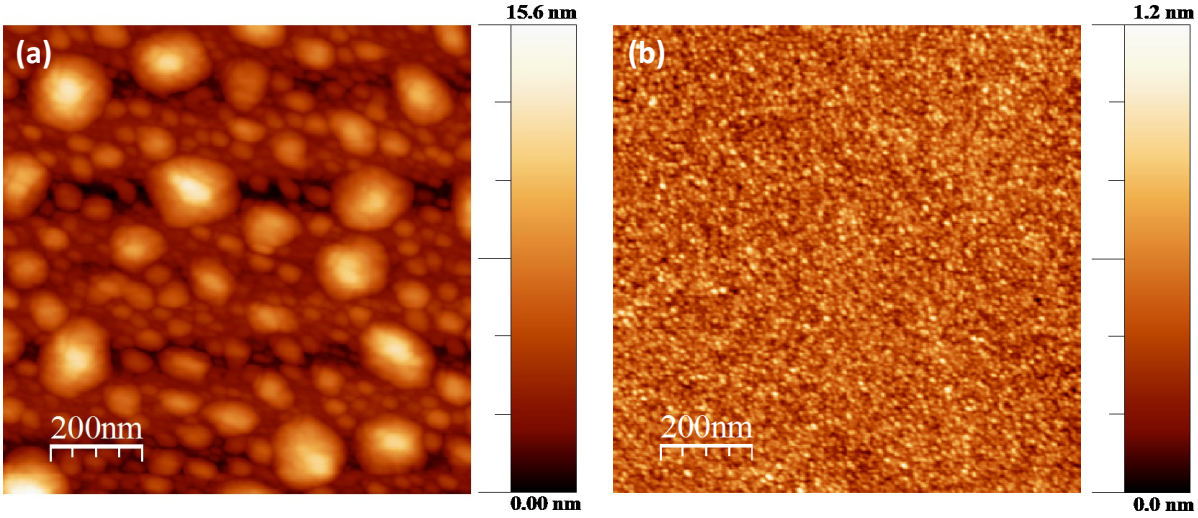

Figure 6-1 AFM images of catalysts nanoparticles formed on the substrate after annealing for 5 min in H_2 at 850ºC for (a) Co catalyst and (b) Co/Ru catalyst.

TEM images illustrate the morphology of SWCNTs grown on Co/Ru (Figures 6-2a and b) and Co (Figures 6-2d and e) catalysts supported on AlO_x. The difference in SWCNT diameters is obvious and further supports the role of high-melting temperature promoter (Ru) to in preventing sintering and supporting growth of smaller-diameter SWCNTs with average diameter between of 1.5 nm as shown in Figure 6-2 (c,f). The average diameter of the grown SWCNT from Fe/Ru was smaller (1.9 nm) compared to Fe catalyst (3.1 nm) as shown in Figure S1. According to Dai et al.,[6] the role of Ru as a

promoter in the formation of smaller-diameter nanotubes is due to its alloying structure and strong Fe-Ru interaction that enhances the stability of smaller catalyst nanoparticles at high temperatures.

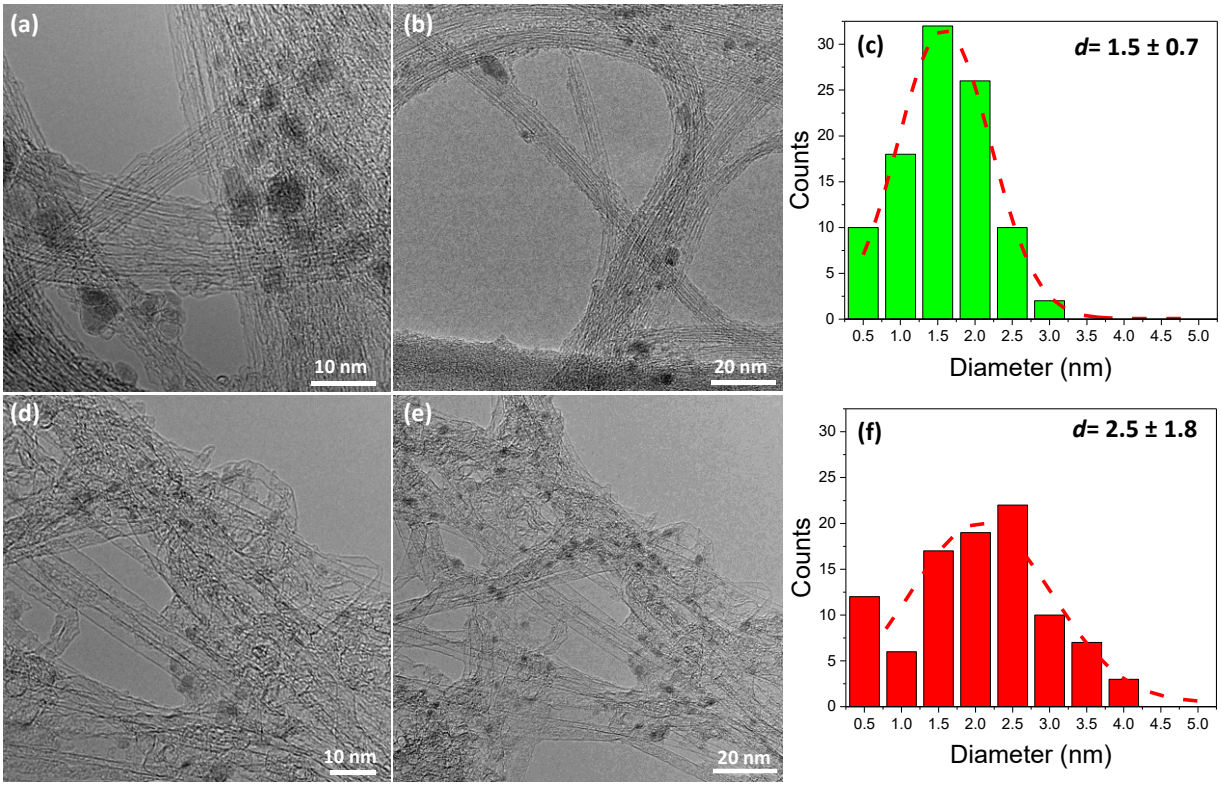

Figure 6-2 HR-TEM images of SWCNT grown by FTS-GP CVD at 850˚C. (a,b) High-and low-magnification images of SWCNTs grown on a Co/Ru catalyst. (d,e) High-and low-magnification images of SWCNTs grown on a Co catalyst. Histogram of SWCNT diameter distributions and their Gaussian fits of SWCNT grown on Co/Ru catalysts (c) and Co catalysts (f); mean diameters for SWCNTs from Co/Ru and Co catalysts were 1.5 and 2.5 nm, respectively.

SWCNTs grown on Co and Fe catalysts with and without Ru were further characterized by multi-excitation Raman spectroscopy. The Raman spectra are characterized by intense G-bands (not shown) and the low frequency radial breathing modes (RBM), which are characteristic of SWCNTs. Figure 3 (a,b) shows the effect of Ru on the growth properties of SWCNTs from Fe/Ru catalyst at 750ºC (optimum growth temperature for Fe); The RBMs shift to higher wavenumbers indicating the formation of SWCNTs with smaller diameters.

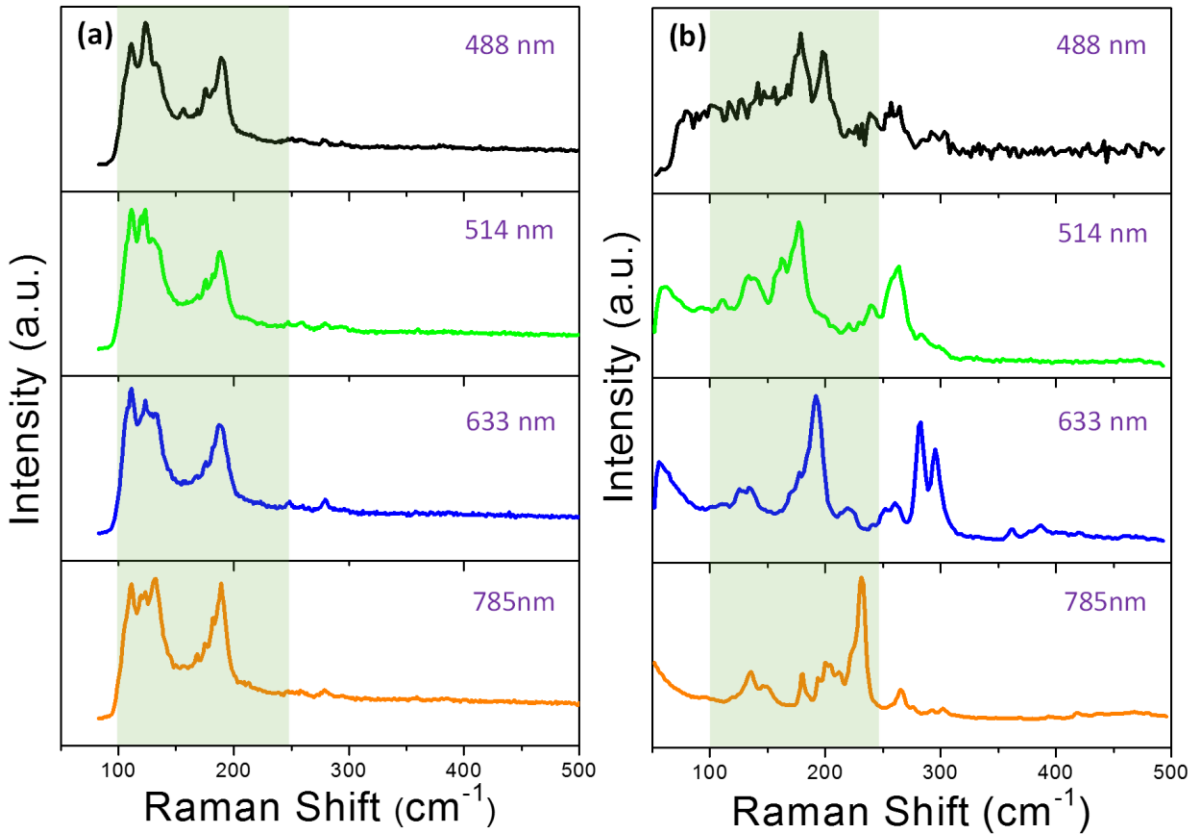

Figure 6-3 Multi-excitation Raman spectra of SWCNT synthesized at 750˚C on (a) Fe catalyst and (b) Fe/Ru catalyst.

Figure 4 shows Raman spectra of SWCNT grown on Co-Ru and Co at the optimum temperature for (850ºC). Clear differences are observed between the two samples. Although the growth of SWCNT has been carried out at higher temperature compared to Fe catalyst, the effect of Ru is still evident. Multiple new peaks at 250 and 265 cm^{-1} are observed at high Raman shift for SWCNTs grown with Co-Ru and they are in good agreement with TEM results. The full Raman spectra shown in Figure 2S reveal that the addition of Ru to Co or Fe as a promoter actually improve the quality of the resulting SWCNTs, evidenced by the relatively higher ratio of tangential G-band to defect-induced D-band.

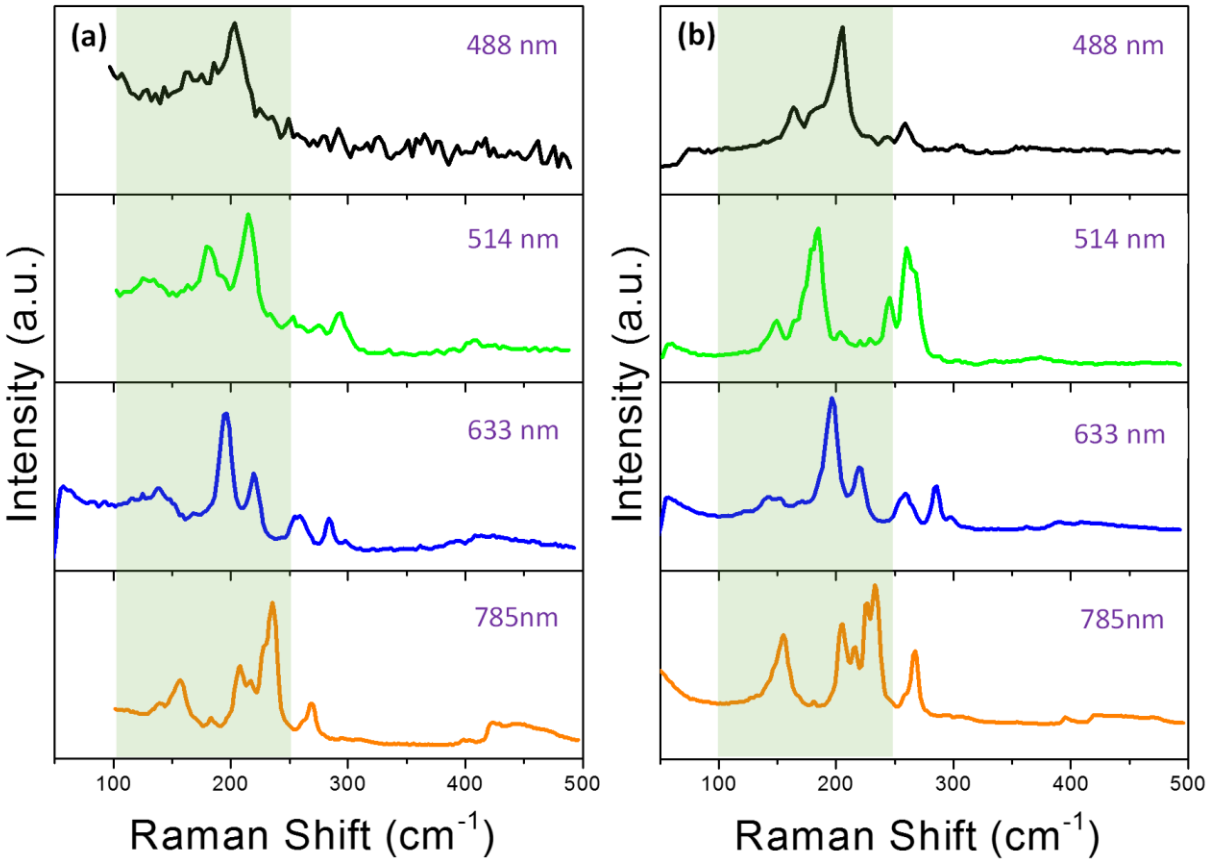

Figure 6-4 Multi-excitation Raman spectra of SWCNT synthesized as 850˚C on (a) Co catalyst and (b) Co/Ru catalyst.

When using high-melting point metals like tungsten (W) with Co as a bimetallic catalyst for synthesizing SWCNT,[29] the growth results show high selectivity towards a specific chirality (12,6). A modeling simulation study by Balbuena et al.[30] to predict the parameters that influence chirality of SWCNTs reveal that changing the catalyst shape during growth is the main factor that can impact chirality and SWCNT diameter. It has also been shown that by strengthening the metal-substrate interactions, a more stable particle shape can be obtained.[31] The AFM, TEM, and Raman data show that using Ru, a high-melting point metal as a promoter, has the ability to limit the mobility of the formed Co nanoparticles and eventually decrease catalyst sintering. The same observation has been reported using Pt with Co as a bimetallic catalyst,[32] where Pt plays a crucial role in stabilizing Co catalyst and support the formation of SWCNTs with a narrower diameter distributions. Also, using Ru

with Fe as a bimetallic catalyst can effectively grow SWCNT with narrow diameter and chiral distributions.[6]

6.4 Conclusions

We have demonstrated the role of Ru, a high-melting point metal, as a catalyst promoter in the growth of SWCNTs on Fe/Ru and Co/Ru catalyst via CVD. FTS-GP was used as a carbon precursor at 750ºC for Fe catalyst and 850ºC for Co. Deposition of 0.1 nm-thick layer of Ru on Fe or Co catalyst was found to impede catalyst sintering at CVD growth temperatures and enhance the quality of the grown SWCNTs, as evidenced by the higher ratio of tangential G-band to defect-induced D-band. In addition, the presence of Ru supports growth of smaller-diameter SWCNTs. The average diameter of SWCNTs produced is decreases from 2.5 nm (using Co catalyst) to 1.5 nm when Ru is used as promoter. While using Ru with Fe catalyst, the diameter of the grown SWCNT decreases from 3.1 to 1.9 nm.

References

(1) Chiashi, S.; Kono, K.; Matsumoto, D.; Shitaba, J.; Homma, N.; Beniya, A.; Yamamoto, T.; Homma, Y. Adsorption effects on radial breathing mode of single-walled carbon nanotubes. *Physical Review B* **2015**, *91*, 155415.

(2) Wilder, J. W. G.; Venema, L. C.; Rinzler, A. G.; Smalley, R. E.; Dekker, C. Electronic structure of atomically resolved carbon nanotubes. *Nature* **1998**, *391*, 59-62.

(3) Li, J.; Ke, C.-T.; Liu, K.; Li, P.; Liang, S.; Finkelstein, G.; Wang, F.; Liu, J. Importance of Diameter Control on Selective Synthesis of Semiconducting Single-Walled Carbon Nanotubes. *ACS Nano* **2014**, *8*, 8564-8572.

(4) Ding, F.; Larsson, P.; Larsson, J. A.; Ahuja, R.; Duan, H.; Rosén, A.; Bolton, K. The Importance of Strong Carbon−Metal Adhesion for Catalytic Nucleation of Single-Walled Carbon Nanotubes. *Nano Letters* **2008**, *8*, 463-468.

(5) Ayre, G. N.; Uchino, T.; Mazumder, B.; Hector, A. L.; Hutchison, J. L.; Smith, D. C.; Ashburn, P.; Groot, C. H. d. On the mechanism of carbon nanotube formation: the role of the catalyst. *Journal of Physics: Condensed Matter* **2011**, *23*, 394201.

(6) Li, X.; Tu, X.; Zaric, S.; Welsher, K.; Seo, W. S.; Zhao, W.; Dai, H. Selective synthesis combined with chemical separation of single-walled carbon nanotubes for chirality selection. *Journal of the American Chemical Society* **2007**, *129*, 15770-15771.

(7) Krupke, R.; Hennrich, F.; Löhneysen, H. v.; Kappes, M. M. Separation of Metallic from Semiconducting Single-Walled Carbon Nanotubes. *Science* **2003**, *301*, 344-347.

(8) Ghosh, S.; Bachilo, S. M.; Weisman, R. B. Advanced sorting of single-walled carbon nanotubes by nonlinear density-gradient ultracentrifugation. *Nat Nano* **2010**, *5*, 443-450.

(9) Chen, Z.; Du, X.; Du, M.-H.; Rancken, C. D.; Cheng, H.-P.; Rinzler, A. G. Bulk Separative Enrichment in Metallic or Semiconducting Single-Walled Carbon Nanotubes. *Nano Letters* **2003**, *3*, 1245-1249.

(10) Strano, M. S.; Dyke, C. A.; Usrey, M. L.; Barone, P. W.; Allen, M. J.; Shan, H.; Kittrell, C.; Hauge, R. H.; Tour, J. M.; Smalley, R. E. Electronic Structure Control of Single-Walled Carbon Nanotube Functionalization. *Science* **2003**, *301*, 1519-1522.

(11) Voggu, R.; Rao, K. V.; George, S. J.; Rao, C. N. R. A Simple Method of Separating Metallic and Semiconducting Single-Walled Carbon Nanotubes Based on Molecular Charge Transfer. *Journal of the American Chemical Society* **2010**, *132*, 5560-5561.

(12) Cheung, C. L.; Kurtz, A.; Park, H.; Lieber, C. M. Diameter-Controlled Synthesis of Carbon Nanotubes. *The Journal of Physical Chemistry B* **2002**, *106*, 2429-2433.

(13) Nasibulin, A. G.; Pikhitsa, P. V.; Jiang, H.; Kauppinen, E. I. Correlation between catalyst particle and single-walled carbon nanotube diameters. *Carbon* **2005**, *43*, 2251-2257.

(14) Tian, Y.; Timmermans, M. Y.; Kivistö, S.; Nasibulin, A. G.; Zhu, Z.; Jiang, H.; Okhotnikov, O. G.; Kauppinen, E. I. Tailoring the diameter of single-walled carbon nanotubes for optical applications. *Nano Research* **2011**, *4*, 807-815.

(15) Hedman, D.; Reza Barzegar, H.; Rosén, A.; Wågberg, T.; Andreas Larsson, J. On the Stability and Abundance of Single Walled Carbon Nanotubes. *Scientific Reports* **2015**, *5*, 16850.

(16) Lukas, D.; Jason, G.; Thomas, H.; Matthias, M.; Roland, R.; Christofer, H. Narrowing SWNT diameter distribution using size-separated ferritin-based Fe catalysts. *Nanotechnology* **2009**, *20*, 355601.

(17) Dai, H.; Rinzler, A. G.; Nikolaev, P.; Thess, A.; Colbert, D. T.; Smalley, R. E. Single-wall nanotubes produced by metal-catalyzed disproportionation of carbon monoxide. *Chemical Physics Letters* **1996**, *260*, 471-475.

(18) Kukovitsky, E. F.; L'Vov, S. G.; Sainov, N. A.; Shustov, V. A.; Chernozatonskii, L. A. Correlation between metal catalyst particle size and carbon nanotube growth. *Chemical Physics Letters* **2002**, *355*, 497-503.

(19) Chen, G.; Seki, Y.; Kimura, H.; Sakurai, S.; Yumura, M.; Hata, K.; Futaba, D. N. Diameter control of single-walled carbon nanotube forests from 1.3–3.0 nm by arc plasma deposition. *Scientific Reports* **2014**, *4*, 3804.

(20) Mattevi, C.; Wirth, C. T.; Hofmann, S.; Blume, R.; Cantoro, M.; Ducati, C.; Cepek, C.; Knop-Gericke, A.; Milne, S.; Castellarin-Cudia, C.; Dolafi, S.; Goldoni, A.; Schloegl, R.; Robertson, J. In-situ X-ray Photoelectron Spectroscopy Study of Catalyst−Support Interactions and Growth of Carbon Nanotube Forests. *The Journal of Physical Chemistry C* **2008**, *112*, 12207-12213.

(21) Kim, S. M.; Pint, C. L.; Amama, P. B.; Zakharov, D. N.; Hauge, R. H.; Maruyama, B.; Stach, E. A. Evolution in Catalyst Morphology Leads to Carbon Nanotube Growth Termination. *The Journal of Physical Chemistry Letters* **2010**, *1*, 918-922.

(22) Sakurai, S.; Nishino, H.; Futaba, D. N.; Yasuda, S.; Yamada, T.; Maigne, A.; Matsuo, Y.; Nakamura, E.; Yumura, M.; Hata, K. Role of Subsurface Diffusion and Ostwald Ripening in Catalyst Formation for Single-Walled Carbon Nanotube Forest Growth. *Journal of the American Chemical Society* **2012**, *134*, 2148-2153.

(23) Yang, N.; Li, M.; Patscheider, J.; Youn, S. K.; Park, H. G. A Forest of Sub-1.5-nm-wide Single-Walled Carbon Nanotubes over an Engineered Alumina Support. *Scientific Reports* **2017**, *7*, 46725.

(24) Amama, P. B.; Pint, C. L.; McJilton, L.; Kim, S. M.; Stach, E. A.; Murray, P. T.; Hauge, R. H.; Maruyama, B. Role of Water in Super Growth of Single-Walled Carbon Nanotube Carpets. *Nano Letters* **2009**, *9*, 44-49.

(25) Almkhelfe, H.; Carpena-Núñez, J.; Back, T. C.; Amama, P. B. Gaseous product mixture from Fischer–Tropsch synthesis as an efficient carbon feedstock for low temperature CVD growth of carbon nanotube carpets. *Nanoscale* **2016**, *8*, 13476-13487.

(26) Almkhelfe, H.; Li, X.; Rao, R.; Amama, P. B. Catalytic CVD growth of millimeter-tall single-wall carbon nanotube carpets using industrial gaseous waste as a feedstock. *Carbon* **2017**, *116*, 181-190.

(27) Futaba, D. N.; Miyake, K.; Murata, K.; Hayamizu, Y.; Yamada, T.; Sasaki, S.; Yumura, M.; Hata, K. Dual Porosity Single-Walled Carbon Nanotube Material. *Nano Letters* **2009**, *9*, 3302-3307.

(28) Kharlamova, M. V. Investigation of growth dynamics of carbon nanotubes. *Beilstein Journal of Nanotechnology* **2017**, *8*, 826-856.

(29) An, H.; Kumamoto, A.; Takezaki, H.; Ohyama, S.; Qian, Y.; Inoue, T.; Ikuhara, Y.; Chiashi, S.; Xiang, R.; Maruyama, S. Chirality specific and spatially uniform synthesis of single-walled carbon nanotubes from a sputtered Co-W bimetallic catalyst. *Nanoscale* **2016**, *8*, 14523-14529.

(30) Gomez-Ballesteros, J. L.; Balbuena, P. B. Structure and dynamics of metallic and carburized catalytic Ni nanoparticles: effects on growth of single-walled carbon nanotubes. *Physical Chemistry Chemical Physics* **2015**, *17*, 15056-15064.

(31) Yang, N.; Li, M.; Patscheider, J.; Youn, S. K.; Park, H. G. A Forest of Sub-1.5-nm-wide Single-Walled Carbon Nanotubes over an Engineered Alumina Support. **2017**, *7*, 46725.

(32) Liu, B.; Ren, W.; Li, S.; Liu, C.; Cheng, H.-M. High temperature selective growth of single-walled carbon nanotubes with a narrow chirality distribution from a CoPt bimetallic catalyst. *Chemical Communications* **2012**, *48*, 2409-2411.

Chapter 7

Batch Reactor for the Scale-up Production of Carbon Nanomaterials

Abstract

Scalable synthesis of carbon nanotubes (CNTs), carbon nanofibers (CNFs), and onion like carbon (OLC) in a batch reactor using supercritical fluids as a reaction media is demonstrated. The process utilizes toluene, ethanol, or butanol as a carbon precursor in combination with ferrocene that serves as a catalyst precursor and a secondary carbon source. Growth with supercritical toluene at 600ºC in the absence of water yield large-diameter CNTs and CNFs while the introduction of 0.05 ml of water enhances the product yield by 50% and promotes the formation of smaller-diameter CNTs. The exterior surface of CNTs was decorated with highly monodispersed Fe nanoparticles. At lower temperature (400ºC) in the absence of water, supercritical toluene produces mainly OLC, and the same structure is observed by increasing the amount of added water to 0.1 ml at 600ºC. The tendency for alcohols to produce tubular structures increases in the order $C_2H_5OH < C_3H_7OH < C_4H_9OH$, which suggests a direct correlation between the aliphatic chain length of alcohol and the tendency to form a tubular structure. The use of supercritical fluids for growth does not only provide a route for selective growth of a variety of carbon nanomaterials, but also provides a unique one-step approach that is free of aggressive acid treatment for synthesis of CNT-supported metallic nanoparticle composites for catalysis and energy storage applications.

7.1 Introduction:

Carbon nanomaterials such as carbon nanotubes (CNTs), graphene, carbon nanofibers, onion-like carbon (OLC) and fullerenes have attracted a great deal of interest due to their unique mechanical, chemical, thermal, and electrical properties.[1-5] There have been concerted efforts to scale-up synthesis of nanocarbons for important applications such as composites, [6] heterogeneous catalysis, and energy storage whereby high yield of CNFs, CNTs and OLCs are required.[7-9] As examples, CNTs are good candidates for reinforcing cement composites to enhance the flexural strength, compressive strength, and failure strain of cement composites, and as CNT-polymer composites for heat sinks in electronic devices.[10-11] Scalable production of CNTs are of particular importance as they are strong candidates to replace conventional supports in heterogeneous catalysis[12-13] and electrodes in batteries and proton exchange membrane fuel cells (PEMFCs).The conventional methods used for producing carbon nanomaterials include arc-discharge,[14] laser ablation,[15] and chemical-vapor deposition.[16] However, the relatively low yield, apparatus complexity and high operating cost of these conventional techniques limit the widespread application of carbon nanomaterials. As revealed by bibliometric analysis, the main factor limiting the growth of nanomaterial's application is the industrial scale production of these materials.[17-19]

Efforts to scale up production of multi-walled CNTs (MWCNTs) have focused on developing a supercritical fluid approach (SCFA), widely used for synthesis and processing of mesoporous carbonaceous buckyball, nanowires and MWCNT.[20-22] Zhonglai et al.[23] reported the growth of MWCNTs using the supercritical condition of carbon monoxide. A continuous-flow SCFA approach (P=5.17Mpa, T=750˚C) showed growth of MWCNTs with high yield and selectivity (100%, based on catalyst weight). Scalable production of single-walled carbon nanotube (SWCNTs) with a productivity of up to 10 g/day of SWCNTs has been achieved using HiPCO process under severe conditions (3.1 Mpa and 1050˚C).[24] Korgel's group[25] demonstrated the use of supercritical toluene in nitrogen

environment at 600˚C and 12.4 Mpa for growth of MWCNTs. The catalysts used in batch reactors with supercritical fluids include Fe and Fe/Pt and the catalyst nanoparticles were prepared by thermal decomposition of their precursors (platinum acetylacetonate and iron pentacarbonyl). They found that the yield of MWCNTs is dependent on temperature and catalyst particle size. Scalable growth of bamboo-shaped CNTs was synthesized using ethanol as a carbon source and magnesium as a reductant in a stainless steel autoclave at 650˚C.[26] Further investigations by the same group[27] reported growth of three types of bamboo-shaped CNTs, cubic, and spherical carbon nanocages using ethanol as a carbon source and magnesium as a reductant catalyst. The coexistence of cubic and spherical shaped structures was rationlized as a bending attempt of the graphitic sheets to minimize the highly energetic dangling bonds at the edge of the growing structure[27]. OLCs are typically synthesized by thermal annealing (vacuum or inert gas) of nanodiamond precursor,[28-29] underwater arc discharge,[30] heating a carbon filament in liquid alcohol,[31] or chemical vapor deposition via catalytic decomposition of acetylene using iron as an active catalyst at synthesis temperature of 420ºC followed by heat treated at 1100ºC to obtain a concentric graphitic layers.[32] For CVD, Fe nanoparticles were found to be encapsulated between the graphitic layers. The main limitation of SCFA for its commercialization is the reaction time, Luo et al.[33] synthesis CNTs for it is about 70 h and Liu et al.[26] for 10h. Also the post-treatments of the catalyst which requires several heating stages, a flow of reducing atmosphere (H_2: Ar), loading in inert gas environment, mixing with promotors and preparing a bimetallic catalysts.[23, 25-26, 34] The fabrication of OLC usually requires an expensive apparatus or a high temperature in addition to a better understanding for the growth mechanisms.

In this work, we report a scalable and efficient process for selective growth of carbon nanomaterials using a single-step batch reactor and super critical fluid approach with a variety of precursors: aromatics (toluene, xylene) and alcohols (ethanol, propanol and butanol) along in combination with ferrocene as a catalyst source. The resulting carbon nanomaterials include MWCNTs, spherical carbonaceous materials (carbon like onion structure) and MWCNTs filled/or

decorated with Fe nanowires. The role of water in the growth process using different precursors has been examined along with the growth temperature and loading ratio of ferrocene. This approach has the potential of scaling up the production of carbon nanomaterials to meet industrial demand. The design simplicity of the apparatus, high productivity, and the adjustable product selectivity to the structure types of the carbon nanomaterials favor this approach among others.

7.2 Experimental:

The experimental setup used for synthesis carbon nanomaterials consist of a 50 ml capacity stainless steel cylinder used as a batch reactor as shown in Figure S6. The reactor was loaded with 30 ml of carbon precursor [anhydrous aromatic (toluene, xylene) or anhydrous alcohol (ethanol, propanol and butanol)]. Ferrocene powder (0.01, 0.1, 0.2 and 0.3 g) was dissolved in the carbon precursor and mixed (if present) with DI-water (0.025, 0.05, 0.075 and 0.1 ml). After mixing all the reactants together, the reactor was sealed properly and the initial pressure was maintained at 1 atm. Thereafter, it was heated to 400-600˚C for 1 h using a ceramic heater (Omega) with an iron-chrome-aluminum ribbon elements. Then the reactor was allowed to cool to room temperature naturally. The black solid powder was collected and washed with ethanol and distilled water respectively, and then dried in a vacuum oven at 80˚C for 5h.

7.3 Characterization:

The morphology and microstructure of the reaction products were characterized using transmission electron microscopy (TEM) FEI Tecnai F20 XT, operating at 200 kV and equipped with energy-dispersive X-ray spectroscopy (EDS), and field emission scanning electron microscope (SEM) FEI Versa 3D Dual Beam at different magnifications. For TEM, the final dry products were dispersed in ethanol by sonication for 5 min, dropped on copper microgrid coated with lacy carbon film. The Raman spectra of as-grown nanomaterials were carried out using Renishaw inVia Raman Microscope with a

laser 633 nm as an excitation source. X-ray powder diffraction (XRD) measurement was carried using Rigaku Miniflex II desktop X-ray diffractometer with monochromatic Cu Kα radiation (λ = 0.154 nm) with a step size of 0.1º and a scan speed of 2.0º per minute, to determine phase purity and degree of crystallization. Nitrogen adsorption-desorption measurements were conducted at -196ºC using a Quantachrome Autosorb-1 instrument, and the BET specific surface area (SA_{BET}) and total pore volume measurements were determined from the isotherms. Prior to adsorption measurements, the samples were degassed at 250ºC for 12 h to obtain the base weight of the samples. SA_{BET} was determine from the adsorption branch in the linear range of relative pressure from 0.02 to 0.35. The total volume was evaluated by a single-point pore volume at relative pressure of 0.95.

7.4 Results and Discussion:

7.4.1 Supercritical toluene in the absence of water. Scalable synthesis of carbon nanomaterials in supercritical toluene without the addition of water was investigated at 400, 500, and 600ºC. Figure 7-1 shows a representative Raman spectra and corresponding SEM images of carbon nanomaterials grown at the different temperatures using 30 ml of toluene and 0.2 g of ferrocene for 1 h. The results reveal that the nanocarbon morphology has a strong dependence on temperature of fluid phase (supercritical toluene). At low fluid phase temperature (400ºC), the structure of the synthesized nanocarbons is mainly spherical, further confirmed with TEM (Figure S1). As temperature is increased to 500ºC, cylindrical nanocarbon structures that appear to be carbon filaments are obtained with lengths in the range of 2 – 3μm. A close examination of Figure 7-1d reveals the encapsulation of catalyst in the hollow interior of the filament. Further increase in the fluid phase temperature to 600ºC, yield dense MWCNTs with Fe particles at the tip of the nanotube. The omnipresent disorder-induced mode (D-band) at ~1345 cm^{-1} and tangential stretch mode (G-band) at ~1593 cm^{-1} associated with graphitic materials are present in the Raman spectra of all the samples. The degree of graphitization increases with increasing temperature, evidenced by D- and G-bands that are well defined and the decreasing full-width at half-maximum (FWHM) of the G-band.

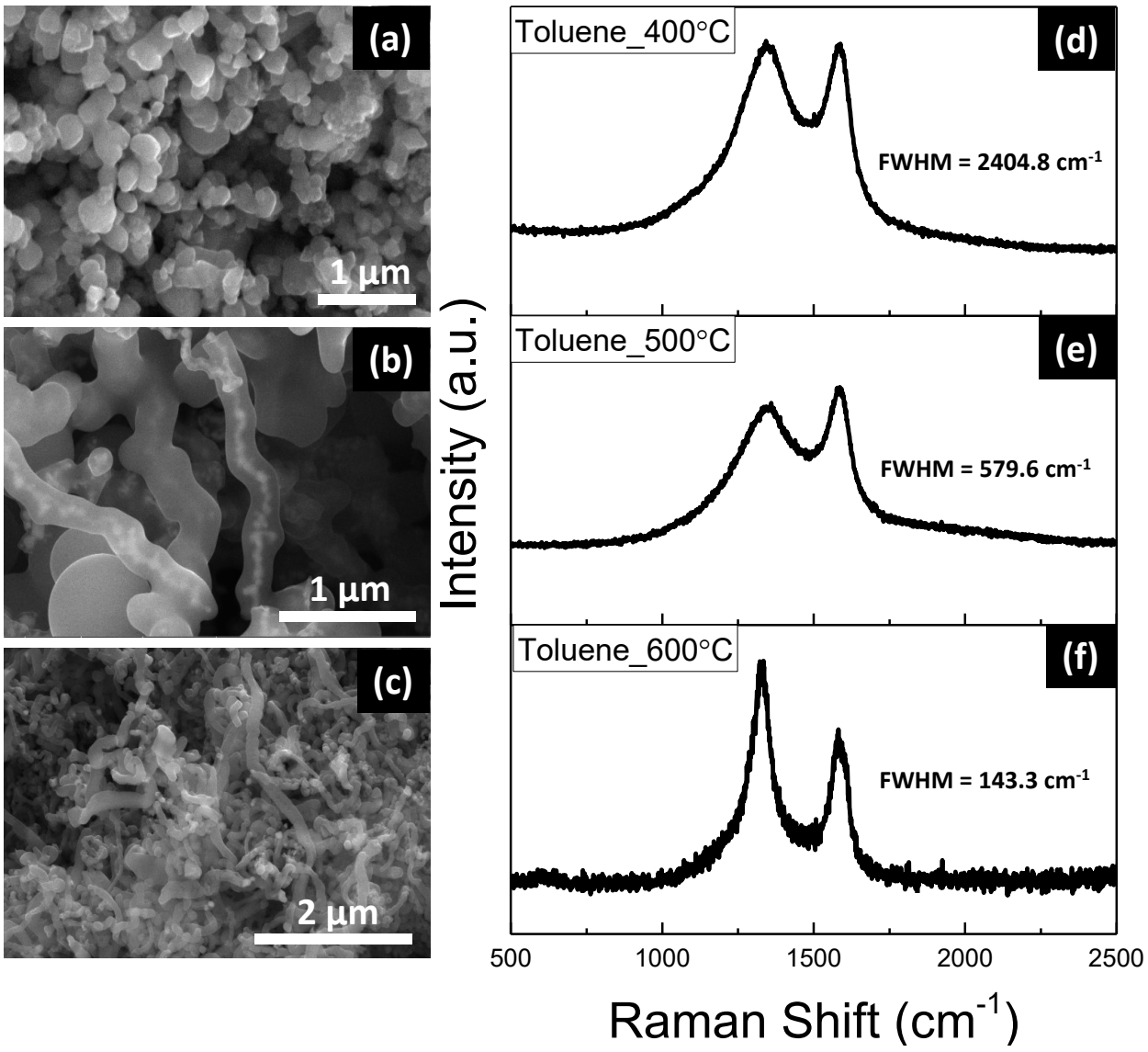

Figure 7-1 SEM images and Raman spectra of carbon nanomaterials synthesized in supercritical toluene in the absence of water using ferrocene as catalyst at 400ºC (a,b), 500ºC (c,d), and 600ºC (e,f).

Figure 7-2 shows the energy dispersive X-ray analysis (SEM/EDS), the iron occupied the entire inner surface of the carbon tubular structure. EDS analysis of the nanocarbon sample grown at 500ºC confirmed that the exterior wall consist of mainly carbon while the hollow interior is completely occupied by Fe, forming structures that appear to be nanowires. The average diameter of the carbon filaments is quite large (~350 nm), which we attribute to the encapsulation of Fe and eventual formation

of Fe nanowires. A similar phenomenon was observed by Weissker et al.[35] whereby the encapsulation Fe in CNT resulted in the enlargement in tube diameter size.

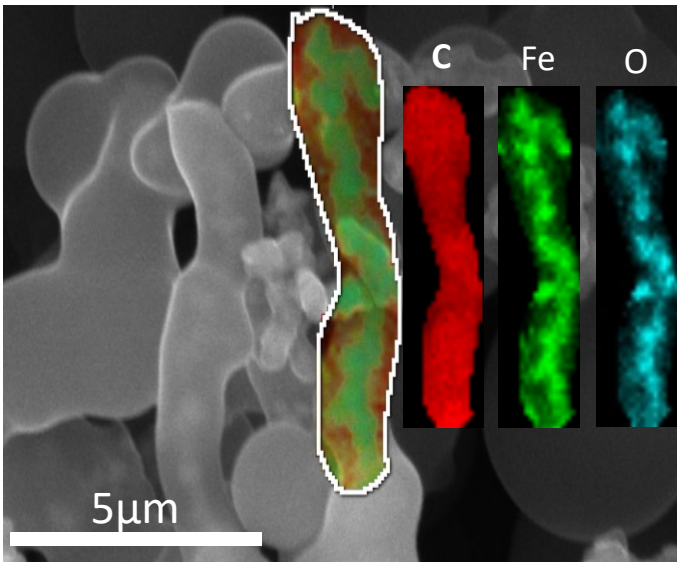

Figure 7-2 SEM image and EDS analysis of carbon nanofilament with encapsulated Fe nanowire obtained by heating 0.035 mole/liter of ferrocene in toluene solution at 500ºC.

Encapsulation of foreign nanomaterial in the hollow interior of CNTs is an attractive approach for tuning their electronic and mechanical properties.[22, 36-37] The mechanism used to explain growth of CNTs and carbon filaments from supported catalyst usually involve a tip-growth or base-growth mode depending on the strength of the catalyst-substrate interactions. The complete filling of Fe catalyst in the hollow interior of the filament at 500°C appear inconsistent with the conventional mechanism for CNT and filament growth as neither of the growth modes are applicable. However, a folded growth model which assumes that the carbon layer formed wraps around nanoparticles[38] appear to be more representative of the observed wrapping of Fe nanowire by the graphitic layer.

Increasing the growth temperature to 600ºC yielded CNTs or filaments with catalyst nanoparticles embedded at the tip as shown in the low- and high-magnification TEM images in Figures 7-3a and b. The high-resolution TEM image (Figure 7-3c) shows the tip of the filament with several graphitic layers encapsulating a large catalyst particle (20 nm).

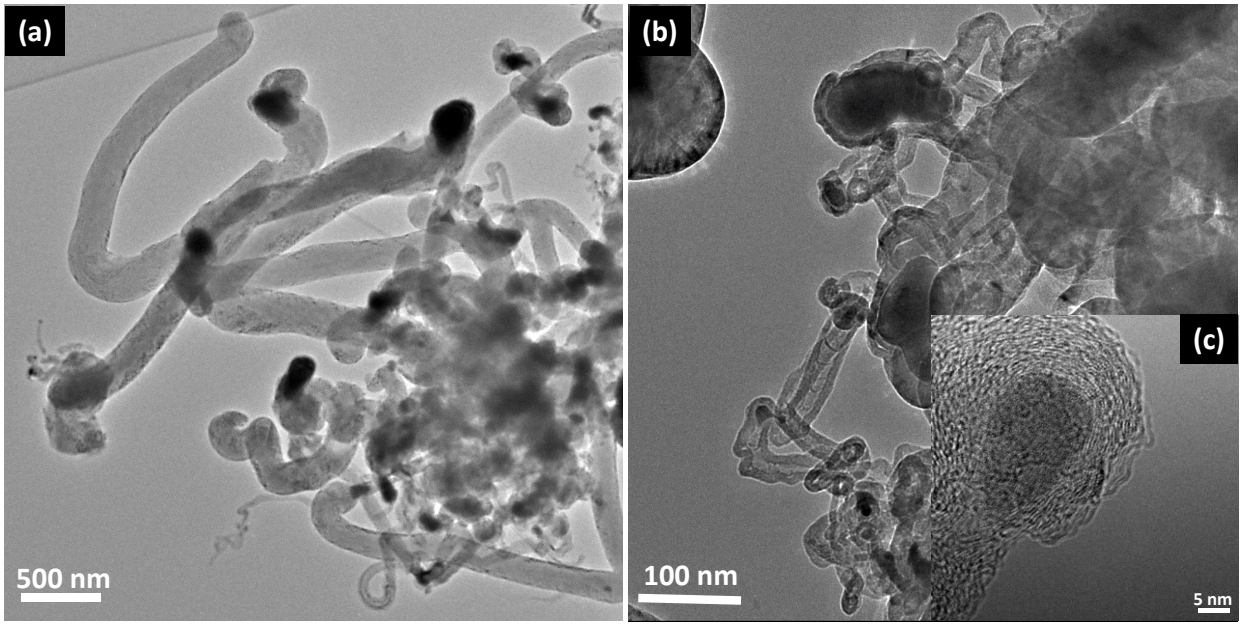

Figure 7-3 TEM images of CNTs and filaments prepared using 0.2 g of ferrocene and 30 ml of toluene, (a) filament with bigger catalyst particle at the end of the tube, (b) CNT with defined hallow interior, and (c) particles embedded at the tip of nanotube.

The main difference between nanotube and filament (fiber) consists in the lack of an hollow cavity for the latter.[9] We distinguished that nanoparticles with size bigger than 50 nm supports the formation of filament, while smaller particles (>40 nm) favor the nanotube structure, same observation reported elsewhere.[27, 37]

The growth of CNTs using supercritical toluene in a batch reactor unavoidably nucleates metal nanoparticles on their external surfaces, SEM and TEM presented in Figure S2 shows highly monodispersed Fe nanoparticles are decorated on the exterior surface of the CNTs. Defects in CNT structures can provide suitable sites for nanoparticle nucleation.[21].

Having determined the impact of temperature on the selectivity of carbon nanomaterials, our next step focused on investigating the effect of the amount of ferrocene on the growth behavior. Increasing the concentration of ferrocene is expected to increase the size of particles formed as well as the diameter of the resulting CNTs. Singh et al. showed a direct correlation between concentration of ferrocene and diameter of grown CNTs,.[40] For SCFA growth process, catalyst synthesis and carbon

precursor decomposition occur during the growth process,[41] and precursors require sufficient amount of catalyst to obtain a high yield of carbon materials. Therefore, increasing the amount of ferrocene is expected to increase the reaction rate However, we found that increasing the pressure of the batch reactor increased with the amount of ferrocene (Figure 7-4 a), suggesting that the dissociation rate of the precursor increased and more free radicals were generated. For all the ferrocene ratios, the final products were mainly a dry black powder, except for 0.01 gm after 1.5 h whereby the final products was a thick dark solution (Figure S3) probably due to insufficient ferrocene to dissociate the high volume of toluene used.

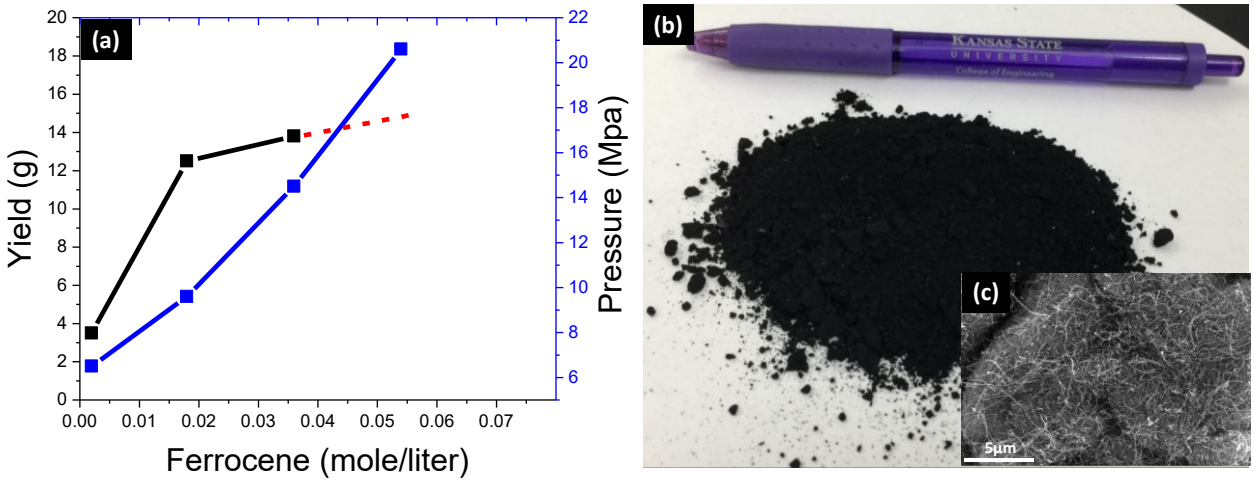

Figure 7-4 (a) Plots of product yield and pressure of batch reactor as functions of ferrocene concentration using 30 ml of toluene at 600°C; (b) picture of bulk quantity ~12.5 g filament and CNTs powder obtained at 0.036 mole/liter ferrocene in toluene solution; (c) Inset low-magnification SEM image of filament and CNTs.

7.4.2 Supercritical toluene in the presence of water. To understand the effect of water on the diameter distribution and yield of CNTs, growth with supercritical toluene was conducted in the presence of different amounts of water (0.025, 0.05, and 0.075 ml); the Raman spectra, SEM images, and corresponding diameter distributions of the resulting CNTs are summarized in Figure 7-5. The products obtained are predominantly CNTs. The highest mass yield of product from 12.5 g (without water) to 18.7g was obtained for growth run with 0.05 ml of water, and thus assumed as the optimum amount of water. The highest I_G/I_D ratio (1.32) and the lowest FWHM (54.4 cm^{-1}) are observed for

CNTs synthesis with 0.05 ml of water, suggesting that this 0.05 ml of water yielded well graphitized CNTs with the fewest defects. Furthermore, a significant decrease the diameter of CNTs was observed in the presence of water, which we attribute to the inhibition of Ostwald ripening analogous to the role of water in super growth.[42] Since the size of catalyst particles determines the diameter of the MWCNT, the smaller particles formed in the presence of water supports growth of smaller-diameter CNTs.[43]

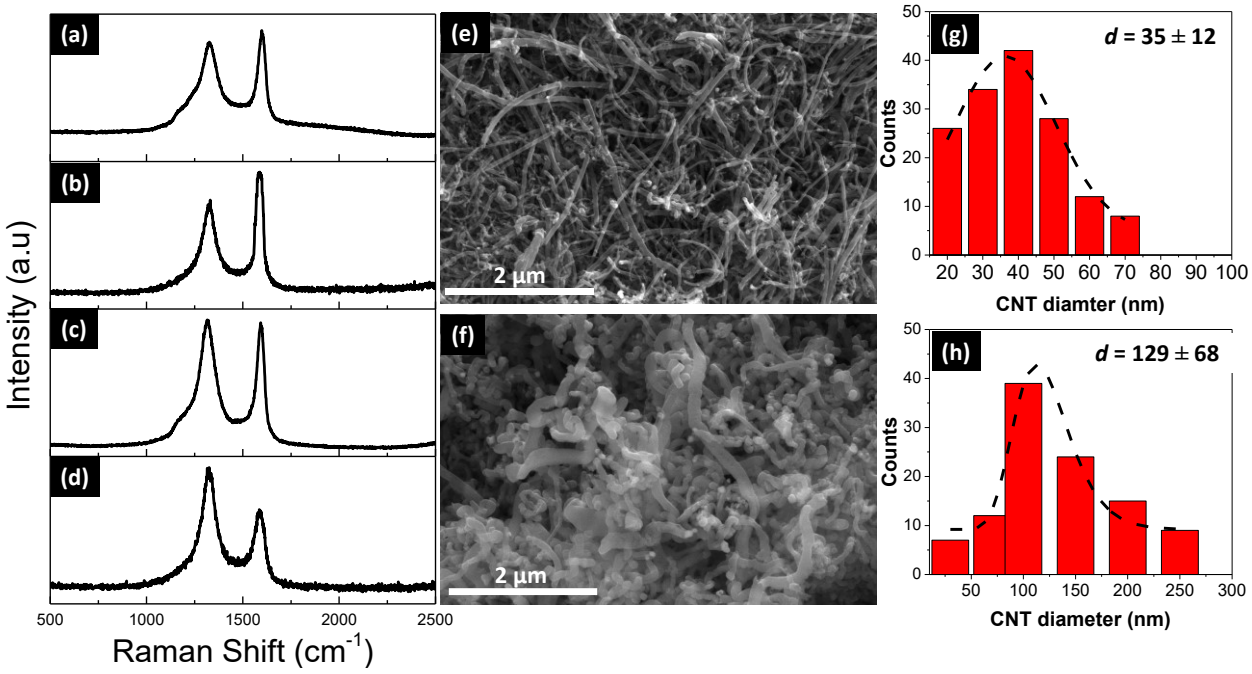

Figure 7-5 Raman spectra of CNTs with different amount of water: 0.075 ml (a), 0.050 ml (b), 0.025 ml (c), and no water (d), under excitation of 633 nm laser. SEM images and corresponding histograms of diameter size distributions with Gaussian analysis fittings of CNTs: 0.05 ml of water (e) and no water (f).

By increasing the amount of water to 0.1 ml under the same operating conditions changes the morphology/structure of the obtained products. A high yield of spherical carbonaceous structure is observed. Figure 7-6 shows SEM (a, b) and TEM (c,d) images which consist of an assembly of concentric spherical graphitic cage, 0.34 nm is the distance between adjacent graphene layers (e).

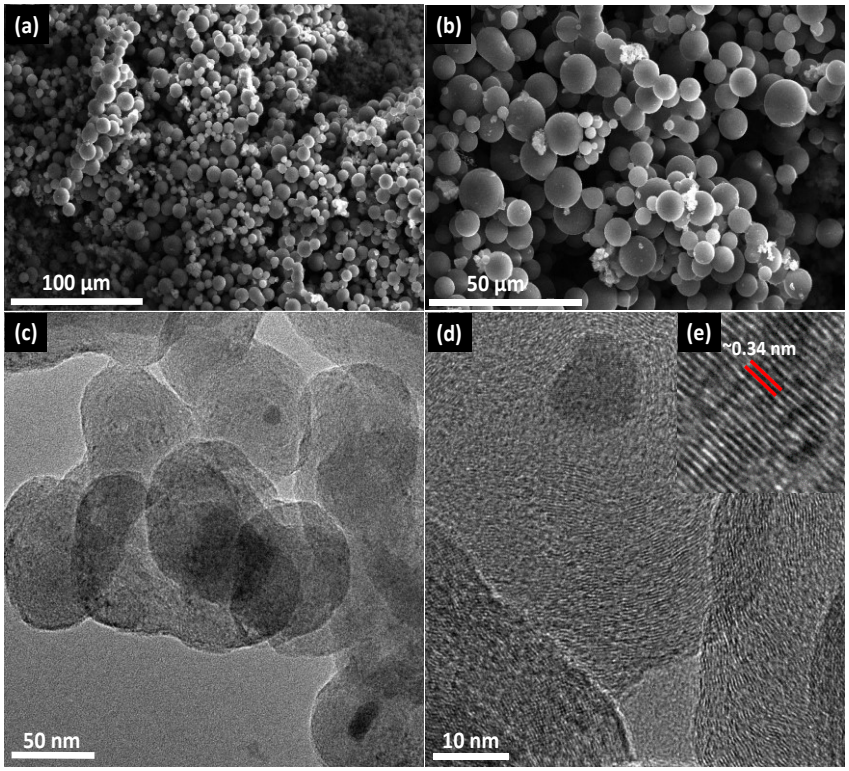

Figure 7-6 SEM (a,b) and TEM (c,d) images of carbon-like onion (OLC) structure synthesized by using 0.035 mole/liter ferrocene in toluene solutions with 0.1 ml of water at 600ºC. Inset TEM image of OLC (e) exhibit concentrically stacked graphite sheets.

During CVD growth of CNTs, the introduction of miniscule amount of water vapor in the widely known "supergrowth" is an effective way of extending the catalyst lifetime by etching carbon precipitate on the catalyst particles surface.[44-46] On the other hand, since water is a weak oxidant, it can change the oxidation state of catalyst particles. Under supercritical condition, water acts as a supercritical oxidant that is able to eliminate excess amount of organic compounds and maintain the activity of the catalyst.[47] Therefore, the addition of optimum amount of water can effectively improve the initial growth rate and extend the catalyst lifetime, and as subsequence result in a higher yield of CNTs.[48]

The thermal Decomposing of toluene along with ferrocene (to form Fe particles)[25] will introduce carbon atoms bounded in infinite hexagonal sheets, which mainly form concentric tubular atomic planes (CNT) if the provided energy exceeds their internal energy.[49] In order for the carbon

hexagonal sheet to grow in a helical orientation, sufficient energy is required, otherwise the formation of curved or closed sheets is favored to eliminate the highly energetic dangling bonds at the edge of growing sheets.[50]

To explain the synthesis of OLC using SCFA with toluene at either low growth temperature (400ºC) or in the presence of excess amount of water at 600 ºC, we hypothesize that OLC forms only when the energy available is insufficient or the available energy has been consumed by excess water. Therefore, the graphitic sheets tend to minimize their energy by curling into onion-like carbon structures as shown in Figure 7-7. We test this hypothesis by using a variety of alcohols (ethanol, propanol and butanol) as carbon precursors under the same reactor conditions. Pyrolysis of alcohol is well known to generate excessive amount of water (Equation 1). To grow CNTs, a reductant such as potassium, magnesium or any earth alkali is typically used as shown in eq. 2:[26-27]

$CH_3CH_2OH \rightarrow 2C+3H_2O$ ---------- (1)

$CH_3CH_2OH + Mg \rightarrow 2C + MgO + 3H_2$ ---------- (2)

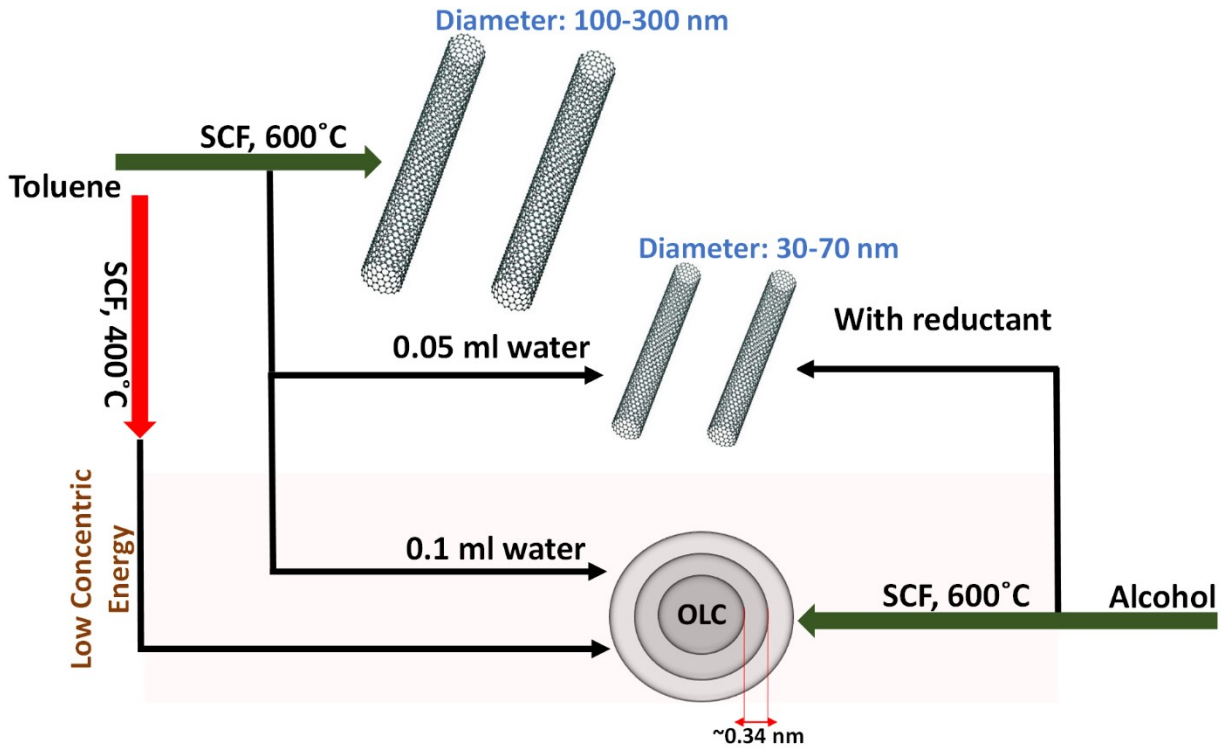

Figure 7-7 Illustration of the synthesis pathways for CNTs and OLC using aromatic and alcohols precursors in a batch reactor.

The use of alcohol precursors also yields the same spherical structures with different size ranges. Figure 7-8 shows detailed SEM images of the structures grown using different alcohol precursors. However, by using toluene (with 0.1 ml of water), the yield was higher than that obtained using other alcohol precursors by a factor of three. The ability of alcohol to selectively grow tubular structures without a reductant (earth alkali) increase in the following order: $C_2H_5OH < C_3H_7OH < C_4H_9OH$; this suggests that as the ratio of generated water and carbon atoms (C: H_2O) in alcohol precursor increases the chances to grow a tubular structures is increased.

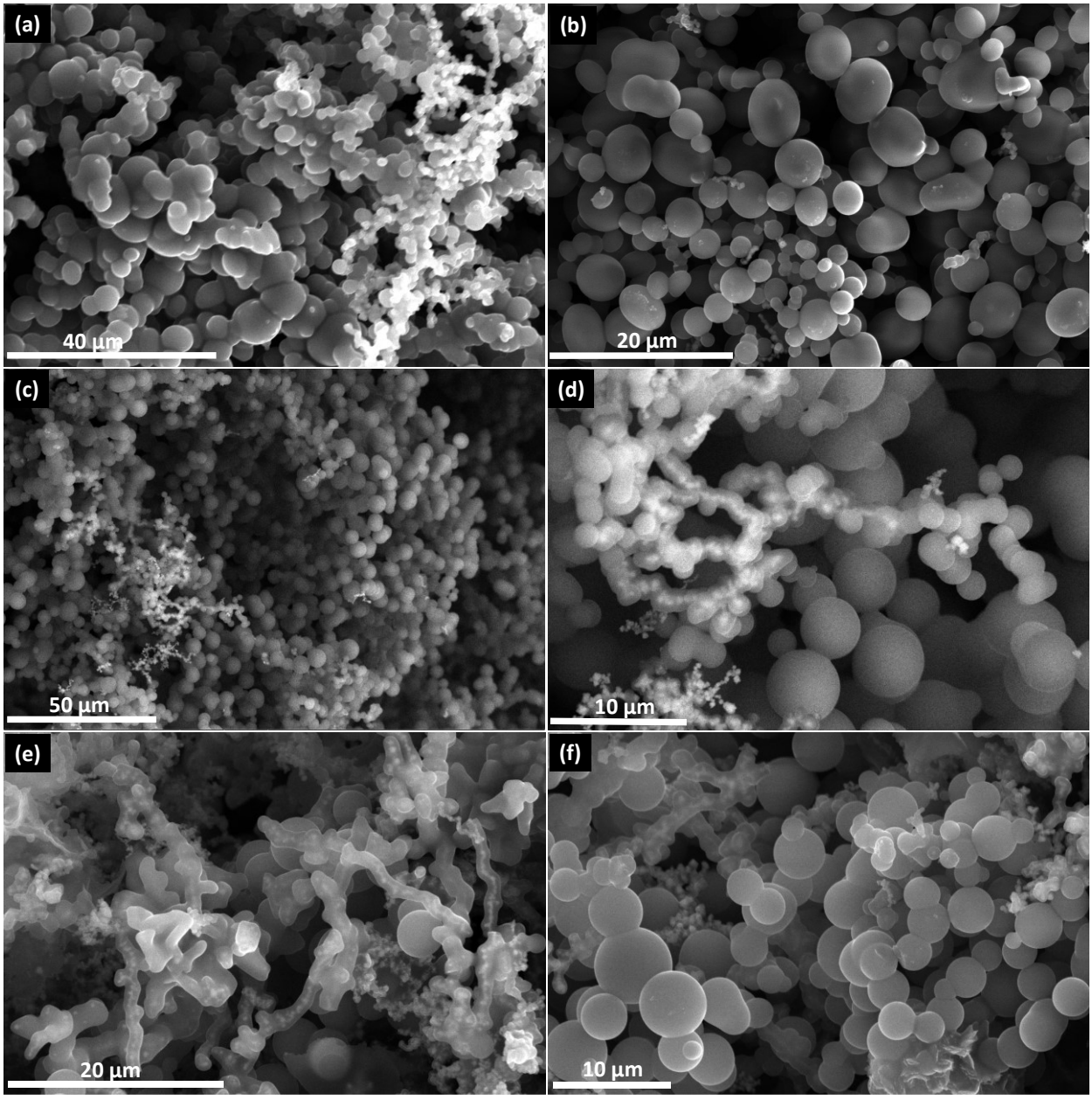

Figure 7-8 SEM images of OLCs grown at 600ºC and 0.035 mole/liter of ferrocene with: ethanol (a,b), propanol (c,d), and butanol (e,f).

Esarte et.al,[51] has reported the effect of different alcohol (methanol, ethanol, isopropanol, and butanol) mixed with acetylene on the soot formation in pyrolysis process. The summary that he draws from this study is that the longer the aliphatic chain of the alcohol, the higher the carbon soot yield

found in the pyrolysis process of corresponding acetylene-alcohol mixtures. Our results are consistent with this observation in terms of cylindrical tube formation.

7.5 Conclusions

A high yield of CNTs, filaments, and carbon with an onion-like structures (OLC) reaching 18.7 g per run was achieved in a one-step process using a supercritical fluid approach in a batch reactor. A systematic variation of the influential growth parameters for toluene supercritical fluid was investigated along with their effects on the growth properties. High yield of CNTs with smaller diameters were obtained using toluene/ferrocene solution at 600ºC with 0.05 ml of water. However, by increasing the amount of water to 0.1 ml, the product was composed mainly of spherical carbon structures (OLC). Lowering the growth temperature to 400ºC also favors the formation of spherical carbon structure. Our hypothesis assumed that excess amount of water will reduce the amount of energy required to form concentric plane (in the case of CNTs), will rather form a curling structures. This hypothesis has been tested using alcohol precursors (known to produce water) without using earth alkali promoters (typically used as water reducer), the same observation was noted. Growth of CNTs and filament in a batch reactor using supercritical fluid approach is a promising, one-step process for synthesizing CNT-metallic nanocomposites. Under 600ºC and 0.035 mole/liter ferrocene in toluene solutions CNTs were decorated with Fe nanoparticles while under 500ºC and 0.035 mole/liter ferrocene in toluene solutions Fe nanowires were encapsulated in carbon filaments. These nanoparticle-CNT (or carbon filament) composites can find applications in heterogeneous catalysis and energy storage.

References

1. Iijima, S., Helical microtubules of graphitic carbon. *Nature* **1991,** *354* (6348), 56-58.

2. Shanmugharaj, A. M.; Bae, J. H.; Lee, K. Y.; Noh, W. H.; Lee, S. H.; Ryu, S. H., Physical and chemical characteristics of multiwalled carbon nanotubes functionalized with aminosilane and its influence on the properties of natural rubber composites. *Composites Science and Technology* **2007,** *67* (9), 1813-1822.

3. Iijima, S., Carbon nanotubes: past, present, and future. *Physica B: Condensed Matter* **2002,** *323* (1), 1-5.

4. Kuan, H.-C.; Ma, C.-C. M.; Chang, W.-P.; Yuen, S.-M.; Wu, H.-H.; Lee, T.-M., Synthesis, thermal, mechanical and rheological properties of multiwall carbon nanotube/waterborne polyurethane nanocomposite. *Composites Science and Technology* **2005,** *65* (11), 1703-1710.

5. Kroto, H. W.; Heath, J. R.; O'Brien, S. C.; Curl, R. F.; Smalley, R. E., C60: Buckminsterfullerene. *Nature* **1985,** *318* (6042), 162-163.

6. Lange, H.; Sioda, M.; Huczko, A.; Zhu, Y. Q.; Kroto, H. W.; Walton, D. R. M., Nanocarbon production by arc discharge in water. *Carbon* **2003,** *41* (8), 1617-1623.

7. Scott, C. D.; Arepalli, S.; Nikolaev, P.; Smalley, R. E., Growth mechanisms for single-wall carbon nanotubes in a laser-ablation process. *Applied Physics A* **2001,** *72* (5), 573-580.

8. Li, Y.-L.; Kinloch, I. A.; Windle, A. H., Direct Spinning of Carbon Nanotube Fibers from Chemical Vapor Deposition Synthesis. *Science* **2004,** *304* (5668), 276-278.

9. Serp, P.; Corrias, M.; Kalck, P., Carbon nanotubes and nanofibers in catalysis. *Applied Catalysis A: General* **2003,** *253* (2), 337-358.

10. Kumar, M.; Ando, Y., Chemical Vapor Deposition of Carbon Nanotubes: A Review on Growth Mechanism and Mass Production. *Journal of Nanoscience and Nanotechnology* **2010,** *10* (6), 3739-3758.

11. Zhang, Q.; Huang, J.-Q.; Qian, W.-Z.; Zhang, Y.-Y.; Wei, F., The Road for Nanomaterials Industry: A Review of Carbon Nanotube Production, Post-Treatment, and Bulk Applications for Composites and Energy Storage. *Small* **2013,** *9* (8), 1237-1265.

12. De Volder, M. F. L.; Tawfick, S. H.; Baughman, R. H.; Hart, A. J., Carbon Nanotubes: Present and Future Commercial Applications. *Science* **2013,** *339* (6119), 535-539.

13. Li, G. Y.; Wang, P. M.; Zhao, X., Pressure-sensitive properties and microstructure of carbon nanotube reinforced cement composites. *Cement and Concrete Composites* **2007,** *29* (5), 377-382.

14. Abu Al-Rub, R. K.; Ashour, A. I.; Tyson, B. M., On the aspect ratio effect of multi-walled carbon nanotube reinforcements on the mechanical properties of cementitious nanocomposites. *Construction and Building Materials* **2012,** *35*, 647-655.

15. Han, Z.; Fina, A., Thermal conductivity of carbon nanotubes and their polymer nanocomposites: A review. *Progress in Polymer Science* **2011,** *36* (7), 914-944.

16. Bauhofer, W.; Kovacs, J. Z., A review and analysis of electrical percolation in carbon nanotube polymer composites. *Composites Science and Technology* **2009,** *69* (10), 1486-1498.

17. Chou, T.-W.; Gao, L.; Thostenson, E. T.; Zhang, Z.; Byun, J.-H., An assessment of the science and technology of carbon nanotube-based fibers and composites. *Composites Science and Technology* **2010,** *70* (1), 1-19.

18. Wang, X.; Li, W.; Chen, Z.; Waje, M.; Yan, Y., Durability investigation of carbon nanotube as catalyst support for proton exchange membrane fuel cell. *Journal of Power Sources* **2006,** *158* (1), 154-159.

19. Bell, A. T., The Impact of Nanoscience on Heterogeneous Catalysis. *Science* **2003,** *299* (5613), 1688-1691.

20. Yoon, B.; Wai, C. M., Microemulsion-Templated Synthesis of Carbon Nanotube-Supported Pd and Rh Nanoparticles for Catalytic Applications. *Journal of the American Chemical Society* **2005,** *127* (49), 17174-17175.

21. Liu, F.; Wagterveld, R. M.; Gebben, B.; Otto, M. J.; Biesheuvel, P. M.; Hamelers, H. V. M., Carbon nanotube yarns as strong flexible conductive capacitive electrodes. *Colloid and Interface Science Communications* **2014,** *3*, 9-12.

22. Lu, X.; Hanrath, T.; Johnston, K. P.; Korgel, B. A., Growth of Single Crystal Silicon Nanowires in Supercritical Solution from Tethered Gold Particles on a Silicon Substrate. *Nano Letters* **2003,** *3* (1), 93-99.

23. Ye, X. R.; Lin, Y.; Wang, C.; Wai, C. M., Supercritical Fluid Fabrication of Metal Nanowires and Nanorods Templated by Multiwalled Carbon Nanotubes. *Advanced Materials* **2003,** *15* (4), 316-319.

24. Reverchon, E.; Adami, R., Nanomaterials and supercritical fluids. *The Journal of Supercritical Fluids* **2006,** *37* (1), 1-22.

25. Li, Z.; Andzane, J.; Erts, D.; Tobin, J. M.; Wang, K.; Morris, M. A.; Attard, G.; Holmes, J. D., A Supercritical-Fluid Method for Growing Carbon Nanotubes. *Advanced Materials* **2007,** *19* (19), 3043-3046.

26. Bronikowski, M. J.; Willis, P. A.; Colbert, D. T.; Smith, K. A.; Smalley, R. E., Gas-phase production of carbon single-walled nanotubes from carbon monoxide via the HiPco process: A parametric study. *Journal of Vacuum Science & Technology A: Vacuum, Surfaces, and Films* **2001,** *19* (4), 1800-1805.

27. Lee, D. C.; Mikulec, F. V.; Korgel, B. A., Carbon Nanotube Synthesis in Supercritical Toluene. *Journal of the American Chemical Society* **2004,** *126* (15), 4951-4957.

28. Wei, L.; Yi, X.; Kun, Z.; Fei, Z., The large-scale synthesis and characterization of carbon nanotubes filled with long continuous inorganic nanowires in supercritical CS 2. *Nanotechnology* **2006,** *17* (22), 5702.

29. Liu, J.; Shao, M.; Chen, X.; Yu, W.; Liu, X.; Qian, Y., Large-Scale Synthesis of Carbon Nanotubes by an Ethanol Thermal Reduction Process. *Journal of the American Chemical Society* **2003,** *125* (27), 8088-8089.

30. Liu, J.; Xu, L.; Zhang, W.; Lin, W. J.; Chen, X.; Wang, Z.; Qian, Y., Formation of Carbon Nanotubes and Cubic and Spherical Nanocages. *The Journal of Physical Chemistry B* **2004,** *108* (52), 20090-20094.

31. Weissker, U.; Hampel, S.; Leonhardt, A.; Büchner, B., Carbon nanotubes filled with ferromagnetic materials. *Materials* **2010,** *3* (8), 4387-4427.

32. Sinnott, S. B.; Andrews, R.; Qian, D.; Rao, A. M.; Mao, Z.; Dickey, E. C.; Derbyshire, F., Model of carbon nanotube growth through chemical vapor deposition. *Chemical Physics Letters* **1999,** *315* (1), 25-30.

33. Brukh, R.; Mitra, S., Mechanism of carbon nanotube growth by CVD. *Chemical Physics Letters* **2006,** *424* (1), 126-132.

34. Dai, H.; Rinzler, A. G.; Nikolaev, P.; Thess, A.; Colbert, D. T.; Smalley, R. E., Single-wall nanotubes produced by metal-catalyzed disproportionation of carbon monoxide. *Chemical Physics Letters* **1996,** *260* (3), 471-475.

35. Bistamam, M. S. A.; Azam, M. A., Tip-growth of aligned carbon nanotubes on cobalt catalyst supported by alumina using alcohol catalytic chemical vapor deposition. *Results in Physics* **2014,** *4*, 105-106.

36. Louchev, O. A.; Laude, T.; Sato, Y.; Kanda, H., Diffusion-controlled kinetics of carbon nanotube forest growth by chemical vapor deposition. *The Journal of Chemical Physics* **2003,** *118* (16), 7622-7634.

37. Xie, W.; Fang, W.; Li, D.; Xing, Y.; Guo, Y.; Lin, R., Coking of model hydrocarbon fuels under supercritical condition. *Energy & Fuels* **2009,** *23* (6), 2997-3001.

38. Janas, D.; Koziol, K. K., Carbon nanotube fibers and films: synthesis, applications and perspectives of the direct-spinning method. *Nanoscale* **2016,** *8* (47), 19475-19490.

39. Ganguli, S.; Reed, A.; Jayasinghe, C.; Sprengard, J.; Roy, A. K.; Voevodin, A. A.; Muratore, C., A simultaneous increase in the thermal and electrical transport in carbon nanotube yarns induced by inter-tube metallic welding. *Carbon* **2013,** *59*, 479-486.

40. Singh, C.; Shaffer, M. S. P.; Windle, A. H., Production of controlled architectures of aligned carbon nanotubes by an injection chemical vapour deposition method. *Carbon* **2003,** *41* (2), 359-368.

41. Dervishi, E.; Biris, A. R.; Watanabe, F.; Umwungeri, J. L.; Mustafa, T.; Driver, J. A.; Biris, A. S., Few-layer nano-graphene structures with large surface areas synthesized on a multifunctional Fe:Mo:MgO catalyst system. *Journal of Materials Science* **2012,** *47* (4), 1910-1919.

42. Brukh, R.; Salem, T.; Slanvetpan, T.; Barat, R.; Mitra, S., Process modeling and on-line monitoring of benzene and other species during the two-stage combustion of ethylene in air. *Advances in Environmental Research* **2002,** *6* (3), 359-367.

43. Karwa, M.; Iqbal, Z.; Mitra, S., Scaled-up self-assembly of carbon nanotubes inside long stainless steel tubing. *Carbon* **2006,** *44* (7), 1235-1242.

44. Yoshihara, N.; Ago, H.; Tsuji, M., Chemistry of Water-Assisted Carbon Nanotube Growth over Fe−Mo/MgO Catalyst. *The Journal of Physical Chemistry C* **2007,** *111* (31), 11577-11582.

45. Almkhelfe, H.; Li, X.; Rao, R.; Amama, P. B., Catalytic CVD growth of millimeter-tall single-wall carbon nanotube carpets using industrial gaseous waste as a feedstock. *Carbon* **2017,** *116*, 181-190.

46. Almkhelfe, H.; Carpena-Nunez, J.; Back, T. C.; Amama, P. B., Gaseous product mixture from Fischer-Tropsch synthesis as an efficient carbon feedstock for low temperature CVD growth of carbon nanotube carpets. *Nanoscale* **2016,** *8* (27), 13476-13487.

47. Xie, K.; Muhler, M.; Xia, W., Influence of Water on the Initial Growth Rate of Carbon Nanotubes from Ethylene over a Cobalt-Based Catalyst. *Industrial & Engineering Chemistry Research* **2013,** *52* (39), 14081-14088.

48. Li, Y.; Zhou, W.; Wang, H.; Xie, L.; Liang, Y.; Wei, F.; Idrobo, J.-C.; Pennycook, S. J.; Dai, H., An oxygen reduction electrocatalyst based on carbon nanotube-graphene complexes. *Nat Nano* **2012,** *7* (6), 394-400.

49. Schünemann, C.; Schäffel, F.; Bachmatiuk, A.; Queitsch, U.; Sparing, M.; Rellinghaus, B.; Lafdi, K.; Schultz, L.; Büchner, B.; Rümmeli, M. H., Catalyst poisoning by amorphous carbon during carbon nanotube growth: fact or fiction? *ACS nano* **2011,** *5* (11), 8928-8934.

50. Amama, P. B.; Pint, C. L.; McJilton, L.; Kim, S. M.; Stach, E. A.; Murray, P. T.; Hauge, R. H.; Maruyama, B., Role of Water in Super Growth of Single-Walled Carbon Nanotube Carpets. *Nano Letters* **2009,** *9* (1), 44-49.

51. Algadri, N. A.; Hassan, Z.; Ibrahim, K.; Bououdina, M., Effect of ferrocene catalyst particle size on structural and morphological characteristics of carbon nanotubes grown by microwave oven. *Journal of Materials Science* **2017,** *52* (21), 12772-12782.

52. Robertson, D. H.; Brenner, D. W.; White, C. T., On the way to fullerenes: molecular dynamics study of the curling and closure of graphitic ribbons. *The Journal of Physical Chemistry* **1992,** *96* (15), 6133-6135.

53. Ugarte, D., Curling and closure of graphitic networks under electron-beam irradiation. *Nature* **1992,** *359* (6397), 707-709.

54. Jonathan, C.; John, K. M.; Filipe, P.; Rene, M.; Ioannis, N.; Yury, G.; Sebastian, O., Raman spectroscopy study of the nanodiamond-to-carbon onion transformation. *Nanotechnology* **2013,** *24* (20), 205703.

55. Kuznetsov, V. L.; Chuvilin, A. L.; Moroz, E. M.; Kolomiichuk, V. N.; Shaikhutdinov, S. K.; Butenko, Y. V.; Mal'kov, I. Y., Effect of explosion conditions on the structure of detonation soots: Ultradisperse diamond and onion carbon. *Carbon* **1994,** *32* (5), 873-882.

56. Alexandrou, I.; Wang, H.; Sano, N.; Amaratunga, G. A. J., Structure of carbon onions and nanotubes formed by arc in liquids. *The Journal of Chemical Physics* **2004,** *120* (2), 1055-1058.

57. Fan, J.-C.; Sung, H.-H.; Lin, C.-R.; Lai, M.-H., The production of onion-like carbon nanoparticles by heating carbon in a liquid alcohol. *Journal of Materials Chemistry* **2012,** *22* (19), 9794-9797.

58. Yang, Y.; Liu, X.; Guo, X.; Wen, H.; Xu, B., Synthesis of nano onion-like fullerenes by chemical vapor deposition using an iron catalyst supported on sodium chloride. *Journal of Nanoparticle Research* **2011,** *13* (5), 1979-1986.

59. Esarte, C.; Abián, M.; Millera, Á.; Bilbao, R.; Alzueta, M. U., Gas and soot products formed in the pyrolysis of acetylene mixed with methanol, ethanol, isopropanol or n-butanol. *Energy* **2012,** *43* (1), 37-46.

Chapter 8

Conclusions and Future Work

8.1 Conclusions

Modified photo-Fenton process offers a green environment to oxidize and decorate the surface of CNTs in a single step. Fe/Co particles supported on CNTs were in the range of ~ 2-5 nm. Following photo-Fenton process, the CNT structure is preserved. Further, there is no calcination treatment required due to the absence of foreign components like nitrate, acetate and chloride. The process is facile, highly scalable, and involves the use of green catalyst precursors and an oxidant. Photo-Fenton catalysts for FTS reaction show high stability and high CO conversion (~80% for Co/CNT and 65% for Fe/CNT) under the same reaction conditions. In comparison to conventional catalysts, photo-Fenton catalysts also show higher selectivity to the liquid hydrocarbons (C5+) at lower reaction temperature. Unlike SiO_2, the use of CNTs (a highly conductive support) in photo-Fenton process ensures that a highly uniform temperature is maintained across the catalyst bed during the highly exothermic FTS reaction. We partly attribute the high CO conversion and C5+ selectivity especially at low temperatures to the absence of significant gradient in temperature.

Growth of CNT carpets via CVD from Fe- and Co-based catalysts at low and high temperatures using a gaseous product mixture from Fischer-Tropsch synthesis (FTS-GP) as a superior carbon feedstock is demonstrated. The efficiency of the process is evidenced by the highly dense, vertically aligned CNT structures from both Fe and Fe-Cu catalysts even at temperatures as low as 400°C – a record low growth temperature for CNT carpets obtained via conventional thermal CVD. The synergistic effect of Fe and Cu show a strong temperature dependence, with Cu being more influential at temperatures greater than 450°C. The apparent activation energies for CNT carpets grown on Fe and Fe-Cu catalysts are 0.71 and 0.54 eV, respectively. The low activation energies, long catalyst lifetimes,

and the growth of CNT carpets at 400°C, where the influence of Cu is low, are attributed to the unique composition of FTS-GP. Our growth results also reveal that FTS-GP is not only an efficient carbon feedstock but also a versatile feedstock that support CNT carpet growth on aluminum foil.

At higher temperatures, well-aligned SWCNT carpets of millimeter-scale heights on Fe and (sub) millimeter-scale heights on Co catalysts were obtained. Growth on Fe is characterized by a growth rate of ~50 μm/min and long catalyst lifetime (> 90 min), with the catalyst showing no deactivation, while growth on a Co catalyst shows a lifetime of ~60 min, with a slower growth rate of ~7μm/min. The resulting area densities of SWCNT carpets grown on Fe and Co, determined by the weight-gain method, were 1.0×10^{12} and 6.0×10^{12} cm^{-2}, respectively — among the highest achieved for SWCNT carpets on standard catalysts. Unlike conventional feedstocks that require strict process control, growth rate, area density of SWCNT carpets, and SWCNT quality (I_G/I_D) are generally less sensitive to the FTS-GP fraction in growth gas and thus allow for easy optimization and scale-up. In addition to the growth efficiency, the window for SWCNT carpet growth is wider for an Fe catalyst than a Co catalyst. A comparison of the growth curve of FTS-GP CVD, using an Fe catalyst with other conventional CVD methods for SWCNT carpet growth, reveals a growth behavior superior to existing approaches.

Investigations to elucidate the role of FTS-GP in the growth enhancement in a batch reactor revealed that water is generated during FTS-GP CVD. We hypothesize that the water formed oxidizes excess carbon or amorphous carbon impurities on the catalyst surface. At low partial pressure of CO, which is similar to the amount of CO in FTS-GP (5 vol%), the reaction between CO and H_2 with a negative free energy value of -90 kJ/mole is favored. The theoretical thermodynamic perspective allowed for direct comparison between the experimental and theoretical data. Both analyses show that amount of water formed during FTS-GP decreases with increasing temperature, in agreement with our proposed mechanisms.

The role of Ru (a high-melting point metal) was demonstrated as a catalyst promoter in the growth of SWCNTs on Fe/Ru and Co/Ru catalyst via CVD. FTS-GP was used as a carbon precursor at 750ºC for Fe catalyst and 850ºC for Co. Deposition of 0.1 nm-thick layer of Ru on Fe or Co catalyst was found to impede catalyst sintering at CVD growth temperatures and enhance the quality of the grown SWCNTs as evidenced by the higher ratio of tangential G-band to defect-induced D-band, as well as enable growth of smaller-diameter SWCNTs. The average diameter of SWCNTs produced is decreases from 2.5 nm (using Co catalyst) to 1.5 nm when Ru is used as promoter. While using Ru with Fe catalyst, the diameter of the grown SWCNT decreases from 3.1 to 1.9 nm. Further, the presence of Ru also support growth of SWCNTs with higher ratio of tangential G-band to defect-induced D-band.

A high yield of CNTs, filaments, and carbon-based onion-like structures (OLC) reaching 18.7 g per run was achieved in a one-step process using a supercritical fluid approach in a batch reactor. A systematic variation of precursor type, growth temperature, ferrocene concentration, and water amount was investigated along with their effects on growth properties. High yield of CNTs with smaller diameters were obtained using toluene/ferrocene solution at 600ºC with 0.05 ml of water. However, by increasing the amount of water to 0.1 ml, the product was composed mainly of OLC. Lowering the growth temperature to 400ºC also favors the formation of OLC. Our results show that growth of CNTs and filaments in a batch reactor using supercritical fluid approach is a promising, one step process for synthesizing CNT-metallic nanocomposites.

8.2 Future work

Recommendations for future work are as follows:

1- Control the diameter of SWCNT using other high melting point noble metals (Pt, Cu, and Cr) as catalyst promoters.

2- Synthesize graphene using FTS-GP as a carbon feedstock on conventional/nonconventional substrates.

3- Study the effect of hydrogen sulfide (H_2S) present in FTS-GP on CNT growth behavior.

4- Investigate the role of catalyst supports in CNT growth by testing different catalyst supports (Al_2O_3, SiO_2, ZrO_2, MgO and C). Ion beam sputtering (IBS) will be used for the deposition process.

5- Investigate the role of crystalline structure of the substrate in CNT growth behavior. This can be achieved by either heating the deposited support to convert it from an amorphous structure (as deposited by IBS) to a crystalline structure. Another approach is making zeolite-like structure, by sandwiching SiO_2 between two layers of Al_2O_3. By heating the substrate up to 350˚C in air, the layers start crosslinking to form the proposed structure.

6- Study the influence of supercritical fluid operation conditions on the CNT-supported metals (Fe, Co) for Fischer-Tropsch reactions.

7- Optimize the operating conditions of batch reactor/supercritical medium by controlling the pressure and investigate the possibility of growing aligned CNTs on substrates.

8- Incorporate the synthesized nanomaterial obtained from batch reactor in applications, like heterogeneous catalysis (FTS), energy storage.

Appendix A - Supplemental Information for Chapter 2

Carbon Nanotube-Supported Catalysts Prepared by a Modified Photo-Fenton Process for Fischer-Tropsch Synthesis

Table S1. Quantitative data from XPS analysis for pristine CNTs, H_2O_2-treated CNTs, UV/H_2O_2-treated CNTs and HNO_3-treated CNTs. The different components or functional groups are C=C (sp2 carbon), C–C (sp3 carbon), C-O (alcohol), C=O (carbonyl), and -C-OOH (carboxylic); Cf/sp2 represents the ratio between functionalized carbon species (Cf) and sp2 graphitic carbon.

Samples	C=C (%)	C–C (%)	C–O (%)	C=O (%)	–C–OOH (%)	CO_3^{2-} (%)	cf/sp2
	284.51 eV	285.07 eV	286.37 eV	287.57 eV	288.76 eV	290.97 eV	
Pristine CNTs	68.37	10.45	12.16	0.15	3.45	5.42	0.23
CNTs-H_2O_2	62.89	14.17	12.15	0.34	4.25	6.20	0.27
CNTs-H_2O_2/UV	48.14	18.27	24.08	0.70	5.57	3.26	0.63
CNTs-HNO_3	45.74	14.24	22.89	0.64	11.15	5.34	0.76

Table S2. Comparison of the selectivity of the different Fe-based catalysts at different conversions and corresponding temperatures.

Catalyst	Fe/CNT-IWI					Fe/CNT-Fenton					Fe/SiO_2-IWI				
Conversion	17	38	57	60	63	22	45	68	68	71	5	19	35	53	60
Selectivity (CH_4)	54	51	42	40	47	27.5	22	12.5	21	28	51	49	45	41	42.4
Selectivity (C2-C4)	21.5	14	10	15	13	44	35	21.6	27.2	32	44	39	31.4	22	23
Selectivity (C5+)	18	26	37.5	41	39	24	39	62.9	49	38	3	10	22	36	34
Temperature (°C)	190	220	250	260	270	190	220	250	260	270	190	220	250	260	270

Table S3. Comparison of the selectivity of the different Co-based catalysts at different conversions and corresponding temperatures.

Catalyst	Co/CNT-IWI					Co/CNT-Fenton					Co/SiO_2-IWI			
Conversion	15	43	65	67	69	18	56	80	83	84	30	41	69	86
Selectivity (CH_4)	39	33	30.5	33.5	43	20.5	13	9.4	23.6	31	39	38.4	36	39
Selectivity (C2-C4)	35	27	22	23	25.4	37.7	28	18.4	27	29.7	40	35	28	29
Selectivity (C5+)	23	37	45	41	29	39	58	70.2	48	38	18	24	33	31
Temperature (°C)	170	190	200	220	240	170	190	200	220	240	190	200	220	240

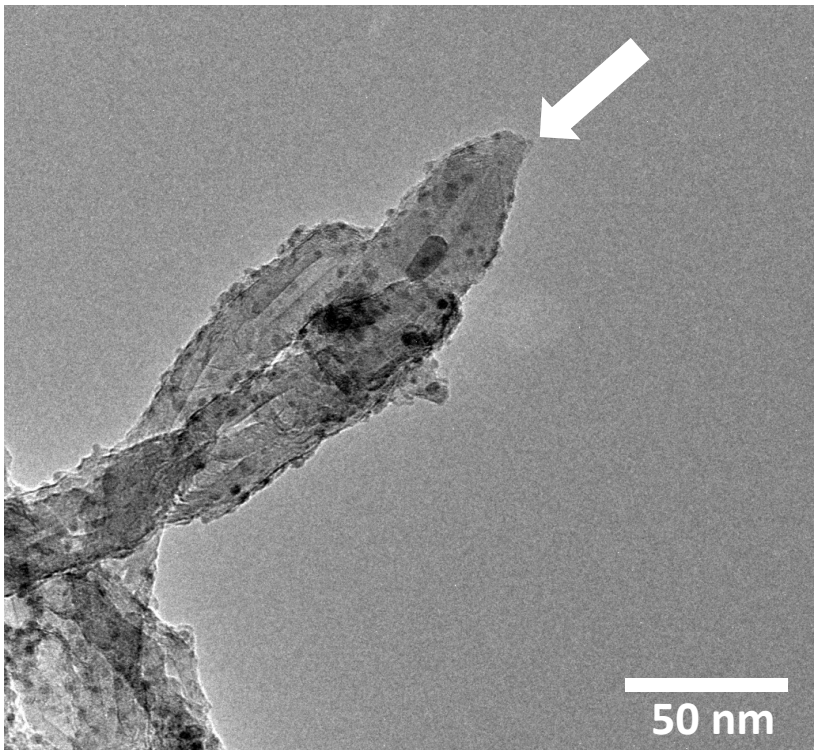

Figure S1. TEM image of CNTs oxidized with UV/H_2O_2. Arrow shows a CNT cap that remains intact.

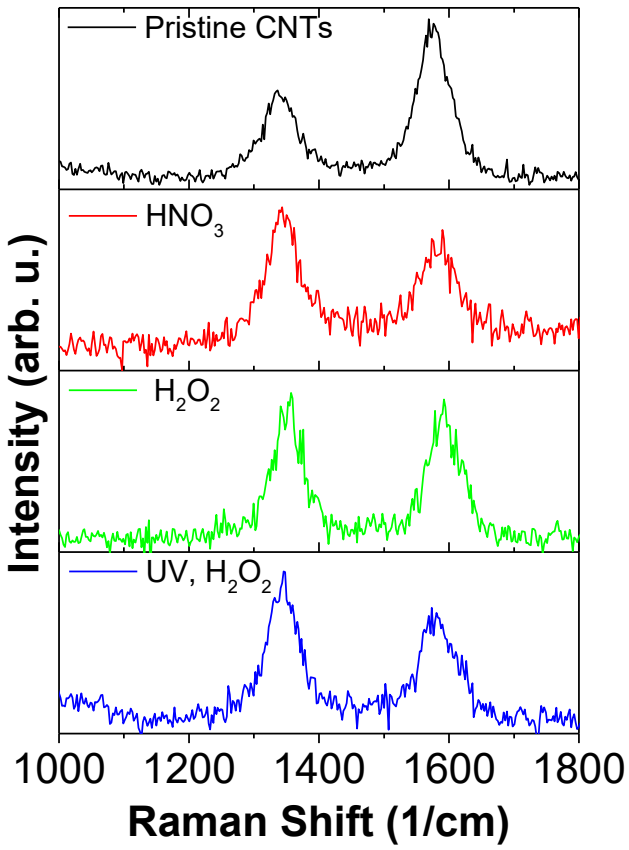

Figure S2. Raman spectra of as-received CNTs and oxidized CNTs from different treatments: HNO_3, H_2O_2, and UV-H_2O_2.

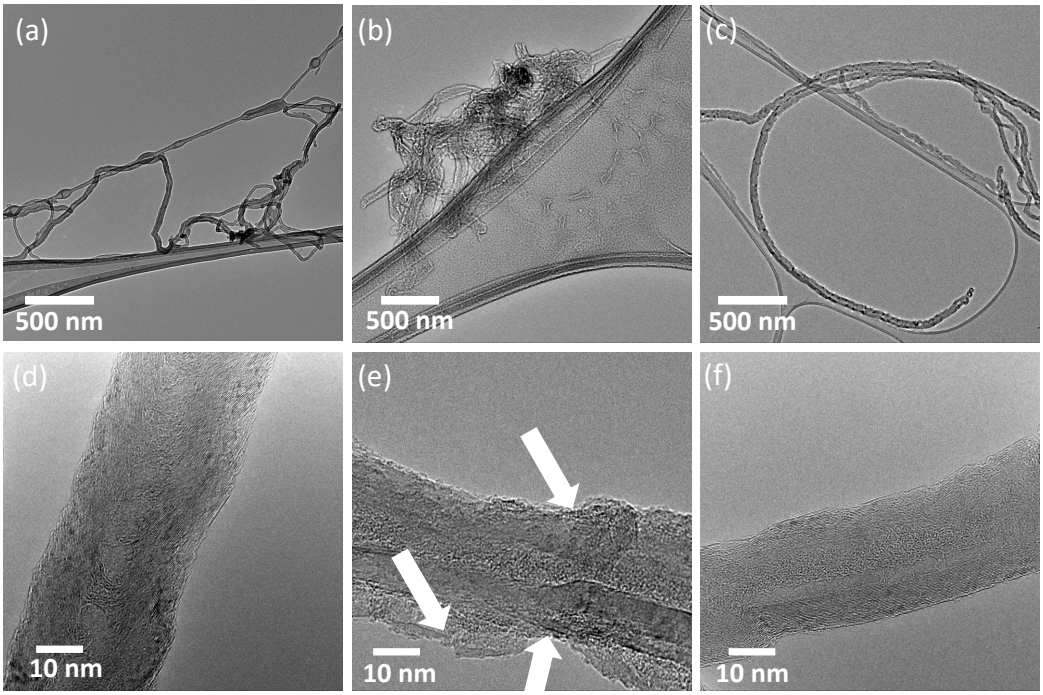

Figure S3. High and low magnification TEM images of as-received CNTs (a,d), HNO_3-treated (b,e), and UV-assisted H_2O_2 treated (c,f).

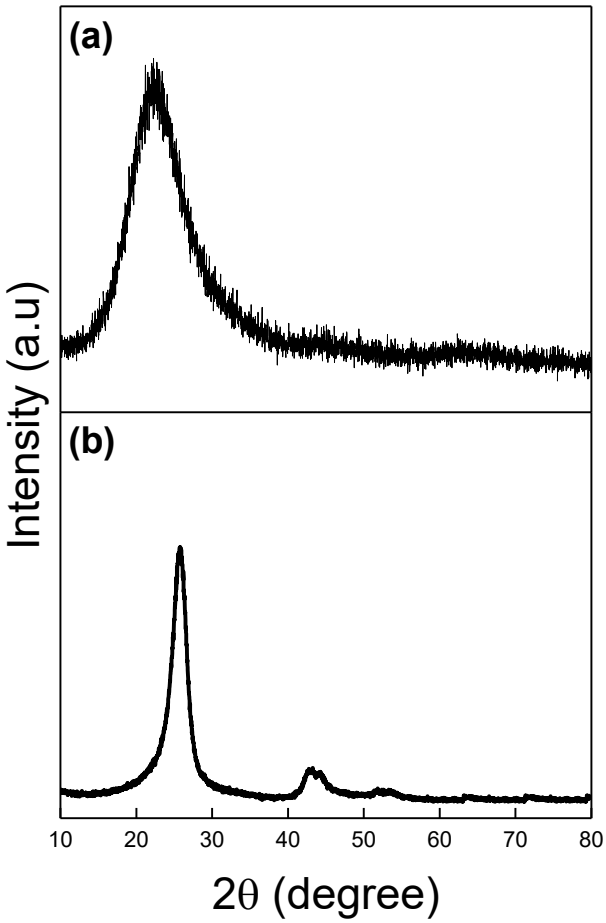

Figure S4. XRD patterns of as received SiO2 (a) and CNT (b).

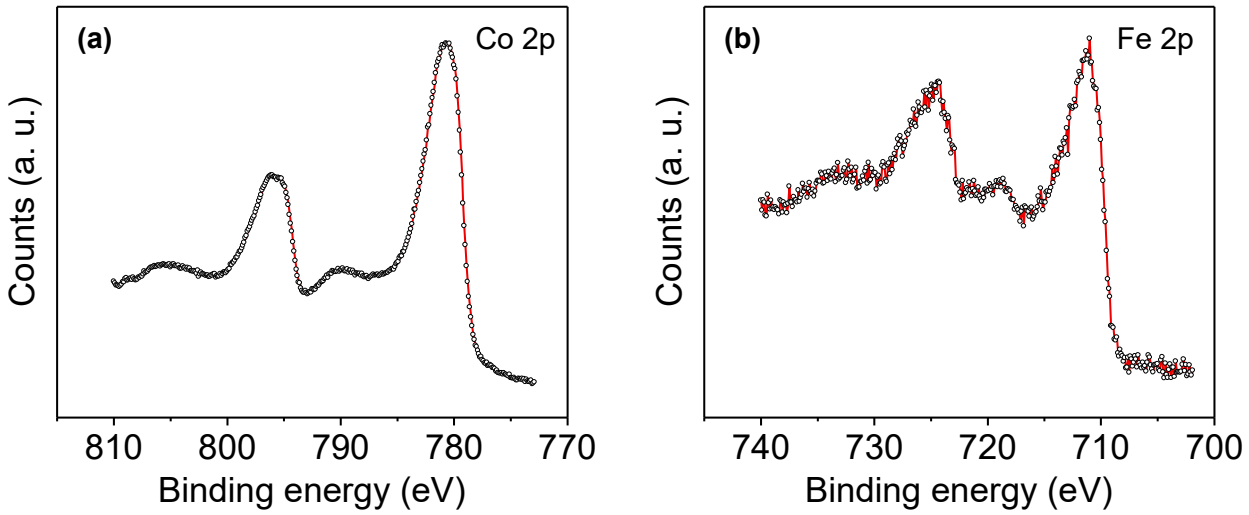

Figure S5. XPS spectra of samples synthesized by photo-Fenton, Co/CNT-Fenton (a) and Fe/CNT-Fenton (b).

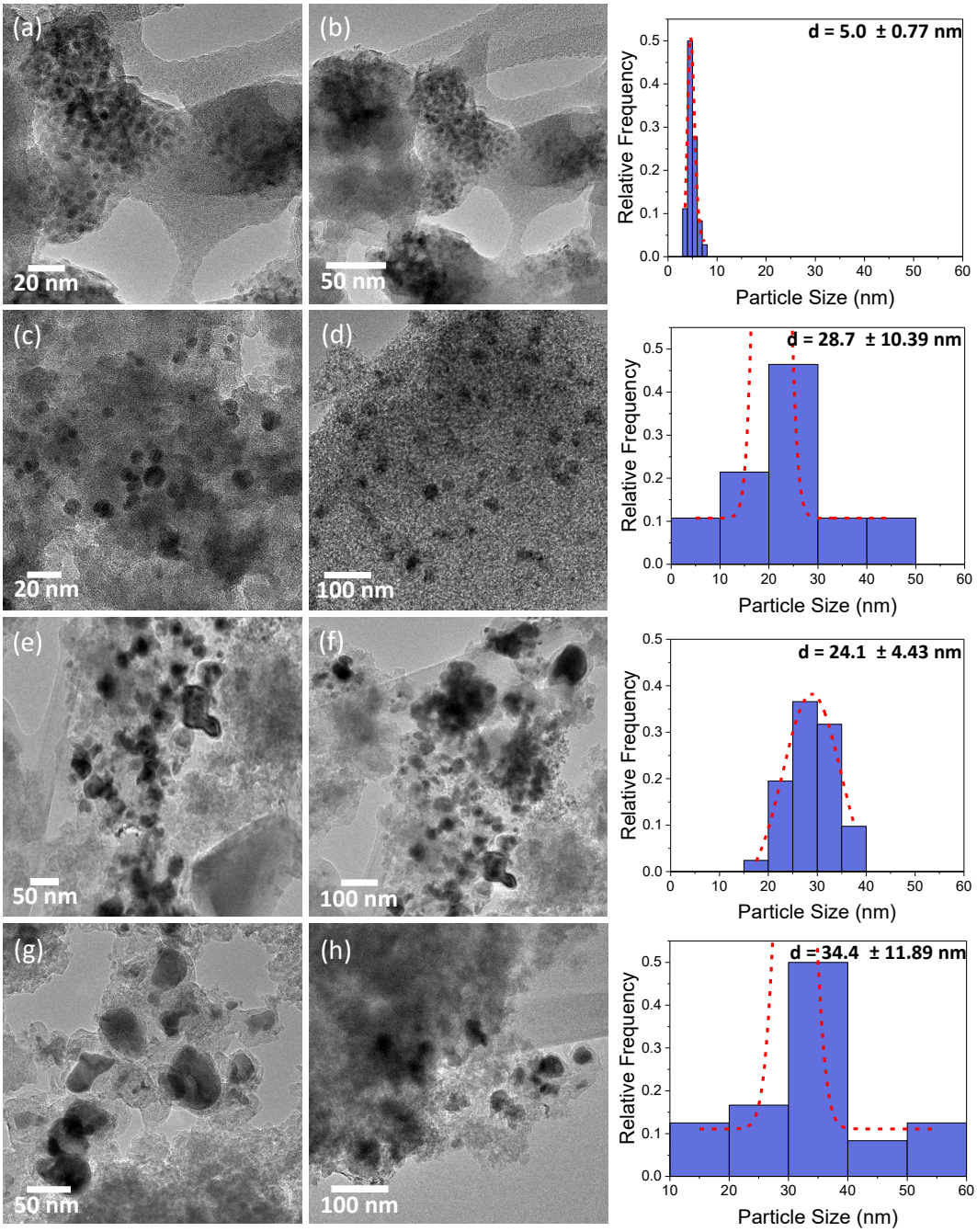

Figure S6. . Low- and high-magnification TEM images and corresponding histograms of PSDs with Gaussian analysis fittings of fresh and used catalysts: fresh_Co/SiO_2-IWI (a,b), fresh_Fe/SiO_2-IWI (c,d), used_ Co/SiO_2-IWI (e,f), and used_ Fe/SiO_2-IWI (g,h).

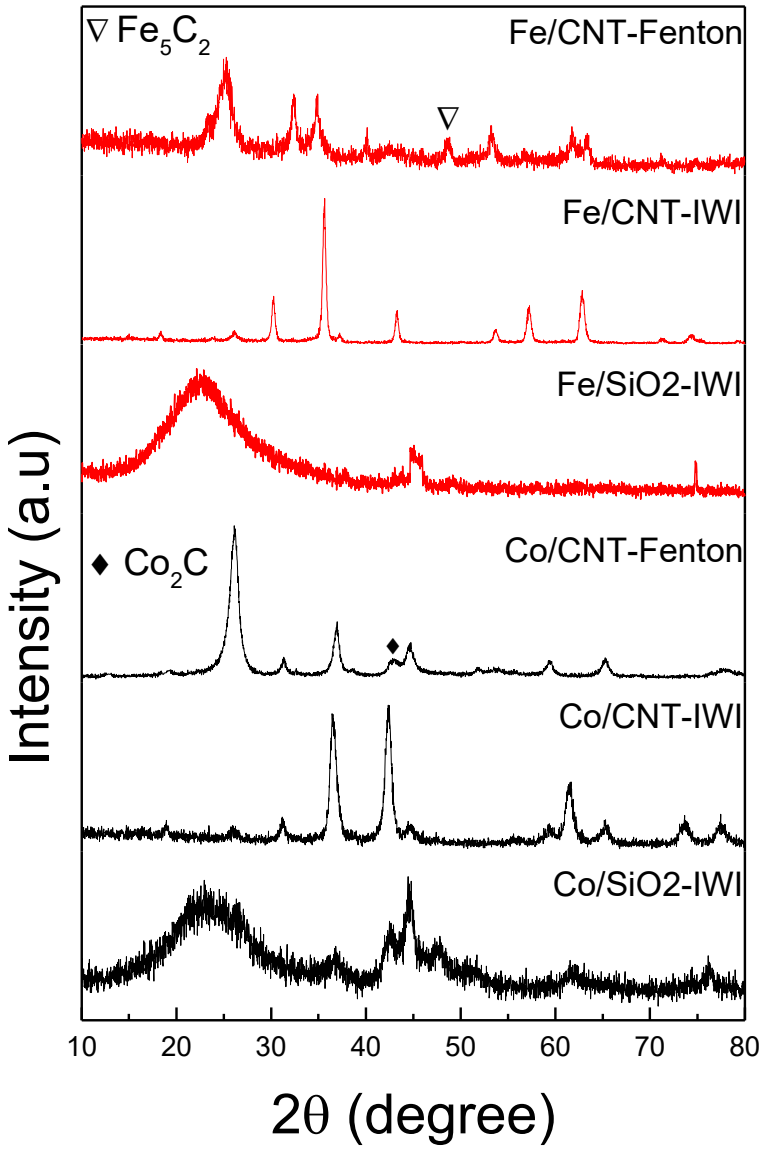

Figure S7. XRD patterns of used Fe and Co catalysts on different supports (CNTs and SiO_2) synthesized by photo-Fenton and IWI methods.

Appendix B - Supplemental Information for Chapter 3

Gaseous Product Mixture from Fischer-Tropsch Synthesis as an Efficient Carbon Source for Low Temperature CVD Growth of Carbon Nanotube Carpets

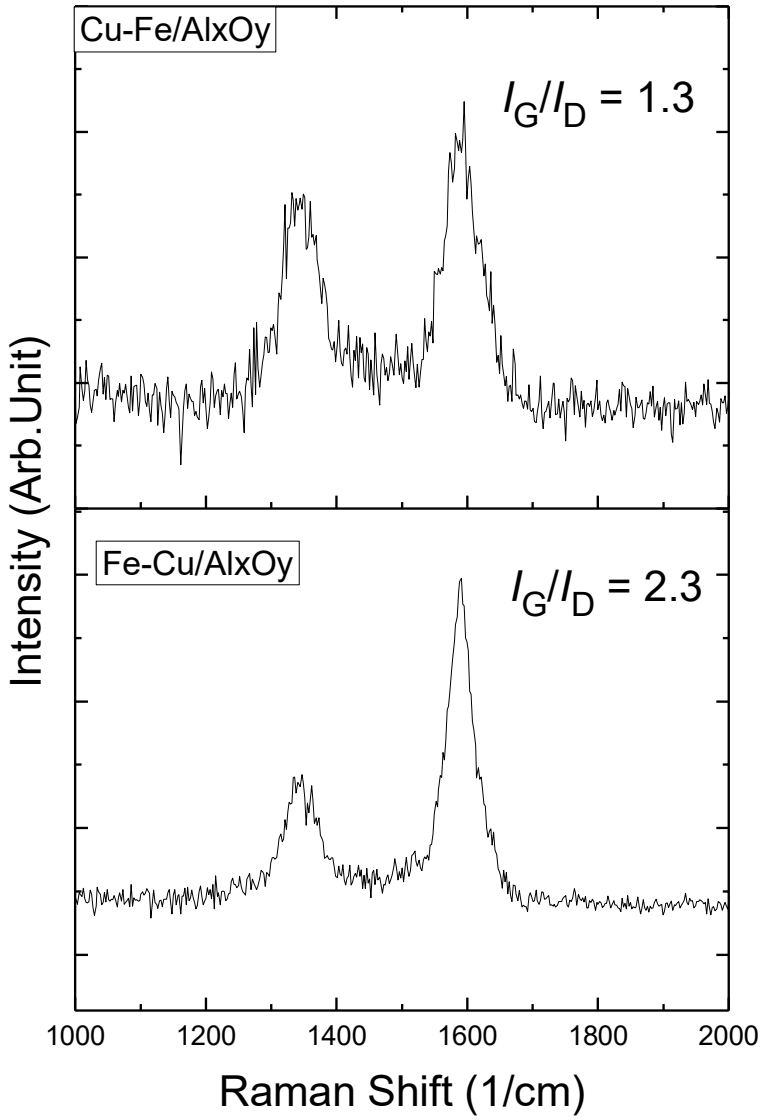

Figure S1. Raman spectra of CNT carpets from Fe-Cu catalysts with the sequence of Fe and Cu depositions reversed to investigate the effect of the different stacking order of metallic layers on CNT carpet growth properties. Fe-Cu/AlxOy catalysts with a thin Cu layer sandwiched between Fe and AlxOy show higher I_G/I_D ratio

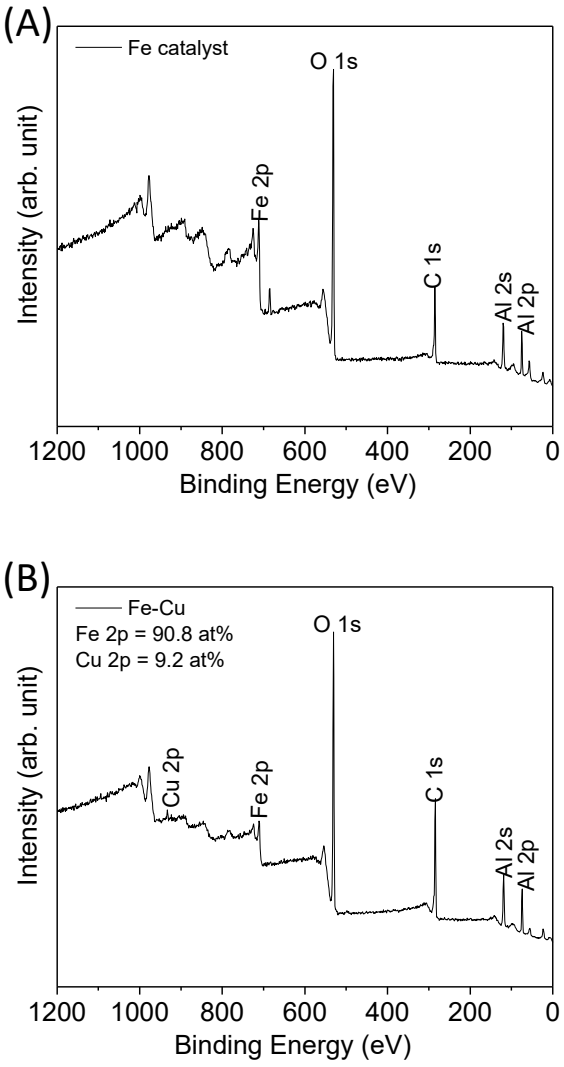

Figure S2. XPS survey scans of Fe (A) and Fe-Cu catalysts with the optimal Cu thickness after CNT carpet growth. The nominal thickness of the Fe, AlxOy, and Cu films were 1.3, 30, and 0.12 nm, respectively; all the films were deposited by an ion beam sputter deposition and etching system.

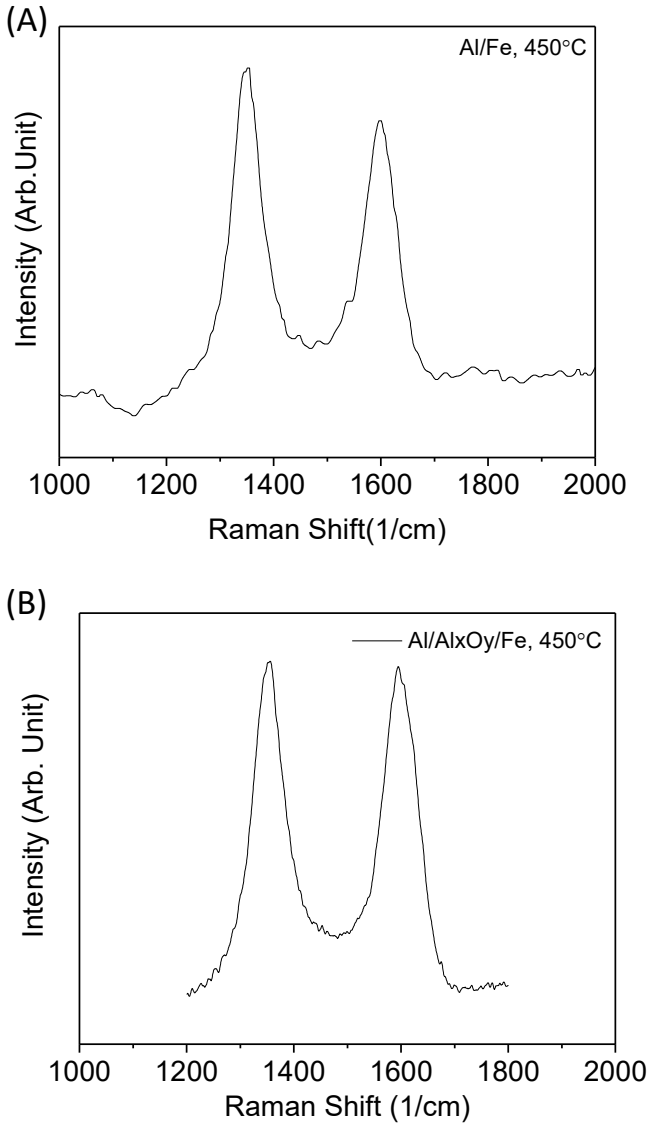

Figure S3. Raman spectra of CNT carpets grown on a 2 nm-thick Fe catalyst deposited directly on Al foil (A) and on Al foil with a 30 nm-thick amorphous Al_xO_y barrier layer (B) at 450°C.

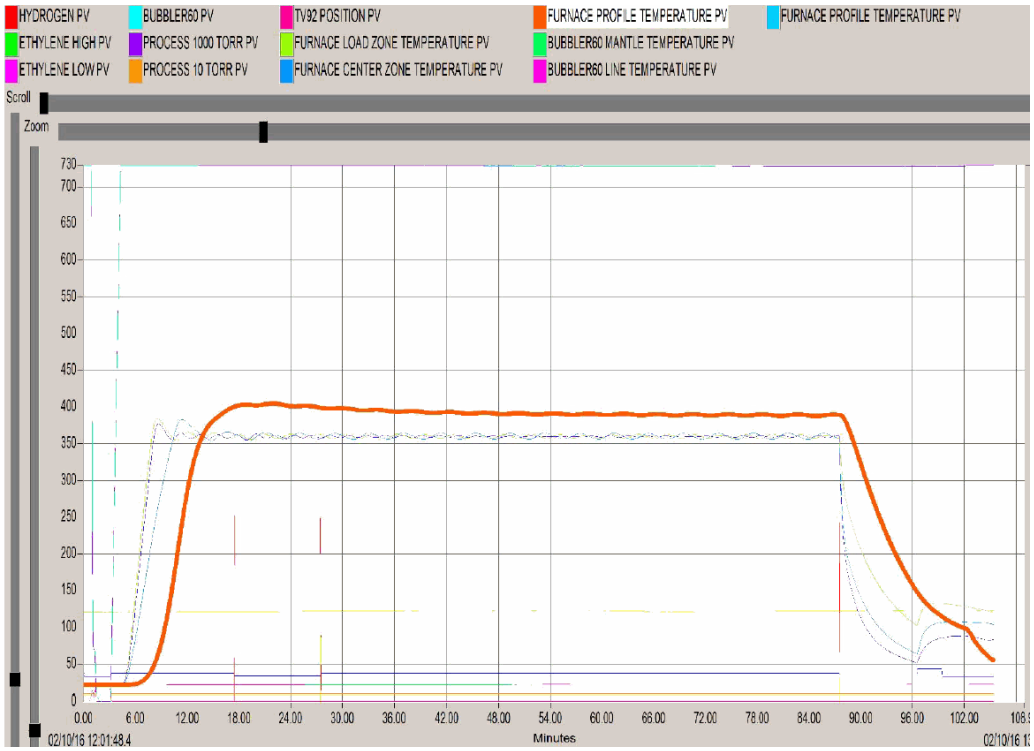

Figure S4. Temperature profile of the CVD reactor during low-temperature growth at 400°C.

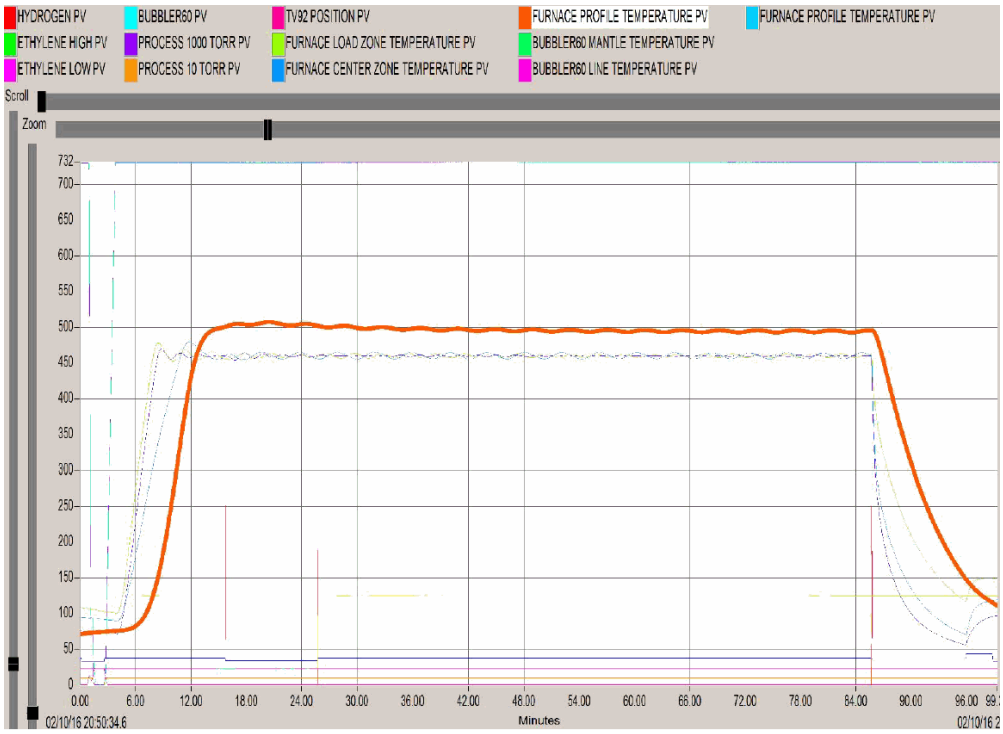

Figure S5. Temperature profile of the CVD reactor during low-temperature growth at 500°C.

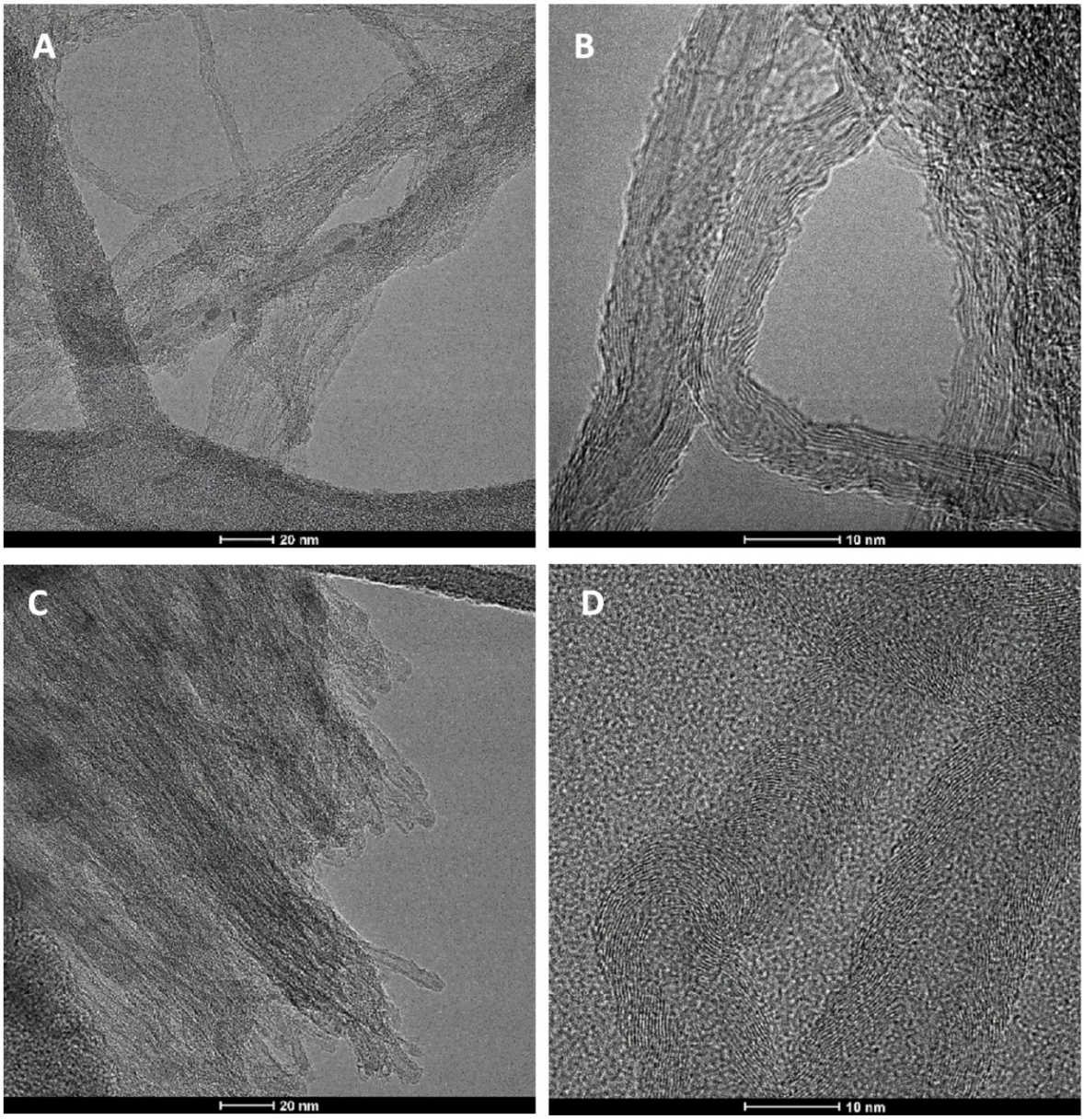

Figure S6. TEM images of CNT carpets grown from Fe (A and B,) and Fe-Cu (C and D) at 400°C.

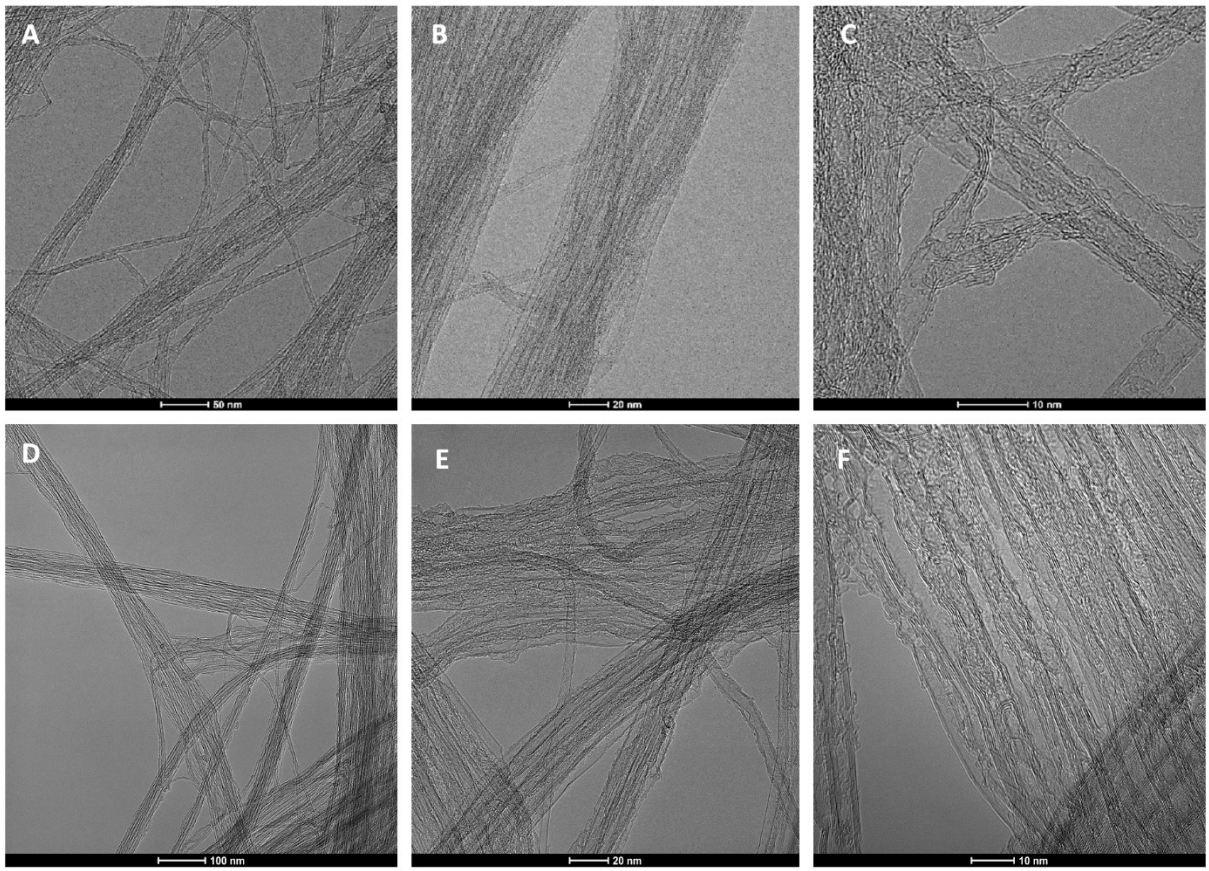

Figure S7. TEM images of CNT carpets grown from Fe (A, B, and C) and Fe-Cu (D, E, and F) at 500°C.

Appendix C - Supplemental Information for Chapter 4

Catalytic CVD Growth of Millimeter-Tall Single-Walled Carbon Nanotube Carpets using an Industrial Gaseous Waste as a Feedstock

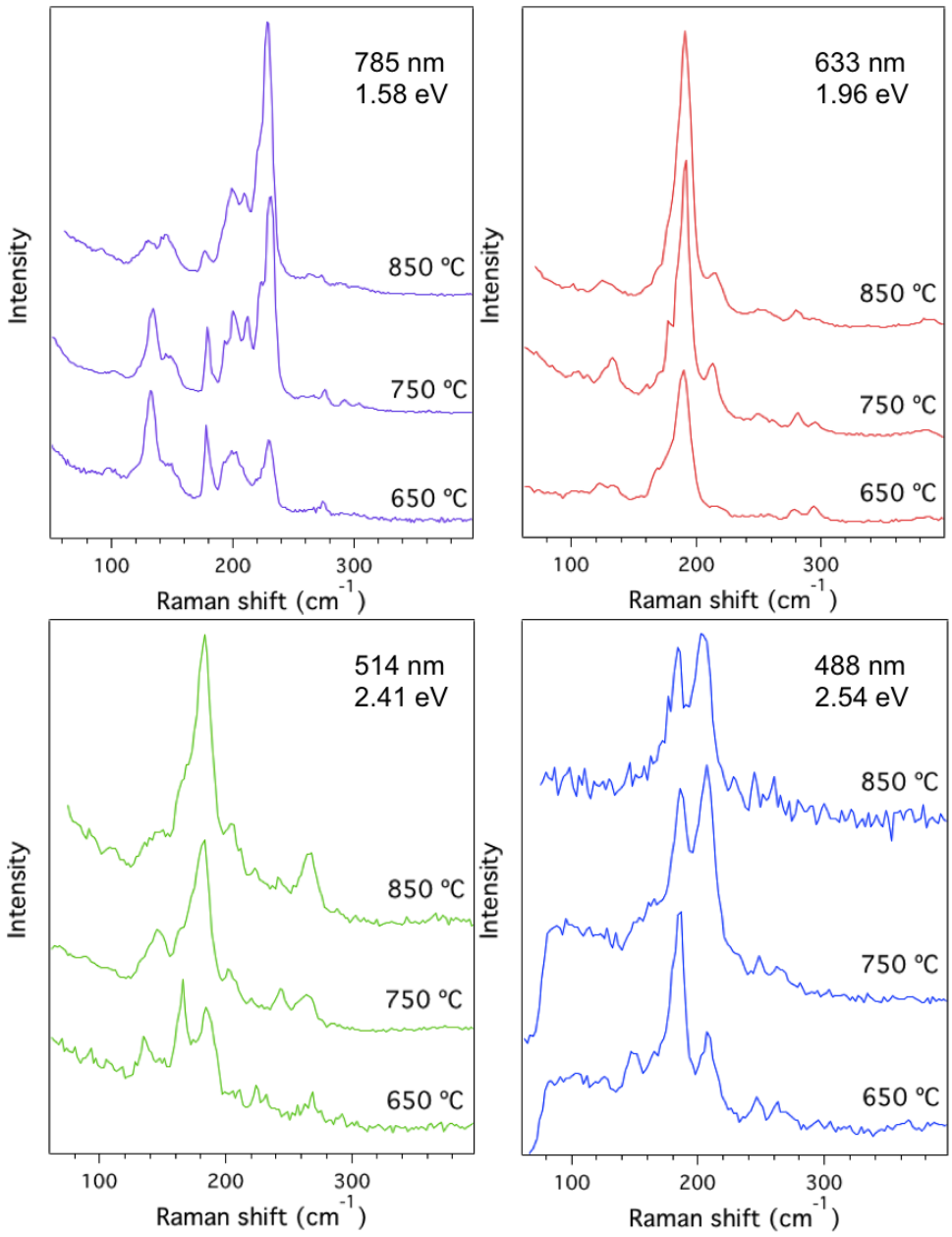

Figure S1. Raman spectra of SWCNT carpets grown by FTS-GP CVD at different temperatures (650, 750 and 850°C) on Fe catalyst acquired using laser excitation energies of 1.58, 1.96, 2.41, and 2.54 eV.

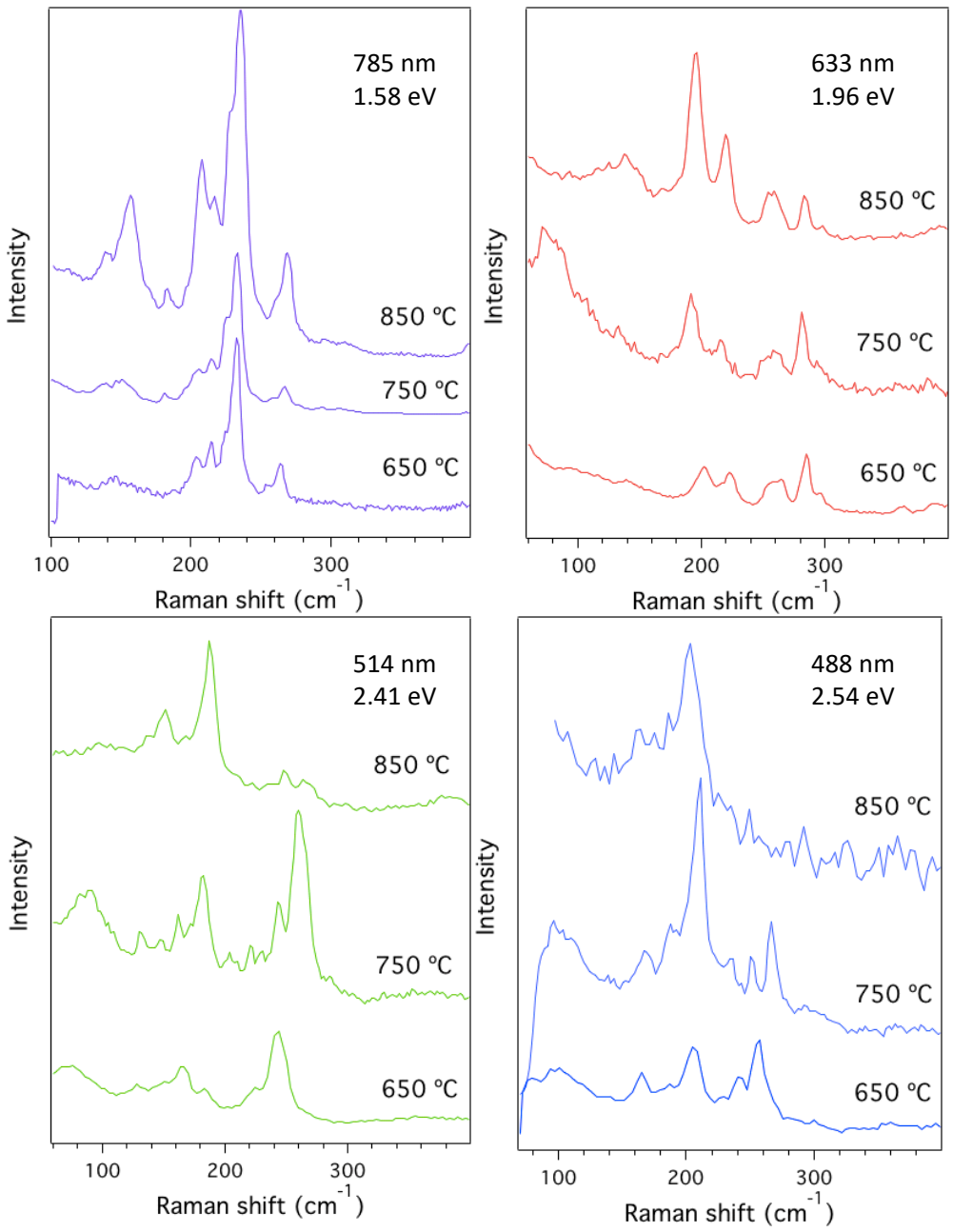

Figure S2. Raman spectra of SWCNT carpets grown by FTS-GP CVD at different temperatures (650, 750 and 850°C) on Co catalyst acquired using laser excitation energies of 1.58, 1.96, 2.41, and 2.54 eV.

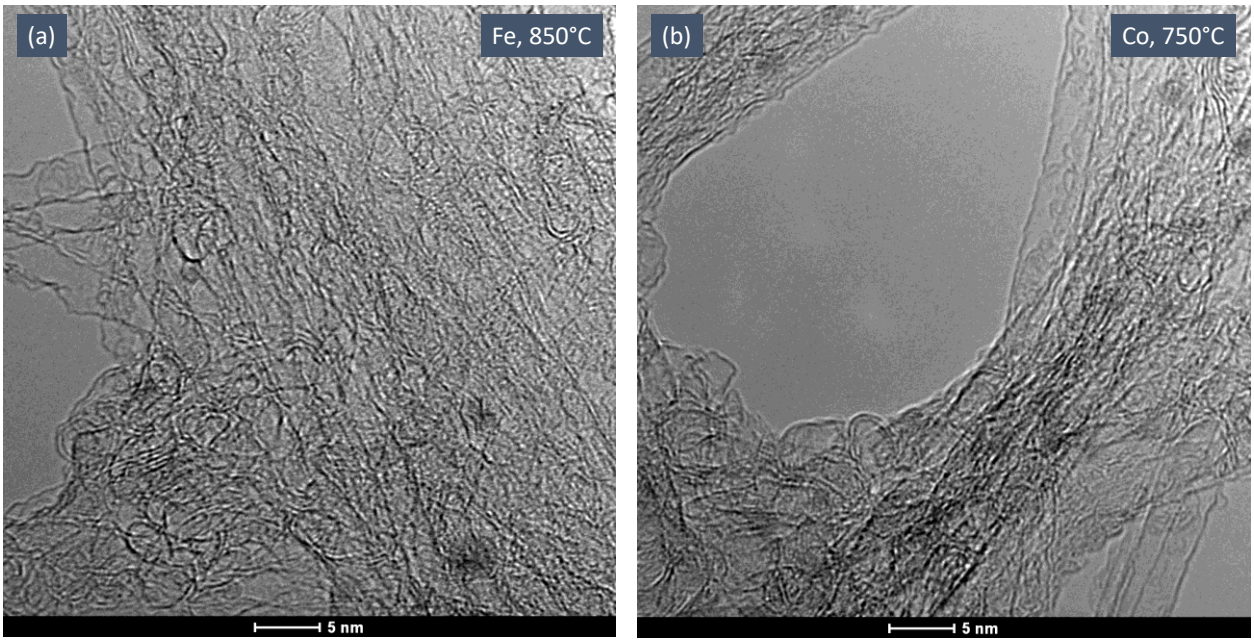

Figure S3. High magnification images of SWCNT carpets grown on Fe and Co at 850°C and 750°C, respectively.

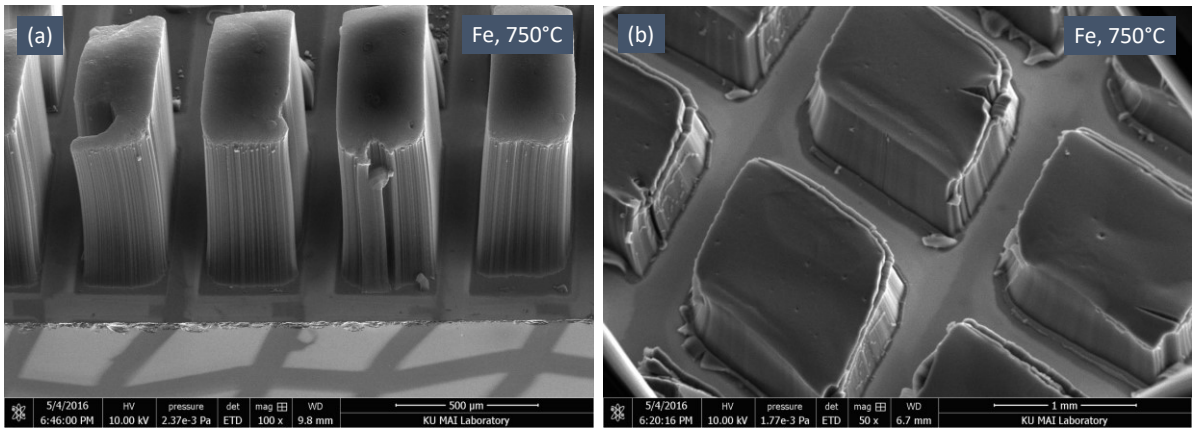

Figure S4. SEM images of SWCNT carpets with different shapes grown from patterned Fe catalyst at 750°C.

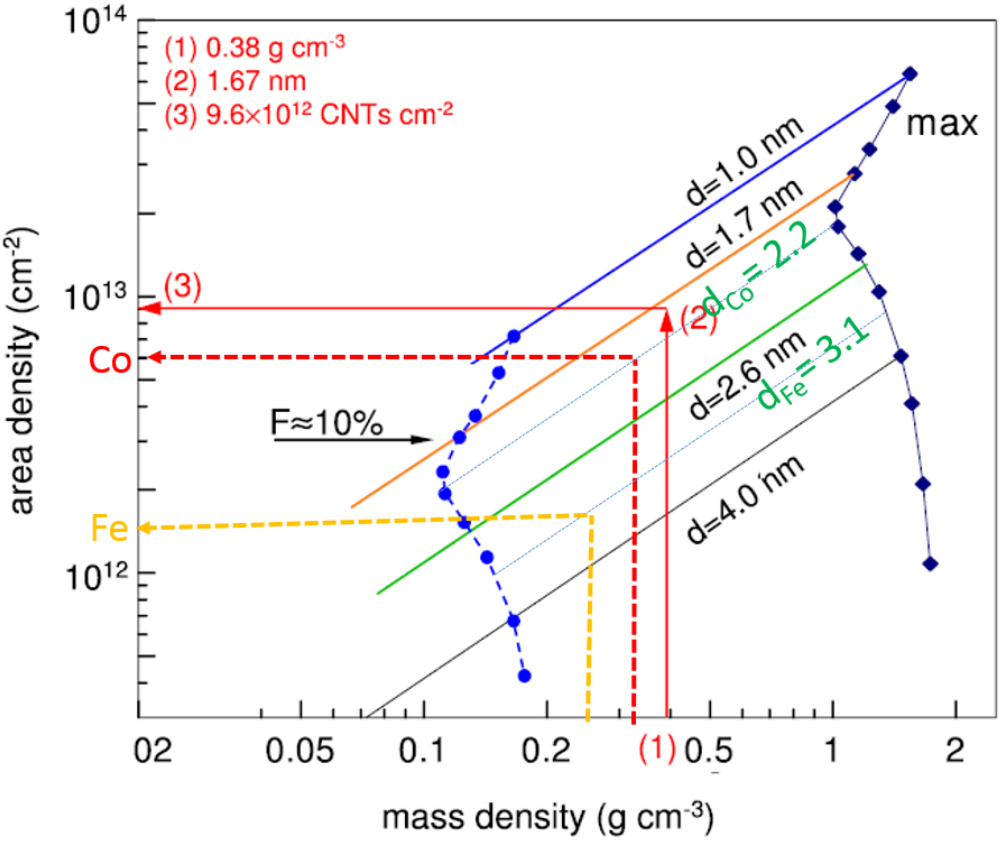

Figure S5. Correlation between area density and mass density of CNT arrays that are closely packed, as a function of SWCNT diameter obtained from Ref. 41. Using values of mass density and mean diameter for SWCNT carpets grown on Fe (mass density = 0.258 g/cm^3, SWCNT diameter = 3.1 nm) and on Co (mass density = 0.321 g/cm^3, SWCNT diameter = 2.2 nm), the area density can be extrapolated from the graph.

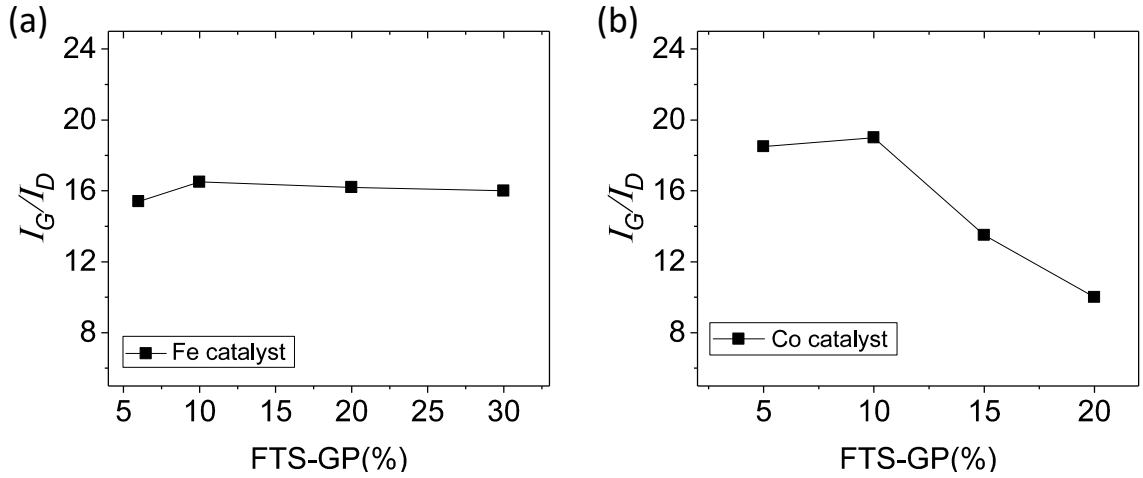

Figure S6. Plots of I_G/I_D as a function of FTS-GP fraction for SWCNT carpets grown on Fe (a) and Co (b). The I_G/I_D were obtained from Raman spectra of SWCNT carpets acquired using an excitation source with a wavelength of 532 nm.

Appendix D - Supplemental Information for Chapter 6

Chiral and diameter control of SWCNTs using high melting point metals as promoters

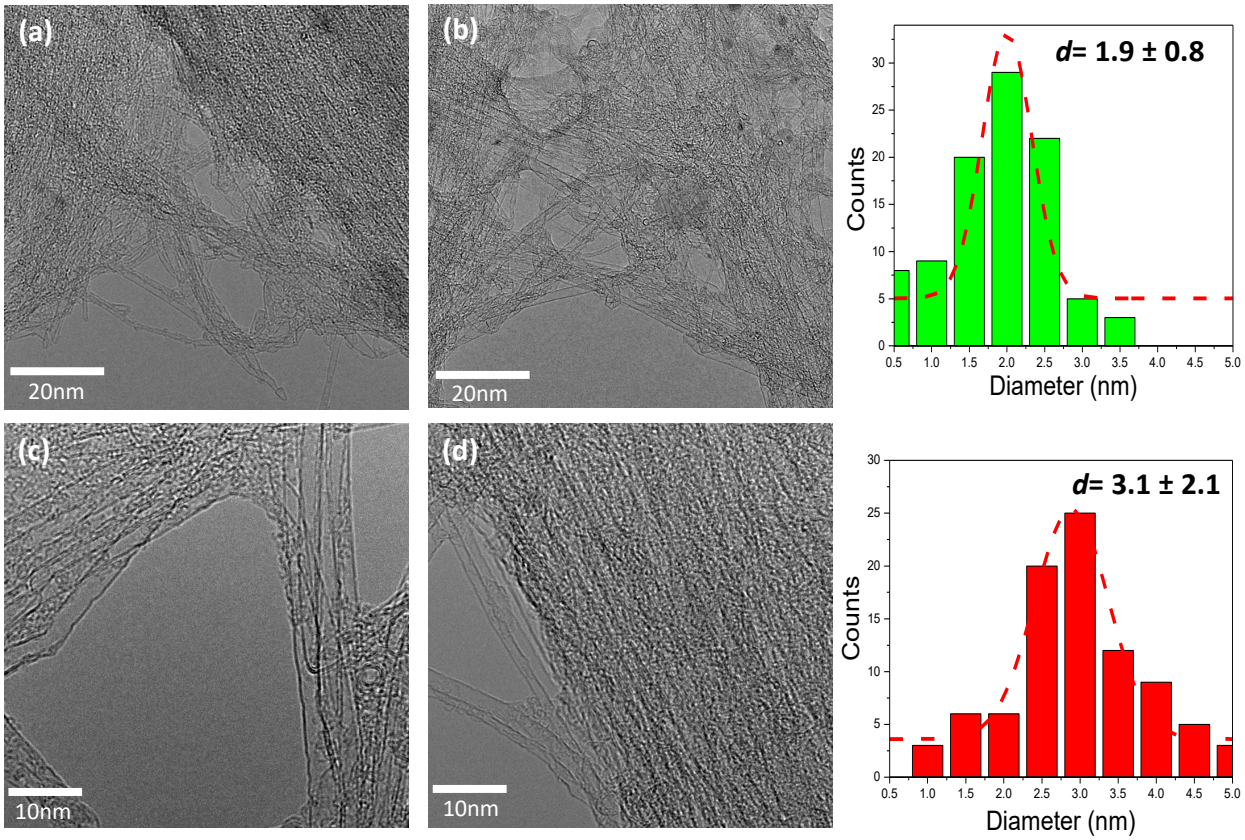

Figure 2. HR-TEM images of SWCNT grown by FTS-GP CVD at 750˚C. (a,b) SWCNTs grown on a Fe/Ru catalyst. (c,d) SWCNTs grown on a Fe catalyst. Histogram of SWCNT diameter distributions and their Gaussian fits of SWCNT grown on Fe/Ru catalysts and Co catalysts.

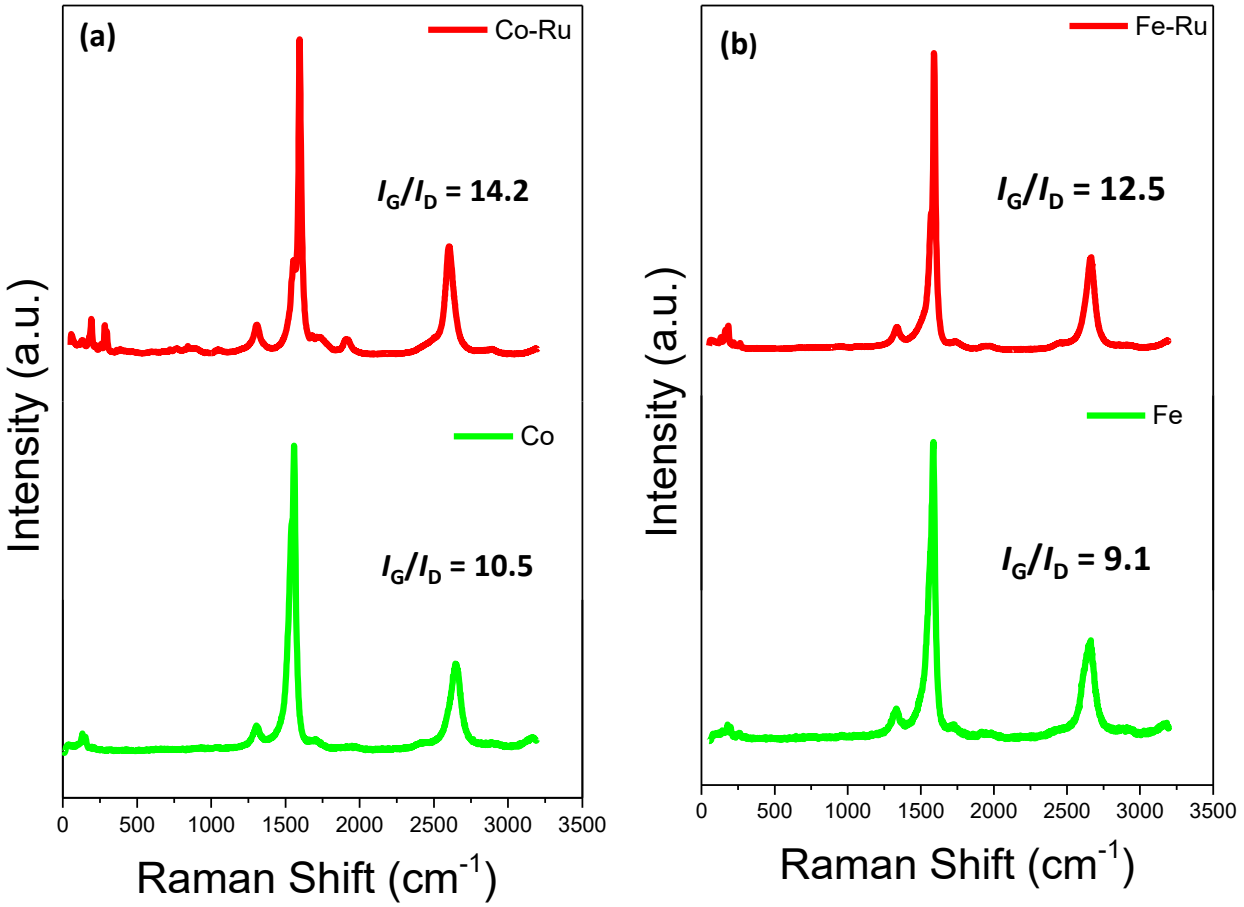

Figure S2. 1. Raman spectra of SWCNT carpets grown by FTS-GP CVD at 750ºC on Fe and Fe/Ru catalysts (a) and at 850 ºC on Co and Co/Ru catalysts (b), using a laser excitation energy source of 1.96 eV.

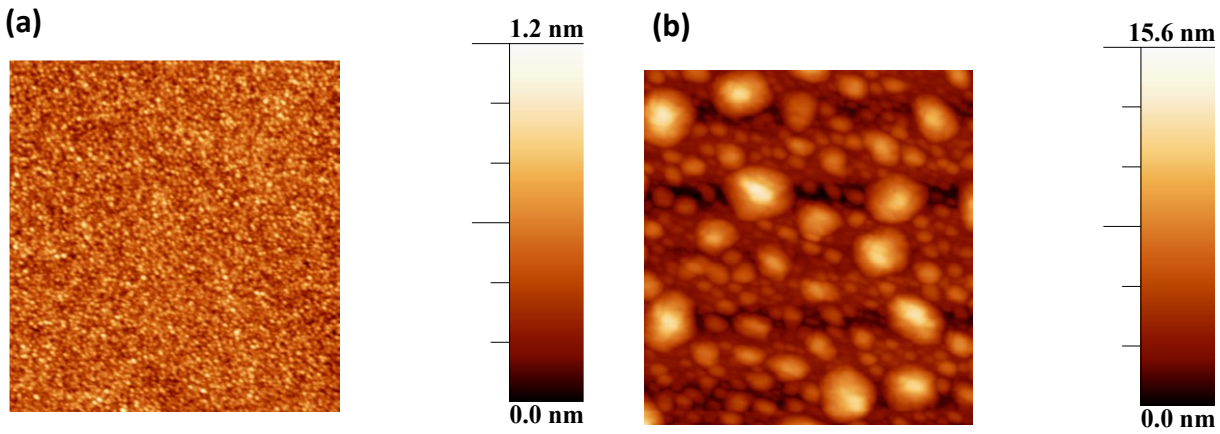

Figure S3. 3D AFM images of catalysts nanoparticles formed on the substrate after annealing (for 5 min) in H_2 at 850˚C for (a) Co/Ru catalyst and (b) Co catalyst.

Appendix E - Supplemental Information for Chapter 7

Batch Reactor for the Scale-up Production of Carbon Nanomaterials

Table S1. BET surface area meaurments of CNT and OLC using SCF approach.

Samples	Surface area (m^2/g)	Total pore volume(cm^3/g)	Average pore size (Å)
CNT using toluene without water, 600°C	90.66	0.63	277.5
CNT using Toluene with 0.05 ml water at 600°C	95.70	0.71	298.9
CNT using toluene at 500°C	45.41	0.13	113.9
OLC using Ethanol at 600°C	67.67	0.22	127.9
OLC using Toluene and 0.1 ml water at 600°C	75.58	0.36	188.1

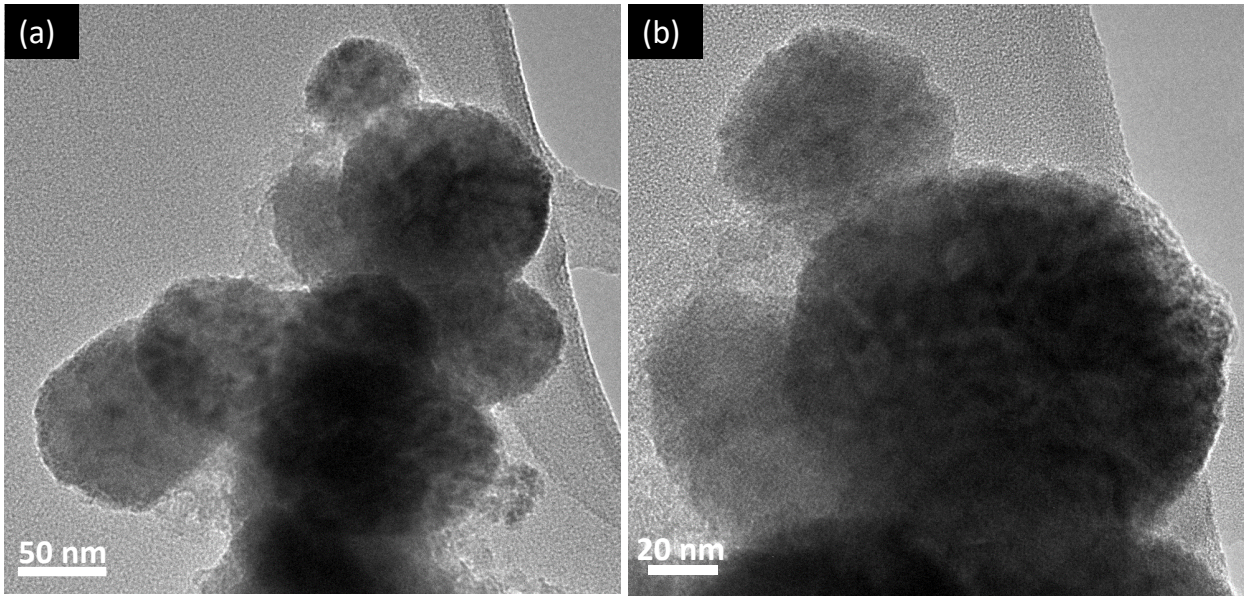

Figure S1. TEM images showing the OLC structure obtained by under supercritical condition of 0.035 mole/liter ferrocene in toluene solution at 400˚C.

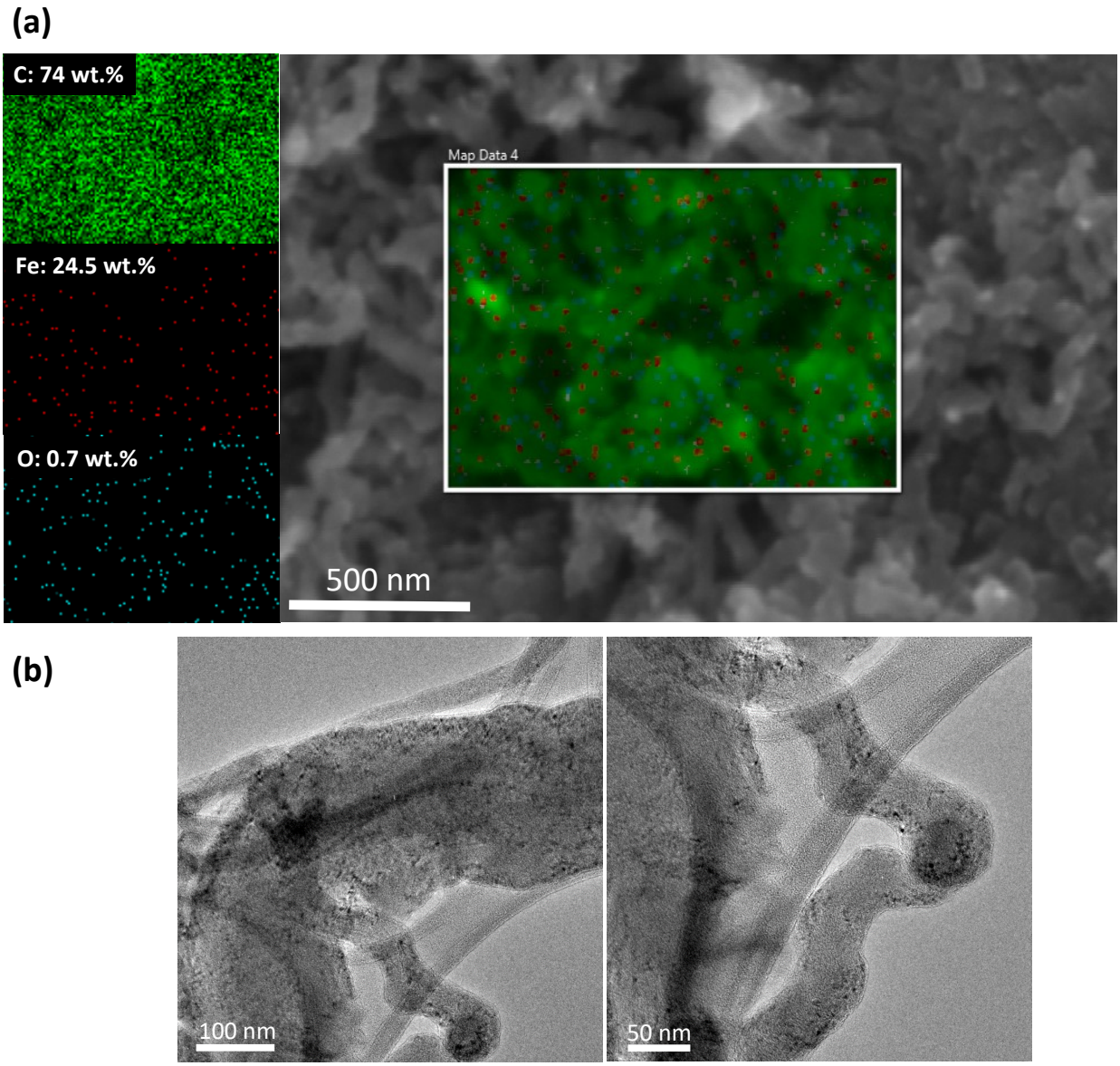

Figure S2. (a) SEM/EDS image showing the Fe nanoparticles deposited on the exterior surface of CNT at 600°C using 0.036 mole/liter of ferrocene in toluene solution, (b) TEM images of iron particles decorating the exterior surface of CNT.

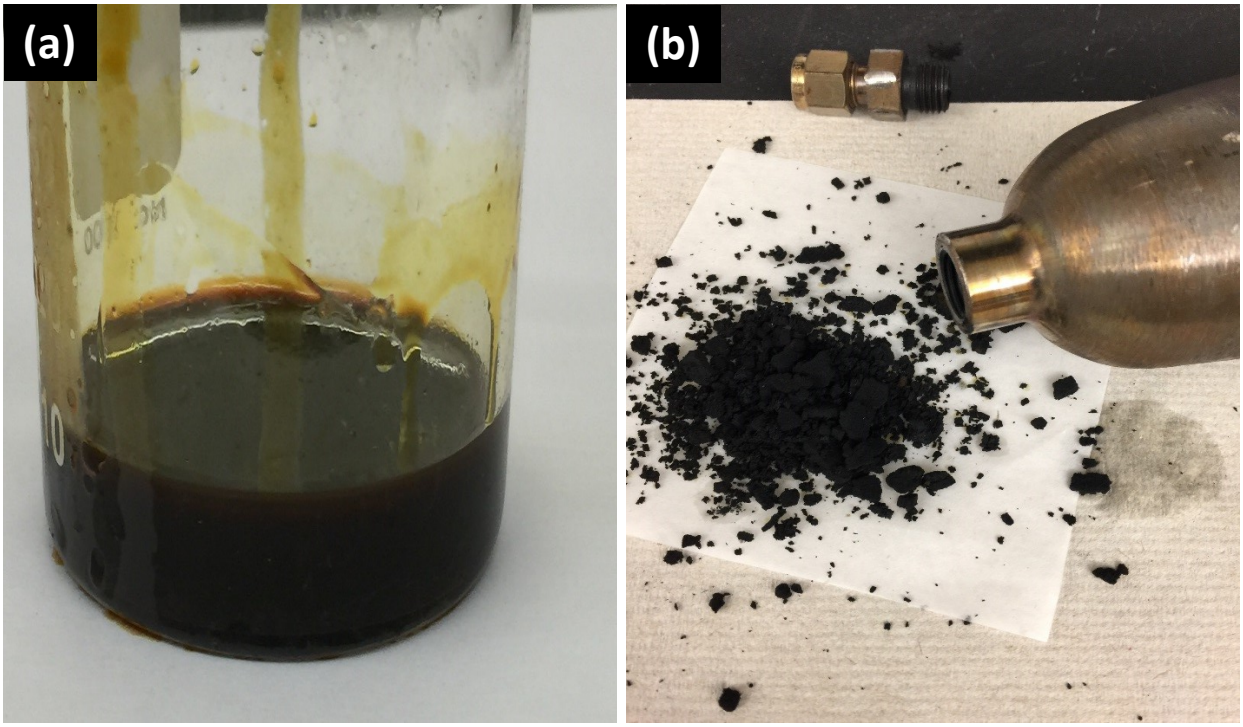

Figure S3. Images of the obtained products after 1.5 h at 600˚C for (a) 0.0018 mole/liter of ferrocene in toluene solution, (b) 0.036 mole/liter of ferrocene in toluene solution.

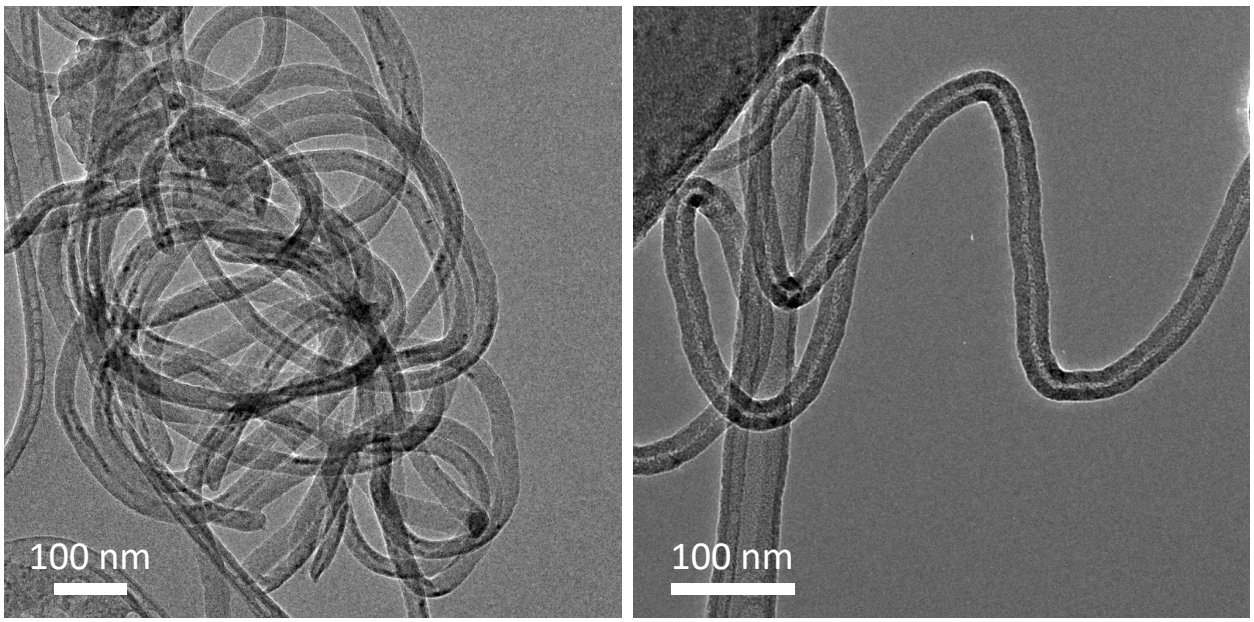

Figure S4. TEM images of CNTs synthesized with 0.036 mole/liter of ferrocene in toluene solution and 0.05 ml of water at 600˚C.

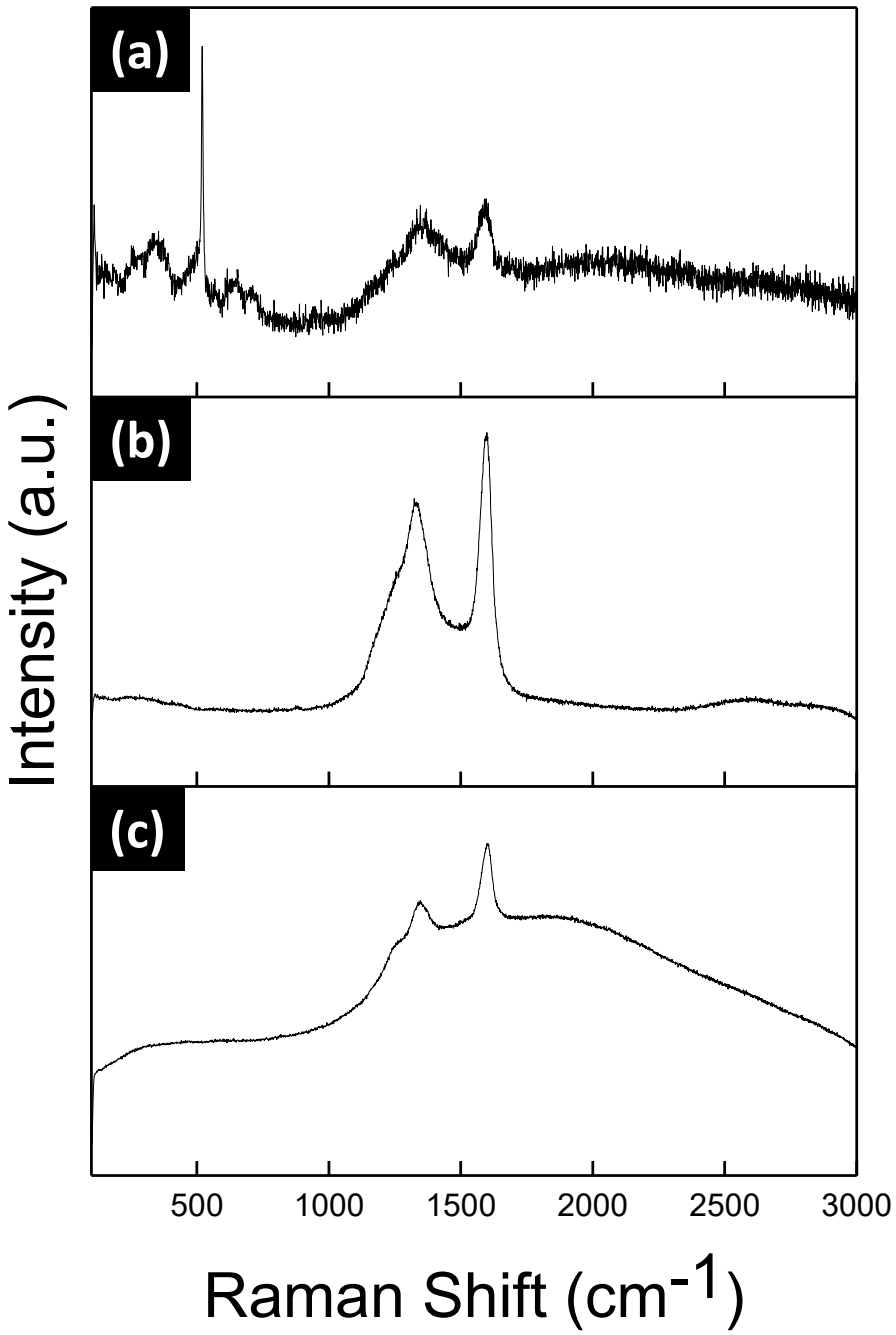

Figure S5. Raman spectroscopy of different alcohol precursors (30ml) in supercritical reaction media, growth temperature 600˚C, with 0.2 g of ferrocene, (a) ethanol, (b) propanol, (c) butanol.

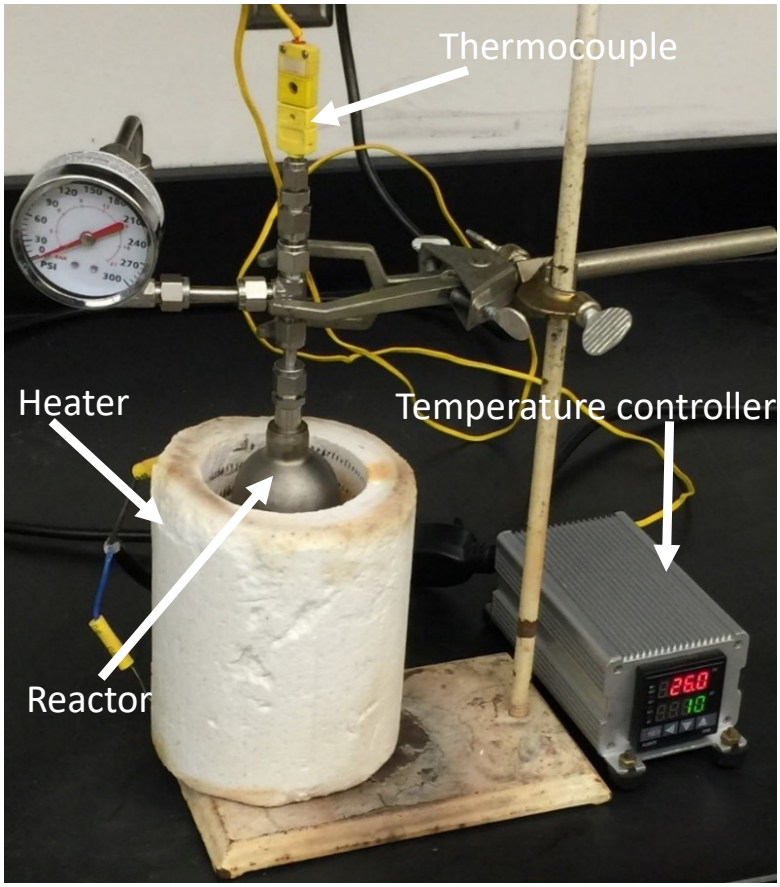

Figure S4. Batch reactor used for the supercritical fluid approach.

Appendix F - Copyright permissions

RE: Re-use permission request

CONTRACTS-COPYRIGHT (shared) <Contracts-Copyright@rsc.org>

Thu 10/12/2017 3:17 AM

To:Haider Almkhelfe <halwan@ksu.edu>;

Dear Haider

The Royal Society of Chemistry (RSC) hereby grants permission for the use of your paper(s) specified below in the printed and microfilm version of your thesis. You may also make available the PDF version of your paper(s) that the RSC sent to the corresponding author(s) of your paper(s) upon publication of the paper(s) in the following ways: in your thesis via any website that your university may have for the deposition of theses, via your university's Intranet or via your own personal website. We are however unable to grant you permission to include the PDF version of the paper(s) on its own in your institutional repository. The Royal Society of Chemistry is a signatory to the STM Guidelines on Permissions (available on request).

Please note that if the material specified below or any part of it appears with credit or acknowledgement to a third party then you must also secure permission from that third party before reproducing that material.

Please ensure that the thesis states the following:
Reproduced by permission of The Royal Society of Chemistry
and include a link to the paper on the Royal Society of Chemistry's website.

Please ensure that your co-authors are aware that you are including the paper in your thesis.

Regards
Gill Cockhead
Publishing Contracts & Copyright Executive

Gill Cockhead
Publishing Contracts & Copyright Executive
Royal Society of Chemistry,
Thomas Graham House,
Science Park, Milton Road,
Cambridge, CB4 0WF, UK
Tel +44 (0) 1223 432134

Follow the Royal Society of Chemistry:
www.rsc.org/follow

Winner of The Queen's Award for Enterprise, International Trade 2013

When you publish in a Royal Society of Chemistry journal, you keep the copyright of the manuscript. On this page you can learn more about our Licence to Publish and the rights you retain as an author. We also explain where you can deposit and share your article, and how to request permission to re-use other people's work.

The following details apply only to authors accepting the standard Licence to Publish. Authors who are interested in publishing open access should visit our open access pages for more information about our open access licences (/journals-books-databases/open-access/#choose) and deposition rights.

On this page

About our licence to publish (/journals-books-databases/journal-authors-reviewers/licences-copyright-permissions/#about-licence) Rights retained by authors (/journals-books-databases/journal-authors-reviewers/licences-copyright-permissions/#author-rights) Deposition & sharing rights (/journals-books-databases/journal-authors-reviewers/licences-copyright-permissions/#deposition-sharing) Re-use permission requests (/journals-books-databases/journal-authors-reviewers/licences-copyright-permissions/#reuse-permission-requests)

About our licence to publish

In order to publish material the Royal Society of Chemistry must acquire the necessary legal rights from the author(s) of that material. In general, we must obtain from the original author(s) the right to publish the material in all formats, in all media (including specifically print and electronic), with the right to sublicense those rights.

For all articles published in our journals, we require the author to accept a 'licence to publish'. This licence is normally requested on submission of the article. By signing this licence the author (who is either the copyright owner or who is authorised to sign on behalf of the copyright owner, for example his/her employer) grants to the Royal Society of Chemistry "the exclusive right and licence throughout the world to edit, adapt, translate, reproduce and publish the manuscript in all formats, in all media and by all means (whether now existing or in future devised)".

The Royal Society of Chemistry thus acquires an exclusive licence to publish and all practical rights to the manuscript, except the copyright. The copyright of the manuscript remains with the copyright owner. The copyright owner also retains certain rights regarding the sharing and deposition (/journals-books-databases/journal-authors-reviewers/licences-copyright-permissions/#deposition-sharing) of their article and the re-use of the published material (/journals-books-databases/journal-authors-reviewers/licences-copyright-permissions/#reuse-permission-requests). For short items in journals (news items, etc) we take a non-exclusive licence in the form of a brief 'terms and conditions for acceptance' document.

ELSEVIER LICENSE
TERMS AND CONDITIONS

Oct 03, 2017

This Agreement between Kansas State University -- Haider Almkhelfe ("You") and Elsevier ("Elsevier") consists of your license details and the terms and conditions provided by Elsevier and Copyright Clearance Center.

License Number	4201621385415
License date	Oct 03, 2017
Licensed Content Publisher	Elsevier
Licensed Content Publication	Carbon
Licensed Content Title	Catalytic CVD growth of millimeter-tall single-wall carbon nanotube carpets using industrial gaseous waste as a feedstock
Licensed Content Author	Haider Almkhelfe,Xu Li,Rahul Rao,Placidus B. Amama
Licensed Content Date	May 1, 2017
Licensed Content Volume	116
Licensed Content Issue	n/a
Licensed Content Pages	10
Start Page	181
End Page	190
Type of Use	reuse in a thesis/dissertation
Portion	full article
Format	both print and electronic
Are you the author of this Elsevier article?	Yes
Will you be translating?	No
Title of your thesis/dissertation	Scalable Carbon Nanotube Growth and Design of Efficient Catalysts for Fischer-Tropsch Synthesis
Expected completion date	Nov 2017
Estimated size (number of pages)	110
Requestor Location	Kansas State University 1005 Durland Hall 1701A Platt St Chemical Engineering MANHATTAN, KS 66502 United States Attn: Kansas State University
Publisher Tax ID	98-0397604
Total	0.00 USD
Terms and Conditions	

INTRODUCTION

1. The publisher for this copyrighted material is Elsevier. By clicking "accept" in connection with completing this licensing transaction, you agree that the following terms and conditions apply to this transaction (along with the Billing and Payment terms and conditions